

Flow-Induced Vibration of a Circular Cylinder Undergoing Rotary Motions

by

Ka Wai Lawrence Wong

A Thesis submitted to Monash University
for the degree of
Doctor of Philosophy

August 2017

Department of Mechanical and Aerospace Engineering
Monash University

Notices

1. Under the Copyright Act 1968, this thesis must be used only under the normal conditions of scholarly fair dealing. In particular no results or conclusions should be extracted from it, nor should it be copied or closely paraphrased in whole or in part without the written consent of the author. Proper written acknowledgement should be made for any assistance obtained from this thesis.
2. I certify that I have made all reasonable efforts to secure copyright permissions for third-party content included in this thesis and have not knowingly added copyright content to my work without the owner's permission.

This thesis is dedicated to my parents


Eric Wong,

and

Willa Lam.

Statement of Originality

I, Ka Wai Lawrence Wong, declare that this thesis is my own work and contains no material that has been accepted for the award of a degree or diploma in this, or any other, university. To the best of my knowledge and belief, information derived from the published and unpublished work of others has been acknowledged in the text of the thesis and a list of references is provided in the bibliography.



Candidate: Ka Wai Lawrence Wong

Submitted: 18 August 2017

Abstract

This thesis investigates the effect of active vortex-induced vibration (VIV) suppression methods on an elastically-mounted circular cylinder over a range of flow and rotary forcing parameters. Two active suppression methods are of particular interest, one involves forcing the cylinder to undergo constant rate rotation and the other involves forcing the cylinder to undergo sinusoidal rotary oscillation. Consequently, this thesis consists of two main components. The first component focuses on constant rate rotation. Using displacement and imaging data, the dynamic response and wake structure of an elastically-mounted circular cylinder undergoing crossflow VIV and constant rate rotation is studied. The second component characterises the dynamic response and wake structure of an elastically-mounted circular cylinder undergoing crossflow VIV and sinusoidal rotary oscillations.

In order to characterise the response and wake of a rotating cylinder, a low-friction air bearing was used to elastically-mount the test cylinder such that it oscillates only in the crossflow direction. A rotation rig was designed and built to control the rotary motion of the cylinder.

Active VIV suppression methods have been studied in the past with varying level of effectiveness. Constant rate rotation is of particular interest to researchers due to its simplicity and relevance to industrial applications such as offshore oil and gas exploration. A number of studies involving rotating a rigid cylinder have shown its ability to suppress vortex shedding, which is a key component to VIV. Limited studies have been done to examine the effect of constant rotation on an elastically-mounted cylinder. Of the few studies done, they are limited to very low Reynolds numbers. The present study investigates the effectiveness of constant rotation on an elastically-mounted cylinder at higher Reynolds numbers where the intrinsic flow characteristics are different. Results from the present study showed that at sufficiently high rates of rotation, vortex shedding and large amplitude vibrations cease. Constant rate rotation is found to introduce asymmetry to some of the known VIV wake patterns. Some new wake structures were also observed. The dynamic response of the cylinder undergoing rotation are generally different to that of a non-rotating cylinder. Compared to similar studies at very low Reynolds numbers, results from the present study exhibit some similar trends for some response variables.

The second active suppression technique involves sinusoidal rotary oscillations. A number of studies have been done on rigid cylinders and found rotary oscillation to be very effective at suppressing large fluid forces at certain rotary forcing parameters. One other study was done on an elastic body at a very low Reynolds number. The present study showed that previously observed response trends continue at higher Reynolds numbers. At certain combinations of forcing parameters, large amplitude oscillations are suppressed. The wake structure from imaging results showed that an elastically-mounted cylinder undergoing rotary oscillations is generally different to those seen in non-rotating VIV and rigid rotary oscillation studies.

Acknowledgements

My PhD is one of the longest and the most challenging journeys I have undertaken. There are many people who have assisted and supported me over my candidature.

Firstly, I would like to thank my primary supervisors, Prof. John Sheridan and Prof. Mark Thompson. John gave me the opportunity to do research as a part of the FLAIR group. Under John and Mark's guidance I am able to complete my research and thesis. They supported me with their wealth of scientific knowledge and experience in research. Their understanding, patience and encouragement had a profound impact on my PhD and the completion of this thesis. Furthermore, I would like to thank them for the financial support and opportunity for me to attend conferences and present my research.

I would like to thank my co-supervisors, Dr. David Lo Jacono and Dr. Jisheng Zhao. Their continual support and supervision is wholeheartedly appreciated. I am thankful for their assistance during my PhD and I have learnt a lot by working with them.

I would also like to acknowledge the financial support from Australian Research Council (ARC) Discovery Project grants DP110102141 and DP150102879 for my research project. I acknowledge that my living expenses throughout my PhD candidature is covered in form of a scholarship. This scholarship is a Commonwealth sponsored Australian Postgraduate Award (APA). Furthermore, I would like to thank and acknowledge the financial support from Monash University and its Department of Mechanical and Aerospace Engineering.

A number of administrative staffs of the Department of Mechanical and Aerospace Engineering have provided their support during my candidature. Among others, I would like to thank Stelios Konstantinidis, Fiona Pyrczak, Helen Frost, Nicole Bodenstaff, Bev Pearce and Jacelyn Tan for their support. A significant part of this research project is the experiment apparatus, I must thank the technical expertise and workmanship of the mechanical engineering workshop staffs who helped constructed the rotation rig and test cylinder; especially Hugh Venables, Nat DeRose, Andrew Smith and Mark Symonds.

A number of colleagues from FLAIR have had an impact on my research and my experience as a PhD candidate through their knowledge in fluid mechanics, support, technical assistance and friendship. I would like to thank Dr. Andras Nemes, Dr. Alexander Radi, Dr. James Venning, Dr. Justin Leontini, Dr. Anirudh Rao, Shantanu Bhat and Anchal Sareen.

I would also like to thank Dr. Scott Wordley for giving me the opportunity work as a demonstrator for his engineering classes over the last 4 years. Scott provided me the opportunity to gain experience in teaching and maintain a source of income to support my living expenses during my candidature. Most importantly it is through demonstrating for Scott where I got to work with a team of great people, many I have become good friends with. Among others, I would like to thank Damien McArthur, Matthew Corallo, Terence Avadiar, Cindy Huang for their friendship and support.

I am thankful for the unwavering support and encouragement of my parents and loved ones: Eric Wong, Willa Lam and Joey Pang. Their love, patience and understanding helped me through one of the toughest tasks I have undertaken, without them my thesis would have been an impossible task to complete. Thank you.

Nomenclature

English Symbols

Symbol	Description
\mathcal{R}	Aspect ratio
A_m	Velocity ratio
A_o	Initial displacement in free decay tests
A^*	Normalised transverse oscillation amplitude
A_{10}^*	Mean of the highest 10% of normalised transverse oscillation amplitude
A_{\max}^*	Maximum normalised transverse oscillation amplitude
c	Damping coefficient
C_A	Potential flow added-mass coefficient
C_{pot}	Potential force coefficient
C_L	Lift coefficient of a rotating cylinder
\bar{C}_L	Time-averaged lift coefficient of a rotating cylinder
$C_{L,\max}$	Maximum lift coefficient of a rotating cylinder
C_v	Vortex force coefficient
$C_{v,\text{RMS}}$	Root mean square values of the vortex force coefficient
C_y	Total lift force coefficient
$C_{y,\text{RMS}}$	Root mean square values of the total lift force coefficient
\bar{C}_y	Time-averaged lift coefficient
d_{opt}	Optimal spatial displacement
d_κ	Distance measurement from ruler test
D	Cylinder diameter
DOF	Degree of freedom
DAQ	Data acquisition
f_d	Damped natural frequency in vacuum (Hz)

Continued on next page...

Continued from previous page...

Symbol Description

f_{ls}	Large-scale vortex shedding frequency (Hz)
f_n	Natural frequency of an oscillating system (Hz)
f_{na}	Natural frequency of an oscillating structure in vacuum (Hz)
f_{nw}	Natural frequency of an oscillating structure in water (Hz)
f_{osc}	Rotary forcing frequency (Hz)
f_{pump}	Pump frequency of water channel (Hz)
f_{sh}	Vortex shedding frequency (Hz)
f	Oscillation frequency (Hz)
f_{VIV}	Oscillation frequency of a non-rotating cylinder undergoing vortex-induced vibration (Hz)
f_r	Normalised forcing frequency
f_{St}	Strouhal frequency, the dominant vortex shedding frequency (Hz)
f^*	Normalised oscillation frequency
f_{rot}^*	Rotary forcing frequency ratio (normalised by the natural frequency of an oscillating structure in water, f_{nw})
$f_{rot,VIV}^*$	Rotary forcing frequency ratio (normalised by the oscillation frequency of a cylinder undergoing non-rotating VIV, f_{VIV})
F_L	Total lift force
F_{pot}	Potential force component
F_{vor}	Vortex force component
F_y	Transverse lift force
FIV	Flow-induced vibration
FFT	Fast Fourier transform
i, j, k	Spatial coordinate induces
k	Spring constant or structural stiffness
l	Cylinder length
l_{ch}	Characteristic length
l_{ms}	Immersed length
l_{FS}	Free-surface water level
LVDT	Linear variable differential transformer
m	Mass of an oscillating system

Continued on next page...

Continued from previous page...

Symbol	Description
m_{fld}	Mass of the fluid displaced by an immersed body
m_{osc}	Total mass of an oscillation structure
m_A	Added mass
m^*	Mass ratio
m_{crit}^*	Critical mass ratio
$m^*\zeta$	Non-dimensionalised mass-damping parameter
px	Pixels
PIV	Particle image velocimetry
POD	Proper orthogonal decomposition
PSD	Power spectra density
Re	Reynolds number
R_{block}	Blockage ratio
RMS	Root mean square value
S_f	Forcing Strouhal number
St	Strouhal number
t	Time
T	Oscillation period
T_d	Damped oscillation period
T_{mod}	Modulation period
TTL	Transistor-transistor logic
$\vec{\mathbf{u}}$	Three-dimensional velocity fields in x - y - z Cartesian coordinates
U_∞	Free-stream velocity
U^*	Reduced velocity
v_θ	Peak tangential velocity of the cylinder surface
V	Voltage
VIV	Vortex-induced vibration
x, y, z	Rectangular Cartesian coordinates in space (mm)
\bar{y}	Time-averaged transverse displacement
y^* or y/D	Normalised transverse displacement
y'	Mean-subtracted transverse displacement

Greek Symbols

Symbol	Description
\S	Thesis section

Continued on next page...

Continued from previous page...

Symbol	Description
α	Normalised rotation rate
α_{crit}	Critical normalised rotation rate
Δt	PIV time interval between each image pair
δ	Ratio between any two consecutive amplitude peaks
δ_{Am}	Mean relative error of velocity ratio for a rotary oscillating cylinder
δ_{ω}	Mean relative error of angular velocity for a rotating cylinder
κ	Magnification Factor
λ	Free decay rate
ν	Kinematic viscosity
Ω	Normalised peak rotation rate
$\vec{\omega}$	Vorticity
ω	Angular frequency of transverse oscillation
ω_d	Damped natural angular frequency
ω_{in}	Motor input
ω_{out}	Rotary encoder output
ω_n	Angular natural frequency
ω_{nw}	Undamped natural angular frequency
ω_{rc}	Angular velocity of a rotating cylinder
ϕ	Proper orthogonal decomposition temporal coefficients
ϕ_T	Total phase angle, defined as the phase angle between the transverse lift force and cylinder displacement
ϕ_V	Vortex phase angle, defined as the phase angle between the vortex force component and cylinder displacement
ρ	Density
θ_{dev}	Rotational deviation in rotary oscillations
ζ	Structural damping ratio
ζ_a	Structural damping ratio measured in air
ζ_d	Total damping
ζ_{sw}	Structural damping ratio with added mass effect

Contents

1	Introduction	1
1.1	Overview	1
1.2	Structure of the thesis	4
2	Literature review	5
2.1	Introduction	5
2.2	Flow past a stationary cylinder	6
2.2.1	Flow regimes	6
2.2.2	Vortex shedding fundamentals	7
2.3	Vortex-induced vibration of a circular cylinder	10
2.3.1	Vibration amplitude and frequency responses	11
2.3.2	Synchronisation	14
2.3.3	Fluid forces, phases and wake structures	16
2.4	Circular cylinder undergoing rotary motions	21
2.4.1	Constant rotation	22
2.4.1.1	Fluid forces	22
2.4.1.2	Wake structures	23
2.4.2	Sinusoidal rotary oscillations	29
2.4.2.1	Lock-on regimes and frequency modulation	29
2.4.2.2	Fluid forces	31
2.4.2.3	Wake structures	34
2.5	Vortex-induced vibration of a cylinder undergoing rotary motions	36
2.5.1	Constant rotation	37
2.5.1.1	Vibration amplitude and frequency responses	37
2.5.1.2	Fluid forces, phases and wake structures	40
2.5.2	Sinusoidal rotary oscillations	44
2.5.2.1	The impact of lock-on	44
2.5.2.2	Effects of rotary oscillation frequency	47
2.5.2.3	Effects of rotary oscillation amplitude	48
2.5.2.4	Effects of reduced velocity and mass ratio	50
2.6	Chapter summary and research questions	50
3	Experimental methodology	53
3.1	Chapter overview	53
3.2	Flow control system	53
3.3	Experimental configuration	56
3.4	Motion control systems	57
3.4.1	Air bearing system	57
3.4.2	Rotation rig and motion controller	61

Contents

3.5	Data measurement systems	62
3.5.1	Data acquisition (DAQ) system	62
3.5.2	Linear displacement measurement	63
3.5.3	Rotary motion measurement	66
3.5.4	Flow visualisation: particle image velocimetry (PIV) system	66
3.6	Experiment procedures	69
3.6.1	Free decay measurement in air	69
3.6.2	Free decay measurement in stationary water	72
3.7	Chapter summary	73
4	Flow-induced vibration of a rotating cylinder	75
4.1	Experiment details and validation	75
4.1.1	Experimental details	75
4.1.2	Related validation	76
4.2	Vibration response	77
4.3	Wake structures	84
4.3.1	Wake intermittency in the upper amplitude branch	88
4.4	Force and phases	91
4.4.1	Chapter summary	93
5	Flow-induced Vibration of a Rotary Oscillating Cylinder	97
5.1	Introduction	97
5.2	Experimental details	97
5.3	The phenomenon of ‘rotary-lock-on’	98
5.4	Amplitude responses, fluid forces and phase responses	102
5.5	Response at fixed forcing velocity ratios	106
5.6	Response at fixed forcing frequency ratios	130
5.7	Wake modes	132
5.8	Response over a range of reduced velocities	141
5.9	Chapter summary	143
6	Conclusions and Recommendations for Future Investigations	145
6.1	Conclusions	145
6.1.1	Flow-induced vibration of a cylinder undergoing constant rate rotation	145
6.1.2	Flow-induced vibration of a cylinder undergoing sinusoidally-driven rotary oscillations	146
6.2	Recommendations for future investigations	148
6.2.1	Flow-induced vibration of a cylinder undergoing constant rate rotation	148
6.2.2	Flow-induced vibration of a cylinder undergoing sinusoidally-driven rotary oscillations	148
A	Rotary Motion Validation	151
A.1	Constant rate rotation motion profile validation	151
A.2	Sinusoidal rotary oscillation motion profile validation	151
	Bibliography	155

List of Figures

2.1	The development of vortices for a circular cylinder.	8
2.2	A $St - Re$ function curve.	9
2.3	Experimental flow visualisation of oblique shedding and parallel shedding.	9
2.4	A schematic of a circular cylinder undergoing cross-flow VIV.	11
2.5	The vibration response of a cylinder with different mass and damping.	13
2.6	An illustration of the two distinct types of VIV amplitude responses.	15
2.7	An illustration of the frequency response of the synchronisation region of an elastically-mounted circular cylinder undergoing VIV.	16
2.8	Amplitude response of an oscillating system with a mass ratio below the critical value.	16
2.9	An illustration of the relationships between the three force components and the phases in VIV.	18
2.10	The dynamic response of a circular cylinder undergoing VIV.	19
2.11	Wake modes of a low mass-damping circular cylinder undergoing VIV.	20
2.12	Characteristics of a low mass-damping circular cylinder undergoing VIV.	22
2.13	Lift force time histories of a rigidly-mounted rotating cylinder.	24
2.14	Wake stability and critical rotation rates of a rigidly-mounted rotating cylinder.	25
2.15	Near wake of a rigidly-mounted rotating cylinder.	26
2.16	Wake of a rigidly-mounted rotating cylinder.	27
2.17	The Strouhal number of a rigidly-mounted cylinder rotating at different rotation rates.	28
2.18	A parametric ($S_f - A_m$) lock-on map of a rigidly-mounted cylinder undergoing rotary oscillations.	30
2.19	Frequency modulation of fluid forces of a rigidly-mounted cylinder undergoing rotary oscillations.	31
2.20	Time histories and power spectra of the fluid forces of a rigidly-mounted cylinder undergoing rotary oscillations at $Re = 100$	32
2.21	Mean lift coefficient of a rigidly-mounted cylinder undergoing rotary oscillations.	33
2.22	Time histories of the fluid forces of a rigidly-mounted cylinder undergoing rotary oscillations at $Re = 1000$	34
2.23	A parametric map ($S_f - A_m$) of the time-averaged lift of a rigidly-mounted cylinder undergoing rotary oscillations.	34
2.24	Wake modes of a rigidly-mounted cylinder undergoing rotary oscillations at $Re = 100$	35
2.25	Development of vortex structures of a rigidly-mounted cylinder undergoing rotary oscillations over one frequency modulation period.	36
2.26	Orbiting secondary vortex structure of a rigidly-mounted cylinder undergoing rotary oscillations at $Re = 1000$	37
2.27	Time-averaged displacement of an elastically-mounted cylinder undergoing constant rate rotation.	38
2.28	Vibration region and amplitude response of an elastically-mounted cylinder undergoing constant rate rotation.	39

List of Figures

2.29	The frequency response of an elastically-mounted cylinder undergoing constant rate rotation.	40
2.30	A map of the different wake patterns of an elastically-mounted cylinder undergoing constant rate rotation.	41
2.31	Vorticity contours of the different wake modes of an elastically-mounted cylinder undergoing constant rate rotation.	41
2.32	Phases of an elastically-mounted cylinder undergoing constant rate rotation.	43
2.33	The power spectra density of the displacement of an elastically-mounted cylinder undergoing rotary oscillations.	45
2.34	The power spectra density of the fluid forces of an elastically-mounted cylinder undergoing rotary oscillations.	46
2.35	Wake structures of an elastically-mounted cylinder undergoing rotary oscillations.	47
2.36	A parametric map (A_m-U^*) of the lock-on and non lock-on states of an elastically-mounted cylinder undergoing rotary oscillations at forcing frequency ratio $f_{rot}^* = 2.0$.)	47
2.37	Amplitude response of an elastically-mounted cylinder undergoing rotary oscillations over a range of forcing frequency ratios.	48
2.38	Amplitude response of an elastically-mounted cylinder undergoing rotary oscillations over a range of forcing velocity ratios.	49
2.39	The power spectra density of the displacement and fluid forces of an elastically-mounted cylinder undergoing rotary oscillations.	49
2.40	Amplitude response an elastically-mounted cylinder undergoing rotary oscillations over a range of reduced velocities.	50
3.1	A photograph of the FLAIR water channel facility.	54
3.2	Schematic of the FLAIR water channel.	54
3.3	PIV measurement of the free-stream velocity.	55
3.4	PIV measurement of the boundary layer profile.	55
3.5	An illustration of the fluid-structure configurations of the present experiment.	56
3.6	Schematic of the present experiment.	58
3.7	A photograph of the experiment apparatus.	59
3.8	An illustration of the porous-medium type air bushings used in the air bearing.	59
3.9	An illustration on the reduction of a one-spring-one-mass system.	60
3.10	Cross-sectional schematic of the rotation rig.	61
3.11	Block diagram of the experiment apparatus and measurement systems.	62
3.12	Wiring schematic of a linear variable differential transformer (LVDT).	64
3.13	Examples of linear displacement measurement.	64
3.14	Photograph of the installed optical linear encoder.	65
3.15	Analytical procedures to cross-correlate PIV images.	67
3.16	PIV phase-band averaging technique.	70
3.17	A comparison of the instantaneous and phase-band averaged PIV images.	70
3.18	The response of an underdamped one degree-of-freedom system.	71
4.1	Validation of the vibration response of a non-rotating circular cylinder undergoing VIV.	77
4.2	Comparison of the time-averaged displacement results of an elastically-mounted cylinder rotating at different rotation rates.	78
4.3	The vibration response of an elastically-mounted cylinder rotating at fixed rotation rates over a range of reduced velocities.	79
4.4	The vibration response of an elastically-mounted cylinder rotating at a range of rotation rates at selected reduced velocity cases.	81

4.5	Comparison of the present amplitude results of an elastically-mounted cylinder undergoing constant rate rotation with previous work.	83
4.6	A parametric map (U^* - α) of the different wake maps observed in the present study of an elastically-mounted cylinder undergoing constant rate rotation.	84
4.7	2S wake mode of an elastically-mounted cylinder undergoing constant rate rotation.	87
4.8	Chaotic nature of the C(AS) wake mode.	88
4.9	Effects of rotation rate on the 2S wake mode.	89
4.10	Sign switching of the P+S mode.	90
4.11	Wake mode switching of an elastically-mounted cylinder undergoing constant rate rotation between 2P and 2S mode.	90
4.12	Wake mode switching of an elastically-mounted cylinder undergoing constant rate rotation between P+S ⁺ and 2S mode.	91
4.13	Wake mode switching of an elastically-mounted cylinder undergoing constant rate rotation between P+S ⁻ and 2P mode.	92
4.14	Comparison of the lift force and phases of between a non-rotating and rotating elastically-mounted cylinder.	94
5.1	Power spectra density of the displacement signal showing lock-on and non lock-on behaviour at $U^* = 5.5$	99
5.2	Power spectra density of the displacement signal showing lock-on and non lock-on behaviour at $U^* = 8.0$	100
5.3	Boundaries of the rotary-lock-on and tertiary-lock-on regions.	101
5.4	An overview of the dynamic responses of an elastically-mounted cylinder undergoing rotary oscillations at $U^* = 5.5$	102
5.5	An overview of the dynamic responses of an elastically-mounted cylinder undergoing rotary oscillations at $U^* = 8.0$	105
5.6	An illustration showing the different cases of dynamic responses to be examined.	107
5.7	Response quantities of an elastically-mounted cylinder undergoing rotary oscillations at $A_m = 0.5$ and $U^* = 5.5$	108
5.8	The response time history and distribution of quantities of an elastically-mounted cylinder undergoing rotary oscillations at $f_{rot}^* = 0.65$, $A_m = 0.5$ and $U^* = 5.5$	110
5.9	The response time history and distribution of quantities of an elastically-mounted cylinder undergoing rotary oscillations at $f_{rot}^* = 1.15$, $A_m = 0.5$ and $U^* = 5.5$	111
5.10	The response time history and distribution of quantities of an elastically-mounted cylinder undergoing rotary oscillations at $f_{rot}^* = 1.80$, $A_m = 0.5$ and $U^* = 5.5$	112
5.11	The response time history and distribution of quantities of an elastically-mounted cylinder undergoing rotary oscillations at $f_{rot}^* = 2.75$, $A_m = 0.5$ and $U^* = 5.5$	113
5.12	The response time history and distribution of quantities of an elastically-mounted cylinder undergoing rotary oscillations at $f_{rot}^* = 3.30$, $A_m = 0.5$ and $U^* = 5.5$	114
5.13	Response quantities of an elastically-mounted cylinder undergoing rotary oscillations at $A_m = 1.0$ and $U^* = 5.5$	115
5.14	Response quantities of an elastically-mounted cylinder undergoing rotary oscillations at $A_m = 1.3$ and $U^* = 5.5$	118
5.15	The response time history and distribution of quantities of an elastically-mounted cylinder undergoing rotary oscillations at $f_{rot}^* = 1.40$, $A_m = 1.3$ and $U^* = 5.5$	119
5.16	The response time history and distribution of quantities of an elastically-mounted cylinder undergoing rotary oscillations at $f_{rot}^* = 2.00$, $A_m = 1.3$ and $U^* = 5.5$	120
5.17	The response time history and distribution of quantities of an elastically-mounted cylinder undergoing rotary oscillations at $f_{rot}^* = 3.40$, $A_m = 1.3$ and $U^* = 5.5$	121

List of Figures

5.18	Response quantities of an elastically-mounted cylinder undergoing rotary oscillations at $A_m = 2.0$ and $U^* = 5.5$	122
5.19	Response quantities of an elastically-mounted cylinder undergoing rotary oscillations at $A_m = 0.5$ and $U^* = 8.0$	123
5.20	The response time history and distribution of quantities of an elastically-mounted cylinder undergoing rotary oscillations at $f_{rot}^* = 0.65$, $A_m = 0.5$ and $U^* = 8.0$	124
5.21	The response time history and distribution of quantities of an elastically-mounted cylinder undergoing rotary oscillations at $f_{rot}^* = 1.15$, $A_m = 0.5$ and $U^* = 8.0$	126
5.22	Response quantities of an elastically-mounted cylinder undergoing rotary oscillations at $A_m = 1.0$ and $U^* = 8.0$	127
5.23	Response quantities of an elastically-mounted cylinder undergoing rotary oscillations at $A_m = 1.3$ and $U^* = 8.0$	128
5.24	Response quantities of an elastically-mounted cylinder undergoing rotary oscillations at $A_m = 2.0$ and $U^* = 8.0$	129
5.25	Response quantities of an elastically-mounted cylinder undergoing rotary oscillations at $f_{rot}^* = 1.0$ and $U^* = 5.5$	131
5.26	Response quantities of an elastically-mounted cylinder undergoing rotary oscillations at $f_{rot}^* = 3.0$ and $U^* = 5.5$	132
5.27	A parametric map ($f_{rot}^*-A_m$) of the wake modes of an elastically-mounted cylinder undergoing rotary oscillations at $U^* = 5.5$	133
5.28	A parametric map ($f_{rot}^*-A_m$) of the wake modes of an elastically-mounted cylinder undergoing rotary oscillations at $U^* = 8.0$	134
5.29	The SW wake mode of an elastically-mounted cylinder undergoing rotary oscillations and its switching behaviour.	135
5.30	The 2SO wake mode of an elastically-mounted cylinder undergoing rotary oscillations.	136
5.31	Mode I-O wake mode of an elastically-mounted cylinder undergoing rotary oscillations and its orbiting secondary vortex.	138
5.32	The CS wake mode of an elastically-mounted cylinder undergoing rotary oscillations.	139
5.33	The CF2P wake mode of an elastically-mounted cylinder undergoing rotary oscillations.	140
5.34	The 2S-OC wake mode of an elastically-mounted cylinder undergoing rotary oscillations.	141
5.35	Response quantities of an elastically-mounted cylinder undergoing rotary oscillations at $f_{rot}^* = 0.65$ and $A_m = 0.5$ over a range of reduced velocities.	142
A.1	Motion profile validation of a cylinder undergoing constant rate rotation.	151
A.2	The motion profile of a cylinder undergoing sinusoidal rotary oscillations at $U^* = 5.0$, $A_m = 0.1$ and $f_{rot}^* = 0.25$	153
A.3	The motion profile of a cylinder undergoing sinusoidal rotary oscillations at $U^* = 8.0$, $A_m = 2.0$ and $f_{rot}^* = 4.5$	154

Chapter 1

Introduction

1.1 Overview

Flow-induced vibration (FIV) of bluff bodies is a phenomenon that surrounds us. In windy conditions, FIV can be observed from the swaying of television antennae and flag poles to the span of power cables suspended between support towers. These are examples of the body vibration caused by fluctuating forces generated by a moving fluid. While these examples may seem gentle and harmless; those encountered in engineering applications can have severe consequences. Common examples of FIV seen in engineering applications are cylinder arrays in a nuclear power generator cooling system, tall civil structures such as chimneys and riser tubes and floating structures used in offshore engineering. Flow-induced vibration can be a problem that becomes critical when they have a negative impact on the fatigue life of structures, which has the potential to cause catastrophic structural failures. The best known example of structure failure caused by FIV is the collapse of the original Tacoma Narrows Bridge. In high-winds the structure was excited causing large body oscillations that led to the destruction of the bridge in the 1940's (Billah & Shinozuka 1991).

Researchers have spent decades studying and predicting FIV. Due to its unpredictable nature, designing against FIV often involves active and passive suppression devices or large safety factors. These solutions usually increase the cost of engineering projects and can hinder their progress and operational efficiency. In the past century, research has been conducted to further our understanding of FIV of bluff bodies. Much of this research was oriented towards finding active and passive FIV suppression techniques.

Two common forms of FIV are Vortex-induced vibration (VIV) and galloping. Vortex-induced vibration is caused by the shedding of vortices in the wake of a body that subsequently causes structural vibration. Due to its potential to have a negative effect on engineering structures VIV has been extensively studied. The current paradigm of VIV research owes its origin to pioneering work by Feng (1968). Many studies have concentrated on characterising FIV under various flow and geometric conditions, including those likely achieve active and passive suppression. These have been reviewed by Griffin *et al.* (1973); Blevins (1977); Bearman (1984); Carberry *et al.* (2001); Sarpkaya (2004); Williamson & Govardhan (2004a); Naudascher & Rockwell (2005). Galloping occurs when the cross-sectional geometry of the body is asymmetric. This makes the body aerodynamically unstable to oscillations transverse to the direction of the fluid flow (Parkinson & Wawzonek 1981).

Vortex-induced vibration occurs when vortices shed alternately from a bluff body to produce a wake. These vortices generate regions of low pressure resulting in fluctuating forces that act on the body. For any elastically-mounted or flexible bodies this results in the body vibrating. As vortex shedding is the result of flow instabilities VIV is intrinsically an unstable phenomenon (Naudascher & Rockwell 2005) that occurs over a range of flow velocities. Within this range, the body oscillation frequency and vortex-shedding frequency will synchronise with the natural frequency of

the oscillating structure, which results in large body oscillations. This phenomenon is known as ‘lock-in’. Under lock-in, the vortex-shedding frequency of an elastically-mounted body can substantially deviate from the vortex-shedding frequency of a stationary cylinder. As a result of added-mass effects, the body oscillation frequency can also deviate from the vortex-shedding frequency of a stationary cylinder under lock-in (Williamson & Govardhan 2004a).

Galloping is characterised by low-frequency body oscillations in which the amplitude monotonically increases with flow velocity. Nemes *et al.* (2012) showed a square section cylinder with an angle of attack that is asymmetric to the oncoming fluid flow can undergo combinations of VIV and galloping. When symmetry is broken, a mixed-mode response was found. This response is accompanied by a new amplitude response branch where its response is larger than those observed in the ‘upper’ amplitude response branch in VIV. The frequency response at this higher branch is lower at half that of VIV responses; a behaviour that resembles those of galloping. As a result, the study showed features of both VIV and galloping. Of particular interest to the current study is VIV of a circular cylinder. This geometry was chosen not because it is symmetric but could produce flow asymmetries by other means independent of geometry. One method of introducing flow asymmetries is to impose a forced, rotary motion to the body such as forced constant rotation and forced rotary oscillation.

Over the past century, a rigidly-mounted circular cylinder undergoing forced rotation has been studied and reviewed by (*e.g.* Prandtl & Tietjens (1934); Swanson (1961); Coutanceau & Menard (1985); Mittal & Kumar (2003); Rao *et al.* (2013)) due to its potential to manipulate the wake of the body. When a cylinder in a flow is rotated about its axis it experiences an asymmetric pressure distribution. This is caused by the cylinder experiencing higher velocity on the side where the rotational velocity adds to the free-stream, whereas on the other side the rotational and free-stream velocities are in opposite directions. The force caused by the differences in pressure on the two sides gives rise to the Magnus effect. This has been extensively studied and reviewed (*e.g.* Prandtl & Tietjens (1934); Coutanceau & Menard (1985); Badr *et al.* (1990); Kang *et al.* (1999); He *et al.* (2000); Stojković *et al.* (2002); Mittal & Kumar (2003); Rao *et al.* (2013)). Notable work by Mittal & Kumar (2003) have characterised a number of different wake regimes over a range of body rotation rates. These were found to depend on the ratio between the tangential velocity of the rotating cylinder’s surface and the free-stream velocity is defined as the rotation rate.

For low rotation rates, Von Kármán vortex shedding dominates the flow as Kármán vortex streets are observed in experimental and numerical studies over a range of Reynolds number (Coutanceau & Menard 1985; Badr *et al.* 1990; Kang *et al.* 1999; He *et al.* 2000; Stojković *et al.* 2002; Mittal & Kumar 2003; Rao *et al.* 2013). In a band of moderate rotation rates where the tangential velocity of the cylinder surface is approximately two to four times that of the free-stream velocity of the flow, the wake is stabilised (Mittal & Kumar 2003; El Akoury *et al.* 2008). As rotation rate is increased, however, a secondary region of wake instability exists. This region is characterised by its low frequency, one-sided vortices (Stojković *et al.* 2003; Mittal & Kumar 2003; Pralits *et al.* 2010). A number of steady and unsteady wake modes exist depending on the rotation rate of the cylinder and Reynolds number (Pralits *et al.* 2013; Rao *et al.* 2013, 2015). The capacity to manipulate and stabilise the wake by rotating the cylinder could be of significant interest to VIV studies if it provides a way to actively reduce the strength of vortices and consequently the body’s vibration.

By rotating an elastically-mounted cylinder it is possible to study how the addition of body rotation affects the known VIV characteristics of a non-rotating cylinder. Previous work, *e.g.* Mittal & Kumar (2003), have shown that at certain rotation rates the lift forces acting on the cylinder will have an oscillating component where the lift fluctuates about some mean value. This is not unexpected as the body rotation generates a mean lift, a Magnus force, proportion to the body’s rate of rotation (Prandtl & Tietjens 1934) and the oscillating component of the lift is the result of vortex shedding. Mittal & Kumar (2003) showed that the oscillating component of the lift forces to

be periodic and in some cases of rotation rate the cylinder the amplitude of the oscillating lift can be larger than those seen in non-rotating cases. The amplitude of the oscillating component of the lift forces is of great significance as it can directly influence the vibration response of an elastically-mounted body. Rotating an elastically-mounted body at rotation rates where vortex shedding and the oscillating component of the lift forces is absent will reduce or even eliminate VIV. Bourguet & Lo Jacono (2014) appear to have been the first to conduct such a study numerically, they did this for a Reynolds number of 100, with minimal system damping. They found that for an elastically-mounted body, large amplitude vibrations and vortex shedding can still occur at ranges of rotation rate where the flow was previously considered to be steady in rigid cylinder studies (*e.g.* Mittal & Kumar (2003); El Akoury *et al.* (2008)). Bourguet & Lo Jacono (2014) observed a number of differences between the amplitude and frequency response of an elastically-mounted rotating cylinder and that of a non-rotating one. Notably, the global peak amplitude of the rotating cylinder is approximately three times higher than the non-rotating cylinder. Furthermore, the frequency response of the rotating cylinder decreases with increasing in body rotation. They also discovered a new wake mode. It is referred as the T+S pattern and it consists of a triplet of vortices and a single vortex being shed per cycle. This wake pattern is observed at high rotation rates where large amplitude body vibrations persist. Zhao *et al.* (2014c) conducted a numerical study of a cylinder rotating in both 1 and 2 degrees of freedom, again the study was done at low Reynolds numbers. The 2 degree of freedom case showed significant differences in the vibration response between a non-rotating cylinder and a rotating one. In particular is the vibration amplitude response of the cylinder in the streamwise direction. When the cylinder is not undergoing rotation, the amplitude response is significantly smaller than the cross-flow direction. However, with added body rotation, the streamwise amplitude response increases with rotation rate. In their study where the tangential velocity of the cylinder surface equals the free-stream velocity, the streamwise amplitude response is marginally lower than the cross-flow values. A low Reynolds number, experimental study by Seyed-Aghazadeh & Modarres-Sadeghi (2015) showed moderate changes in vibration response. Contrary to findings from Bourguet & Lo Jacono (2014), they did not observe a threefold increase in peak amplitude response. Instead Seyed-Aghazadeh & Modarres-Sadeghi (2015) observed a peak amplitude response that is approximately 50% higher than that of a non-rotating cylinder.

Until recently, studies on rotary motions of circular cylinders has primarily been focused on constant body rotation. In comparison, the study of a rigidly-mounted circular cylinders undergoing rotary oscillations about its axis has received less attention until the 1990's. Rotary oscillation has the potential to modify the wake structure of a body. This is achieved through interactions between the rotary oscillation frequency and the vortex shedding frequency of the body. One of the first studies on rotary oscillating cylinders was conducted by Okajima *et al.* (1975). They discovered frequency synchronisation behaviour similar to those observed in VIV. When "lock-on" occurs, the vortex-shedding frequency synchronises with the forcing frequency. Such phenomenon occurs over a range of forcing frequencies (Okajima *et al.* 1975; Tokumaru & Dimotakis 1991; Choi *et al.* 2002). The ability for rotary oscillation to control the vortex-shedding frequency of a body is of significant interest to VIV studies. Instead of suppressing the strength of vortices, rotary oscillation has the potential manipulate the vortex-shedding frequency of a body away from the natural frequency of an oscillating structure. This can prevent the vortex-shedding and body oscillation frequency from synchronising with the natural frequency of the oscillating structure; hence, prevents large body oscillations.

The effectiveness of rotary oscillations on manipulating vortex shedding of a rigidly-mounted cylinder is well established. Du & Sun (2015) appear to have been the first to numerically study the effects of rotary oscillation on vortex shedding on an elastically-mounted circular cylinder at low Reynolds numbers. They found rotary oscillations to be effective at suppressing vortex shedding on elastically-mounted cylinders. Suppression is achieved by synchronising the vortex-shedding

frequency to the forcing frequency. By changing the shedding frequency away from the natural frequency of the oscillating structure; significant suppression can be achieved with appropriate rotary oscillation control.

From the current state of FIV research, the effects of rotary motions on VIV of an elastically-mounted circular cylinder have been studied at relatively low Reynolds numbers. No studies have yet been done to investigate the effects of Reynolds number. The focus of this thesis is on two areas:

1. The comparison between a non-rotating, elastically-mounted circular cylinder and that of a cylinder undergoing forced, constant rotation over a range of Reynolds numbers. The focus of the investigation will be on the vibration response and wake structure of the rotating cylinder and how body rotation suppresses vortex shedding strength.
2. The comparison between a non-rotating, elastically-mounted circular cylinder and that of a cylinder undergoing forced, rotary oscillation over a range of Reynolds numbers. The investigation will focus on how shedding frequency manipulation through rotary forcing can affect the vibration response and wake structure of the cylinder.

1.2 Structure of the thesis

With the exception of the Introduction; each subsequent chapter will begin with a brief outline of the chapter's contents and conclude with a short summary on the key findings of the chapter. The thesis is structured as follows:

Chapter 2: Review of relevant literature on the current state of knowledge. This chapter will cover fundamental fluid mechanic concepts, vortex-induced vibration of elastically-mounted circular cylinders, rigidly-mounted circular cylinders undergoing rotary motions and vortex-induced vibration of elastically-mounted circular cylinders undergoing rotary motions. The review will highlight gaps in knowledge and what remains to be answered.

Chapter 3: The methodology of the current experiment will be described. This chapter will provide a detailed overview of the facilities, experiment apparatus, data measurement and processing techniques.

Chapter 4: Results on the vortex-induced vibration of an elastically-mounted circular cylinder undergoing forced, constant rotation is presented. The results on the vibration response and wake structure will be discussed and compared to that of an elastically-mounted, non-rotating cylinder.

Chapter 5: Effects of rotary oscillation of the cylinder on vortex-induced vibration of an elastically-mounted circular cylinder are studied. The results on the vibration response and wake structure will be discussed and compared to that of an elastically-mounted, non-rotating cylinder.

Chapter 6: A comprehensive conclusion of the thesis. This will summarise key findings and discussions from each chapter. Future work will also be discussed at the end of this chapter.

Bibliography: References cited in this thesis are listed in this bibliography.

Chapter 2

Literature review

2.1 Introduction

The flow-induced vibration (FIV) of bluff bodies have been extensively investigated by a number of research groups over the past decades. This is due to its increasing relevance in a broad range of engineering industries such as offshore oil production, cooling systems in nuclear power generation and aerodynamics of industrial structures. Comprehensive reviews about FIV have been presented in works by Griffin *et al.* (1973); Blevins (1977); Bearman (1984); Carberry *et al.* (2001); Sarpkaya (2004); Williamson & Govardhan (2004*a*); Naudascher & Rockwell (2005). Research on the flow past a rigidly-mounted circular cylinder undergoing axial rotary motions, such as Coutanceau & Menard (1985); Badr *et al.* (1990); Tokumaru & Dimotakis (1991); Choi *et al.* (2002); Mittal & Kumar (2003); El Akoury *et al.* (2008); Rao *et al.* (2013), have shown that rotary motions have the potential to actively control and manipulate the cylinder's fluid forces and vortex shedding. Limited research has been undertaken to investigate the effects of these rotary motions on the FIV of elastically-mounted bluff bodies. This chapter will present a brief review of literature describing the fundamentals and the current state of knowledge on topics which are relevant and served as motivation to the research presented in this thesis. Topics concerning vortex shedding fundamentals, VIV of elastically-mounted non-rotating circular cylinders; rigidly-mounted circular cylinders undergoing constant rotation and sinusoidally-driven rotary oscillations will be surveyed in detail. The current state of knowledge on VIV of elastically-mounted circular cylinders undergoing rotary motions will be presented at the end of the chapter.

To understand how the fluid interacts with a circular cylinder under a range of cross-flow and rotary motions, it is essential to first examine the flow past a stationary circular cylinder. The chapter begins by describing the different flow regimes, the fundamentals of vortex shedding and the fluid forces acting on a stationary circular cylinder in §2.2. Vortex-induced vibration has been extensively researched since the pioneering experiment conducted by Feng (1968). The current state of knowledge on VIV of elastically-mounted circular cylinders are presented in §2.3. This section will focus on the vibration response (*i.e.* the amplitude and frequency response) of the cylinder, the wake-body synchronisation phenomenon (commonly known as 'lock-in'), fluid forces, phase response between the body displacement and forces, and lastly, the wake structure of the cylinder at different flow conditions. Due to the destructive effects VIV have on structures, researchers have experimented with a number of passive and active VIV control techniques.

Few active VIV control techniques have been as extensively investigated as constant rate rotation of a rigidly-mounted cylinder. The study of flow past rigidly-mounted circular cylinders undergoing constant rotation dates to early experiments conducted by Prandtl & Tietjens (1934). Many studies on this subject have followed over the past century (*e.g.* Swanson (1961); Coutanceau & Menard (1985); Badr *et al.* (1990); Chen *et al.* (1993); Chen (2000); Mittal (2001); Stansby & Rainey (2001);

Mittal & Kumar (2003); El Akoury *et al.* (2008); Rao *et al.* (2013)) due to the motions ability to manipulate the fluid forces and wake structure. As the effects of constant rate rotation on an elastically-mounted body is one of the motivations of the present research, literature on the fluid forces and wake structures of a rigidly-mounted circular cylinder undergoing constant rotation will be reviewed in §2.4.1.

An alternate method to actively manipulate vortex shedding is through steady sinusoidally-driven rotary oscillations. Rigidly-mounted cylinders undergoing rotary oscillations was first studied experimentally by Okajima *et al.* (1975) as they observed changes in wake structure by the forcing motion. Many studies followed (*e.g.* Tokumaru & Dimotakis (1991); Cheng (2001); Choi *et al.* (2002); Thiria *et al.* (2006)). Choi *et al.* (2002) have shown the vortex shedding frequency to synchronise with the oscillation forcing frequency at specific oscillation forcing amplitudes and frequencies. The ability to manipulate the shedding frequency has applications in controlling VIV as it can potentially manipulate the wake-body synchronisation phenomenon. Discussion on steady sinusoidally-driven rotary oscillations will be presented in §2.4.2.

A limited number of studies have been undertaken to investigate the effects of rotary motions on VIV of elastically-mounted circular cylinders. To the author's knowledge, Bourguet & Lo Jacono (2014) were the first to present a low Reynolds number numerically study of the effects of constant rotation on an elastically-mounted cylinder restricted to vibrate in the cross-flow direction. Low Reynolds number simulation by Zhao *et al.* (2014c) and experiment by Seyed-Aghazadeh & Modarres-Sadeghi (2015) followed. A review on the current state of knowledge on the effects of constant rate rotation on VIV is presented in §2.5.1.

The effects of sinusoidal rotary oscillations on VIV has not been thoroughly surveyed. Du & Sun (2015) were the first to study the effects of sinusoidally-driven rotary oscillations on elastically-mounted cylinders that oscillate in the cross-flow direction. Their low Reynolds number simulation showed the efficacy of rotary oscillation in controlling vortex shedding, even for an elastically-mounted body. An in-depth discussion on sinusoidal rotary oscillations is presented in §2.5.2.

2.2 Flow past a stationary cylinder

2.2.1 Flow regimes

In bluff body fluid aerodynamics, the circular cylinder is regarded as the prototypical model in steady flow. Its symmetry enables fluids researchers to study the behaviour the flow independently of the body geometry. In addition to its geometric symmetry, its simplicity enables the cylinder to be described simply by its length (l) and diameter (D). Due to these advantages, extensive studies have been undertaken over the past century to characterise the flow past a stationary circular cylinder.

For bluff bodies immersed in a steady Newtonian fluid flow, the characteristics of the flow regimes can be quantified by the Reynolds number (Re), which is the ratio of inertial to viscous forces. This is mathematically expressed as

$$Re = \frac{U_\infty l_{ch}}{\nu}, \quad (2.1)$$

where U_∞ is the free-stream velocity, l_{ch} is the characteristic length of the body and ν is the kinematic viscosity of the fluid. For cylinders the characteristic length is the diameter, D and eq. 2.1 is commonly expressed as

$$Re = \frac{U_\infty D}{\nu}. \quad (2.2)$$

As Re is increased from zero the flow transitions through several different regimes, each having distinct features. Several works have described the different flow regimes a circular cylinder transitions through as the Reynolds number is increased (*e.g.* Williamson (1996); Fredsoe & Sumer (1997); Leontini *et al.* (2007); Nazarinia *et al.* (2009); Zhao (2012)).

At $Re < 5$, the dynamics of the fluid flow around the cylinder is dominated by viscous forces. As the flow passes the cylinder neighbouring streamlines will contour to the shape of the cylinder and uniform flow is recovered downstream. In this regime, the flow topology is steady and flow separations do not occur. This is often called creeping flow.

The onset of flow separation is indicated by the formation of a pair of symmetric vortices in the near wake of the cylinder. The vortex pair formation results in a recirculation region (Fredsoe & Sumer 1997). This occurs at $Re \simeq 5$.

When Reynolds number is increased above $Re \simeq 46$, the flow undergoes the phenomenon of vortex shedding, as described in Taneda (1956); Roshko (1993); Williamson (1996). Vortex shedding occurs when the wake of the cylinder becomes unstable and as a result vortices are shed from alternating sides of the cylinder at a specific frequency. This frequency is known as the vortex shedding frequency (f_{sh}) and it can be defined by a non-dimensionalised quantity called the Strouhal number St . A detailed discussion on the Strouhal number is provided in §2.2.2. In this flow regime, vortices shed are in a two-row, staggered formation. They form a laminar vortex street commonly known as the Kármán vortex street. As vortices of opposite sign are shed alternately they exert a fluctuating force on the cylinder. If the cylinder is elastically-mounted this fluctuating force will excite the cylinder to vibrate, leading to the important phenomenon of VIV.

At $46 < Re < 190$, the flow remains laminar and two-dimensional meaning there are negligible variations in the vortex shedding along the span of the cylinder. As Reynolds number is increased pass $Re \approx 260$, the boundary layer of the cylinder surface remains laminar while the wake of the cylinder becomes turbulent (Fredsoe & Sumer 1997).

2.2.2 Vortex shedding fundamentals

Vortex shedding develops when the symmetric vortex pair becomes unstable and susceptible to small perturbations in the flow, typically at $Re > 46$. The vortex shedding mechanism is described in detail in Fredsoe & Sumer (1997). Figure 2.1 illustrates the development of vortex formations in the near wake of a circular cylinder. The small perturbations in the flow cause asymmetric growth in the pair of counter rotating vortices. Figure 2.1(a) shows vortex A (clockwise) growing longer in streamwise length and stronger than vortex B (anti-clockwise). When vortex A is sufficient in strength, it draws in the opposite shear layer containing vortex B. Vortex B curls upwards towards the wake/ streamwise axis as illustrated by fig. 2.1(b). As vortex B is drawn towards the shear layer that is linked with vortex A the anti-clockwise vorticity in vortex B severs the supply of clockwise vorticity to vortex A from the shear layer. This ceases the growth of vortex A and detaches it from its shear layer. At this point, vortex A becomes a free vortex and is carried downstream by the flow, as illustrated in fig. 2.1(c). Over this single shedding cycle, the strength of vortex A and vortex B varies with time as the vortex structure is formed and shed.

A new vortex, C, is formed from the upper shear layer. As vortex B grows to a sufficient length and strength, it draws in the shear layer of vortex C across the wake, which then severs vortex B from its shear layer before being shed and flowing downstream. Repeating this process forms vortex streets. The strength of vortex A and B Periodic shedding of vortices from alternating sides of the cylinder results in the continual interaction between the two shear layers (Gerrard 1966). Fredsoe & Sumer (1997) suggested that controlling these shear layers could suppress their interaction, which could suppress or prevent the shedding of vortices.

A number of works have described the phenomenon of vortex shedding as a global instability that is self-excited and which affects the entire wake (Huerre & Monkewitz 1990; Williamson 1996; Paidoussis *et al.* 2007). Over a range of Reynolds numbers, the robust process of vortex shedding occurs at a well-defined shedding frequency. As mentioned in §2.2.1, the vortex shedding frequency can be non-dimensionalised and expressed as the Strouhal number St . This is mathematically

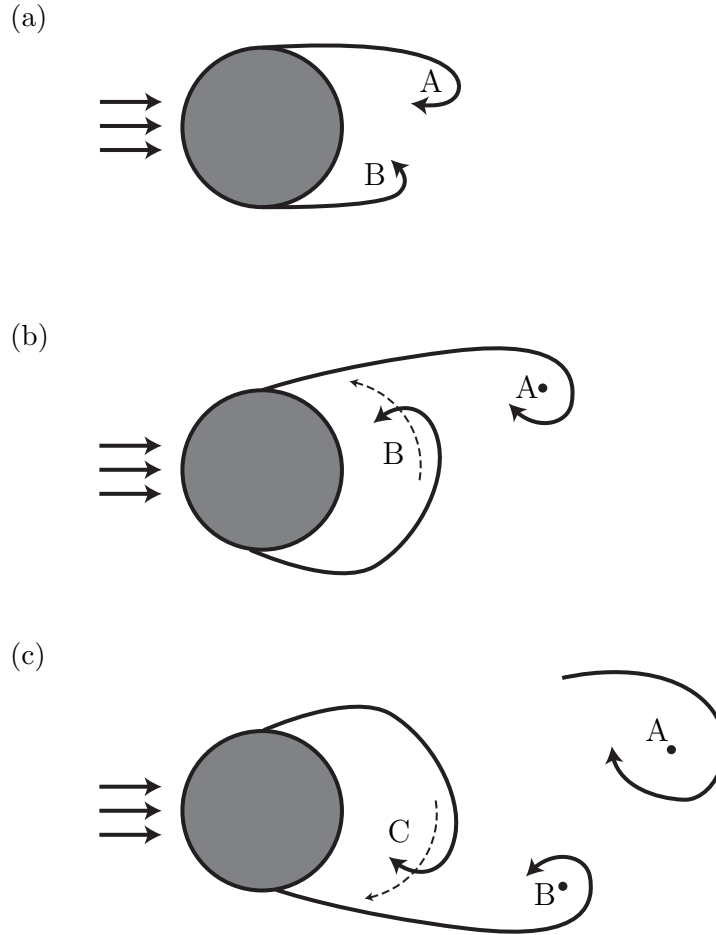


FIGURE 2.1: The development of vortices for a circular cylinder. (a): Clockwise rotating vortex A grows stronger and larger than the anti-clockwise rotating vortex B, (b): At the onset of vortex A being shed, vortex B is drawn across the wake axis and towards the shear layer connecting vortex A; (c): Vortex A is shed and carried downstream as vortex B grows and draws the newly developed vortex C across the wake axis and towards its shear layer. Illustration modified from Zhao (2012).

expressed as

$$St = \frac{f_{St}D}{U_\infty}, \quad (2.3)$$

where f_{St} is the dominant vortex shedding frequency (also known as the Strouhal frequency) of a stationary cylinder, D is the cylinder diameter (the characteristic length of a circular cylinder) and U_∞ is the free-stream velocity. Strouhal reported in Strouhal (1878) that the non-dimensionalised Strouhal frequency remained constant. As illustrated in fig. 2.2, studies involving smooth circular cylinders have shown that the Strouhal number remains close to a constant value of $St \approx 0.2$ (Williamson 1992; Williamson & Brown 1998; Norberg 2001).

Williamson (1989) reported discrepancies in Strouhal number (St) between oblique and parallel vortex shedding modes caused by end effects of the cylinder. Figure 2.3 shows the difference between oblique (a) and parallel shedding (b). In oblique shedding mode, the vortices are shed at an angle with respect to the spanwise cylinder axis but parallel to each other. In parallel shedding mode vortices are shed parallel to the cylinder axis over most of the span.

The effect oblique shedding is not limited to the topology of the wake and vortex shedding fre-

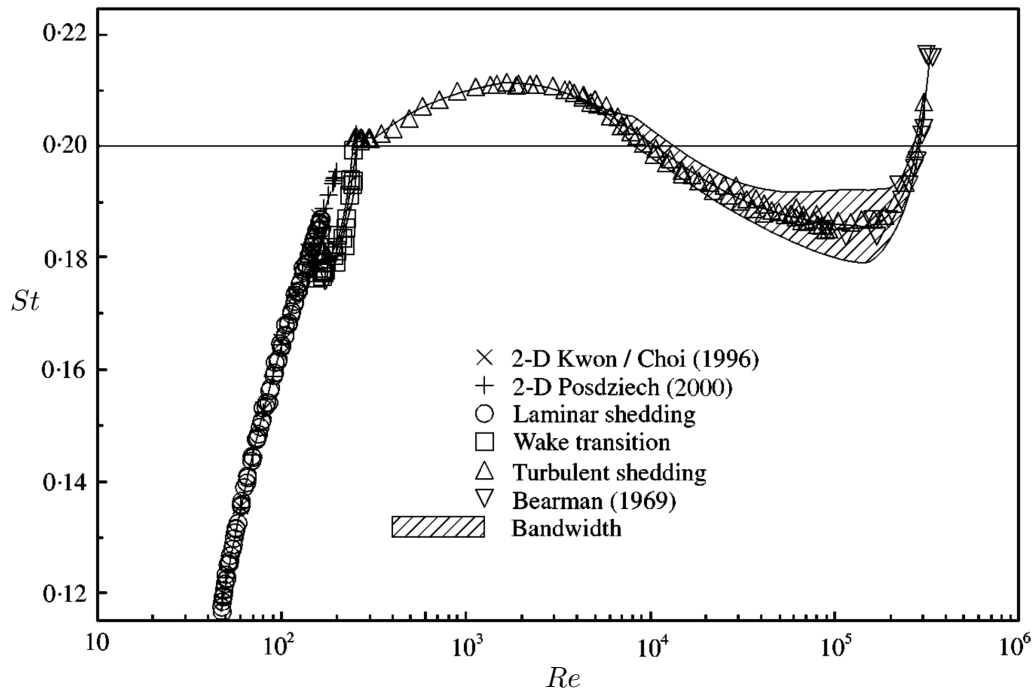


FIGURE 2.2: A $St - Re$ function curve showing the convergence of the Strouhal number towards $St \approx 0.2$ as the Reynolds number is increased between $10 < Re < 10^6$. Figure and references from Norberg (2001).

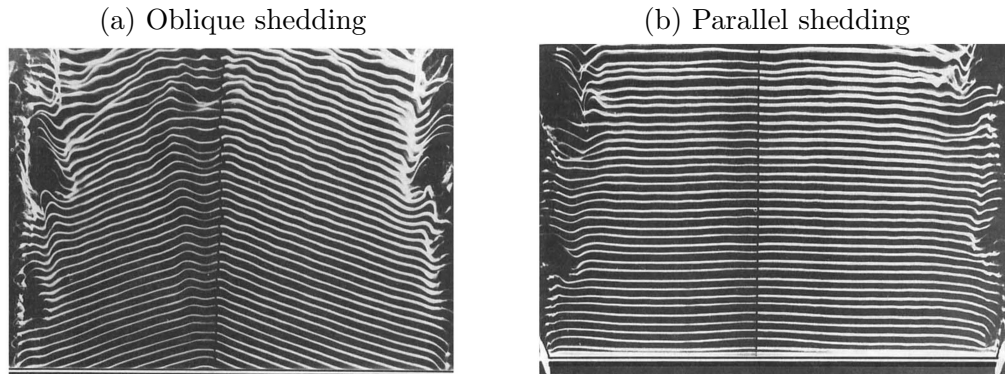


FIGURE 2.3: Experimental flow visualisation of (a) oblique shedding at Reynolds number $Re = 85$ and length-to-diameter ratio $L/D = 140$ and (b) parallel shedding at $Re = 110$ and $L/D = 130$ from Williamson (1989).

quency. The fluid forces of a cylinder undergoing oblique shedding were investigated experimentally by Khalak & Williamson (1996). They showed variations in lift and drag forces with different end conditions and oblique shedding modes. In the Reynolds number range investigated by Khalak & Williamson (1996), the comparison shows a 15 – 20% increase in time-averaged drag when the cylinder undergoes parallel shedding. The lift produced by a cylinder with parallel shedding has a significantly higher RMS values and the instantaneous time trace of the lift signal is stronger and more periodic. Furthermore, they showed that oblique shedding is dominated by two weaker fre-

quencies of lower power due to the weaker and less periodic lift. Parallel shedding shows a single dominant frequency of higher power. This demonstrates that proper end conditioning, via the use of end platform and end plates, is essential to promote parallel shedding in experiments with cylinders.

Studies, notably by Szepessy & Bearman (1992); Norberg (1994), have found that the fluid forces and wake structure depend on the cylinder aspect ratio (\mathcal{R}), defined as

$$\mathcal{R} = \frac{l_{\text{ms}}}{D}, \quad (2.4)$$

where l_{ms} is the immersed length of the cylinder and D is the cylinder diameter. Norberg (1994) reported that low aspect ratio cylinders ($\mathcal{R} < 40$) can significantly delay the critical Reynolds number for the onset of vortex shedding. Szepessy & Bearman (1992) showed that using end plates on a low aspect ratio cylinder ($\mathcal{R} = 6.7$) can reduce variations in fluctuating lift forces and vortex shedding frequency.

From the review of literature, it is clear that the end conditioning and aspect ratio of the cylinder have influences on the response of the cylinder and wake structure. An end plate should be used to limit the influence of oblique shedding and promote parallel shedding. From Szepessy & Bearman (1992), the test cylinder must have an aspect ratio greater than 6.7 to minimize aspect ratio effects.

2.3 Vortex-induced vibration of a circular cylinder

Section 2.2.2 discussed the development of vortices and the process of vortex shedding. Bishop & Hassan (1964); Fredsoe & Sumer (1997) showed that the in-line force component (*i.e.* drag) fluctuates at twice the vortex-shedding frequency (*e.g.* $2f_{sh}$) and the cross-flow force component (*i.e.* lift) fluctuates at the vortex-shedding frequency (*e.g.* f_{sh}). These fluctuating force components can cause the cylinder to vibrate if it is elastically-mounted or flexible. The drag and lift force components can induce vibration in the in-line and cross-flow directions, respectively. This is generally known as vortex-induced vibration (VIV). Due to the complex cylinder motions in VIV, experimental studies are often simplified to the VIV of a rigid circular cylinder that is restrained to freely vibrate in the cross-flow direction, which leads to a better understanding of the fundamental characteristics of the interaction between the flow and the structure. Using a rigid circular cylinder as the test body has several benefits: (1) its axial symmetry and geometric simplicity means a circular cylinder can be defined simply by its length and diameter without the need to consider the relation between the cylinders dimensional parameters with respect to the orientation of the flow, (2) due the circular cylinder's axial symmetry, it is immune from galloping, a FIV phenomenon caused by geometric asymmetry; and (3) circular cross-section is a commonly used geometry in engineering. When the vibration system is restrained to one degree-of-freedom (DOF) in the cross-flow direction, the complex body motions are simplified while maintaining the system's maximum amplitude response because the vibrational amplitudes are significantly larger in the cross-flow than the in-line direction.

Figure 3.5 presents a schematic of a rigid circular cylinder undergoing cross-flow VIV. The cylinder is immersed in a uniform free-stream with velocity U_∞ and is elastically-mounted to give one DOF for the cylinder to freely oscillate in the y -direction, transverse to the free-stream flow. When vortices are shed from alternating sides of the cylinder, the cylinder experiences a fluctuating force, $F_y(t)$, that causes it to oscillate. The oscillatory motion of the cylinder undergoing cross-flow VIV is governed by the equation of motion, given by

$$F_y = m\ddot{y} + c\dot{y} + ky, \quad (2.5)$$

where F_y is the lift force acting transverse to the direction of the free-stream flow, m is the mass of the oscillating system, c is the structural damping and k is the spring constant. The governing

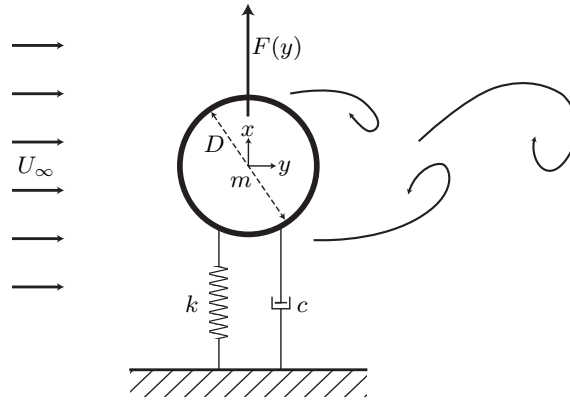


FIGURE 2.4: A schematic of a circular cylinder undergoing cross-flow VIV. The cylinder immersed is a free-stream flow with velocity U_∞ and it is restrained to freely oscillate in the cross-flow y direction. F_y is the lift force, m is the mass of the oscillating system, c is the structural damping and k is the spring constant.

equation of motion can also be expressed in terms of the system's natural frequency of damping

$$\frac{F_y}{m} = \ddot{y} + 2\zeta\omega_n\dot{y} + \omega_n^2 y, \quad (2.6)$$

where ζ is the damping ratio and ω_n is the angular natural frequency of the system, they are mathematically expressed as

$$\zeta = \frac{c}{2m\omega_n}, \quad (2.7)$$

$$\omega_n = \sqrt{\frac{k}{m}}. \quad (2.8)$$

A number of articles and books (*e.g.* Bearman (1984); Blevins (1990); Fredsoe & Sumer (1997); Sarpkaya (2004); Williamson & Govardhan (2004a); Naudascher & Rockwell (2005); Gabbai & Benaroya (2005); Williamson & Govardhan (2008); Paidoussis *et al.* (2007)) have surveyed and comprehensively reviewed elastically-mounted circular cylinders undergoing cross-flow VIV. The following sections focuses on the literature relevant to the present thesis.

2.3.1 Vibration amplitude and frequency responses

Two variables, the vibration amplitude and frequency response, are critical to understanding any VIV system. An early study that examined these was conducted by Feng (1968) in a wind tunnel. His pioneering study characterised the vibration (*i.e.* amplitude and frequency) responses of a circular cylinder at a high mass ratio of 248. Mass ratio (m^*) is the ratio between the system mass and mass of the fluid displaced by the immersed body, it is expressed as

$$m^* = \frac{m}{m_{\text{fld}}}, \quad (2.9)$$

where m is the mass of the oscillating system and m_{fld} is the mass of the fluid displaced by cylinder. Quantities such as amplitude, frequency, force and phases in VIV studies are often presented as a function of a non-dimensionalised parameter, reduced velocity, U^* , it is defined as

$$U^* = \frac{U_\infty}{f_n D}, \quad (2.10)$$

where U_∞ is the free-stream velocity, f_n is the natural frequency of the oscillating structure and D is the diameter of the cylinder. Feng (1968) discovered that the cylinder vibration amplitude is the largest within a range of reduced velocities where the wake and structure becomes synchronised. This is known as the ‘lock-in’ region (synchronisation is discussed in further detail in §2.3.2). The oscillation frequency (f) of an elastically-mounted cylinder in a free-stream flow follows the Strouhal frequency (f_{St}) of a stationary cylinder (*i.e.* $f \cong f_{St}$). When synchronisation occurs, oscillation frequency and the vortex-shedding frequency (f_{sh}) will lock-in with the natural frequency of the oscillating structure,

$$f \cong f_{sh} \cong f_n \quad (2.11)$$

f_{sh} in eq. 2.11 is the vortex-shedding frequency of an elastically-mounted cylinder in a VIV system and should not be confused with the dominant shedding or Strouhal frequency of a stationary cylinder, f_{St} .

The large increase in amplitude associated with synchronisation is shown in fig. 2.5, where fig. 2.5(a) presents the normalised amplitude and (b) the normalised frequency response as a function of U^* . The amplitude response of the oscillating system is often expressed in terms of cylinder diameter (D) by normalising the amplitude output, this is defined as

$$A^* = \frac{y}{D}. \quad (2.12)$$

Normalised oscillation amplitude (A^*), has previously been expressed in different forms. It has been presented in terms of the maximum amplitude, an arbitrary percentage of highest amplitude peaks and RMS amplitude values. Here, to avoid confusion, the type of normalised amplitude data will be denoted in the subscript. Similarly, the oscillation frequency is non-dimensionalised and expressed in terms of the natural frequency of the oscillating structure, the normalised frequency (f^*) is expressed as

$$f^* = \frac{f}{f_n}. \quad (2.13)$$

Data from Feng (1968) presented in fig. 2.5(a) shows there is a significant increase in vibration amplitude over a range of reduced velocities when $5 \leq U^* \leq 7$. Over the same range of U^* , the normalised frequency (see fig. 2.5(b)) locks to values close to unity (*i.e.* $f^* \approx 1$). This fulfils the mathematical relationship presented in eq. 2.11 for wake-structure synchronisation and subsequently the oscillation frequency, vortex shedding frequency and natural frequency of the structure synchronises.

Extensive research conducted by Prof. Williamson’s research group at Cornell University has expanded our understanding and characterisation of VIV vibration responses. The low mass ratio ($m^* \leq 20.6$) water channel experiments reported in Khalak & Williamson (1996, 1997*b*, 1999) observed two distinct discontinuities in the $A_{\max}^* - U^*$ curve that forms three amplitude response branches. fig. 2.5(a) shows the three distinct amplitude response branches, the ‘initial’, ‘upper’ and ‘lower’ branches. In the high mass ratio study ($m^* = 248$) by Feng (1968), only the initial and the lower branches were observed. Khalak & Williamson (1997*a*) showed that at lower mass ratios synchronisation and body oscillations occur at lower reduced velocities. This increases the width of the synchronisation region as it extends over a range of reduced velocities to $4 \leq U^* \leq 12$. The cylinder also experiences larger amplitude responses at lower mass ratios. From see fig. 2.5(a) it can be seen that the peak amplitude value at $A_{\max}^* \approx 1$ is approximately 40% higher than the peak value observed in Feng (1968). After the initial deviation from f_{St} , Khalak & Williamson (1997*b*) also observed that f^* within the synchronisation region increased above unity monotonically with U^* (see fig. 2.5(b)).

It is evident that the peak amplitude response, the number of amplitude response branches, frequency response characteristics and the width of the synchronisation region are influenced by m^* . In addition to m^* , the amplitude response can be influenced by a non-dimensionalised mass-damping

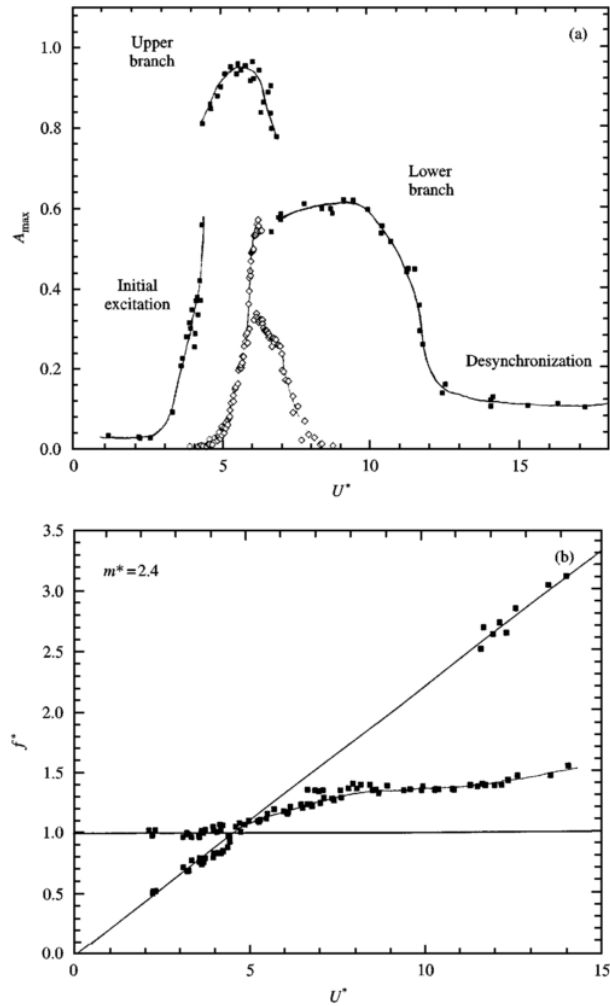


FIGURE 2.5: The (a) normalised amplitude (A^*) and (b) normalised frequency response (f^*) of a cylinder with low mass and damping presented as a function of reduced velocity (U^*). \diamond represent data from Feng (1968) with a mass ratio of $m^* = 248$ and \blacksquare represents data from Khalak & Williamson (1997a) with $m^* = 2.4$. In (b), the horizontal solid line represents the natural frequency of the oscillating system (f_n) and the angled solid line represents the vortex-shedding frequency (f_{sh}) of a stationary cylinder. Figure taken from Khalak & Williamson (1997a).

parameter ($m^*\zeta$), where ζ is the structural damping ratio. It has been shown that the width of the synchronisation region principally depends on m^* where $m^*\zeta$ remains constant (Khalak & Williamson 1996, 1997b, 1999). In general, the amplitude response within the entire synchronisation region is influenced by $m^*\zeta$ of the system. In low m^* cases, the upper amplitude response branch is more sensitive to changes in $m^*\zeta$ than other branches. A change in the system's $m^*\zeta$ will result in a larger change in amplitude values in the upper branch than the initial and lower response branches. Therefore, the peak amplitude response primarily depends on $m^*\zeta$ (Khalak & Williamson 1999). The effects of mass ratio, m^* , and mass-damping, $m^*\zeta$, are illustrated in fig. 2.6(b).

The study of mass and damping effects on VIV systems have been exhaustively surveyed and discussed by Feng (1968); Khalak & Williamson (1999), this review will focus on low mass and low damping systems because they produce larger amplitude responses. For a high mass-damping system, similar to the that of Feng (1968), there are two amplitude response branches, initial and lower branch (see schematic illustration in fig. 2.6(a)). The transition between the initial and lower branch is hysteretic. A system with relatively low mass-damping exhibits three amplitude response

branches, initial, upper and lower branch. It is further characterised by the deviation of the frequency response from the natural frequency of the oscillating system within the synchronisation region. These characteristics were first presented in Khalak & Williamson (1997b) and have been confirmed in other experimental (Govardhan & Williamson 2000, 2002; Brankovic 2004; Zhao 2012) and numerical (Leontini *et al.* 2006; Klamo 2007) studies. The amplitude response branches and transition characteristics of a low mass-damping system is schematically illustrated in fig. 2.6(b).

The initial branch begins at very low U^* . Khalak & Williamson (1997b) showed that the initial branch can occur at reduced velocities as low as $U^* \approx 1$. This branch is characterised by (1) low to moderate amplitude responses that increases with U^* and (2) an oscillation frequency response that locks to the Strouhal frequency of a stationary cylinder. Due to the influence of the natural frequency of the structure and the vortex shedding frequency, the oscillation observed in this branch is not highly periodic but quasi-periodic (Khalak & Williamson 1999). The system undergoes hysteretic transition from the initial branch to upper branch as the reduced velocity is increased past $U^* \approx 1/St \approx 4.8$. As the transition occurs, f^* begins to lock-in to the natural frequency of the structure.

In the upper branch, A^* is significantly larger. It is known that the maximum amplitude response A_{\max}^* is influenced by the oscillating system's mass and damping ratios (Khalak & Williamson 1996, 1997b, 1999) but work by Govardhan & Williamson (2006); Klamo (2007) have shown that the maximum amplitude can also be influenced by the effects of Reynolds number. This maximum amplitude response is self-limited and Govardhan & Williamson (2000) have reported that for a system with very low mass ratio, the maximum amplitude response could reach $A_{\max}^* \approx 1.2$. The oscillation frequency in the upper branch initially deviates from the Strouhal frequency of a stationary cylinder and locks onto the natural frequency of the structure. As U^* is increased, the frequency response increases monotonically with reduced velocity and deviates from the natural frequency of the structure (*i.e.* $f^* > 1$). Oscillations in the upper branch are highly periodic up to the onset of the transition to the lower branch. Here, the system switches intermittently between the two amplitude response branches. This intermittent switching was documented in Khalak & Williamson (1999) and indicated by the instantaneous phase difference between the measured cylinder displacement and lift force.

Compared to the initial and upper amplitude response branches, the lower branch spans a larger portion of the synchronisation region. Its amplitude response remains in the proximity of $A^* \approx 0.6$ over a large section of the response branch. As the oscillation frequency increases with reduced velocity the amplitude response gradually decreases.

When the reduced velocity is increased further the system desynchronizes from the natural frequency of the structure and a sharp reduction in amplitude response. When the oscillation system desynchronizes from the natural frequency of the structure it resumes following the Strouhal frequency of a stationary cylinder. Both the natural frequency of the structure and the shedding frequency influence this region, known as the desynchronization region, which is characterised by chaotic oscillations and very small amplitude responses.

2.3.2 Synchronisation

In vortex-induced vibration, the synchronisation between wake and structure is known as 'lock-in'. In the synchronisation region, the vortex shedding frequency deviates from the Strouhal frequency of a stationary cylinder and follows the frequency response of the cylinder. For a high mass-damping system, similar to the wind-tunnel studies by Feng (1968), the phenomenon of synchronisation is characterised by the oscillation frequency response (and subsequently the vortex shedding frequency) in close approximation of the natural frequency of the structure. This is schematically illustrated in fig. 2.7(a) and mathematically expressed in eq. 2.11. In the synchronisation region in a low mass-damping system, as is typically observed in water-channel experiments, the oscillation frequency deviates from the natural frequency of the structure and monotonically increases above unity with

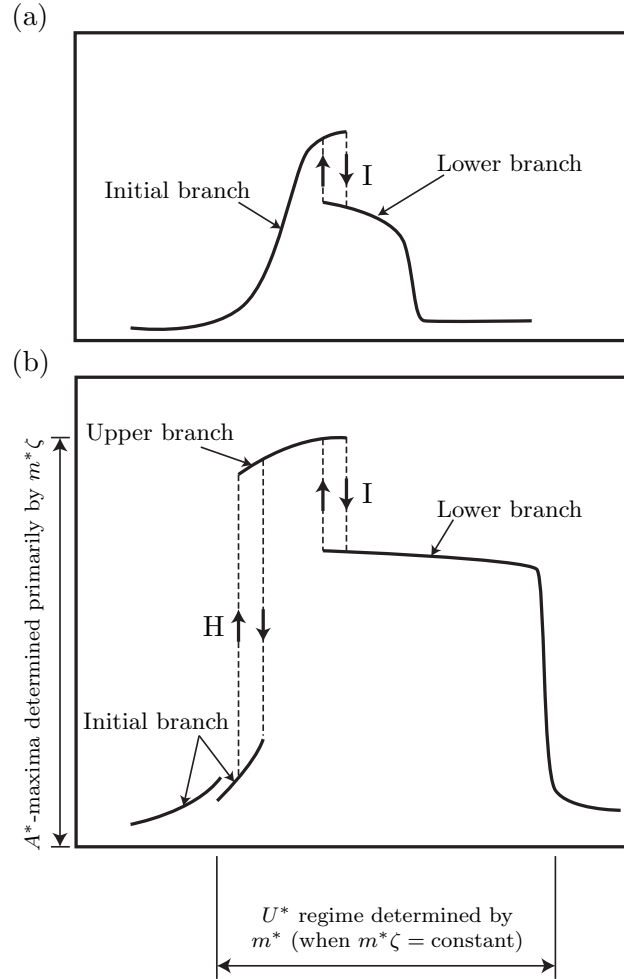


FIGURE 2.6: An illustration of the two distinct types of VIV amplitude responses for an elastically-mounted circular cylinder: (a) a high mass-damping ($m^*\zeta$) system characterised by two response branches (initial and lower branch), and (b) a low $m^*\zeta$ system characterised by three response branches (initial, upper and lower branch). Transition between branches are either hysteretic (H) or involves intermittent switching (I). Illustration reproduced from Khalak & Williamson (1999).

reduced velocity (see fig. 2.7(b)). Studies by Fredsoe & Sumer (1997); Govardhan & Williamson (2000) have discussed that this deviation from the natural frequency of the structure results from added-mass effects arising from the acceleration of the oscillating cylinder.

Differences in the definition of synchronisation continues to exist, as some work defines synchronisation as the matching of the cylinder oscillation frequency response with a periodic wake mode (Gabbai & Benaroya 2005). A definition adopted by Williamson's research group and the present thesis was first defined by Sarpkaya (1995). He defined synchronisation as being when the frequency of the total lift force F_L matches the oscillation frequency of the cylinder, f .

A number of studies have shown that the mass ratio of the oscillation system significantly influences the synchronisation regime (Govardhan & Williamson 2000; Williamson & Govardhan 2004b; Brankovic 2004; Ryan *et al.* 2005). The effects of mass ratio were first reported in Govardhan & Williamson (2000, 2002). In his experimental studies, he observed the existence of a critical mass ratio, $m_{crit}^* = 0.542 \pm 0.01$. Below this critical value, the range of reduced velocity within which the synchronisation region exist expands to infinity (see fig. 2.8). Brankovic (2004) reported a critical mass ratio of $m_{crit}^* = 0.4$ in her experimental study. Ryan *et al.* (2005) presented nu-

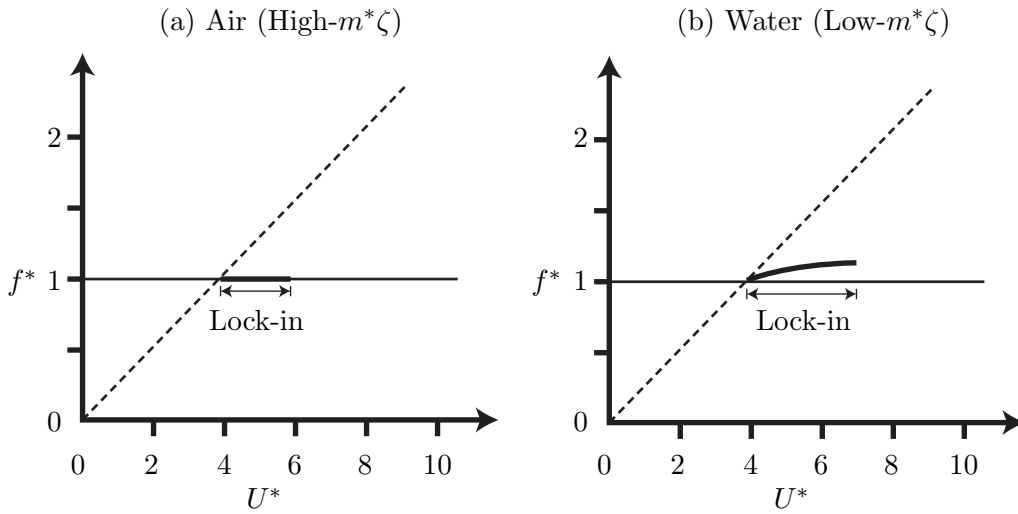


FIGURE 2.7: An illustration of the frequency response (f^*) of the synchronisation region of an elastically-mounted circular cylinder undergoing VIV. (a) shows that f^* lock-in with the natural frequency of the structure (f_n) through the VIV synchronisation region in air. (b) shows that in water, f^* deviates from unity and increases monotonically through the synchronisation region with reduced velocity (U^*). Illustration reproduced from Fredsoe & Sumer (1997).

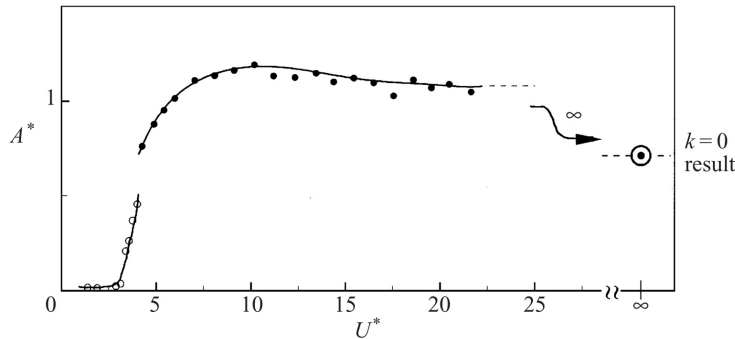


FIGURE 2.8: Amplitude response (A^*) of an oscillating system where the mass ratio $m^* = 0.52$ is below the critical value $m^* < m^*_{crit}$. The synchronisation region extends to infinitely with reduced velocity (U^*) and the amplitude response at infinity remains large at $A^* \approx 0.7$. The spring constant is set at $k = 0$. \circ represents the initial branch and \bullet represents the upper branch. Illustration from Govardhan & Williamson (2002).

merical results showing the effects of Re on m^*_{crit} . The critical mass ratio varied within the range $0.075 \leq m^*_{crit} \leq 0.51$ as a function of Reynolds number within the range $30 \leq Re \leq 200$.

2.3.3 Fluid forces, phases and wake structures

The characterisation of amplitude and frequency responses help researchers predict the vibrational responses of the structures, however, they alone are insufficient in providing a complete understanding of mechanics and wake-structure interactions. To understand the mechanics and wake-structure interactions of a circular cylinder undergoing VIV, it is essential to characterise: (1) the fluid forces,

(2) phase relationship between fluid forces and the body motion and (3) wake modes. Direct fluid force measurements have been taken in the past in forced oscillation studies (*e.g.* Bishop & Hassan (1964); Staubli (1983)), however, not until recent is there such measurement for a freely oscillating system. The first direct fluid force measurements of a circular cylinder undergoing VIV was presented by Khalak & Williamson (1997*b*). In addition to direct force measurements, Khalak & Williamson (1997*b*) applied Hilbert transformation (HT) and computed the instantaneous total phase angle (ϕ_T) between the cross-flow lift force and body displacement. From this, it was found that ϕ_T intermittently switches between $\phi_T \approx 0^\circ$ and $\phi_T \approx 180^\circ$, this corresponded with the intermittent switching that occurs during the transition between the upper ($\phi_T \approx 0^\circ$) and lower ($\phi_T \approx 180^\circ$) amplitude branches.

The fluid force decomposition method was first proposed by Lighthill (1986) and used by Govardhan & Williamson (2000) to decompose the total lift force F_y from eq. 2.5 into two components: (1) the potential force component (F_{pot}) arise from the potential added-mass force and (2) the vortex force component (F_{vor}) arisen from fluid vorticity. This decomposition is mathematically expressed as

$$F_y = F_{pot} + F_{vor}. \quad (2.14)$$

By dividing the above force equation by $\frac{1}{2}\rho U^* DL$, where ρ is the fluid density, eq.2.14 is non-dimensionalised into force coefficients

$$C_y(t) = C_{pot}(t) + C_v(t). \quad (2.15)$$

Khalak & Williamson (1999); Govardhan & Williamson (2000) have shown that when the cylinder oscillation frequency response, f^* , is lock onto the vortex shedding frequency, f_{sh} , the cylinder displacement, y , and total cross-flow lift force, F_y , is approximated by

$$y(t) = A_o \sin \omega t, \quad (2.16)$$

and

$$F_y(t) = F_Y \sin \omega t + \phi_T, \quad (2.17)$$

where A_o is the magnitude of the cylinder displacement, F_Y is the magnitude of the cross-flow lift force; ϕ_T is the total phase and ω is angular frequency of oscillation and is defined as

$$\omega = 2\pi f. \quad (2.18)$$

The instantaneous potential force ($F_{pot}(t)$) acting on the cylinder is defined by

$$F_{pot}(t) = -m_A \ddot{y}(t) = \frac{C_A \pi \rho D^2 L}{4} \ddot{y}(t), \quad (2.19)$$

where m_A is the added mass. It is termed as

$$m_A = C_A m_{fd}, \quad (2.20)$$

with C_A being the potential flow added-mass coefficient (For a circular cylinder $C_A = 1$), and m_{fd} is the mass of the fluid displaced. For a circular cylinder, m_{fd} is expressed as

$$m_{fd} = \frac{\pi \rho D^2 L}{4}, \quad (2.21)$$

By substituting eq. 2.20 and eq. 2.21 into eq. 2.20, the potential force can be expressed as

$$F_{pot}(t) = \frac{C_A \pi \rho D^2 L}{4} \ddot{y}(t). \quad (2.22)$$

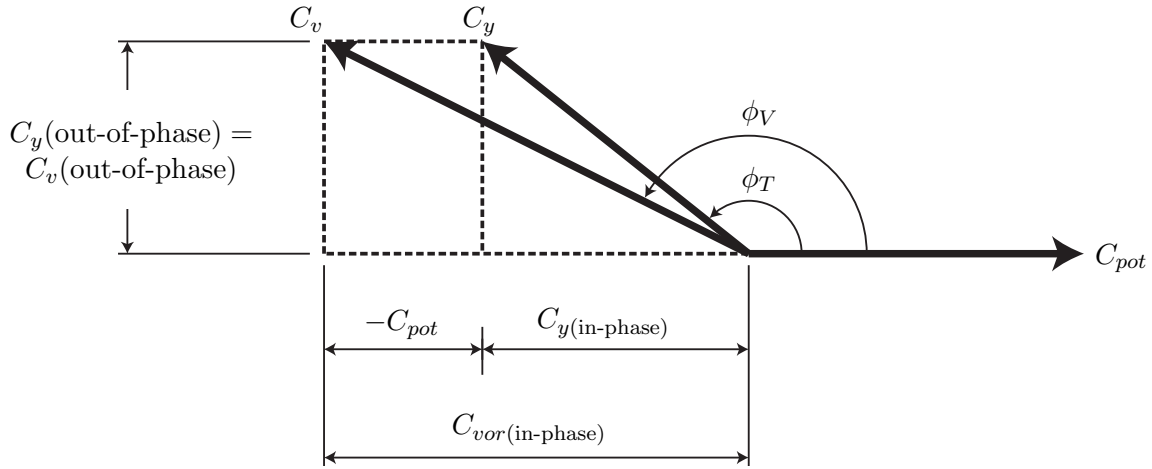


FIGURE 2.9: An illustration of the relationships between the three force components and the phases. Figure reproduced from Zhao (2012).

By normalising eq. 2.22 with $\frac{1}{2}\rho U^* DL$ and substituting for the cylinder displacement from eq. 2.16, the potential force coefficient is found and it is expressed as

$$C_{pot}(t) = 2\pi^3 \frac{y(t)/D}{(U^*/f^*)^2}. \quad (2.23)$$

As expected, the equation above shows that the instantaneous potential added-mass force ($C_{pot}(t)$) is in phase with the displacement of the cylinder $y(t)$.

Consequently, when the cylinder is undergoing vortex-induced oscillations the governing equation of motion can be termed as

$$m\ddot{y} + c\dot{y} + ky = F_o \sin \omega t + \phi_T. \quad (2.24)$$

The above equation can be rewritten to only retain the vortex force term by combining eq. 2.14 and eq. 2.22, thus, eq.2.24 can be expressed as

$$(m + m_A)\ddot{y} + c\dot{y} + ky = F_{vor} \sin \omega t + \phi_V, \quad (2.25)$$

where ϕ_V is the vortex phase. It is defined as the phase angle between the vortex force ($F_{vor}(t)$) and the cylinder displacement $y(t)$. The relationship between the forces and phases are illustrated fig. 2.9.

The vortex structure is important to a body undergoing VIV because it directly influences the fluid forces and the phase between them and body motion. A number of experiments have characterised the different wake modes of a circular cylinder undergoing VIV. This was perhaps first performed with sinusoidally-driven cylinders by Williamson (1988). He presented a map showing the different wake modes with respect to different regimes of A^* and U^* . Flow visualisation studies by Brika & Laneville (1993); Khalak & Williamson (1999) observed changes in wake mode corresponding to the transition of amplitude response branches. Govardhan & Williamson (2000) presented particle image velocimetry (PIV) (see §3.5.4) results on the wake modes of a circular cylinder undergoing VIV. They showed that, depending on the mass-damping, $m^*\zeta$, of the oscillating system, the cylinder exhibits two distinct types of response. At high $m^*\zeta$, it was observed there is one wake mode transition, which corresponds to the transition from the initial amplitude response branch to the lower branch. When the oscillating system has low $m^*\zeta$, there exist two distinct transitions in the amplitude response branches. A wake mode transition was observed to occur at the transition in amplitude response between the initial and upper branch.

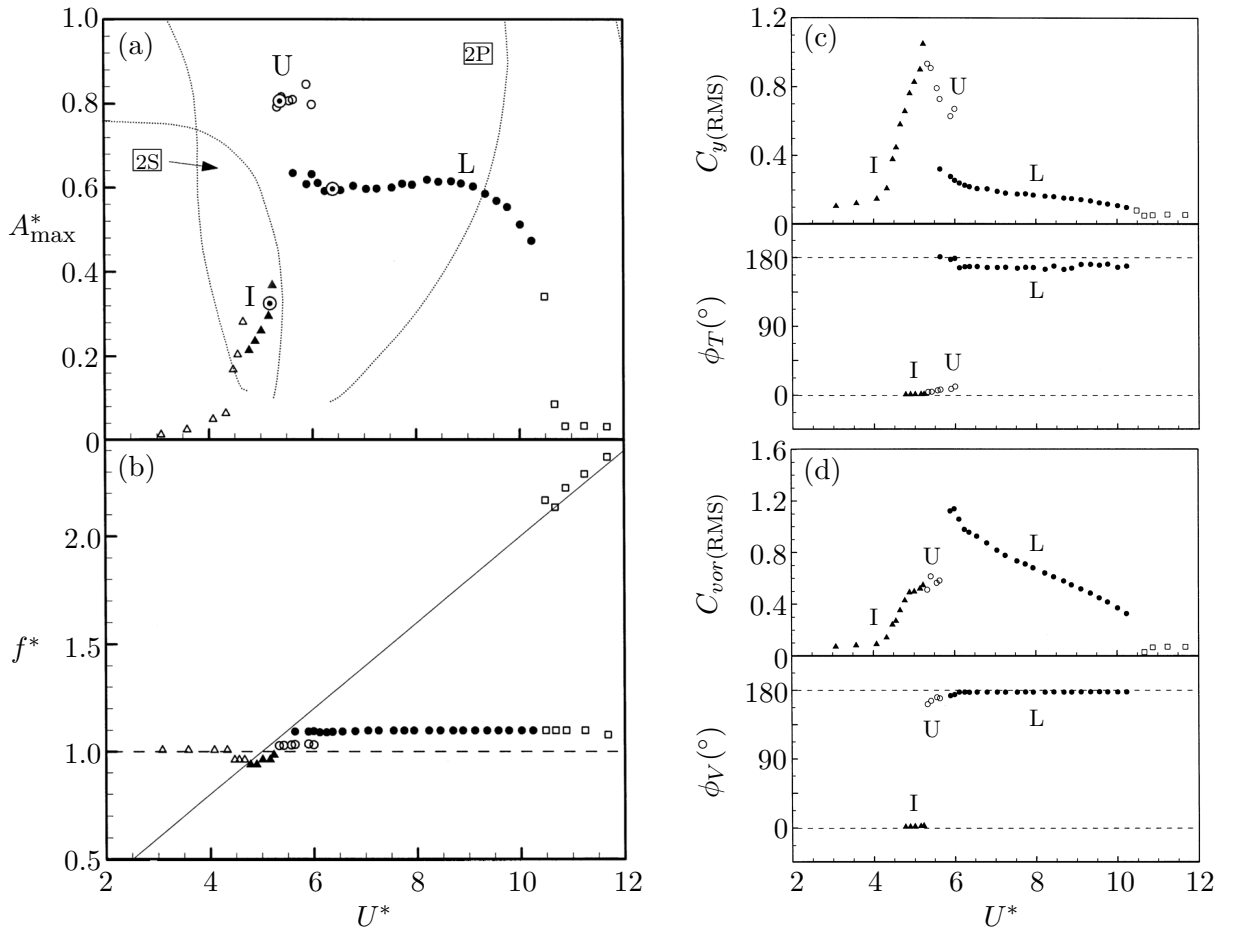


FIGURE 2.10: The response of a circular cylinder undergoing VIV with a mass ratio of $m^* = 8.63$ and damping ratio of $\zeta = 0.00151$. Presented as a function of reduced velocity (U^*): (a) the maximum amplitude response (A_{\max}^*), (b) frequency response (f^*); (c) the RMS values of the total transverse lift force coefficient ($C_{y,RMS}$) and the total phase (ϕ_T); and (d) the RMS values of the vortex force coefficient ($C_{v,RMS}$) and the vortex phase (ϕ_V). (Δ , \blacktriangle), initial (I) branch; \circ , upper (U) branch; \bullet , lower (L) branch; and \square , desynchronization region. \odot , location of PIV measurements. \cdots represents the wake mode boundaries from Williamson (1988). Figures taken from Govardhan & Williamson (2000).

The relationships between the oscillation amplitude, frequency response, fluid forces, phases and the wake modes occurring at low mass-damping ($m^* = 8.63$, $\zeta = 0.00151$) is shown in fig. 2.10 from the research of Govardhan & Williamson (2000). Figure 2.10(a) presents the amplitude response from Govardhan & Williamson (2000) with the bullseyes, which show the locations of PIV measurements, it is overlaid with the wake mode boundaries from the forced oscillation results from Williamson (1988). As predicted by Williamson (1988), the free vibration study by Govardhan & Williamson (2000) observed two distinct wake modes. The wake of the initial amplitude response branch is characterised by the 2S mode, in which two single vortices are shed per body oscillation cycle. In the upper and lower amplitude response branches the 2P mode was observed. This mode comprises of two pairs of vortices shed per body oscillation cycle. PIV flow measurements of the 2S and 2P wake modes in the initial, upper and lower amplitude response branches are presented in fig. 2.11. Anti-clockwise vorticity is presented in red and clockwise vorticity in blue.

The development of 2S mode vortices and their shedding is shown in fig. 2.11(a). Two single

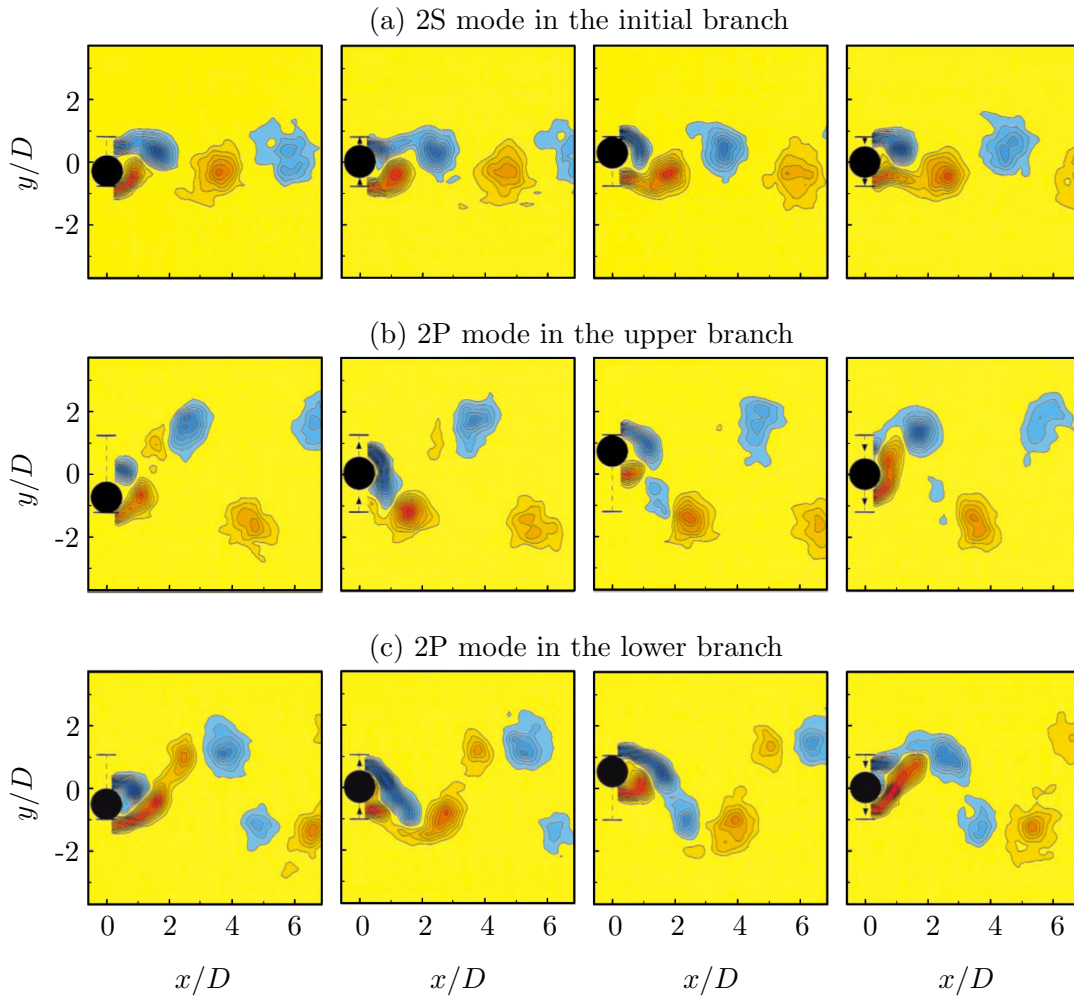


FIGURE 2.11: Vorticity contour plots of the wake modes of a circular cylinder undergoing VIV with low mass-damping ($m^* = 8.63$ and $\zeta = 0.00151$). Closewise vorticity in blue and anti-clockwise vorticity in red. (a) shows the wake of the 2S mode associated with the initial branch (normalised amplitude response $A^* = 0.33$ and reduced velocity $U^* = 5.18$), (b) shows the wake of the 2P mode in the upper branch ($A^* = 0.81$ and $U^* = 5.39$); and (c) shows the wake of the 2P mode in the lower branch ($A^* = 0.6$ and $U^* = 6.40$). Contour images taken from Govardhan & Williamson (2000).

vortices of opposite vorticity were shed from alternate sides of the cylinder per oscillation cycle. This forms a narrow row of vortices along the wake centreline. When the oscillation transitions from the initial to upper amplitude response branch the wake mode transitions from 2S to the 2P mode.

The 2P mode (presented in fig. 2.11(b)) consist of a pair of vortices of opposite vorticity shed per half oscillation cycle from only one side of the cylinder. Over a complete oscillation cycle, two pairs of vortices are shed from alternating sides of the cylinder. They form two rows of vortices flowing downstream parallel to the wake centreline. Each pair consists of a strong first vortex and a weaker second vortex. The relatively stronger first vortex puts strain on the second vortex and results in it being rapidly weakened (Govardhan & Williamson 2000). Five cylinder lengths downstream (*i.e.* $x/D > 5$), the weaker second vortex decays completely and takes on the appearance of the 2S mode. Govardhan & Williamson (2000) remarked that the rapid decay of the second weaker vortex in the upper branch is the reason behind the difficulty in identifying this mode in Khalak & Williamson (1999). The wake remains in 2P mode as it transitions from the upper to the lower amplitude

response branch. However, the 2P mode in the lower branch exhibits a stronger second vortex that is comparable in strength to the first vortex in the pair. In addition to relating wake modes to amplitude response branches, the vortex modes can be predicted by the changes in fluid forces and phase angle.

In the transition from the initial to upper amplitude response branch, the vortex phase jumps from $\phi_V \approx 0^\circ$ to $\phi_V \approx 160^\circ$ and continues to converge towards $\phi_V \approx 180^\circ$ with increases in reduced velocity in the upper branch, as shown in fig. 2.10(d). In contrast, the total phase shown in fig. 2.10(c) remained at $\phi_T \approx 0^\circ$ during the transition between the initial and upper branch. It increased marginally with U^* in the upper branch. This jump in ϕ_V corresponds to the wake transition from 2S to 2P mode.

A jump in total phase was observed from $\phi_T \approx 0^\circ$ to $\phi_T \approx 180^\circ$ when the amplitude response transitioned from upper to lower branch, as seen in fig. 2.10(c). The vortex phase gradually increases from $\phi_V \approx 160^\circ$ at the start of the upper branch to, and remained at, $\phi_V \approx 180^\circ$ throughout of the lower branch. Moreover, there is a sharp jump in vortex force as the oscillating system transitions to the beginning of the lower branch. The vortex force reaches a peak value of $C_{v,\text{RMS}} \approx 1.2$ before it gradually decreases with U^* . As the vortex phase plateaued and vortex force peaked in the lower branch, the 2P wake mode, as shown in fig. 2.11(c), becomes clearer in its structure and stronger in vorticity compared to the 2P mode in the upper branch.

A summary of the characteristics of a low $m^*\zeta$ VIV system is presented in fig. 2.12. This is a reproduction of the figure presented in Govardhan & Williamson (2000) for experimental results at mass ratios significantly higher than the critical mass ratio (*i.e.* $m^* = 8.63 \gg m^*_{\text{crit}} = 0.54$). As the amplitude response transitions from the initial to the upper branch, the oscillation frequency increases past the natural frequency of the oscillating structure in water, (*i.e.* $f \approx f_{nw}$). Here, the wake mode transitions from 2S to 2P mode with a sharp jump in ϕ_V . The transition from the upper to lower branch occurs when the oscillation frequency approaches the natural frequency of the oscillating structure in vacuum, (*i.e.* $f \approx f_{na}$). A sharp jump in ϕ_T occurs with the transition from upper to lower branch. There is no significant change in vortex phase throughout the upper and lower branch and the wake remains in the 2P mode in the lower branch.

2.4 Circular cylinder undergoing rotary motions

When vortex-induced vibrations resonate with the structure, large amplitude oscillations occur. In engineering applications, these large amplitude oscillations can cause catastrophic failures. Therefore, researchers have conducted studies into active and passive suppression techniques. Passive VIV suppression techniques involve geometric alterations or attachments on the oscillating structure to alter its wake-structure interactions. Wong & Kokkalis (1982); Hover *et al.* (2001); Owen *et al.* (2001); Bearman & Branković (2004); Assi *et al.* (2009) have characterised the behaviour of a number of passive VIV suppression techniques and a review of these techniques is presented in Kumar *et al.* (2008). Active VIV suppression techniques, where the flow is manipulated using motion control of the body has been the focus of recent research. Research in active flow control techniques are often conducted with a circular cylinder, due to its spanwise geometric symmetry. This enables researchers to study the effects of the body motion independent from the effects of any geometric and orientation asymmetry with respect to the free-stream flow. Research has focussed on two types of active flow control techniques (1) body rotation about the spanwise axis (z axis) at a constant rate and (2) sinusoidally-driven rotary oscillations about the spanwise axis of the body (z axis).

As the focus of the present thesis is on active flow manipulation via body rotation, a brief review of relevant literature is presented. The effects of constant rate rotation on the fluid forces and wake regimes of a rigidly-mounted circular cylinder is discussed in §2.4.1. Section §2.4.2 reviews work on sinusoidally-driven rotary oscillation of rigidly-mounted circular cylinders.

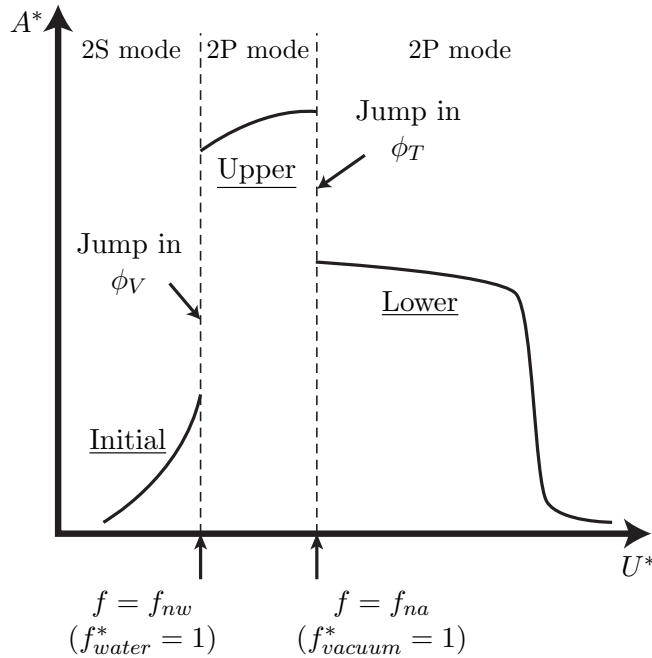


FIGURE 2.12: An illustration showing the characteristics of a low mass-damping ($m^*\zeta$) circular cylinder undergoing VIV: the three-branch amplitude response, corresponding wake modes and phase jumps during branch transitions. Illustration reproduced from Govardhan & Williamson (2000).

2.4.1 Constant rotation

The phenomenon of a rotating body moving through fluids has captured the interest of researchers for well over a century because of its effect on the flight path of projectiles. In the 1850's, German researcher H.G Magnus was one of the first to publish the effects of rotation on musket balls and cylinders moving through air (Swanson 1961). He observed that the interaction between the spinning body and the velocity of the fluid flow creates an asymmetric pressure distribution. As the body undergoes rotation the boundary layer on the windward side of the body is accelerated, meanwhile, the boundary layer is decelerated on the leeward side of the body. This creates an asymmetric pressure distribution, producing a force to act on the body (Magnus 1993), which was became known as the Magnus force. When a body is rotating through its axis of rotation, the Magnus force acts in a direction that is perpendicular to the direction of the free stream flow and the axis of rotation. The magnitude of this force is proportional to the rate of body rotation.

A core parameter in rotating cylinder studies is the rotation rate, α , which is defined as the cylinder's surface tangential velocity normalised by the free stream velocity, U_∞ . Its mathematical form is

$$\alpha = \frac{D\omega_{rc}}{2U_\infty}, \quad (2.26)$$

where D is the cylinder diameter and ω_{rc} is the cylinder's angular velocity, in radians per second.

2.4.1.1 Fluid forces

A parameter that is of particular interest is the lift force rotating cylinders can generate. One of the earliest investigators into the fluid flow past a rigidly-mounted rotating cylinder was Prandtl (1925).

He proposed that there exists a maximum lift ($C_{L,\max}$) that a rotating cylinder in a uniform flow can generate. This prediction is based on the rotation rate at which the stagnation point moves to a location on the windward side of the cylinder such that shedding ceases. This ideal rotation rate is predicted to be $\alpha = 2$. From this, the predicted maximum lift is limited to $C_{L,\max} = 4\pi \approx 12.6$. The two-dimensional numerical study by Chew *et al.* (1995) shows agreement with Prandtl's prediction. At a Reynolds number of $Re = 1000$, Chew *et al.* (1995) found that with increasing α , the mean lift coefficient approaches an asymptotic value.

However, there are questions on the existence of a limit to maximum lift. Chen *et al.* (1993) reported in his numerical study ($Re = 200$) and at rotation rate $\alpha \leq 3.25$ that the instantaneous lift values exceeded Prandtl's limit of $C_{L,\max} = 4\pi \approx 12.6$. More recent studies (see Mittal (2001); Stansby & Rainey (2001); Mittal & Kumar (2003)) conducted at a low Reynolds number of $Re = 200$ and rotation rates $0 \leq \alpha \leq 5$ have shown instantaneous and time-averaged lift values much larger than Prandtl's prediction.

The experimental study by Tokumaru & Dimotakis (1993) at a Reynolds number of $Re = 3800$ also showed that Prandtl's limit can be exceeded. In that experiment, a cylinder with an aspect ratio of $\mathcal{R} = 18.7$ rotating at a rate of $\alpha = 10$ produced an estimated lift 20% larger than Prandtl's limit. They suggested that three-dimensionality and end effects are the likely cause of the increase in lift coefficient values compared to those reported in two-dimensional numerical studies. Furthermore, they remarked, from the trends of their results, that the lift coefficient (C_L) can be increased further with higher α and using a cylinder with larger \mathcal{R} .

These claims in Tokumaru & Dimotakis (1993) are unsurprising because a number of studies have shown the effect of end conditions and aspect ratio effects on a rotating cylinder. Prandtl (1925) concluded that the overall lift coefficient can be increased by utilising end disc/plates and cylinders with larger aspect ratios. Thom (1935) remarked that as the aspect ratio of the finite length cylinder decreases the magnitude of the maximum lift also decreases as the rotation rate at which the maximum lift is achieved.

The exceeding of Prandtl's limit has also been observed in studies involving impulsively rotated cylinders. Notable studies by Badr *et al.* (1990); Chen *et al.* (1993); Chen (2000) have shown that the lift generated by the cylinder increases with time until it reaches a stable band of values. Figure 2.13 from Mittal & Kumar (2003) presents the time histories of C_L at different α . Their low Reynolds number ($Re = 200$) numerical study showed that with sufficient time the lift generated by the rotating cylinder achieves a steady state at specific rotation rates. This was also observed at high Reynolds number ($Re = 50000$) by Karabelas *et al.* (2012). There is a direct correlation between the system's steady and unsteady fluid force states to the wake structure and vortex shedding behind the cylinder. Wake modes and their correlation with the fluid forces are discussed in the following section.

2.4.1.2 Wake structures

The wake structure of a rotating cylinder has been extensively studied over the past three decades. To characterise the wake structures and their development with body rotation, it is essential to understand the different steady and unsteady flow states. Researchers, most notably El Akoury *et al.* (2008); Rao *et al.* (2013), have presented a map highlighting the different flow states at various α with respect to Re . Figure 2.14 presents this map, it shows the three different flow states where Reynolds number $Re \leq 500$; (1) unsteady flow, (2) steady-state flow and (3) the second instability. These have been reported in a number of studies (*e.g.* Mittal & Kumar (2003); El Akoury *et al.* (2008); Rao *et al.* (2013, 2015)).

The unsteady flow state has previously been observed by (*e.g.* Díaz *et al.* (1983); Coutanceau & Menard (1985); Badr *et al.* (1990); Tokumaru & Dimotakis (1991); Chen *et al.* (1993); Kang *et al.* (1999); Mittal & Kumar (2003); El Akoury *et al.* (2008); Rao *et al.* (2013)). This flow state

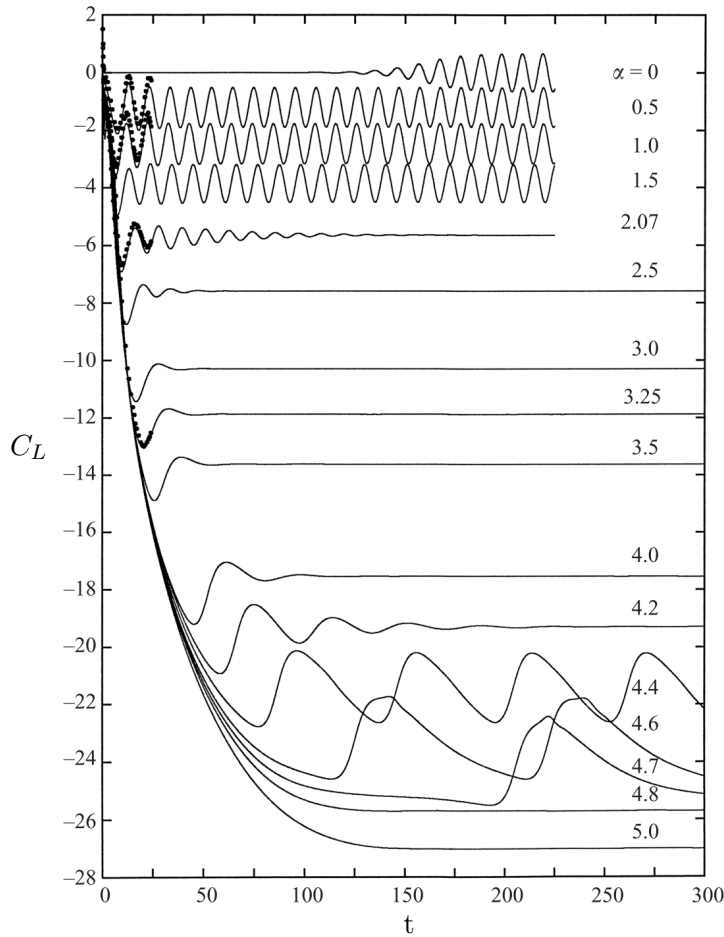


FIGURE 2.13: Time histories of lift coefficients (C_L) of a rigidly-mounted rotating cylinder for different rotation rates (α) at Reynolds number $Re = 200$. • represents numerical data from Chen *et al.* (1993). Figure and reference from Mittal & Kumar (2003).

ranges from a non-rotating cylinder ($\alpha = 0$) case to the first critical rotation rate ($\alpha_{crit.1}$) at which it marks the boundary between unsteady and steady-state flow. However, there is some dispute over the value of $\alpha_{crit.1}$. Díaz *et al.* (1983); Coutanceau & Menard (1985); Badr *et al.* (1990) found that above a rotation rate $\alpha \geq 2$, vortex shedding is suppressed and concluded that $\alpha_{crit.1} \approx 2$. Numerical work by Kang *et al.* (1999) showed that $\alpha_{crit.1}$ exhibits a logarithmic dependence on Re . More recent numerical work by Rao *et al.* (2013) showed that over a range of low Reynolds numbers ($100 < Re \leq 350$, the critical rotation rate is $1.8 \leq \alpha_{crit.1} \leq 2.1$. This is in good agreement with the $\alpha_{crit.1} = 1.91$ value mentioned in Mittal & Kumar (2003). Results presented in fig.2.14 from El Akoury *et al.* (2008) shows larger variations as the critical rotation rate ranged between $1.9 \leq \alpha_{crit.1} \leq 2.5$ at the same Reynolds number ($Re = 200$). The wake of the cylinder within the unsteady flow state is characterised by the Kármán vortex street. Two single vortices of opposite vorticity are shed from alternate sides of the cylinder per shedding cycle. As α is increased the wake deflect away from its centreline and this increases with α while the lateral width decreases. This is seen in the vorticity fields presented in fig. 2.15 and fig. 2.16 (cases where the rotation rate $\alpha < 2.08$). The wake, and subsequently the fluid forces, are unsteady in this flow state, however, they are periodic as evidenced by the time histories of the lift forces (see fig. 2.13) and the Kármán vortex street.

2.4. Circular cylinder undergoing rotary motions

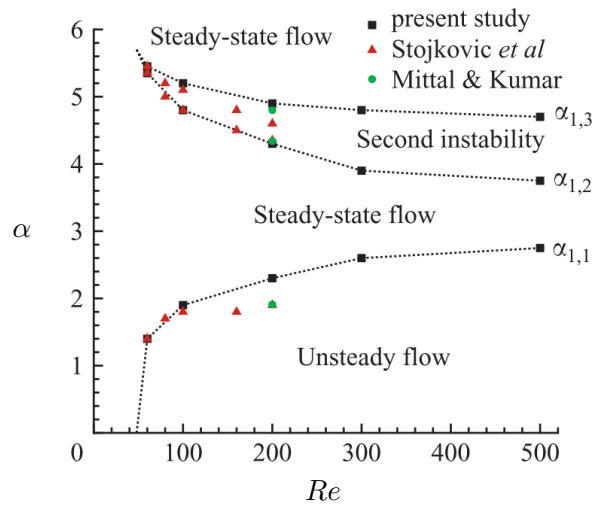


FIGURE 2.14: Wake stability diagram based on critical rotation rates (α_{crit}) and Reynolds number (Re). The dashed lines represent the three α_{crit} values and outline the different flow states. Figure and reference from El Akoury *et al.* (2008).

When the rotation rate increases above $\alpha_{crit.1} \approx 2$, the fluid transitions to steady-state flow. This steady-state flow exists between $\alpha \approx 2$ and a second critical rotation rate ($\alpha_{crit.2}$). The second critical rotation rate marks the upper limit of the steady-state and defines the boundary with the second instability. Unlike $\alpha_{crit.1}$, which marks the boundary between unsteady and steady-state flow, the value of $\alpha_{crit.2}$ is better defined for different work. El Akoury *et al.* (2008) (see fig. 2.14) showed that at $Re = 200$, the second critical rotation rate is $\alpha_{crit.2} \approx 4.35$. This agrees well with Mittal & Kumar (2003). A logarithmic relationship exists between flow state boundaries and Re as discussed in Kang *et al.* (1999). The value of $\alpha_{crit.2}$ decreases and converges towards $\alpha_{crit.2} \approx 3.8$ as Reynolds number is increased ($Re \geq 500$). The wake in the steady-state flow regime is characterised by three features: (1) the absence of vortex shedding, (2) long elongated regions of vorticity and (3) vorticity reversal. These features can be seen in fig.2.15 and fig. 2.16 (cases where the rotation rate $1.9 \leq \alpha \leq 4.3$). The cylinder in fig.2.15 and fig. 2.16 are rotating counter-clockwise with solid lines denoting positive clockwise and dashed lines denoting negative anti-clockwise vorticity. In a typical Kármán vortex street, positive and negative vorticity is generated from the two sides of the cylinder and feed into the near wake. For a rotating cylinder in the steady-state flow region, as α is increased (with reference to fig.2.15 and fig. 2.16), positive vorticity increases from the windward side that then curls upwards by the rotation. This exposes the region of negative vorticity to the oncoming free-stream flow. Vortex shedding stops as both vorticity regions become stabilised, elongated and carried downstream. The reversal of the location of the positive and negative vorticity (not the sign of the vorticity) occurs when the cylinder rotation begins to wrap the negative vorticity on the leeward side of the cylinder around to the windward side (see $\alpha = 2.5 - 4.3$ cases in fig.2.15). As rotation rate is increased between $2.5 \leq \alpha \leq 4.3$, the amount of negative vorticity on the leeward side of the cylinder decreases as the cylinder rotation wraps it on the windward side of the cylinder forming a ‘tongue’ like structure as described by Mittal & Kumar (2003). As the reversal occurs, negative vorticity exists on both side of the cylinder until it is completely wrapped around under the region of positive vorticity. In this process, the wake deflects further away from the wake centreline.

No oscillating lift forces are generated as a result of the absence of vortex shedding, however, the Magnus force generated by the cylinder rotation remains. This is evidenced in fig. 2.13 (see $2.07 \leq \alpha \leq 4.2$ cases) where C_L increases with α , however, each of these cases reaches steady-state

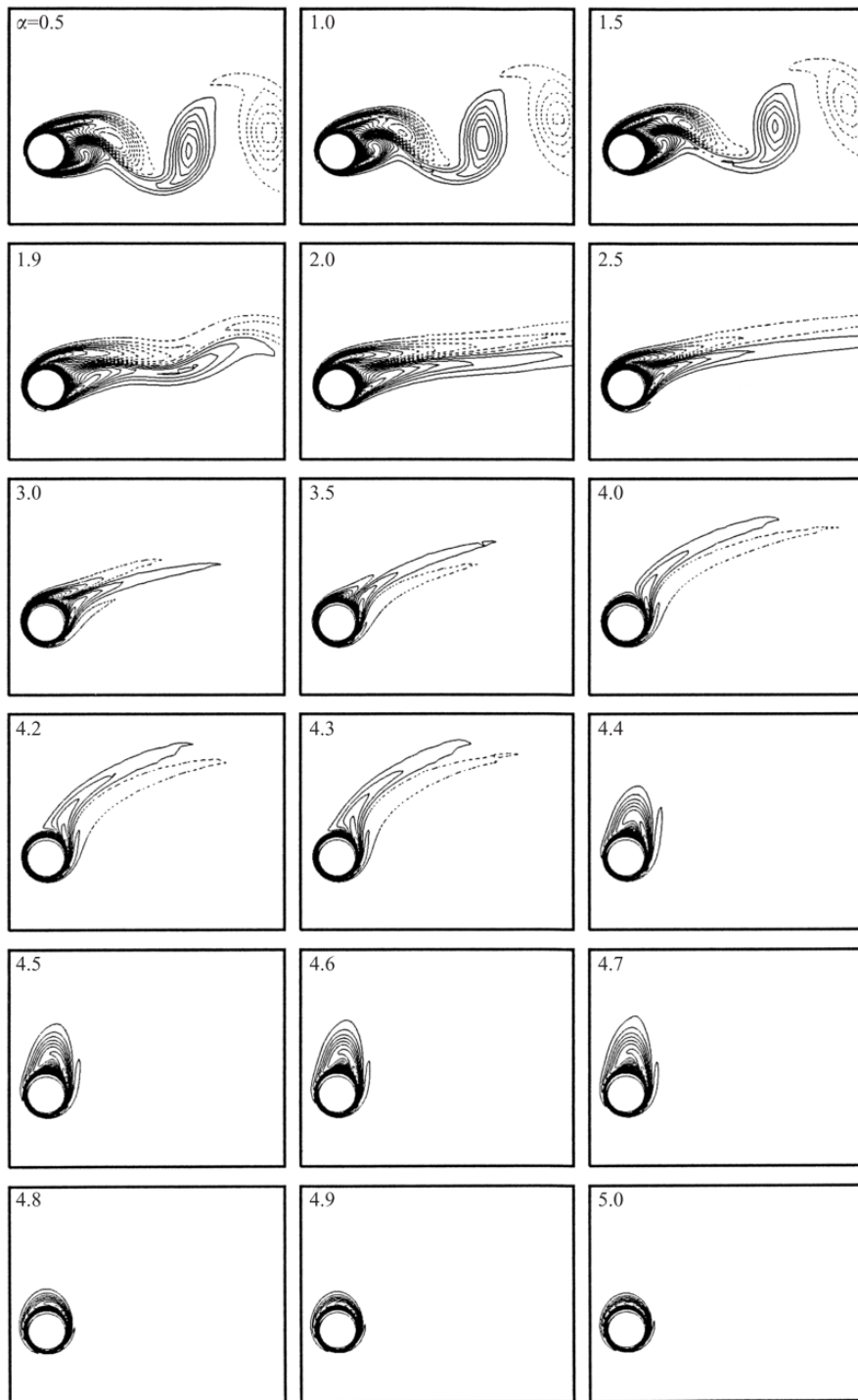


FIGURE 2.15: Vorticity contours of the near wake of a rigidly-mounted circular cylinder rotating at various rotation rates (α) at Reynolds number $Re = 200$. Solid lines represent positive, clockwise vorticity, dashed lines represent negative, anti-clockwise vorticity. Figure from Mittal & Kumar (2003).

due to the absence of the oscillating lift component arisen from vortex shedding. Increasing the rotation rate above $\alpha_{crit.2} \approx 4.3$ results in the system transitioning to a flow regime known as the second instability. This regime extends from the second critical rotation rate, $\alpha_{crit.2}$, to the third critical rotation rate, $\alpha_{crit.3}$. $\alpha_{crit.3}$ marks the boundary between the second instability and a second

2.4. Circular cylinder undergoing rotary motions

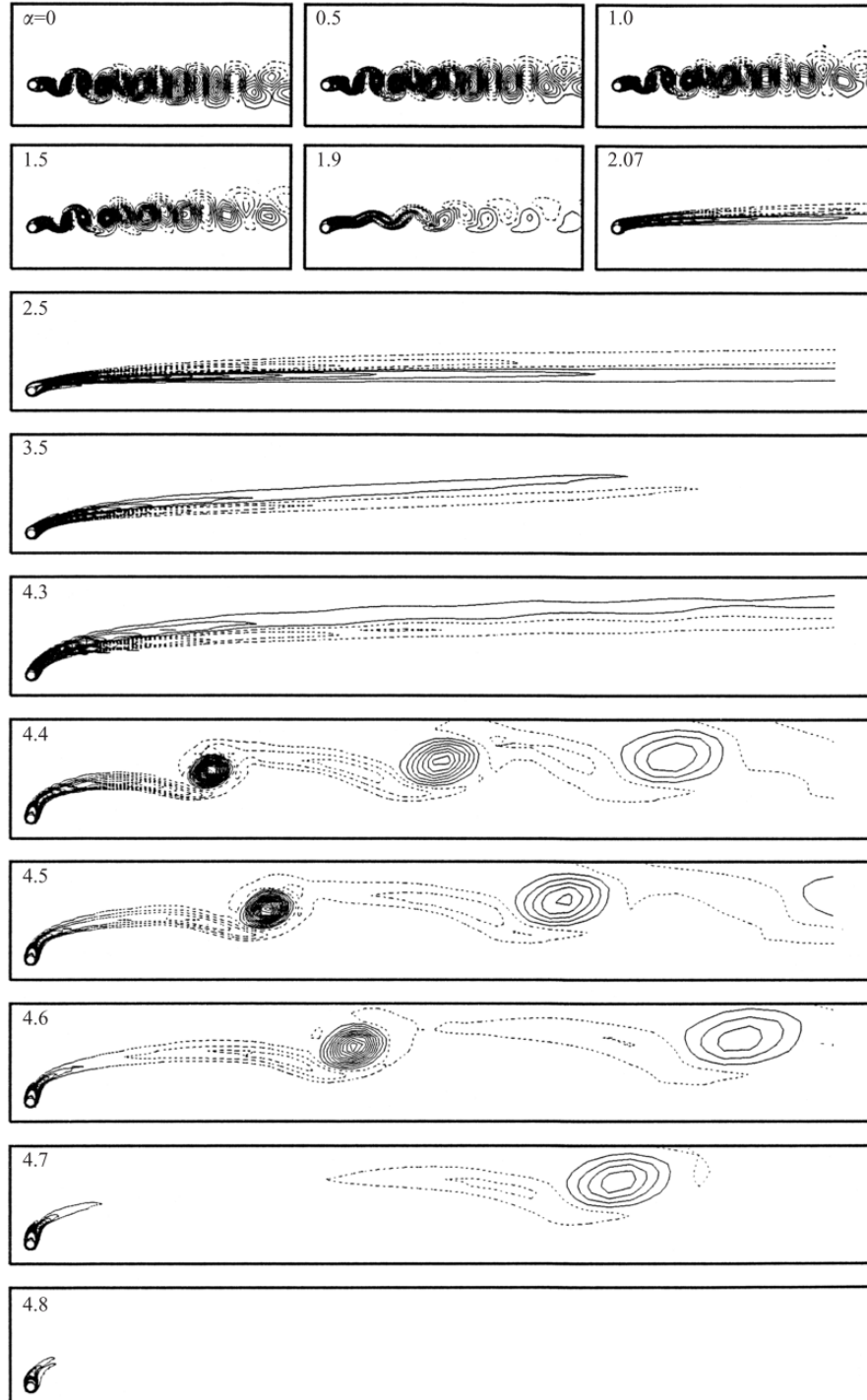


FIGURE 2.16: Global vorticity contours of a rigidly-mounted circular cylinder rotating at various rotation rates (α) at Reynolds number $Re = 200$. Solid lines represent positive, clockwise vorticity, dashed lines represent negative, anti-clockwise vorticity. Figure from Mittal & Kumar (2003).

region of steady-state flow associated with even higher rotation rates ($\alpha > 4.8$). Mittal & Kumar (2003); El Akoury *et al.* (2008) both showed that $\alpha_{crit.3}$ is located at $\alpha_{crit.3} \approx 4.9$ for a Reynolds number of $Re = 200$. As Re is increased, $\alpha_{crit.3}$ decreases towards $\alpha_{crit.3} \approx 4.8$ at $Re = 500$ (El Akoury *et al.* 2008). Rao *et al.* (2015) presented similar findings with $\alpha_{crit.3}$ decreasing towards

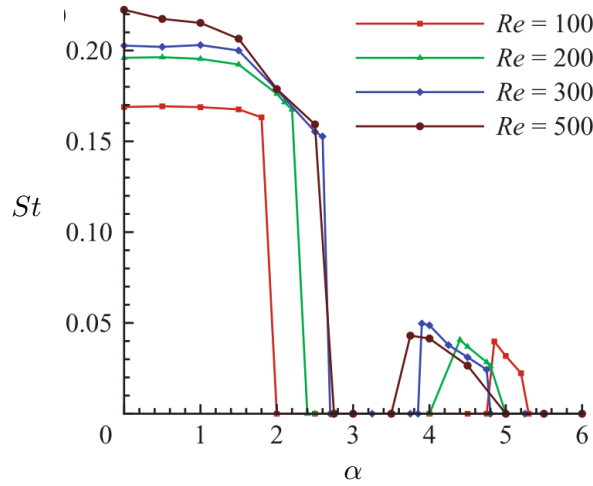


FIGURE 2.17: The Strouhal number (St) of a rotating cylinder presented as a function of rotation rate (α) at various Reynolds numbers (Re). Figure from El Akoury *et al.* (2008).

$\alpha_{crit.3} \approx 4.5$ at $Re \approx 400$ The wake of the second instability is characterised by very low-frequency, single-sided vortex shedding. This is shown in the global vorticity contours of Mittal & Kumar (2003) (see fig. 2.16, $4.5 \leq \alpha \leq 4.7$ cases), and frequency data by El Akoury *et al.* (2008) (see in fig. 2.17). El Akoury *et al.* (2008) presented frequency results showing a significant reduction in Strouhal number from $St \approx 0.2$ in the unsteady flow state to $St \approx 0.05$ in the second instability. In the near wake (see fig. 2.15, $4.5 \leq \alpha \leq 4.7$ cases), the length of the ‘tongue’ like structure previously described is significantly reduced. At these high rotation rates, both positive and negative vorticity regions would wound into a spiral (Mittal & Kumar 2003). The impact these low-frequency vortices have on C_L is shown in fig. 2.13 ($4.4 \leq \alpha \leq 4.8$ cases). Periodic, low-frequency fluctuations in C_L is observed at these rotation rates after the cylinder has passed its transition period from being stationary to undergoing rotation. Periodic oscillations in C_L occur over very large oscillation periods compared to those in the unsteady flow state, in good agreement with El Akoury *et al.* (2008).

Above the third critical rotation rate, $\alpha_{crit.3}$, the cylinder returns to steady-state flow, as vortex shedding is suppressed (Mittal & Kumar 2003; El Akoury *et al.* 2008; Rao *et al.* 2015). Figure 2.13 shows that C_L approaches steady-state after the initial transition from a stationary body. Frequency data from El Akoury *et al.* (2008) further support this as the Strouhal number decreases to $St \approx 0$. However, there are some striking differences in the wake between this second region of steady-state flow and the first ($2 \leq \alpha < 4.4$). Firstly, the near wake containing the tightly wounded positive and negative vorticities is deflected such that it is almost perpendicular (on the leeward side) to the wake centreline and free-stream flow. Secondly, the global wake takes the ‘tongue’ shape described by Mittal & Kumar (2003) instead of the elongated wake observed between $2 \leq \alpha < 4.4$.

The review of literature on rigidly-mounted circular cylinders undergoing constant rate rotation has shown that by manipulating the flow through body rotation the system can achieve steady-state flow for certain ranges of rotation rates. Under steady-state flow, oscillatory vortex shedding is suppressed, meaning the oscillating lift force is also suppressed. Constant rotation is a method that primarily suppresses the strength of the vortices, which reduces the amplitude of oscillating forces and consequently any structural vibrations they may cause. In the following section, the literature on rigid cylinders undergoing sinusoidally-driven rotary oscillations will be reviewed.

2.4.2 Sinusoidal rotary oscillations

In addition to constant body rotation, several other active VIV control methods have been proposed and studied over the last four decades. Notably, the moving surface boundary layer control by Mittal (2001) and the windward suction, leeward blowing study by Dong *et al.* (2008) demonstrated effective suppression and control of vortex shedding. However, these methods can be sensitive to the flow orientation and may lose their effectiveness when the flow changes direction. An active control method of interest that is insensitive to the orientation of the flow is sinusoidally-driven rotary oscillation of cylinders. This was first examined by Okajima *et al.* (1975) at $Re = 40 - 160$ and $3050 - 6100$. They showed that when the forcing frequency of oscillation is close to the vortex shedding frequency of a stationary cylinder the shedding frequency synchronises with the forcing frequency. Taneda (1978) reported that at $Re = 30 - 300$, rotary oscillation at high forcing frequencies can almost eliminate vortex shedding and the recirculation region behind the cylinder. More recent studies by Tokumaru & Dimotakis (1991); Cheng (2001); Choi *et al.* (2002); Thiria *et al.* (2006) have further investigated the wake structure, fluid forces and the influence of Reynolds number and phase between the fluid forces and the cylinder motion.

Two important parameters define the rotary oscillation motion of the cylinder: (1) the normalised peak rotation rate, and (2) the forcing frequency. The normalised peak rotation rate (Ω), otherwise known as the forcing velocity ratio (A_m), is defined as the ratio between the peak tangential velocity of the cylinder surface, v_θ , and the free-stream velocity, U_∞ . It is expressed as

$$\Omega \equiv A_m \equiv \frac{v_\theta}{U_\infty} = \frac{D\dot{\theta}}{2U_\infty}, \quad (2.27)$$

where D is the cylinder diameter and $\dot{\theta}$ is the peak rotation rate of the cylinder. The forcing frequency of the cylinder previously have been presented in two normalised forms. The first is in form of forcing Strouhal number

$$S_f \equiv \frac{Df_{osc}}{U_\infty}, \quad (2.28)$$

where f_{osc} is the forcing frequency. Alternatively, it can be expressed as the normalised forcing frequency (f_r)

$$f_r \equiv \frac{f_{osc}}{f_{St}}, \quad (2.29)$$

where f_{St} is the Strouhal frequency of a stationary cylinder. The forcing Strouhal number, S_f , can be used to compare the forcing and shedding frequencies Strouhal numbers and the normalised forcing frequency f_r expresses the forcing frequency as a ratio of f_{St} .

Due to the large parametric field, literature in the following sections focuses on characterising the fluid forces and wake inside and outside of the lock-in regime. The synchronisation regime for a rigidly-mounted cylinder undergoing sinusoidally-driven rotary oscillations will first be discussed and defined. The fluid forces and the wake structure of a rotary oscillating cylinder will then be reviewed.

2.4.2.1 Lock-on regimes and frequency modulation

For a rigidly-mounted cylinder undergoing sinusoidally-driven rotary oscillations, synchronisation between the forcing motion and the wake is important. It occurs when the vortex-shedding frequency (f_{sh}) synchronises with the rotary forcing frequency (f_{osc}), deviating from the Strouhal frequency (f_{St}) of a non-rotating cylinder. This is expressed as

$$f_{sh} \cong f_{osc}. \quad (2.30)$$

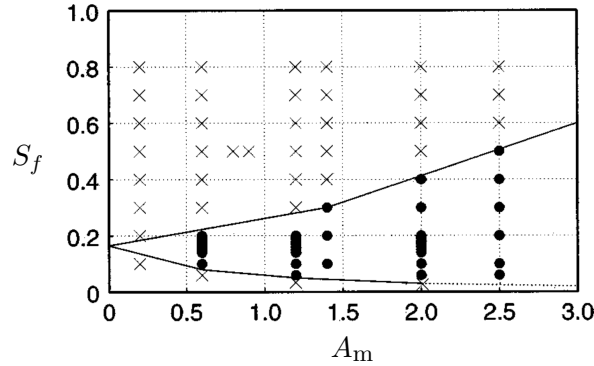


FIGURE 2.18: A lock-on map presented in the forcing Strouhal number (S_f) and forcing velocity ratio (A_m) domain. The solid line delimits the boundary between lock-on and non lock-on regions. Figure from Choi *et al.* (2002) and re-labelled using the terminology conventions of the present thesis.

This has been reported by a number of works (*e.g.* Okajima *et al.* (1975); Tokumaru & Dimotakis (1991); Cheng *et al.* (2001); Cheng (2001); Choi *et al.* (2002)) and it is commonly referred as ‘lock-on’. Note that ‘lock-on’ should not be confused with *lock-in*, a term commonly used in this thesis referring to the wake-body synchronisation of cylinders undergoing VIV.

While lock-on will occur when the cylinder undergoes forcing at the Strouhal frequency of a stationary cylinder (*i.e.* $f_{osc} = f_{St}$), Cheng *et al.* (2001); Cheng (2001); Choi *et al.* (2002) have shown that lock-on can also occur over certain ranges of A_m and S_f . Figure 2.18 is a map showing the lock-on regimes as a function of S_f and A_m at a low Reynolds number of $Re = 100$. In fig. 2.18, • represents lock-on, × non lock-on and the solid line shows the approximate boundary between the two regimes. Choi *et al.* (2002) discussed that the determination of lock-on is based on the characteristics of the lift forces. They showed that lock-on occurs when the forcing frequency is close to the Strouhal frequency of a non-rotating cylinder (*i.e.* $f_{osc} \approx f_{St}$). As A_m increases, the lock-on region widens. This was also observed in Lu & Sato (1996); Cheng *et al.* (2001); Cheng (2001).

Another phenomenon associated with motion-wake synchronisation occurs outside the lock-on regime. Tertiary lock-on occurs when the vortex-shedding frequency, f_{sh} , becomes synchronised with one-third the rotary forcing frequency, f_{osc} , it is defined as

$$f_{sh} \cong \frac{1}{3}f_{osc}. \quad (2.31)$$

A comprehensive study on tertiary lock-on has been done by Baek & Sung (2000).

A number of works (*e.g.* Baek & Sung (1998); Cheng *et al.* (2001); Cheng (2001); Choi *et al.* (2002)) have documented the presence of frequency modulation, however, the conditions at which it occurs are disputed. Baek & Sung (1998) reported that modulation occurs when the rotary forcing frequency approximately equals the Strouhal frequency of a non-rotating cylinder (*i.e.* $f_{osc} \approx f_{St}$). Contrary to earlier work, at sufficiently large A_m Cheng *et al.* (2001); Cheng (2001); Choi *et al.* (2002) observed frequency modulation outside the lock-on regime where $f_{osc} \neq f_{St}$. Figure 2.19 from Choi *et al.* (2002) shows the presence of frequency modulation in the lift and drag coefficient time histories.

While frequency modulation was not extensively discussed in Cheng *et al.* (2001), a number of low-frequency peaks can be observed in their data. In particular, the power spectra density (PSD) plots in fig. 2.20(right column) (in cases outside the lock-on f_r values). They remarked that the presence of a large-scale vortex shedding frequency (f_{ls}), low in value, is related to the Strouhal frequency f_{St} of a stationary cylinder. Choi *et al.* (2002) elaborated that the presence of f_{ls} and frequency modulation is the result of discrepancies between f_{osc} and f_{sh} of a non-rotating cylinder. Cheng *et al.* (2001) mentioned that f_{ls} is the result of the coalescence of small-scale vortex

2.4. Circular cylinder undergoing rotary motions

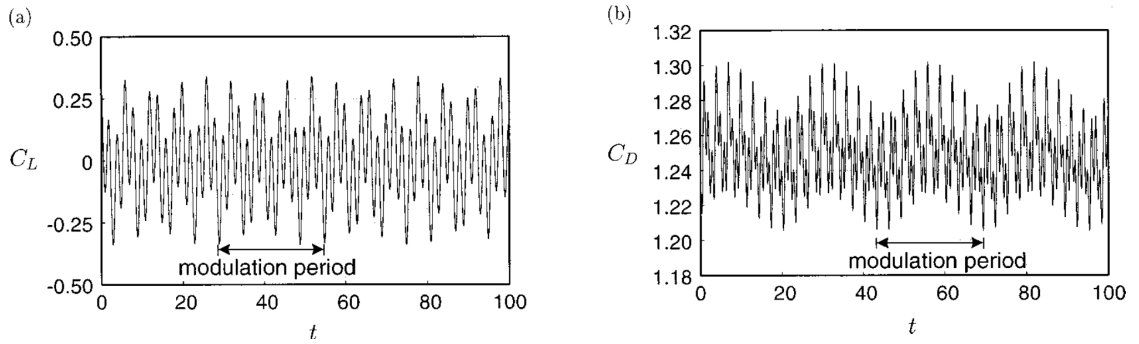


FIGURE 2.19: Presence of frequency modulation in the (a) lift (C_L) and (b) drag (C_D) coefficient time histories for a rigidly-mounted cylinder undergoing sinusoidally-driven rotary oscillation at Reynolds number $Re = 100$ and forcing velocity ratio $A_m = 1.4$ and forcing Strouhal number $S_f = 0.5$. Figure from Choi *et al.* (2002).

structures within the Kármán vortex formation length scale. Choi *et al.* (2002) reported similar findings. These small-scale vortex structures are shed at relatively higher frequencies; as they flow downstream, they form larger, lower frequency structures. The low- f_{ls} modulation becomes more apparent as f_r increases and shifts f_{osc} away from f_{ls} . Therefore, the influence of f_{ls} and the level of frequency modulation increases with f_r . In higher f_r cases ($f_r = 2.0$), f_{ls} is higher in power than the combined f_{osc} and f_{sh} peak. As a result, the f_{osc} (and f_{sh}) becomes modulated by f_{ls} . Choi *et al.* (2002) remarked that frequency modulation exist at varying levels when the fluid-structure is not under lock-on.

2.4.2.2 Fluid forces

To further understand the effects of sinusoidal rotary oscillations on a rigidly-mounted cylinder, researchers studied fluid forces. Previous work has shown that significant drag reductions can be achieved using sinusoidally-driven rotary oscillations. Tokumaru & Dimotakis (1991) showed there was a six-fold reduction in drag compared to the non-rotating case at some optimal ranges of forcing at $Re = 15000$. There are, however, some discrepancies between studies. Low Reynolds number ($Re = 100$) simulation by Choi *et al.* (2002) showed that drag increases to some maxima when the forcing Strouhal number S_f approaches the Strouhal number of a stationary cylinder ($S_f \approx St$). Furthermore, they found that drag reduction is only achieved near the lock-on boundaries and that the six-fold reduction in Tokumaru & Dimotakis (1991) was not observed. Choi *et al.* (2002) suggested this discrepancy may result from the large differences in Reynolds number. Other work by Shiels & Leonard (2001); Cheng *et al.* (2001); Cheng (2001); Thiria *et al.* (2006) have also reported reductions in drag. Of particular interest to the present thesis is the lift force as this directly influences the characteristics and flow mechanisms that causes an elastically-mounted system to undergo VIV. This section will focus on characterising the lift forces of a rigidly-mounted cylinder undergoing rotary oscillations. Tokumaru & Dimotakis (1991); Chou (1997); Fujisawa *et al.* (1998); Shiels & Leonard (2001); Cheng *et al.* (2001); Cheng (2001); Choi *et al.* (2002); Thiria *et al.* (2006) provide further details on the drag forces of a rigidly-mounted cylinder undergoing rotary oscillations.

Several studies have focused on characterising the effects of rotary oscillation on drag but lift forces have received considerably less attention. Simulations at a low Reynolds number of $Re = 1000$ by Chou (1997) showed that \bar{C}_L of the cylinder monotonically decreases towards zero with f_r while it increases with A_m . The time histories at these non-zero mean lift \bar{C}_L points show that the lift signals are non-sinusoidal about zero (but are generally periodic) after the initiation of the oscillatory motion. Later work by Cheng *et al.* (2001); Cheng (2001) showed similar findings when forcing was

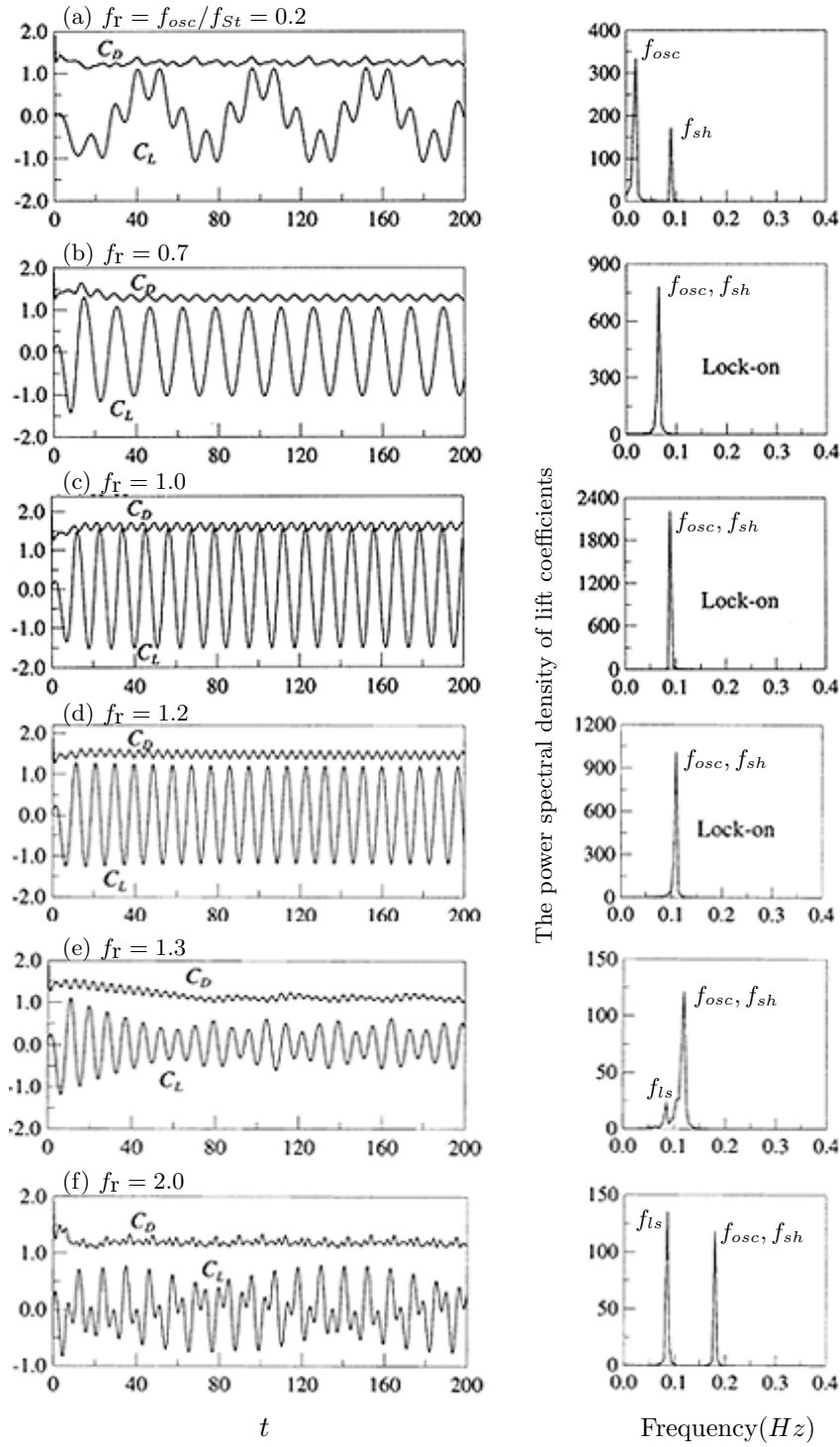


FIGURE 2.20: The time histories of the lift (C_L) and drag (C_D) coefficients (left column) and the power spectra density (PSD) of the C_L signal (right column) for a rigidly-mounted cylinder undergoing sinusoidally-driven rotary oscillations at Reynolds number $Re = 100$ and forcing velocity ratio $A_m = 0.5$ at several normalised forcing frequency ratio (f_r) cases are presented. f_{osc} is the forcing frequency, f_{St} is the Strouhal frequency of a stationary cylinder, f_{sh} is the vortex shedding frequency and f_{ls} is the large-scale vortex shedding frequency. Figures extracted from Cheng *et al.* (2001) and re-labelled using the terminology conventions of the present thesis.

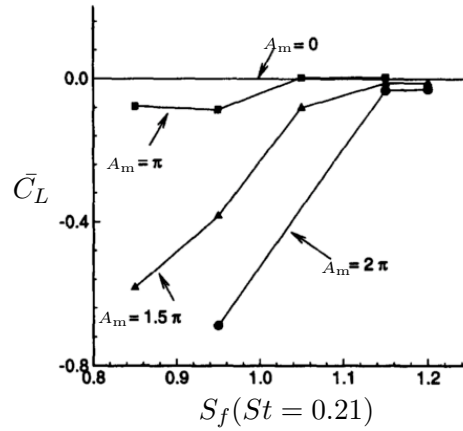


FIGURE 2.21: The mean lift coefficient (\bar{C}_L) of a rigidly-mounted cylinder undergoing sinusoidally-driven rotary oscillations presented as a function of forcing Strouhal number (S_f) and forcing velocity ratio (A_m) at Reynolds number $Re = 1000$. Figure from Chou (1997) and re-labelled using the terminology conventions of the present thesis.

outside the lock-on regime.

As Cheng *et al.* (2001); Cheng (2001); Choi *et al.* (2002) reported frequency modulation outside the lock-on regime, this casts doubt on the magnitude of \bar{C}_L results from Chou (1997) in Fig. 2.21. As can be seen in fig. 2.19, the modulation period can be very large, meaning a large sampling time is required to capture even a single modulation period. The force coefficient time histories presented in Chou (1997) are approximately 40 s in duration, with the transition time for the oscillatory motion and wake taking up a significant portion of the sampled data, as evidenced by fig. 2.22. It is possible that \bar{C}_L is overestimated due to their limited sampling duration. With a sampling duration long enough to capture a sufficient number of modulation periods, \bar{C}_L of the cylinder could be smaller than what is reported in Chou (1997).

More recent numerical work by Cheng *et al.* (2001); Cheng (2001); Choi *et al.* (2002) has shown that there is no significant reduction in lift with sinusoidally-driven rotary oscillations over most forcing parameters. In fact, within the lock-on regime lift can increase significantly. This is evident from the lift coefficient time histories in fig. 2.20(left column). At a forcing velocity ratio $A_m = 0.5$ and at forcing frequencies below lock-on (see fig. 2.20(a)), the peak lift ($C_{L(\max)}$) increases compared to that of a non-rotating cylinder from $0.52 < C_{L(\max)} \leq 0.8$ (calculated based on data from Norberg (2001)) to $C_{L(\max)} \approx 1.05$. As lock-on initially occurs (fig. 2.20(b)), there are no significant changes in lift magnitudes, however, frequency modulation ceases as the force signals become sinusoidal and periodic. Figure 2.20(c) shows that further increases in forcing frequency to $f_r = 1.0$ results in significant increases in lift to $C_{L(\max)} > 1.5$. Within the lock-on regime, further increases in forcing frequency above $f_r = 1.0$ causes the peak lift decreases. As evidenced in fig. 2.20(d), peak lift decreased from $C_{L(\max)} \approx 1.6$ at $f_r = 1.0$ to $C_{L(\max)} \approx 1.25$ at $f_r = 1.2$. Increasing the forcing frequency above the lock-on range will result in an initial reduction in peak lift (see fig. 2.20(e) at $f_r = 1.3$). In this non lock-on regime, the peak lift gradually increases with further increases in forcing frequency. As A_m is increased, $C_{L(\max)}$ also increases.

Choi *et al.* (2002) also reported similar findings and fig. 2.23 from their work presents a map of $C_{L(\max)}$ overlaying the lock-on regime map from fig. 2.18 in the $S_f - A_m$ parameter space.

This section has shown that rotary oscillations can significantly change the magnitude and profile of the lift forces acting on the cylinder. The changes in wake structure as a result of rotary forcing as well as the wake modes observed in and outside the lock-on regime are discussed in the section to follow.

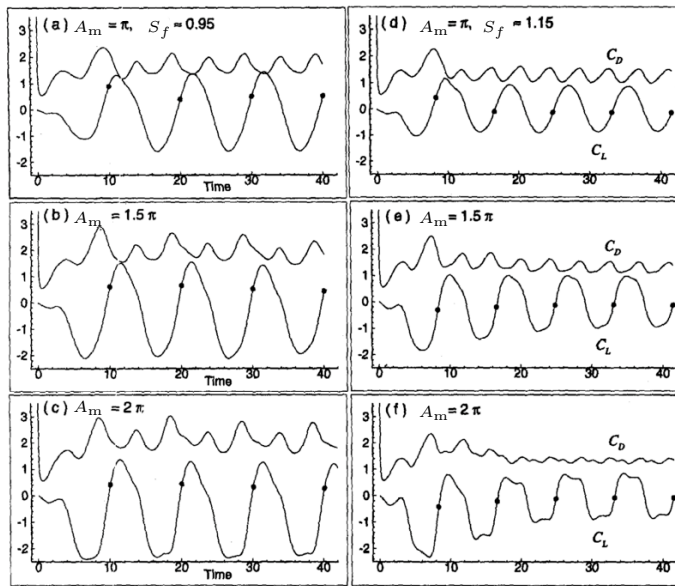


FIGURE 2.22: The time histories of the drag coefficient (C_D) and lift coefficient (C_L) of a rigidly-mounted cylinder undergoing sinusoidally-driven rotary oscillations at various forcing Strouhal number (S_f) and forcing velocity ratio (A_m) and at Reynolds number $Re = 1000$. Each dot on the C_L curve denotes the beginning of a cycle of rotary oscillation. Figure from Chou (1997) and re-labelled using the terminology conventions of the present thesis.

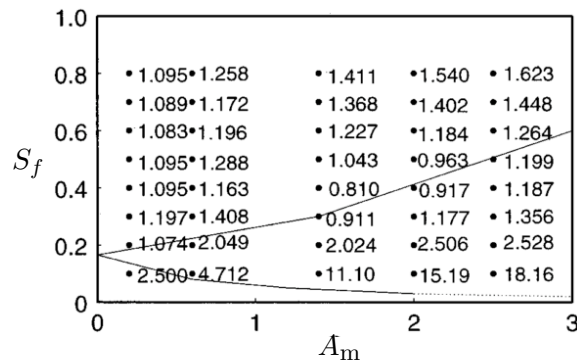


FIGURE 2.23: The time-averaged lift coefficient (\bar{C}_L) of a rigidly-mounted cylinder undergoing sinusoidally-driven rotary oscillations presented as a function of forcing Strouhal number (S_f) and forcing velocity ratio (A_m) at Reynolds number $Re = 100$. The solid line delimits the boundary between lock-on and non lock-on regions. Figure from Choi *et al.* (2002) and re-labelled using the terminology conventions of the present thesis.

2.4.2.3 Wake structures

The wake of a rigid cylinder undergoing rotary oscillations was studied experimentally by Okajima *et al.* (1975); Tokumaru & Dimotakis (1991) and later numerically by Chou (1997); Cheng *et al.* (2001); Cheng (2001); Choi *et al.* (2002). Tokumaru & Dimotakis (1991) observed four distinct wake structures that changes with S_f at $Re = 15000$. Figure 2.24 illustrates the four wake structures they referred as Mode I to VI. Mode I, as shown in fig. 2.24(a), is characterised by the shedding of two vortices of the same sign per half cycle. Figure 2.24(b) illustrates Mode II, the wake structure of this mode persist a large distance downstream of the cylinder and it is synchronised with S_f . In Mode III (see fig. 2.24(c)), the wake structure is also synchronised with S_f , however, due to instability the

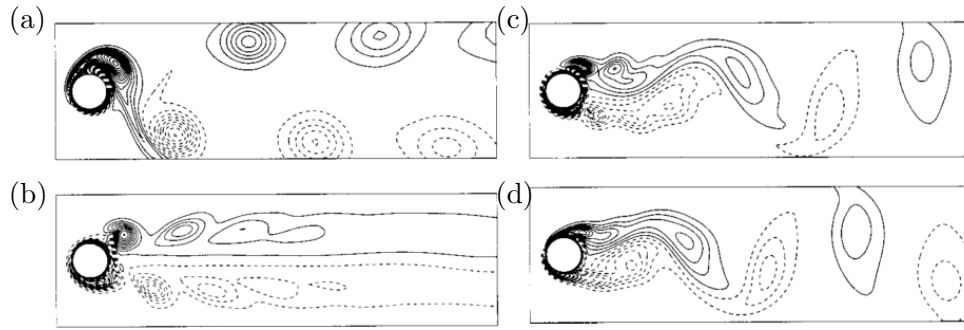


FIGURE 2.24: Instantaneous vorticity contours showing (a) Mode I (forcing velocity ratio $A_m = 2.0$ and forcing frequency ratio $S_f = 0.165$), (b) Mode II ($A_m = 2.0$, $S_f = 0.4$), (c) Mode III ($A_m = 2.0$, $S_f = 0.8$), and (d) Mode IV ($A_m = 0.6$, $S_f = 0.8$). Original figure taken from the low Reynolds number simulation ($Re = 100$) by Choi *et al.* (2002).

higher frequency structures transform into a lower frequency structure at some distance downstream. Figure 2.24(d) illustrates Mode VI, rotary oscillation only have an effect on the shear layers of the cylinder. At some distance downstream the wake structure resembles the 2S structure of a stationary cylinder.

Chou (1997); Cheng *et al.* (2001); Cheng (2001); Choi *et al.* (2002) have presented complex wake structures from their simulations. Chou (1997); Choi *et al.* (2002) reported the evolution of the wake at different forcing parameters and Cheng *et al.* (2001); Cheng (2001) reported the evolution of the wake of an impulsively oscillating cylinder. A few common trends have arisen from their reports of the cylinder wake at varying forcing parameters. Their simulations observed the shedding of multiple vortices in the near wake, as they flow downstream, they transform into a larger, lower frequency structure. This is similar to Mode III reported in Tokumaru & Dimotakis (1991). Choi *et al.* (2002) presented the evolution of the wake over many shedding cycles to show the presence of frequency modulation. Figure 2.25 presents a time history of the C_L and the evolution of the cylinder's spanwise vorticity over one modulation period. It can be seen that vortices shed into the near wake occur at a higher rate than the coalesce and merging of small structures further downstream. From this, it is clear that a large sampling time is required to capture the effect of frequency modulation. For experiments, capturing even one modulation period will be exceptionally difficult. Due to turbulences in the flow and variation of vortices structures, a modulation period may not be clear or requires a significant amount of resources to capture; hence, it has yet to be observed in an experiment.

Chou (1997); Cheng *et al.* (2001); Cheng (2001) presented results that, under specific flow conditions and forcing parameters, a tandem vortex pair is shed per half shedding cycle. Figure 2.26 presents the evolution of the vortex structure at $Re = 1000$. Two pairs of counter-rotating vortices are shed per shedding cycle. Each vortex pair is composed of a larger primary and followed by the shedding of a smaller secondary vortex. Close inspection reveals that the secondary vortex orbits around the primary vortex as the pair moves downstream. This is not unexpected as the rotary oscillation forces the shedding of primary vortices, which is high in strength, to draw counter-rotating vorticity from the opposite side of the cylinder and form a secondary vortex.

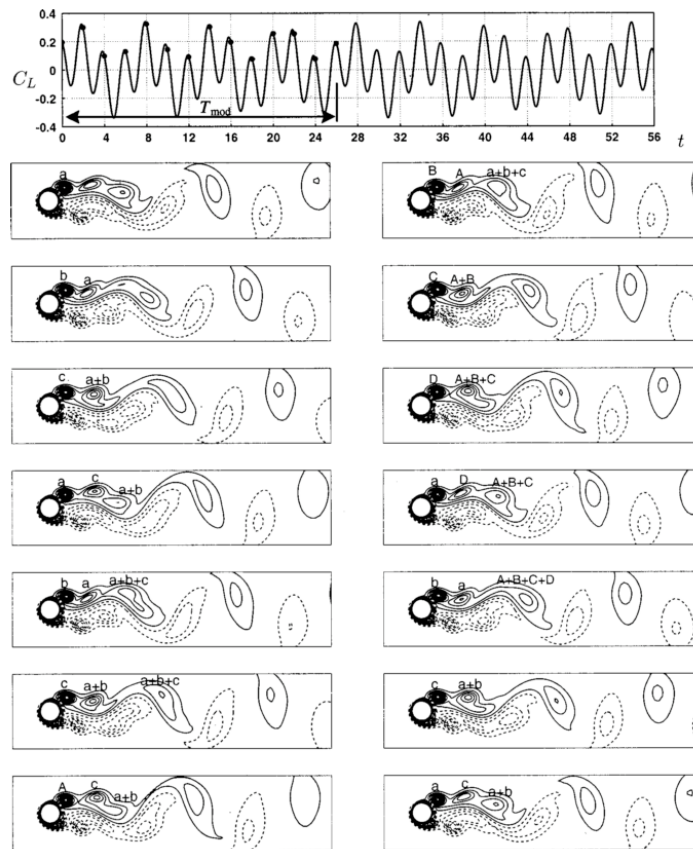


FIGURE 2.25: The evolution of the spanwise vorticity contour over approximately one modulation period ($T_{mod} \approx 26$) at forcing velocity ratio $A_m = 1.4$ and forcing Strouhal number $S_f = 0.5$. At the top is the time history of the lift coefficient (C_L) marked with solid circles to indicate the instant corresponding to each vorticity snapshot. Time of each vorticity snapshots increases from top to bottom in the left column and then to the right column. Figure taken from the low Reynolds number simulation ($Re = 100$) by Choi *et al.* (2002).

2.5 Vortex-induced vibration of a cylinder undergoing rotary motions

From the literature reviewed in the previous section active control methods such as constant rate rotation and sinusoidally-driven rotary oscillations can clearly affect the wake, fluid forces and motion-wake synchronisation of a rigidly-mounted cylinder. However, it is an open question whether such active control methods can affect a cylinder mounted elastically causing it to freely vibrate. Moreover, it is not known how the cylinder will and whether the wake structure will differ from that of a non-rotating cylinder undergoing VIV or a rigidly-mounted cylinder undergoing rotary motions. Bourguet & Lo Jacono (2014) appear to have been first to present a low Reynolds number ($Re = 100$) simulation of the effects of constant rotation on an elastically-mounted cylinder that can freely vibrate in only the cross-flow direction. Two other studies followed. Zhao *et al.* (2014c) numerically studied both one and two degree-of-freedom oscillations at a low Reynolds number. Seyed-Aghazadeh & Modarres-Sadeghi (2015) presented experimental work at relatively low Reynolds numbers between $350 \leq Re \leq 1000$. Literature on an elastically-mounted cylinder undergoing constant rate rotation is presented in §2.5.1 Du & Sun (2015) appear to have been first to study the effects of sinusoidally-driven rotary oscillation on elastically-mounted cylinders in the cross-flow direction.

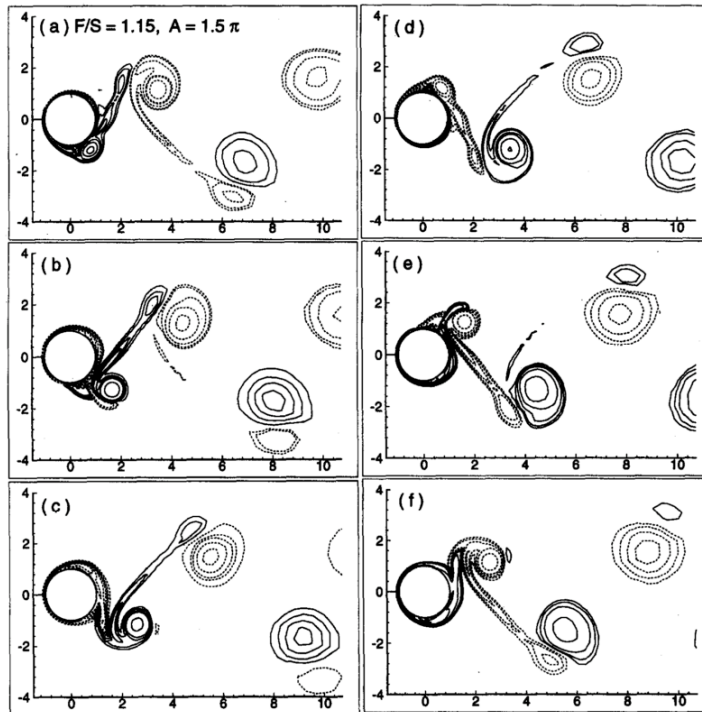


FIGURE 2.26: The evolution of the spanwise vorticity contour over one shedding cycle at forcing velocity ratio $A_m = 1.5\pi$ and forcing frequency ratio $f_r = 1.15$. Figure taken from the low Reynolds number ($Re = 1000$) simulation by Chou (1997) and re-labelled using the terminology conventions of the present thesis.

Their low Reynolds number ($Re = 350$) simulation showed the efficacy of rotary oscillation in controlling vortex shedding even for an elastically-mounted body. Findings from their work is reviewed in §2.5.2

2.5.1 Constant rotation

It is fundamental to any VIV systems, even with the addition of constant rate rotation, to characterise: 1, the amplitude and frequency response of the body, and 2, the fluid forces, phase differences between forces and motion, and the structure of vortex shedding. In §2.5.1.1, the time-averaged position of the cylinder will be discussed prior to the oscillatory component of the cylinder's motion. The phenomenon of 'lock-in' and the frequency response of the oscillatory component of the cylinder's motion will then be presented. The wake structure will be reviewed at the beginning of §2.5.1.2 followed by the fluid forces, in particular the lift forces in the cross-flow direction, and phase of the cylinder.

2.5.1.1 Vibration amplitude and frequency responses

The time-averaged position of the cylinder, \bar{y} , in the cross-flow direction from the low Reynolds number, Re , simulation by Bourguet & Lo Jacono (2014) is presented in fig. 2.27(a). A zero \bar{y} value in fig. 2.27(a) and fig. 2.27(b) represents the natural position of the cylinder in stationary flow i.e. $\bar{y} = 0$). Their results showed that as the rotation rate, α , is increased at any given U^* , a corresponding increase in deviation from the cylinder's natural position is observed. Similarly, at any fixed α , increases in U^* will also increase the time-averaged position (\bar{y}) deviation from the natural position. This is not an unexpected result as it is established in rigidly-mounted cylinder literature,

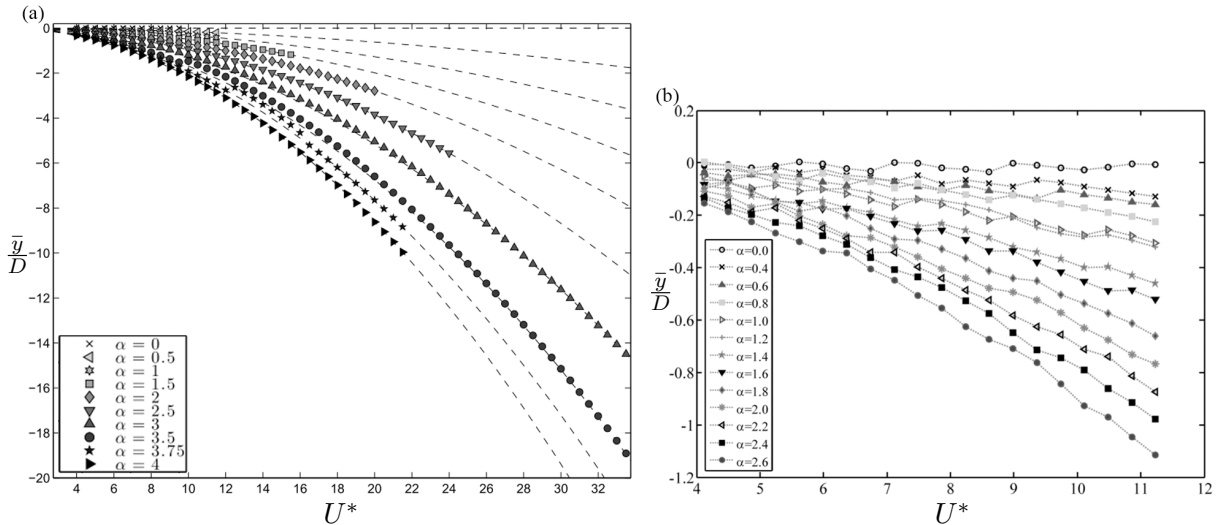


FIGURE 2.27: The normalised time-averaged displacement (\bar{y}/D) of an elastically-mounted cylinder undergoing constant rate rotation presented as a function of reduced velocity (U^*) and rotation rate (α). (a) figure taken from the low Reynolds number ($Re = 100$) simulation by Bourguet & Lo Jacono (2014), and (b) figure taken from the low Reynolds number ($Re = 350 - 1000$) experiment by Seyed-Aghazadeh & Modarres-Sadeghi (2015).

covered in §2.4.1, that when a cylinder undergoes constant rate rotation, the lift force generated by the Magnus effect increases correspondingly. Results from Seyed-Aghazadeh & Modarres-Sadeghi (2015) is presented in fig. 2.27(b) and they are in good agreement with those from Bourguet & Lo Jacono (2014). Zhao *et al.* (2014c) also reported similar trends in their one DOF data set. The time-averaged lift force will be discussed in further detail in §2.5.1.2.

While the time-averaged position of the cylinder sheds light on an aspect of the cylinder's response, researchers have a stronger interest in the dynamic response of the cylinder. For elastically-mounted cylinders free to vibrate, the amplitude of the oscillatory component of the cylinder's position is examined. This was previously done in VIV studies (*e.g.* Feng (1968); Williamson (1988); Khalak & Williamson (1996); Govardhan & Williamson (2000)) to quantify the amplitude response of the cylinder at different U^* . It was found that the amplitude response of a cylinder undergoing VIV in the cross-flow direction is typically well within one diameter of the cylinder ($A^* < 1D$).

Figure 2.28(a) from Bourguet & Lo Jacono (2014) presents the maximum normalised amplitude response A_{\max}^* of the cylinder as a function of U^* and α . The same results from Seyed-Aghazadeh & Modarres-Sadeghi (2015) is presented in fig. 2.28(b). Figure 2.28(a) shows that body vibrations persist up to a rotation rate of $\alpha \approx 4$ and that the maximum amplitude response observed was 1.9 times the cylinder diameter. Bourguet & Lo Jacono (2014) found in their simulation that the amplitude of the cylinder is quite unresponsive where the rotation rate is $\alpha < 1$. When the rotation rate is increased to the range of $1 \leq \alpha \leq 1.5$, there is a notable increase in A_{\max}^* , however, the trend remains similar to that on a non-rotating cylinder. Further increases in rotation rate to $1.5 < \alpha \leq 3$ will result in large increases in A_{\max}^* as well as large shifts in the location of the amplitude peak to higher U^* values. The global peak response of $A_{\max}^* \approx 1.9D$ occurred at a rotation rate of $\alpha = 3.75$ and Bourguet & Lo Jacono (2014) did not observe any vibration response at $\alpha = 4$. The similarity between the rotating and non-rotating amplitude response curves suggest the vibration is caused by the wake-body synchronisation and not a galloping response. Figure 2.28(b) presents the vibration region map by Bourguet & Lo Jacono (2014) delimiting regions of vibration response (where $A_{\max}^* < 0.05D$) in the U^* and α domain. It is evident that at sufficiently high α , the

2.5. Vortex-induced vibration of a cylinder undergoing rotary motions

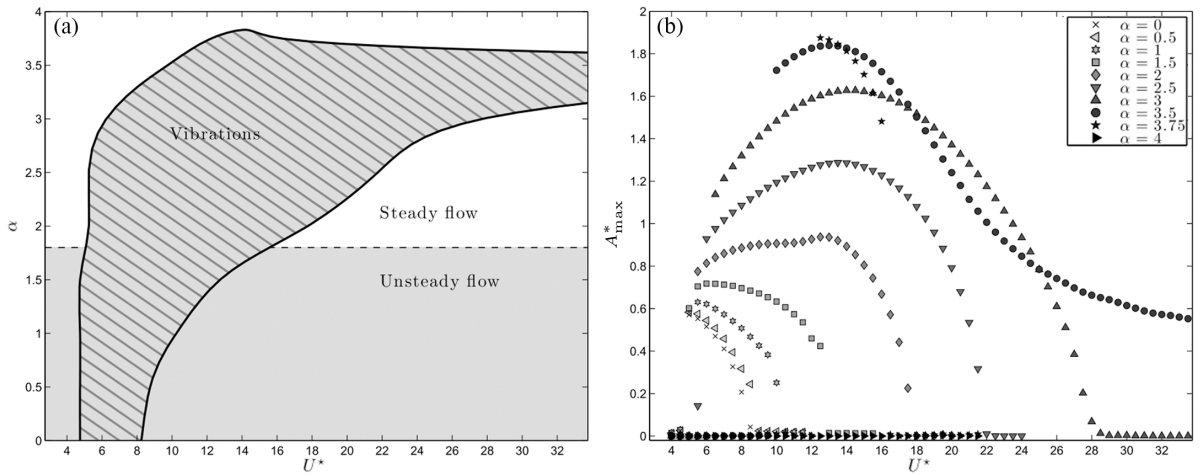


FIGURE 2.28: (a) presents a map in the rotation rate (α) and reduced velocity (U^*) domain delimiting the vibration region and regions where steady and unsteady flow is observed. (b) presents the maximum normalised amplitude response (A_{\max}^*) of the oscillating component of the cylinder’s motion about its time-averaged position (\bar{y}) as a function of U^* and α . Figures taken from Bourguet & Lo Jacono (2014) and re-labelled using the terminology conventions of the present thesis.

vibration region can extend to higher U^* . From this it is clear that the lock-in region in which large body oscillations occur widens with increased rotation rates at low Reynolds numbers. Zhao *et al.* (2014c) also reported similar observations in the widening trend to the lock-in region, however, large increases in amplitude response in the cross-flow direction is not observed.

This, however, is not observed in the experiment by Seyed-Aghazadeh & Modarres-Sadeghi (2015). Their results showed no vibration above a rotation rate of $\alpha \approx 2.55$ and the vibration region do not extend to higher reduced velocities once the wake and body becomes desynchronized. In fact, their lock-in region becomes narrower with α . Seyed-Aghazadeh & Modarres-Sadeghi (2015) reported a global peak amplitude response of $A_{\max}^* \approx 0.6$, which is approximately 50% larger than the non-rotating case. While the increase in response is still large, it is significantly less than those observed in Bourguet & Lo Jacono (2014). This is likely due to the differences in experimental variables such as mass and damping as Bourguet & Lo Jacono (2014) performed their simulation at a mass ratio of $m^* = 10$ with zero damping $\zeta = 0$ while Seyed-Aghazadeh & Modarres-Sadeghi (2015) conducted their experiments at $m^* = 11.5$ and $\zeta = 0.01$. Furthermore, the Reynolds number of the two studies are very different as Bourguet & Lo Jacono (2014) maintained $Re = 100$ while Seyed-Aghazadeh & Modarres-Sadeghi (2015) varied between $Re = 350 - 1000$.

Bourguet & Lo Jacono (2014) reported that the body oscillations they observed are typically periodic and exhibits strong sinusoidal characteristics. The normalised frequency responses (f^*) as a function of U^* and α from Bourguet & Lo Jacono (2014) and Seyed-Aghazadeh & Modarres-Sadeghi (2015) are presented in fig. 2.29(a) and fig. 2.29(b). Both studies share similar trends in frequency response. The response of rotating cases is comparable to those of a non-rotating cylinder. In Bourguet & Lo Jacono (2014), at low U^* , f^* bends downwards to follow approximately the Strouhal frequency (f_{St}) of a stationary cylinder (shown as a dashed line in fig. 2.29(a)). This bending in f^* is also observed at α associated with the suppression of vortex shedding for a rigidly-mounted cylinder. At moderate to high U^* , f^* is relatively constant and remain in the proximity of f_{nw} but differs from it ($f^* \neq 1$). As α is increased, there is a global decrease in f^* .

To better understand the fluid mechanics behind the changes in the cylinder’s amplitude and frequency responses as a result of body rotation; a review of the wake structure, with respect to

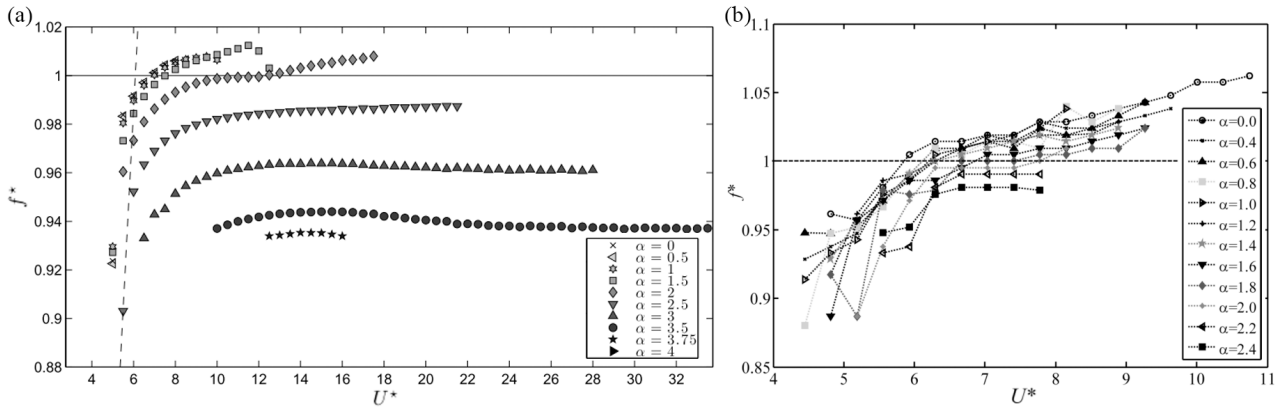


FIGURE 2.29: The normalised frequency response (f^*) of an elastically-mounted cylinder undergoing constant rate rotation presented as a function of reduced velocity (U^*) and rotation rate (α). (a) figure taken from the low Reynolds number ($Re = 100$) simulation by Bourguet & Lo Jacono (2014), and (b) figure taken from the low Reynolds number ($Re = 350 - 1000$) experiment by Seyed-Aghazadeh & Modarres-Sadeghi (2015).

the vibration region described in Bourguet & Lo Jacono (2014), will be presented in the following section followed by the fluid forces and their phases with the cylinder’s motion.

2.5.1.2 Fluid forces, phases and wake structures

The identification of vortex shedding patterns downstream of a cylinder undergoing free or forced vibration in the cross-flow direction have been characterised by previous work such as Williamson (1988); Govardhan & Williamson (2000). Their work has shown that the wake structure downstream of a vibrating cylinder may differ to the Kármán vortex streets observed behind stationary cylinders. The wake structure of a rigidly-mounted cylinder undergoing constant rate rotation have also been extensively studied (see Badr *et al.* (1990); Mittal & Kumar (2003); El Akoury *et al.* (2008); Rao *et al.* (2013, 2015)). It is of interest for researchers to know whether these wake patterns seen in non-rotating VIV and rigidly-mounted rotating cylinders continues to exist when an elastically-mounted cylinder is subjected to constant rate rotation. Furthermore, to understand the changes to the cylinder’s vibration and force responses with rotation, it is essential to characterise the changes in wake pattern.

Figure 2.30, extracted from Bourguet & Lo Jacono (2014), is a map of the different wake modes observed in their $U^* - \alpha$ parameter space. They made clear that the boundaries between wake modes on the map are approximates as hysteresis and wake-mode switching may occur in transition regions between modes, as documented by Khalak & Williamson (1999). The instantaneous iso-contours of spanwise vorticity presented in fig. 2.31 shows the different wake modes Bourguet & Lo Jacono (2014) observed. Outside their vibration region, the wake is dominated by three wake structures: the 2S, D^+ and D^- . These structures, shown in fig. 2.31(a), (b) and (c), have been previously reported in non-rotating VIV and rigidly-mounted rotating cylinder studies. Outside their vibration region and at rotation rates $\alpha < 1.8$, the 2S mode is observed. Shown in fig. 2.31(a), this mode is characterised by the shedding of two single counter-rotating vortices per shedding cycle, as typically seen in stationary cylinder studies. The D^+ and D^- mode was previously seen in Mittal & Kumar (2003). As discussed in §2.4.1.2, the body rotation creates an asymmetry in the strength of the positive and negative vortices that then causes the wake to deflect away from the streamwise centreline. At rotation rates $\alpha \geq 1.8$, the flow becomes steady and the wake is composed of two

2.5. Vortex-induced vibration of a cylinder undergoing rotary motions

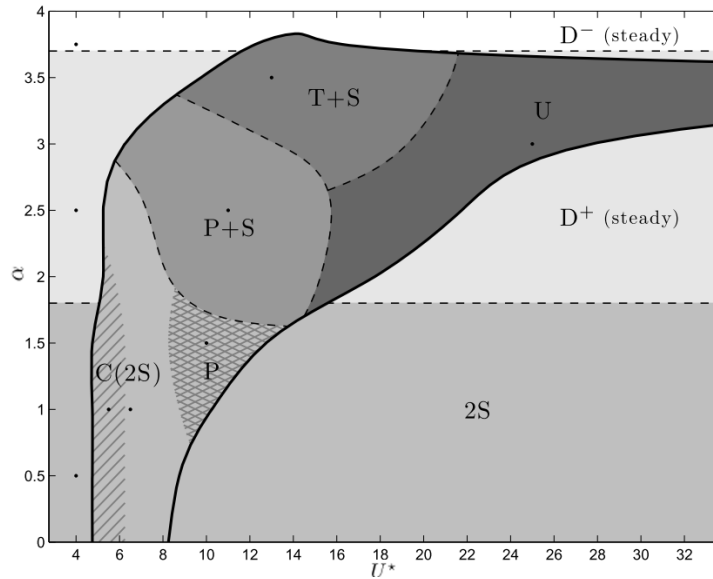


FIGURE 2.30: Wake pattern of an elastically-mounted cylinder undergoing constant rate rotation presented as a function of reduced velocity (U^*) and rotation rate (α). The thick black line delimits the approximate boundaries of the vibration region. Figure taken from the low Reynolds number ($Re = 100$) simulation by Bourguet & Lo Jacono (2014).

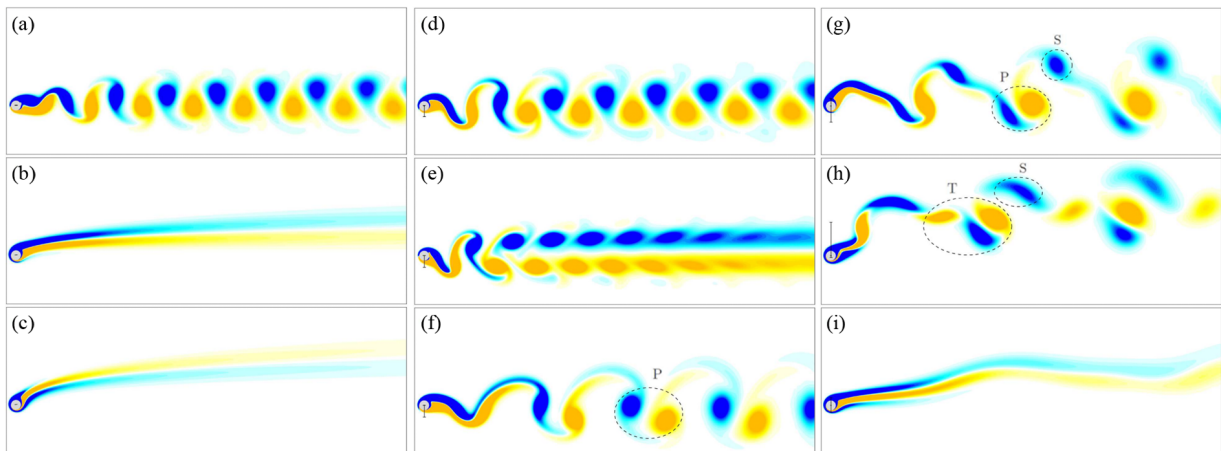


FIGURE 2.31: Instantaneous vorticity iso-contours of the different wake modes of an elastically-mounted cylinder undergoing constant rate rotation are shown. (a) and (d) shows the 2S pattern, (b) D^+ pattern, (c) D^- pattern, (e) C(2S) pattern, (f) P pattern, (g) P+S pattern, (h) T+S pattern, and (i) U pattern. Figures taken from the low Reynolds number ($Re = 100$) simulation by Bourguet & Lo Jacono (2014).

elongated vorticity layers of opposite signs deflected away from the streamwise centreline. Between rotation rates $1.8 < \alpha \lesssim 3.7$, the D^+ mode exhibits a negative vorticity layer above the positive layer (see fig. 2.31(b)). When the rotation rate becomes sufficiently high ($\alpha \gtrsim 3.7$), the negative vorticity layer wraps around the cylinder like a ‘tongue’ and the positive vorticity layer is now positioned above the negative layer. This is denoted as the D^- mode as shown in fig. 2.31(c).

Within their vibration region, Bourguet & Lo Jacono (2014) observed a number of wake structures. At low α , the wake is characterised by the 2S mode (see fig. 2.31(d)) and its two variant: (1)

C(2S) (see fig. 2.31(e)) and (2) P (see fig. 2.31(f)). At low U^* , the shed vortices tend to coalesce in the wake, hence, it is referred to as C(2S). This mode was previously reported in Singh & Mittal (2005). At higher U^* , the two counter-rotating vortices shed per cycle exhibits a tendency to collect in pairs which lead to it being referred as P, as it resembles the P pattern reported in Williamson (1988) Seyed-Aghazadeh & Modarres-Sadeghi (2015) presented dye visualisation of their wake at similar reduced velocity ($U^* = 5.2$) over a range of α . At rotation rates $\alpha < 1.4$, they observed the 2S mode and asymmetric variants of the 2S mode. The vortices shed in these asymmetric 2S variants deflects from the streamwise centreline with its deflection increases with α . Between rotation rates $1.4 \leq \alpha \leq 1.8$, the P mode is observed. These findings are in good agreement with those reported in Bourguet & Lo Jacono (2014). Zhao *et al.* (2014c) also reported observing the C(2S) and 2S modes at comparable U^* and α .

Within the vibration region reported in Bourguet & Lo Jacono (2014), at higher α and moderate U^* , the wake is dominated by the P+S mode (see fig. 2.31(g)). This wake pattern is composed of a pair (P) of counter-rotating vortices and a single (S) vortex. This mode was previously reported in forced and freely vibrating cylinders (see Blackburn & Henderson (1999); Singh & Mittal (2005)). At moderate U^* and rotation rates $\alpha \gtrsim 2.5$, Bourguet & Lo Jacono (2014) observed a new wake mode.. As it differs in topology to the 2P mode and resembles an extension of the P+S mode, this new wake structure, compose of a collection of a triplet (T) of vortices and a single (S) vortex is referred to as T+S. The T+S mode is illustrated in fig. 2.31(h). The last wake mode Bourguet & Lo Jacono (2014) observed within their vibration region is associated with high U^* . They reported a wake mode that is composed of two undulating vorticity layers and exhibited no signs of vortex shedding. This mode has not been reported in previous work on VIV. Due to its undulating behaviour, this mode is referred as U and is shown in fig. 2.31(i).

From the review, it is evident that some wake modes previously seen in non-rotating VIV and rigidly-mounted rotating cylinder studies continue to exist even for an elastically-mounted cylinder undergoing constant rate rotation. A new wake mode, the T+S mode, was reported by Bourguet & Lo Jacono (2014) and it is associated with regions of high amplitude responses. To further understand the mechanics, the fluid forces, in particular the lift forces acting in the cross-flow direction will be review.

As discussed in §2.5.1.1, the deviation of time-averaged position of the cylinder, \bar{y} , from its natural position when the cylinder is undergoing rotation is the result of a net force acting on the cylinder. This time-averaged force is the net lift which acts on the cylinder in the cross-flow direction. They reported a global decrease in the time-averaged lift coefficient (\bar{C}_y) with increasing α . This explains the global increase in the deviation of \bar{y} from its natural position with α .

To study the impact of body rotation on the fluctuating force component, the RMS values of the total lift force coefficients ($C_{y,RMS}$) from Bourguet & Lo Jacono (2014) and Seyed-Aghazadeh & Modarres-Sadeghi (2015) are studied. Bourguet & Lo Jacono (2014) remarked that the addition of body rotation did not have a significant impact on the trends of $C_{y,RMS}$ from that of a non-rotating cylinder. The RMS values of the pressure component (C_y^p) from their simulation follows the total lift coefficient (C_y) closely. The evolution of C_y^v with increasing U^* at each α case is generally smoother and at lower RMS values compare to C_y and C_y^p . Seyed-Aghazadeh & Modarres-Sadeghi (2015) also reported similar behaviour in the RMS lift. The magnitude of $C_{y,RMS}$ from Bourguet & Lo Jacono (2014) and Seyed-Aghazadeh & Modarres-Sadeghi (2015) are in good agreement.

The phasing between the fluid forces and motion of the body has been extensively studied for a non-rotating cylinder undergoing VIV (see Khalak & Williamson (1999); Carberry *et al.* (2001); Williamson & Govardhan (2004a)). Bourguet & Lo Jacono (2014) presented the first decomposition of the phasing between forces and displacement of an elastically-mounted cylinder undergoing constant rate rotation. Figure 2.32 presents the phase differences between the first harmonics of the cylinder displacement, y , and its force components (total C_y , pressure C_y^p and viscous C_y^v) as

2.5. Vortex-induced vibration of a cylinder undergoing rotary motions

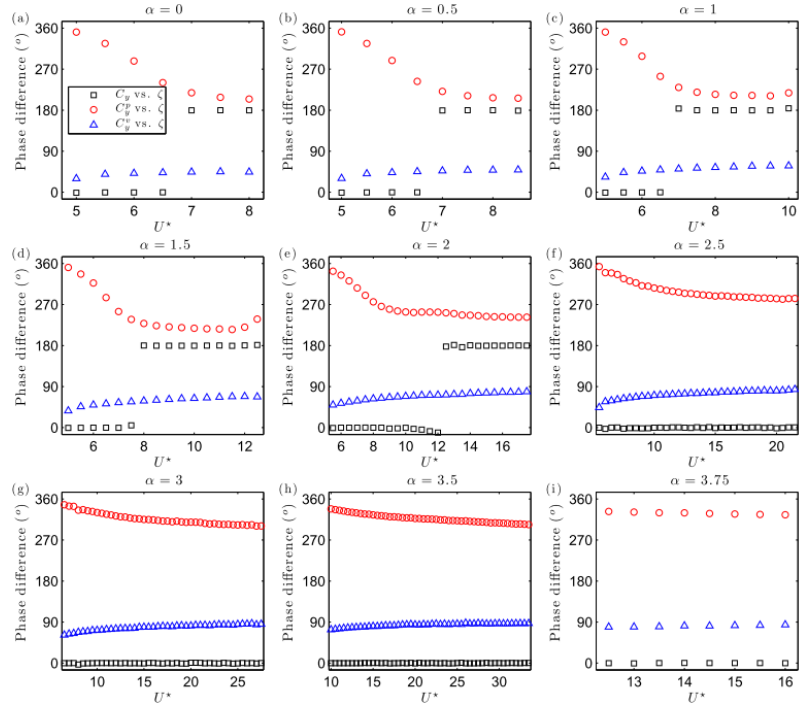


FIGURE 2.32: The phase differences between the total (C_y), pressure (C_y^p), viscous (C_y^v) cross-flow force coefficients and the cylinder displacement (y) as functions of reduced velocity (U^*) and rotation rate (α). Figure taken from the low Reynolds number ($Re = 100$) simulation by Bourguet & Lo Jacono (2014).

a function of U^* for different cases of α . They reported that at rotation rates $\alpha \leq 2$, the phase associated with the total transverse lift, here referred as the total phase, ϕ_T , exhibits two phase states. The first phase state is at $\phi_T = 0^\circ$ (in phase) and then the cylinder jumps to the second state at $\phi_T = 180^\circ$ (out of phase). At rotation rates $\alpha > 2$, the force and motion of the cylinder remains in phase, therefore, the total phase remains at $\phi_T = 0^\circ$ regardless of changes in U^* . Their analysis of the frequency response showed that the phase jump, occurs at low α , consistently coincides with the cylinder oscillating at the natural frequency of the system, *i.e.*, $f^* = 1$. The global decrease in f^* with α seen in fig. 2.29(a) sufficiently explains the shift in the phase jump to higher U^* with α . As α increase, the value of U^* at which the cylinder oscillates at the natural frequency shifts to higher U^* . Furthermore, at rotation rates $\alpha \geq 2.5$, the frequency response remains between the natural frequency (*i.e.* $f^* < 1$) hence there is no phase jump and the total phase remains at $\phi_T = 0^\circ$. Previous work on non-rotating VIV such as Govardhan & Williamson (2000) reported that a jump in phase does not coincide with a switch of the wake mode. Bourguet & Lo Jacono (2014) also reported the phasing between the pressure C_y^p forces and viscous C_y^v forces with the motion of the cylinder (labelled as the ϕ_y^p and ϕ_y^v , respectively). The evolution of the phase response of the pressure ϕ_y^p and viscous ϕ_y^v forces did not exhibit any jump in phase angle, instead they varied smoothly with U^* . They discussed that the jumps in ϕ_T is the result of the continuous variation in both pressure ϕ_y^p and viscous ϕ_y^v force phases.

Seyed-Aghazadeh & Modarres-Sadeghi (2015) reported the presence of two phase states at lower α . The general trends in total phase from their experiment are in good agreement with the simulation by Bourguet & Lo Jacono (2014). However, unlike the numerical results Seyed-Aghazadeh & Modarres-Sadeghi (2015) did not observe a clear jump in ϕ_T . Differences in the phase jump behaviour and phase angle values between their work may perhaps be explained by: (1) the Reynolds number differences, and (2) the experimental nature of the results in Seyed-Aghazadeh & Modarres-Sadeghi

(2015), electrical and mechanical noise is inevitable.

The review of the current state of knowledge on an elastically-mounted cylinder undergoing cross-flow VIV and constant rate rotation showed that the cylinder can exhibit amplitude responses significantly higher than those observed for a non-rotating cylinder. The trends in the frequency response remains comparable to those seen in non-rotating VIV studies but they globally decrease with rotation. Wake patterns previously observed in non-rotating VIV and rigidly-mounted rotating cylinder studies continues to exist. A new T+S mode was reported by Bourguet & Lo Jacono (2014) and it is associated with the region of high amplitude response. In general, the force and phases follow the trend of a non-rotating cylinder with some alterations as α is increased. The following section will review literature related to a freely-vibrating cylinder undergoing sinusoidally-driven rotary oscillations.

2.5.2 Sinusoidal rotary oscillations

To the author's knowledge, Du & Sun (2015) is the first to present work on an elastically-mounted cylinder undergoing sinusoidally-driven rotary oscillations in the cross-flow direction. The following sections will review the results from their low Reynolds number ($Re = 350$) numerical study. The phenomenon of lock-on and its impact on the amplitude response and wake structure will be discussed first. The effects of rotary oscillation amplitude on the cylinder's response will be reviewed prior to examining the effects of rotary oscillation frequency on the cylinder. The effectiveness of rotary oscillation at different U^* and the impact of mass ratio, m^* , will be reviewed at the end. Except their investigation into the effects of m^* , all other results from Du & Sun (2015) were collected with $m^* = 10$.

2.5.2.1 The impact of lock-on

As explained in §2.3, the synchronisation between the fluid and structure occurs when the vortex shedding frequency (f_{sh}) deviates from the Strouhal frequency (f_{sh}) of a stationary cylinder and follows the frequency response of the oscillating system (f^*), which is in close approximation to the natural frequency of the oscillating structure (f_n). This is mathematically defined in eq. 2.11. Under lock-in, the body experiences large amplitude oscillations and fluid forces. The principle behind using sinusoidally-driven rotary oscillations to control VIV is to manipulate the vortex shedding frequency to follow the rotary oscillation's forcing frequency (f_{osc}), therefore, deviating from the natural frequency of the structure. This deviation enables structural resonance of an elastic system to be minimised. When f_{sh} follows approximately f_{osc} , this is known as lock-on and it was mathematically defined in eq. 2.30. The impact of rotary oscillation and the forcing frequency has been extensively studied (e.g. Okajima *et al.* (1975); Tokumaru & Dimotakis (1991); Cheng *et al.* (2001); Cheng (2001); Choi *et al.* (2002)) and reviewed in §2.4.2. It is evident that rotary oscillations are effective in manipulating f_{sh} to follow f_{osc} , however, researchers are interested in investigating the efficacy of rotary oscillations in controlling VIV of an elastic body. In their simulation, the rotary forcing is controlled by two parameters: (1) the forcing velocity ratio (A_m), which is identical to the normalised peak rotation rate described in eq. 2.27, and (2) the forcing frequency ratio, f_r . With the addition of free vibrations in the cross-flow direction, the forcing frequency reported in Du & Sun (2015) is normalised by the natural frequency of the structure, f_n , instead of the Strouhal frequency, f_{St} . To avoid confusion, the normalised forcing frequency ratio, f_r , associated with elastically-mounted bodies will be termed as f_{rot}^* and mathematically defined as

$$f_{rot}^* = \frac{f_{osc}}{f_n}. \quad (2.32)$$

Taken from Du & Sun (2015), fig. 2.33 presents the spectra of the cylinder's normalised displacement (y/D) for four different cases of f_{rot}^* at reduced velocity $U^* = 4.5$ and velocity ratio $A_m = 2.0$.

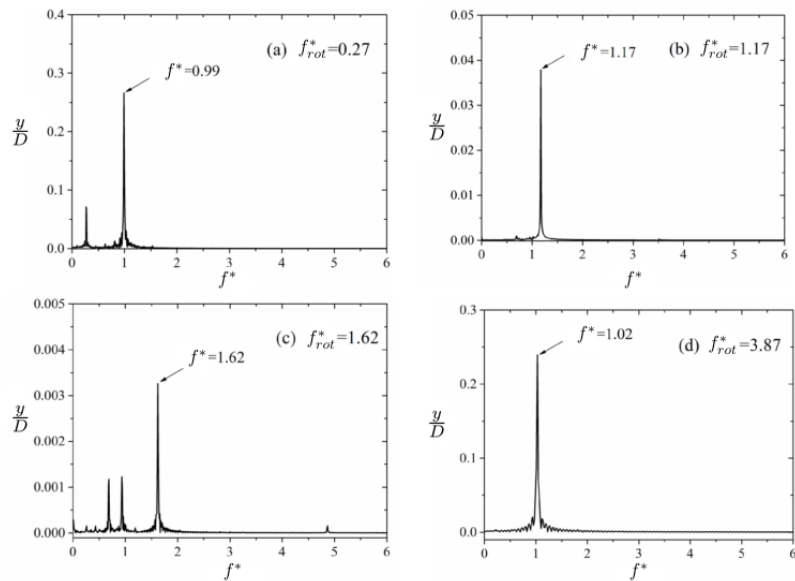


FIGURE 2.33: The power spectra density (PSD) of the displacement (y) of an elastically-mounted cylinder undergoing rotary oscillations is presented as functions of normalised displacement (y/D) and normalised frequency response (f^*). Four forcing frequency ratios (f_{rot}^*) cases are presented at fixed forcing velocity ratio $A_m = 2.0$ and at reduced velocity $U^* = 4.5$. Figure taken from Du & Sun (2015) and re-labelled using the terminology conventions of the present thesis.

Figure 2.34 presents the PSD of the total (C_y) and vortex (C_v) force coefficients at the same parametric values as fig. 2.33. From fig. 2.33 it is evident that the frequency response of the cylinder's motion follows that of the f_{rot}^* at $f_{rot}^* = 1.17$ and 1.62 . Analysis of the force component spectra in fig. 2.34 showed that the dominant total and vortex force frequencies follow the forcing frequency, f_{osc} , and not the natural frequency of the structure in water, f_{nw} (*i.e.* $f^* = 1$) at $f_{rot}^* = 0.27$, 1.17 and 1.62 . Since the mathematical relationship described in eq. 2.30 is satisfied, the elastically-mounted cylinder is lock-on to the rotary motion at $f_{rot}^* = 0.27$, 1.17 and 1.62 . The impact of lock-on is significant as Du & Sun (2015) reported large reductions in the cylinder's amplitude response. In their simulation, the amplitude of the non-rotating case is $A^* \equiv y/D \approx 0.5$. As the cylinder undergoes lock-on, A^* is reduced to $A^* \approx 0.04$ and 0.0035 at $f_{rot}^* = 1.17$ and 1.62 , respectively (see fig. 2.33(b) and (c)). This reduction demonstrates the effectiveness of rotary oscillations in suppressing the vibrational response of an elastically-mounted cylinder. It should be noted that such significant reduction in amplitude response was not observed at forcing frequency ratio $f_{rot}^* = 0.27$. Despite the cylinder locking onto the forcing motion, large oscillation amplitudes of $A^* \approx 0.27$ can be seen in fig. 2.33(a). Figure 2.34(a) shows a weaker peak appearing at the natural frequency of the structure ($f^* = 1$). This suggested that the f_n peak must be sufficiently suppressed in order for the motion of the cylinder to follow that of the rotary forcing. When the cylinder is in the non lock-on regime (at $f_{rot}^* = 3.87$ in fig. 2.33(d) and fig. 2.34(d), the cylinder continues to exhibit a large amplitude response where $A^* > 0.2$. Du & Sun (2015) remarked that both the forcing frequency ratios $f_{rot}^* = 3.87$ and natural frequency $f^* = 1$ continued to influence the vortex shedding process and fluid forces, hence, making rotary oscillations ineffective at suppressing vortex shedding when the system is in the non lock-on region.

The instantaneous wake structures of a cylinder undergoing VIV and rotary oscillations from Du & Sun (2015) are presented in fig. 2.35. They observed stable wake formation at $f_{rot}^* = 1.17$ and 1.62 (see fig. 2.35(b) and fig. 2.35(c)). Furthermore, the vortex formation and the frequency at which they form is controlled by the rotary forcing and not the transverse motion of the cylinder.

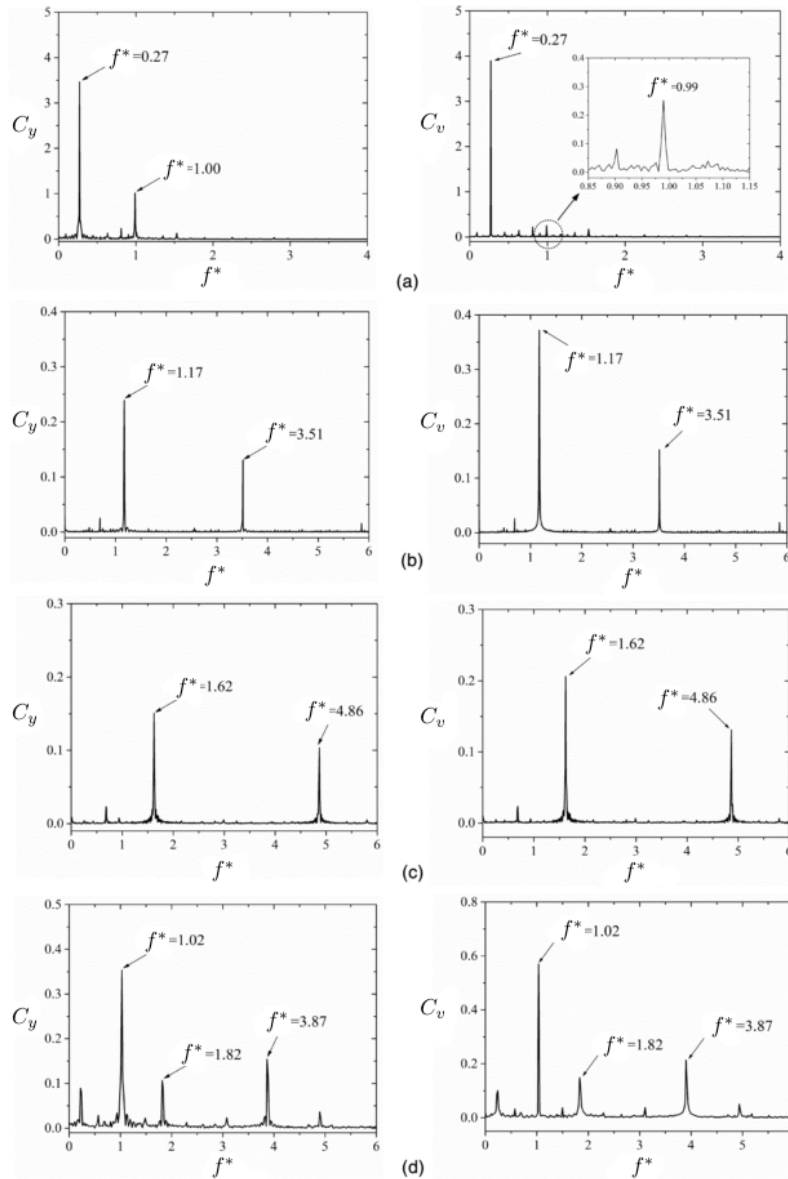


FIGURE 2.34: The power spectra density (PSD) of the total lift (C_y) and vortex lift (C_v) coefficients of an elastically-mounted cylinder undergoing rotary oscillations is presented as functions of normalised frequency response (f^*). Four forcing frequency ratios (f_{rot}^*) cases are presented at fixed forcing velocity ratio $A_m = 2.0$ and at reduced velocity $U^* = 4.5$. (a) $f_{rot}^* = 0.27$, (b) $f_{rot}^* = 1.17$, (c) $f_{rot}^* = 1.62$, and (d) $f_{rot}^* = 3.87$. Figure taken from Du & Sun (2015) and re-labelled using the terminology conventions of the present thesis.

Du & Sun (2015) reported that outside the lock-on region (see $f_{rot}^* = 3.87$ case in fig. 2.35(d)), the stable vortex streets previously observed becomes unsteady as the shedding process is influenced by multiple vortex shedding frequencies as illustrated in fig. 2.34(d).

While understanding the impact of lock-on on an elastically-mounted body is sufficient to show the rotary motion's efficacy in suppressing vortex shedding and the subsequent changes in fluid forces and vibrational response, it is not enough to reveal the evolution of the cylinder's response with the forcing parameters (A_m and f_{rot}^*). The following section will focus on the effects of the forcing frequency ratio.

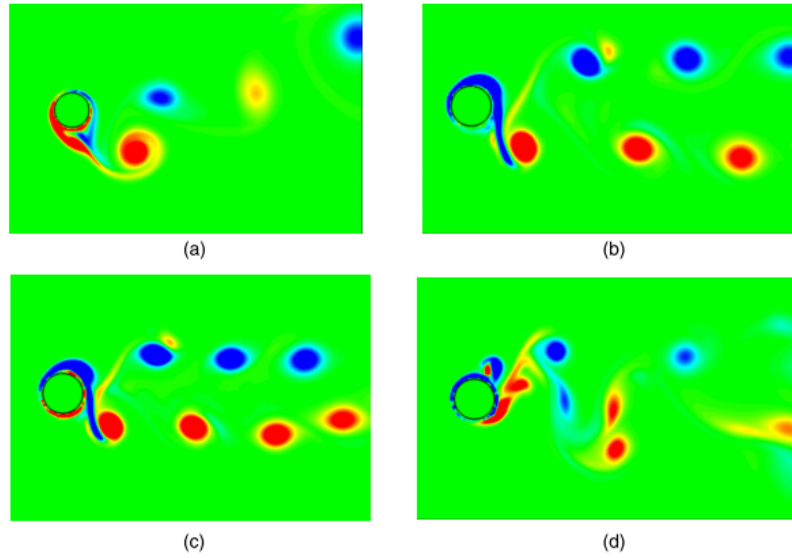


FIGURE 2.35: Instantaneous vorticity contours of an elastically-mounted cylinder undergoing rotary oscillations. Four forcing frequency ratios (f_{rot}^*) cases are presented at fixed forcing velocity ratio $A_m = 2.0$ and at reduced velocity $U^* = 4.5$. (a) $f_{rot}^* = 0.27$, (b) $f_{rot}^* = 1.17$, (c) $f_{rot}^* = 1.62$, and (d) $f_{rot}^* = 3.87$. Figure taken from Du & Sun (2015).

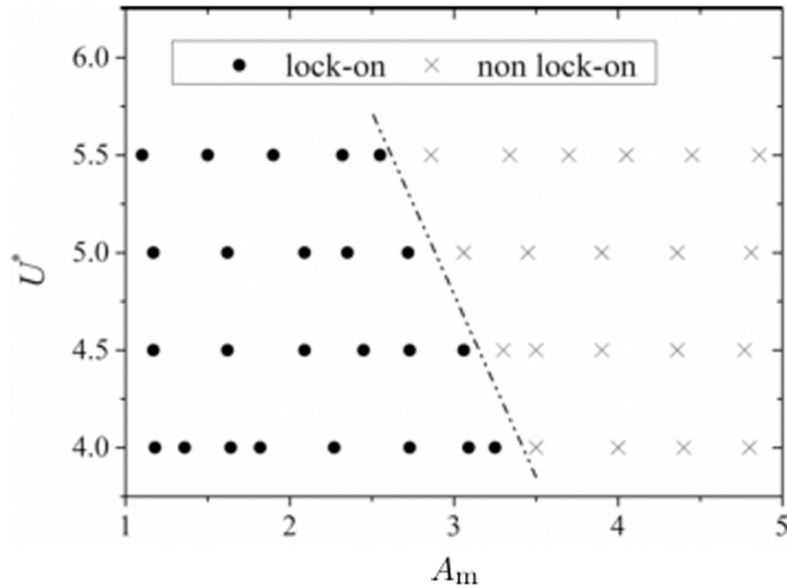


FIGURE 2.36: Flow regime of an elastically-mounted cylinder undergoing rotary oscillations at fixed forcing frequency ratio $f_{rot}^* = 2.0$ and at Reynolds number $Re = 350$. Figure taken from Du & Sun (2015) and re-labelled using the terminology conventions of the present thesis.

2.5.2.2 Effects of rotary oscillation frequency

A map of the lock-on and non lock-on regimes in the reduced velocity (U^*) and forcing frequency ratio (f_{rot}^*) domain is presented in fig. 2.36 for the velocity ratio $A_m = 2.0$ case. Du & Sun (2015) reported that the range of f_{rot}^* at which the cylinder remains locked on decreases with increasing U^* .

This behaviour is further exemplified in fig. 2.37 where the amplitude response (A^*) at two reduced velocities ($U^* = 4.5$ and 5.0) is presented as a function of f_{rot}^* at a fixed velocity ratio of

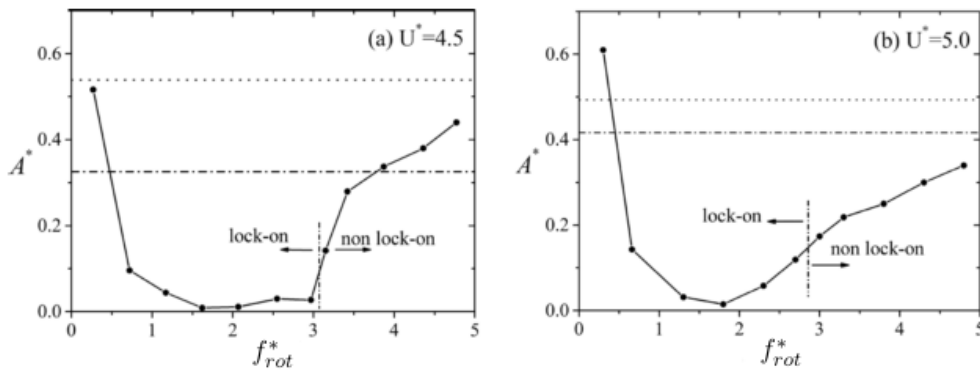


FIGURE 2.37: The normalised amplitude response (A^*) of an elastically-mounted cylinder undergoing rotary oscillations presented as a function of forcing frequency ratio (f_{rot}^*). Two reduced velocity (U^*) cases are presented for the fixed forcing velocity ratio $A_m = 2.0$. Figure taken from Du & Sun (2015) and re-labelled using the terminology conventions of the present thesis.

$A_m = 2.0$. A large amplitude response is observed when the forcing frequency coincides with the natural frequency of the structure (*i.e.* $f_{rot}^* = 1$), this response is highlighted by the dot-dash line in fig. 2.37. This is not unexpected as f_{osc} becomes synchronised with f and f_{nw} . Reduction in A^* can be achieved in both lock-on and non lock-on regions. In both U^* cases (see fig. 2.37(a) and fig. 2.37(b)), a decrease in A^* is observed compare to the non-rotating case (shown as a dotted line). Du & Sun (2015) reported that A^* decreased significantly when the forcing frequency is in the range of $1.2 \leq f_{rot}^* \leq 2.3$. The largest reduction at a reduced velocity of $U^* = 4.5$ is observed at a forcing frequency ratio of $f_{rot}^* = 1.8$ where the amplitude is reduced to less than $0.01D$. Within this region, lock-on occurs where the wake of the elastically-mounted body and the shedding frequency (f_{sh}) is locked to the forcing frequency (f_{osc}). They also reported observing amplitude peaks where f_{osc} matches f_{nw} , *i.e.*, $f_{rot}^* = 1$. The response at $f_{rot}^* = 1$ is illustrated as a dot-dash line in fig. 2.37. This observation is not discussed in detail by Du & Sun (2015), however, it can be speculated that the amplitude peak is due to the rotary forcing operating at a frequency that is in the proximity of the dominant frequency response of a non-rotating cylinder ($f = 0.222$ Hz at $U^* = 4.5$ and the natural frequency is $f_n = 0.228$ Hz).

2.5.2.3 Effects of rotary oscillation amplitude

Du & Sun (2015) also investigated the effect of the velocity ratio, A_m , as previously studies on rigidly-mounted cylinders undergoing rotary motions showed that the occurrences of lock-on are dependent a sufficiently large A_m for a specific forcing frequency ratio, f_{rot}^* (see Choi *et al.* (2002)).

Du & Sun (2015) investigated the effects of A_m at $U^* = 5.0$ and at $f_{rot}^* = 1.3$. Figure 2.38 presents their findings where A^* is presented as a function of A_m . For $A_m \leq 1$, rotary oscillations are ineffective. As the velocity ratio is increased from $A_m = 1.0$ to 1.4, A^* decreased rapidly. When the velocity ratio is $A_m > 1.35$, A^* is reduced to less than $0.04D$.

The power spectra density (PSD) of the cylinder's normalised displacement (y/D) and the power spectra of the vortex force coefficient (C_v) are presented as a function of f^* at different values of A_m and at a fixed reduced velocity of $U^* = 5.0$ in fig. 2.39. With increasing A_m , A^* decreases. Lock-on occurs when the vortex shedding frequency, f_{sh} , follows the forcing frequency, f_{osc} , this is observed in the $A_m = 1.4$ case in fig. 2.39(c). This can be seen through the single frequency peak occurring at a response of $f^* = 1.3$. At lower velocity ratios ($A_m = 1.0$ and 1.3), the A_m is not high enough to completely eliminate the displacement and vortex force peaks occurring at $f^* = 1.0$.

When the velocity ratio is $A_m = 1.0$, the vortex structure downstream of the cylinder is chaotic

2.5. Vortex-induced vibration of a cylinder undergoing rotary motions

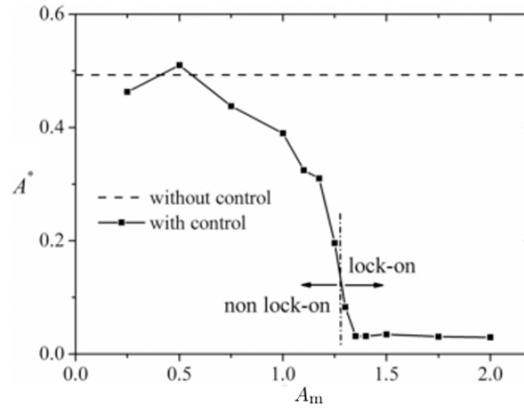


FIGURE 2.38: The normalised amplitude response (A^*) of an elastically-mounted cylinder undergoing rotary oscillations presented as a function of forcing velocity ratio (A_m) at fixed frequency ratio $f_{rot}^* = 1.3$ and reduced velocity $U^* = 5.0$. Figure taken from Du & Sun (2015) and re-labelled using the terminology conventions of the present thesis.

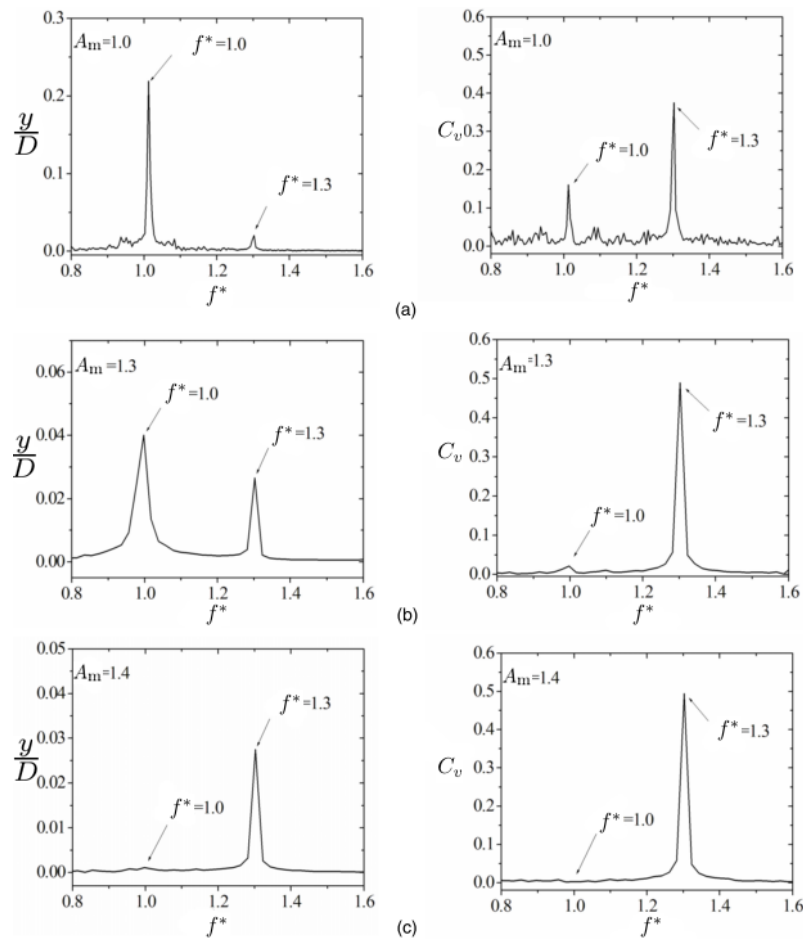


FIGURE 2.39: The power spectra density (PSD) of the normalised displacement (y/D) and vortex lift coefficients (C_v) of an elastically-mounted cylinder undergoing rotary oscillations is presented as functions of normalised frequency response (f^*). Three forcing velocity ratio (A_m) cases are presented at fixed forcing frequency ratio $f_{rot}^* = 1.3$ and at reduced velocity $U^* = 5.0$. Figure taken from Du & Sun (2015) and re-labelled using the terminology conventions of the present thesis.

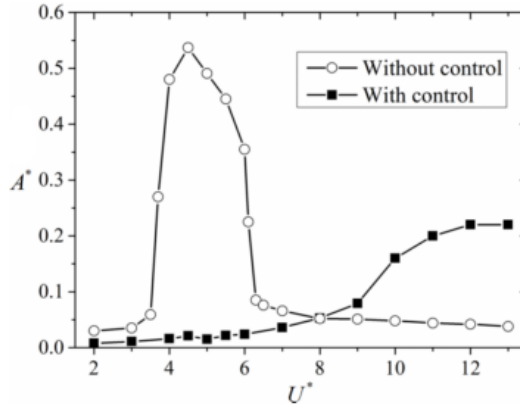


FIGURE 2.40: A comparison of the response of an elastically-mounted cylinder undergoing rotary oscillations and that of a non-rotating cylinder. The normalised amplitude response (A^*) is presented as a function of reduced velocity (U^*). The forcing cylinder was oscillating at fixed frequency ratio $f_{rot}^* = 1.8$ and fixed velocity ratio $A_m = 2.0$. Figure taken from Du & Sun (2015).

because in the non lock-on region, f_{sh} is influenced by both the cylinder oscillation and the rotary forcing. However, as velocity ratio is increased to $A_m = 1.4$, the cylinder sheds counter-rotating vortices that then form two parallel rows further downstream.

The results presented by Du & Sun (2015) on the effects of the rotary forcing parameters showed that, similar to previous rigid cylinder studies, the effectiveness of using rotary oscillations to control vortex shedding and VIV is dependent on the appropriate selection of the A_m and f_{rot}^* . While optimal forcing parameters may be effective, it is limited to specific systems parameters. Du & Sun (2015) investigated how U^* and the system's m^* impact the response of the cylinder. Their results will be reviewed in the following section.

2.5.2.4 Effects of reduced velocity and mass ratio

The amplitude response, A^* , as a function of reduced velocity, U^* , of a cylinder undergoing rotary forcing at velocity ratio $A_m = 2.0$ and frequency ratio $f_{rot}^* = 1.8$ is presented in fig. 2.40. For a non-rotating cylinder, large amplitude oscillations are observed between reduced velocities $3.6 \leq U^* \leq 6.1$ as a result of wake-body excitation. In the same U^* range, the A^* of the cylinder with rotary forcing decreased significantly. When the reduced velocity is $U^* < 7$, A^* is less than $0.03D$ with forcing. However, rotary oscillation is not effective for all ranges of U^* , when $U^* \geq 8.0$, the amplitude response of the cylinder with forcing is equal or large than those observed in the non-rotating case. Figure 2.40 shows that rotary oscillation is most effective in the lock-in region where large amplitude oscillations are typically observed for a non-rotating cylinder. At U^* higher than the upper bound of the lock-in region of a non-rotating cylinder (*i.e.* the desynchronization region), implementing rotary oscillation will increase the amplitude response on the cylinder.

Du & Sun (2015) presented results on the influence of m^* . At a fixed reduced velocity of $U^* = 5.0$ and at a fixed velocity ratio of $A_m = 2.0$, their study showed that A^* decreases with increases in system mass. Reductions in A^* with m^* is significant at low frequency ratios ($f_{rot}^* < 1.2$), however, when $f_{rot} \geq 1.2$, the reduction in A^* with m^* is marginal.

2.6 Chapter summary and research questions

From the review of past literature, it is evident that limited research has been done on characterising response and wake structure of an elastically-mounted cylinder undergoing constant rate rotation

and rotary oscillations. While work by Bourguet & Lo Jacono (2014); Zhao *et al.* (2014c); Seyed-Aghazadeh & Modarres-Sadeghi (2015); Du & Sun (2015) have provided knowledge in the response and wake structure, there exist limitations to their study and some questions remain unanswered. The voids in knowledge and the research statements proposed to answer them will be explained.

1. Simulation by Bourguet & Lo Jacono (2014) and experiment by Seyed-Aghazadeh & Modarres-Sadeghi (2015) of an elastically-mounted cylinder undergoing constant rate rotation have shown that the amplitude and frequency responses exhibits a number of similarities with that of a cylinder undergoing non-rotating VIV. Bourguet & Lo Jacono (2014) observed a number of wake patterns that was previously seen in non-rotating VIV and rigidly-mounted rotating cylinder studies; furthermore, they reported a new T+S wake mode that is associated with large cylinder oscillations. However, all the existing work on this subject studied the cylinder at low Reynolds numbers ($Re \leq 1000$). One might question if the observed similarities in vibrational responses and the appearance of the new T+S wake mode will persist at higher Reynolds numbers. Therefore, the first question for research is: *What are the differences in vibrational response and wake structure between an elastically-mounted circular cylinder undergoing constant rate rotation and a non-rotating cylinder at moderate Reynolds numbers ($Re > 1000$)?*
2. Du & Sun (2015) demonstrated that rotary oscillation is effective at reducing VIV. However, little is known about the amplitude peak observed when the forcing frequency ratio is at $f_{rot}^* = 1$. At very low forcing frequency ratios ($f_{rot}^* < 0.5$), A^* of the cylinder appeared to be larger than the non-rotating case. One might ask will the amplitude response increase further at even lower f_{rot}^* . Tertiary lock-on was observed in rigid cylinder studies, however, Du & Sun (2015) did not observe it. With finer increments in the forcing parameters, will tertiary lock-on appear for an elastically-mounted cylinder? As Du & Sun (2015) conducted their simulation at a low Reynolds number of $Re = 350$, one might wonder if the trends in vibrational response and wake formation can be seen at high Re . Therefore, the second question for research is: *What are the differences in vibrational responses, lock-on boundaries and wake development between an elastically-mounted cylinder undergoing sinusoidally-driven rotary oscillations and a non-rotating cylinder at moderate Reynolds numbers ($Re > 1000$)?*

In order to answer these questions, experimental investigations are necessary to broaden the knowledge of VIV of circular cylinders undergoing rotary motions. The experimental study is divided into two sections: VIV of circular cylinders undergoing constant rate rotation and VIV of circular cylinders undergoing sinusoidally-driven rotary oscillations. Prior to the discussion of results, the experimental methodologies will be reviewed in §3.

Chapter 3

Experimental methodology

3.1 Chapter overview

This chapter provides an overview of the facilities, experiment configuration, apparatus, measurement techniques and procedures used to acquire the data to be presented in later chapters. The experimental facility and flow control system will be described in §3.2. The experimental configuration and an overview of the apparatus set up and test model will be presented in §3.3. Section §3.4 provides details of the air bearing and rotation rig system that control the translational and rotational motion of the cylinder, respectively. Data measurement systems used to record the linear and rotary displacement, fluid forces and flow visualisation data will be explained in §3.5. Section §3.6 explains the experimental procedure and free decay measurements. Key findings of the chapter are summarised in §3.7

3.2 Flow control system

The experiment was conducted in the FLAIR free-surface, recirculating water channel at the Department of Mechanical and Aerospace Engineering at Monash University. A photograph and schematic of the water channel is presented in fig. 3.1 and fig. 3.2, respectively. This closed-loop water channel is driven by a mixed-flow pump powered by an AC electric motor. The free-stream velocity of the water channel was controlled by varying the operating frequency of the pump. This operation frequency of the pump was controlled digitally using the data acquisition software LabVIEW®. By varying the pump frequency between $f_{\text{pump}} = 4.5 - 45$ Hz, the free-stream velocity within the test section can be varied between $U_{\infty} = 0.041 - 0.391$ m/s.

The flow upstream of the test section was conditioned by the devices shown in figure 3.2. When the water leaves the return pipe it is guided through a set of guiding vanes. This is followed by a combination of mesh, settling chamber, honeycomb; and a three-dimensional 3:1 ratio contraction. The test section has internal dimensions measuring 600 mm in width, 800 mm height and 4000 mm in length. It was constructed from glass and reinforced by a steel structure. This enabled the use of flow visualisation imaging techniques. Downstream of the test section are the diffuser and return pipe intake, which feeds water back through the centrifugal pump. The combined upstream flow conditioning measures and the 3:1 contraction reduced the free-stream turbulence in the test section to less than 1%.

To ensure flow characteristics in all experiments were accurate and relevant the free-stream velocity and turbulent intensity were measured periodically. Particle image velocimetry was used to measure these, as it is non-intrusive. Images were taken at the centre of the test section over a range of pump frequencies. Figure 3.3 presents the free-stream velocity (U_{∞}) plotted as a function of pump frequency (f_{pump}) at a water height of 780 mm. The results show that free-stream velocity



FIGURE 3.1: A photograph of the FLAIR water channel. Image from Zhao (2012).

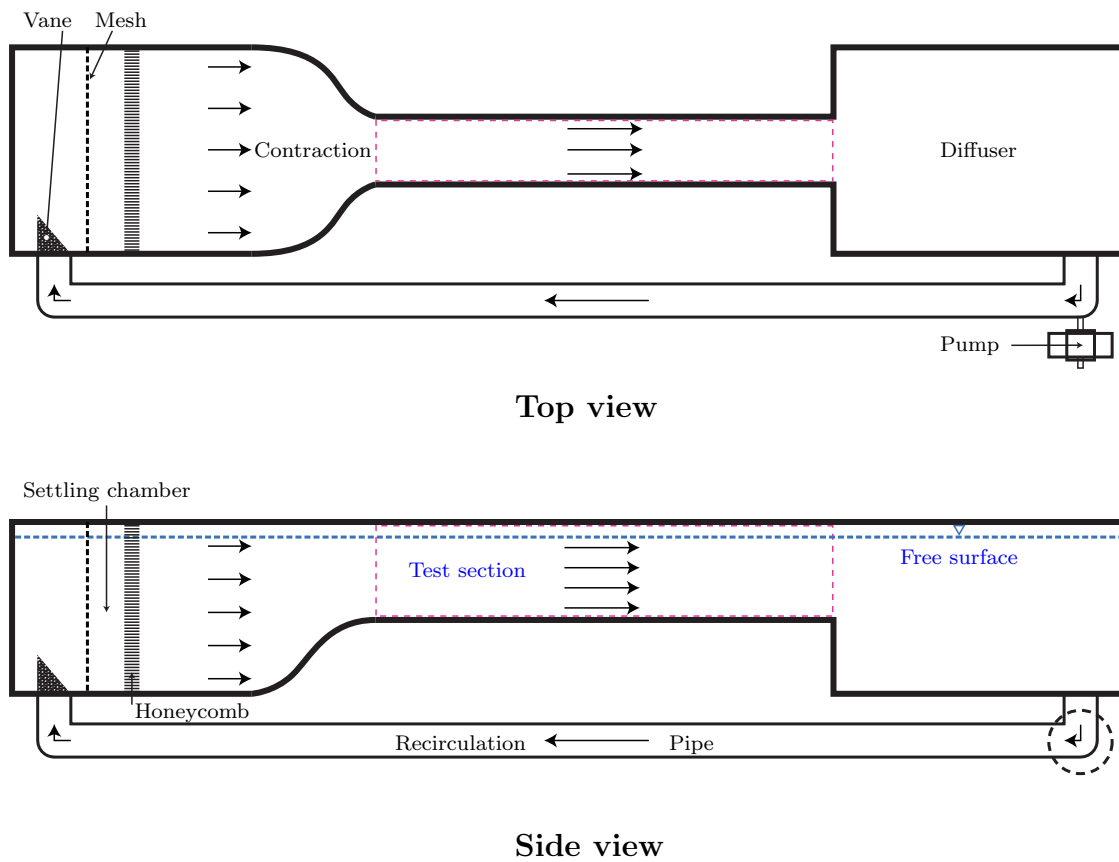


FIGURE 3.2: Schematic of the free surface, recirculating water channel at FLAIR.

varies linearly with pump frequency. This linear relationship enables simple interpolation for any desired free-stream velocity output.

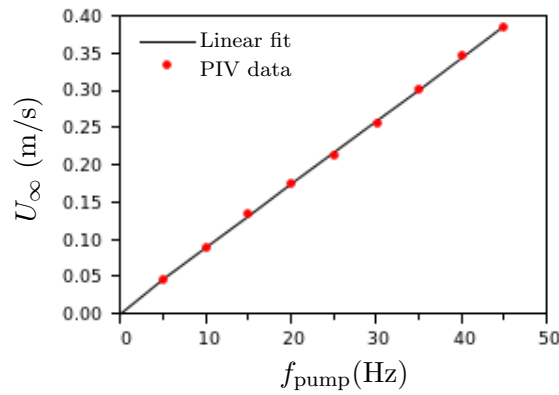


FIGURE 3.3: PIV measurement of the free-stream velocity (U_∞) as a function of the pump frequency (f_{pump}) of the water channel at a water level of $l_{FS} = 780$ mm.

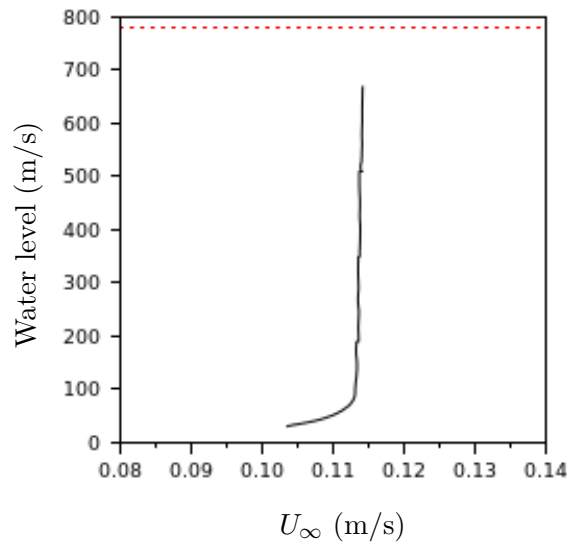


FIGURE 3.4: PIV measurement of the streamwise velocity profile (U_∞) as a function of the water depth of the water channel at a free-surface water level of $l_{FS} = 780$ mm (represented by the red dashed line) and at a free-stream velocity $U_\infty = 0.1143$ m/s.

Viscosity and the ‘no-slip’ condition ensures the layer of fluid in contact with the solid boundary will slow down creating a non-uniform velocity profile. The fluid at the boundary having zero velocity (*i.e.* $U_\infty = 0$ m/s). Therefore, the boundary layer has an impact on the fluid forces along the span of the cylinder (*i.e.* the z -axis). To better understand the boundary layer, the streamwise velocity profile is studied.

The streamwise velocity profile of the water channel was captured at $U_\infty = 0.1143$ m/s. Understanding the streamwise velocity profile is essential to designing the length of the test cylinder and the height of the transparent end platform such that effects of the boundary layer is eliminated and proper end conditioning is achieved to promote parallel shedding. The PIV imaging system was traversed in the z -axis from the bottom of the test section to near the free surface in several sampling sections. The mean velocity profile from each image sampling section was combined to form a single velocity profile which is presented in fig. 3.4. Figure 3.4 shows that at 100 mm above the bottom of the test section, the free-stream velocity is uniform and it is within 1% of its free-stream value.

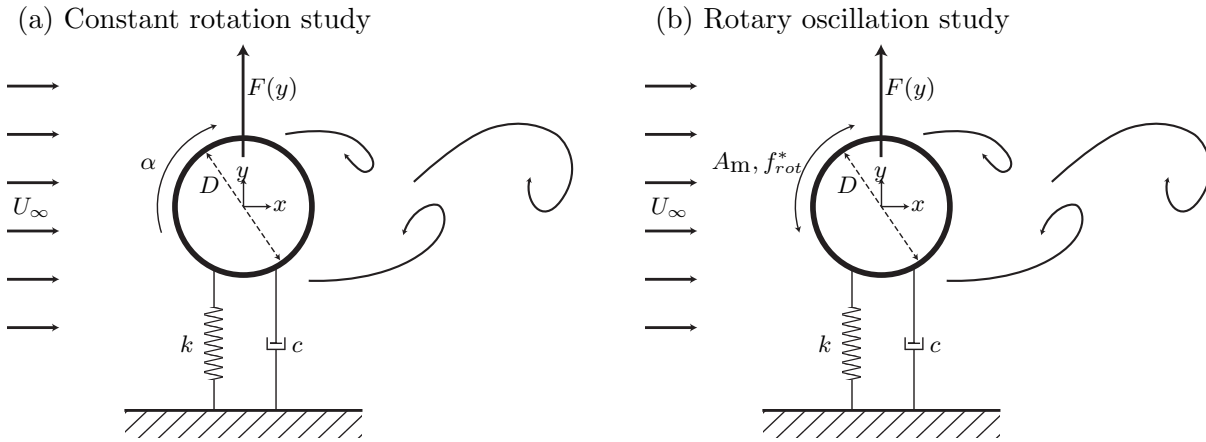


FIGURE 3.5: Fluid-structure configuration of an elastically-mounted circular cylinder undergoing, (a) forced constant rotation and (b) rotary oscillations.

3.3 Experimental configuration

The elastically-mounted circular cylinder was immersed in a free-stream flow parallel to x axis. Figure 3.5 shows the fluid-structure configuration. Structural stiffness and damping in the system arise from springs and energy dissipation, respectively. The stiffness of the oscillating system is defined by the spring constant (k). Damping (c) of the system is quantified by the structural damping ratio (ζ), defined as the product of the structural damping in air and the ratio between the natural frequency of the vibration system in water and air. These will be discussed in further detail in §3.6. A rotary motion was imposed on the cylinder and Figure 3.5 (a) and (b) show the configuration for forced constant rotation and forced rotary oscillation, respectively.

A schematic of the experiment set up is presented in fig. 3.6. An air bearing system was positioned above the water channel to allow hydro-elastic oscillations only in the cross-flow direction. All oscillating masses were supported on two guide shafts that were suspended on four air bushings. A detailed overview of the air bearing system is reported in §3.4.1. An aluminium carriage was attached to the two shafts. The opening on the air bearing base plate can accommodate body oscillations up to ± 123 mm or $\pm 4.1D$ for a 30 mm diameter cylinder from the centre zero position. Stainless steel springs attached between the carriage and the base of the air bearing provided structural stiffness. A magnetic rod was attached to one of the support shafts and this acted as the core of the linear variable differential transformer (LVDT) sensor that measures the linear displacement of the oscillating system. A linear optical encoder is later used to measure the cross-flow linear displacement. More details are provided in §3.5.2. A sting was attached to the bottom of the carriage to measure fluid forces and to support the rotation rig and test cylinder. The rotation rig was attached to the bottom of the sting. It controls the rotary motion of the cylinder via a Parker[®] stepper motor and motor controller. Further details on the rotation rig and rotary motion control system are provided in §3.4.2. Housed within the rotation rig was a US Digital[®] EP5 differential encoder that measures the angular displacement of the cylinder. The rotary displacement measurement system is explained in §3.5.3.

Test cylinders were attached to the rotation rig. The cylinder has a diameter of $D = 30$ mm and is machined from a single circular aluminium tube with a wall thickness of 1.6 mm. For constant rotation experiments the immersed length was $l_{ms} = 604$ mm and for rotary oscillation experiments it was $l_{ms} = 614$ mm. The difference in immersed lengths was due to a change in free-surface

water level (l_{FS}) between the two experiments. The free-surface water levels for constant rotation and rotary oscillation were $l_{\text{FS}} = 770$ mm and 780 mm, respectively. The aspect ratio (\mathcal{R}) of the cylinder is given by eq. 2.4 and it is $\mathcal{R} = 20.1$ for constant rotation and 20.5 for rotary oscillation experiments.

When a body is immersed in a moving fluid, the flow around the body causes the streamlines to expand in the near wake. This expansion can be restricted by any enclosing walls, such as those of a wind tunnel or water channel and these can have a significant effect. This is related to the ratio between the profile cross section area of the body (A_{body}) and the cross section area of the enclosure or the test section ($A_{\text{test section}}$). This is commonly known as blockage and the blockage ratio is given by eq. 3.1

$$R_{\text{block}} = \frac{A_{\text{body}}}{A_{\text{test section}}} \quad (3.1)$$

For both water level configurations, the current study has a blockage ratio of $R_{\text{block}} = 3.9\%$. This value is acceptable in experimental studies. Previously published work by the FLAIR group have similar blockage ratios.

To control the end condition of the test cylinder, an end platform was used. This was constructed from transparent polycarbonate to enable PIV imaging and the top plate was 580 mm wide, 400 mm long and 5 mm thick. An elliptical leading edge reduces turbulent eddies and prevents large flow separations from developing on the platform. Use of such a platform to control end conditions for an elastically-mounted circular cylinder was reported by Khalak & Williamson (1996); Govardhan & Williamson (2000); Morse *et al.* (2008). Controlling the end condition of a low aspect ratio cylinder means the effects of the boundary layer from the floor of the water channel test section and effects of three-dimensionality can be reduced, promoting parallel vortex shedding. Khalak & Williamson (1996) used an end platform that only requires the stationary platform to be positioned $0.04D$ below the end of the oscillating cylinder. Parallel vortex shedding was produced without adding any unwanted mass or inducing any undesired fluid forces on the oscillating system.

The oscillating mass of the system determines the maximum amplitude response of the cylinder if the system damping is constant and is hence considered a key parameter affecting the fluid forces of the oscillating system. The component masses of the current apparatus were measured by a digital scale which has a resolution of 0.1 gm. For constant rotation experiments, the total mass of the oscillation structure was $m_{\text{osc}} = 2.467$ kg. This gives a mass ratio, defined as the ratio between m_{osc} and mass of the fluid displaced by the cylinder (m_{fld}), of $m^* = 5.78$. There were hardware modifications made between the constant rotation and rotary oscillation experiments that changed the oscillating system mass. For the rotary oscillation experiments, $m_{\text{osc}} = 2.448$ kg and the mass ratio was $m^* = 5.641$.

3.4 Motion control systems

In the present study, the motion control of the cylinder can be separated into translational and rotary motions. The free translational motion of the cylinder in the direction transverse to the free-stream flow was restricted by the air bearing system, which is further explained in §3.4.1. A photograph of the experiment apparatus used in the present studies is presented in fig. 3.7. Forced rotary motions of the cylinder were driven by the stepper motor mounted on the rotation rig and controlled by the motor controller. Details on rotary motion control is provided in §3.4.2.

3.4.1 Air bearing system

To best study the fundamental behaviours and maximum body response of bluff bodies undergoing VIV, undesired damping was minimised. Damping is caused by friction in the oscillating system.

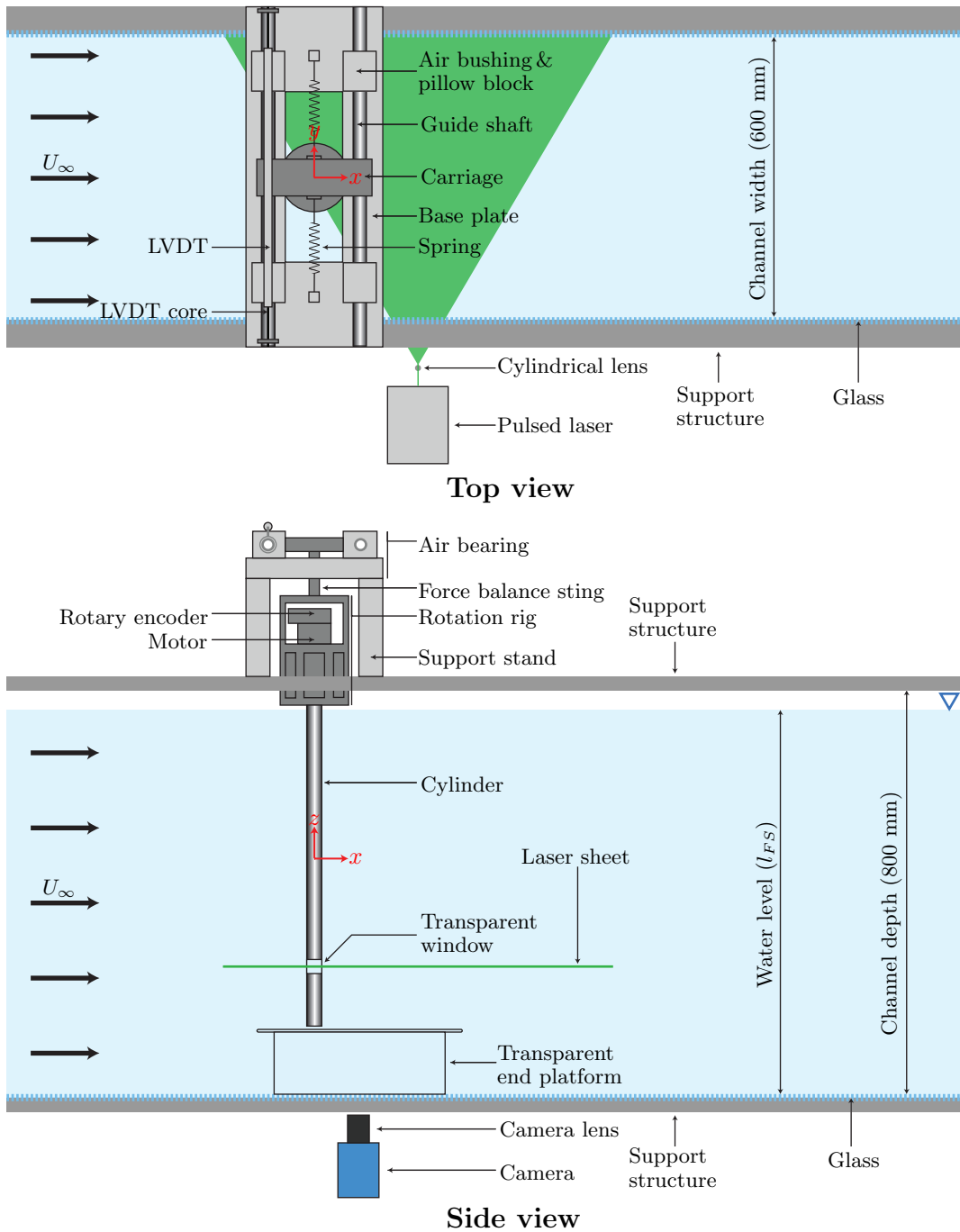


FIGURE 3.6: Schematic of the present experiment.

Previous researchers have used air bearings (*e.g.* Feng (1968); Khalak & Williamson (1996); Govardhan & Williamson (2000); Zhao *et al.* (2014b)) to experimentally simulate the low friction condition and precise translational motion required. The present experiment utilised a system of four air bearing bushings and two circular guide shafts to elastically support the oscillating masses as illustrated in fig. 3.6. The air bearing system used here was designed by Zhao (2012) and constructed in-house by FLAIR and the Department of Mechanical and Aerospace Engineering. An air bearing is a non-contact, friction control system where compressed air is used to form a thin lubrication layer that separates the solid surfaces from coming in contact while they are in relative motion. There

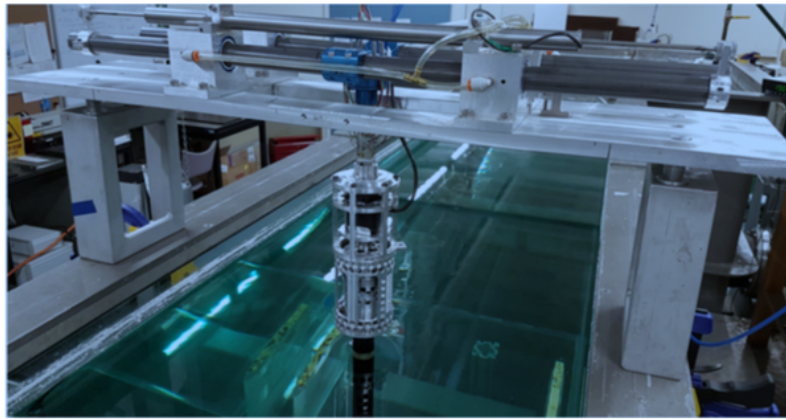


FIGURE 3.7: A photograph of the experiment apparatus used in the present studies.

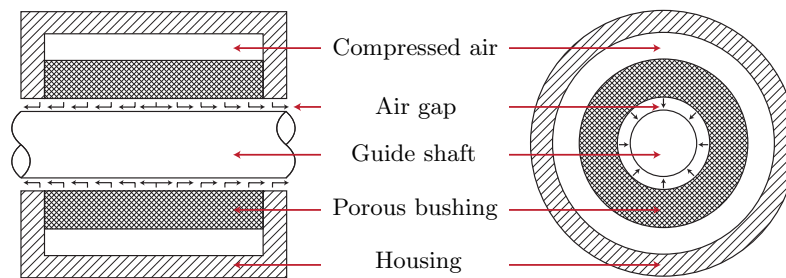


FIGURE 3.8: Cross-sectional view of the porous-media type air bushing used in the current air bearing system.

are two types of air bearings, orifice and porous media. The advantage of using the porous media over the orifice type bearing is that as the compressed air bleeds through the porous media the air pressure is evenly distributed along the length of the bushing. This is illustrated in fig. 3.8. This even distribution of air pressure enables a uniform layer of thin air which increases system stability and decreases vibration from fluctuating air pressures. The current system utilised the porous-type system. The four carbon air bushings used in the current air bearing are model S302502; commercially manufactured by NEWWAY[®] Air Bearings, USA. Compressed air at a pressure of 90 PSI was supplied to all four bushings. The compressed air was filtered, conditioned and regulated upstream of the air bushings to ensure a steady supply of clean, dry air.

The air bushings are housed within aluminium pillow blocks, which were mounted on an aluminium base plate. Exterior dimensions of the base plate measures 208 mm in width, 800 mm in length and 16 mm in thickness. At each corner of the base plate a threaded support pad was used to enable small height and levelling adjustments. The air bearing system was originally designed to be positioned directly on top of the two channel support rails. As illustrated in fig. 3.6, to accommodate the additional height of the rotation rig, large support frames were used to elevate the air bearing system such that the rotation rig clears the water surface. A digital inclinometer and a large digital protractor were used to ensure the air bearing system was horizontal and perpendicular to the direction of the free-stream flow. Both devices have a resolution of 0.05°.

Smooth operation of the air bearings requires the bushings and shafts to work in harmony. This requires the guiding shafts to be very precise. NEWWAY[®] recommended guide shafts diameters to be $\varnothing 25.0000^{+0.0000}_{0.0076}$ mm. The straightness of the shaft is vital to the low friction of the air bearing

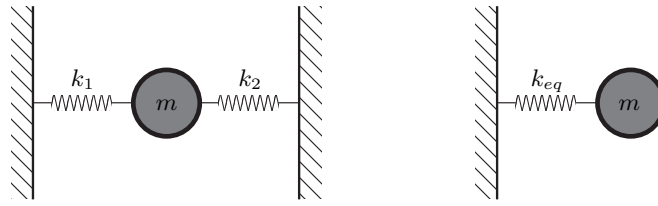


FIGURE 3.9: An illustration of a one-spring-pair one-mass spring system (left); and its reduced, equivalent spring system (right).

system. Extensive work was done by Zhao (2012) to ensure the guide shafts were straight and within the geometric tolerances of the bushings. Two sets of guide shafts were used. The original set of carbon fibre shafts were used for constant rotation experiments. Aluminium shafts with even higher precision were later used in rotary oscillation experiments. They caused a change in the oscillation mass, which was previously discussed.

The stiffness of the oscillating system was provided by springs attached between the two spring anchors mounted on the air bearing base plate and the carriage as illustrated in fig. 3.6. The spring anchors and the attachment points on the carriage are coplanar to the longitudinal centre plane of the base plate. This arrangement constrains the extension of the springs to the direction of the guide shafts’ motion. The stainless steel springs used are model LE014BS13S, commercially manufactured by Lee Springs, UK. They have a free, unextended length of 63.5 mm, an outer diameter of 4.775 mm, a wire diameter of 0.355 mm and a coil count of 151.9.

The carriage is the central connection to all the oscillating masses in the system. Figure 3.9 shows that as springs are attached on either side of the mass (m), it is a one degree-of-freedom, one-spring-pair one-mass system. In such a spring-mass system, the spring pair is considered to act in parallel. The equivalent spring constant for a parallel spring system is given by eq.3.2:

$$k_{eq} = k_1 + k_2 \tag{3.2}$$

where k_1, k_2 are spring constants of individual springs.

The stiffness of the system can be adjusted by attaching additional spring pairs. Two pairs and one pair of springs were used for the constant rotation and rotary oscillation, respectively. Two pairs of springs were used due to the large body oscillations about the mean displacement position. This caused the cylinder to oscillate beyond the opening on the air bearing base plate. The increased system stiffness altered the natural frequency of the oscillating system from that of one pair of springs. The measured equivalent spring constant for two spring pairs in constant rotation experiments is 0.0493 N/mm and for one spring pair in rotary oscillation experiments is 0.0212 N/mm. These stiffness values of the oscillating system were calculated from free decay tests, which are discussed in §3.6. Displacement measurements were acquired by the LVDT and later by optical linear encoder. The magnetic core of the LVDT was suspended by two supports that were clamped onto the ends of one of the guide shaft. This ensured the core moved in the same motion as the rest of the oscillating masses. This core runs through the centre of the LVDT, which remained stationary and was mounted on top of the pillow blocks. In later studies, the optical linear encoder replaces the LVDT. The low noise digital signal from the optical linear encoder enabled accurate estimates of fluid force derived only from the cylinder motion, oscillation masses and structural properties. Important structural properties to the experiment such as the natural frequency, structural stiffness and damping of the oscillating system were measured experimentally through free decay tests. This is outlined in §3.6.

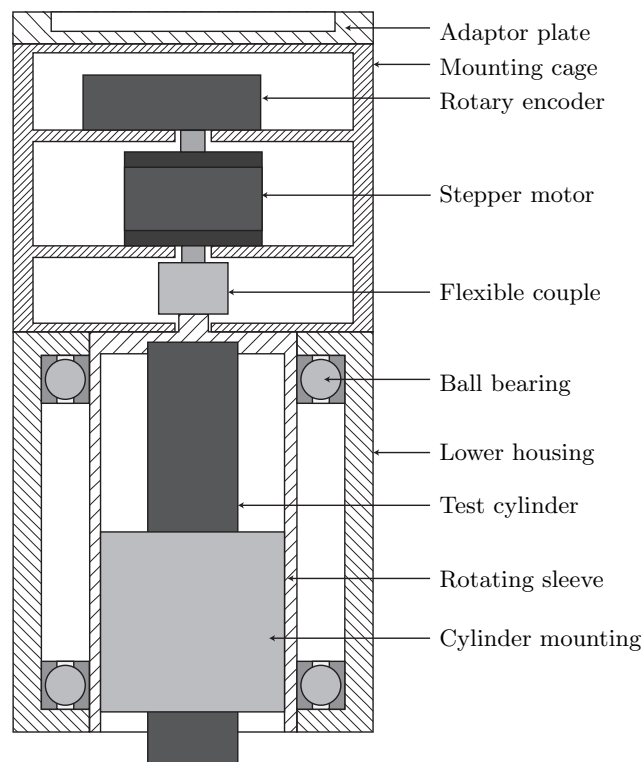


FIGURE 3.10: A detailed cross-sectional schematic of the rotation rig used to control the rotary motion of the cylinder.

3.4.2 Rotation rig and motion controller

A motor and motor controller were used to impart rotation and control the rotary motion of the test cylinder. The rotation rig was designed and manufactured in-house to mount the test cylinder and motor. A Parker[®] motor drivers and controllers were used control the motor. Figure 3.10 shows a detailed schematic of the rotation rig. An adaptor plate on the top of the rotation rig connects to the connection sting. Mounted above the motor is an optical rotary encoder. The rotation rig was designed such that the motor was mounted at the centre of the rig. A helical flexible coupling was installed to allow for axial misalignments and dampens mechanical vibration from the motor. It connects the shaft of the motor to the rotating sleeve that mounts the test cylinder. Two high-precision ball bearings were used to support the rotating sleeve between the sleeve and exterior housing. These two bearings are positioned approximately 90 mm apart in the z -axis. By increasing the length of the cylinder supported between the bearings; axial alignment is maximised and radial vibration minimised.

The motor used in the rotation rig is a Parker[®] model LV172-02-FL DC rotary stepper motor. It was wired as a parallel circuit to increase its drive current. Thus, configuration increases its torque performance over the motor's operational speeds. A schematic including the motor control system is presented in fig. 3.11. The motor control system is outlined in red dash lines. The laboratory computer hosted a digital input-output (I/O) interface that communicates with the Parker[®] 6K motor controller. Information such as motor-controller scaling, operation modes and rotary motion parameters were input into this interface and sent to the controller. This input enables the controller to control the DC motor drivers that then provide power and control the motion of the stepper motor.

To ensure the motor and test cylinder undergoes the desired rotary motion precisely, calibration

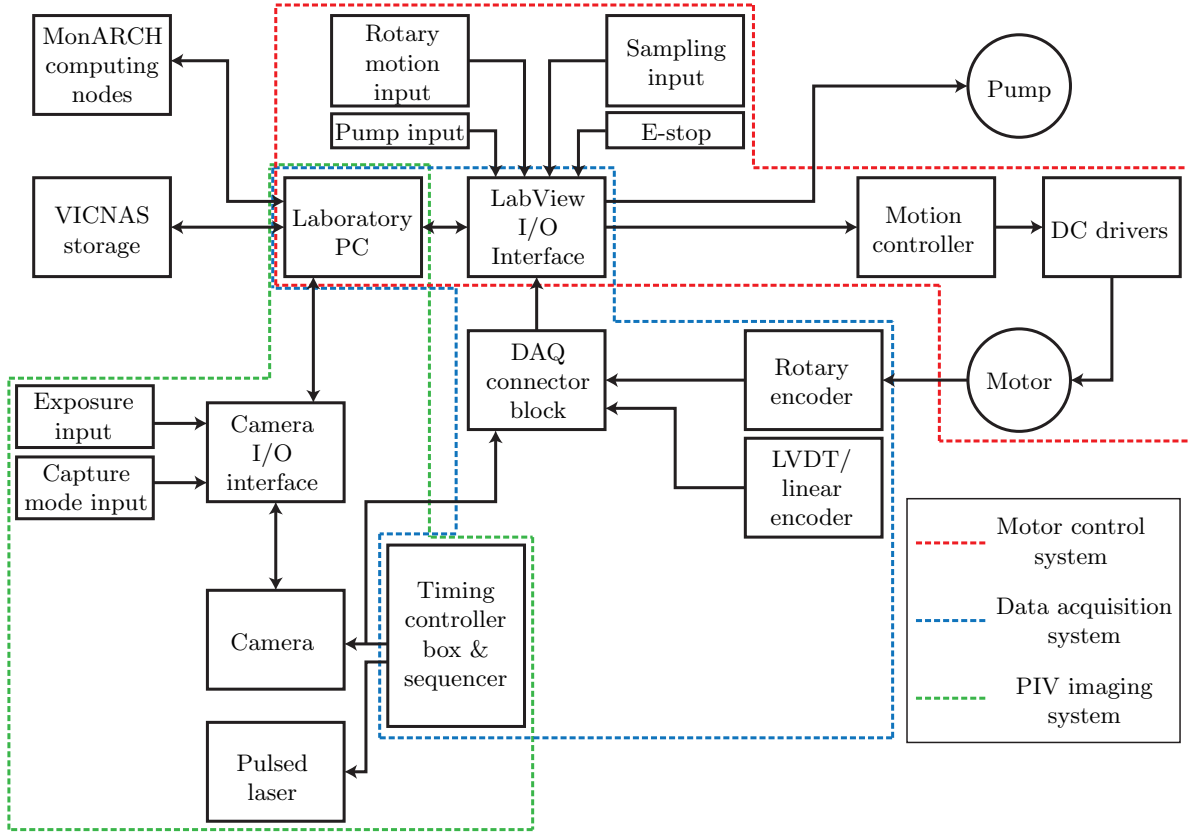


FIGURE 3.11: A complete block diagram of the measurement apparatus and systems used in the present study. Highlighted in coloured dashed lines are sub-systems. The motor control in red, DAQ acquisition in blue and PIV imaging in green dashed lines.

tests were performed using an optical rotary encoder. Validation of the rotary motion profile of a cylinder undergoing constant rate rotation and sinusoidally-driven rotary oscillation is presented in Appendix A.

3.5 Data measurement systems

To study the vibration response and wake structure, a number of quantitative measurements are required. A comprehensive measurement and acquisition system was used to acquire the necessary data. Data acquisition (DAQ) hardware and software used in conjunction with other sensory devices are described in §3.5.1. The LVDT and the linear optical encoder was used to measure the linear displacement of the cylinder is explained in §3.5.2. The acquisition of rotary motion measurements is presented in §3.5.3. The PIV system used to acquire quantitative flow visualisation data is reported in §3.5.4.

3.5.1 Data acquisition (DAQ) system

Figure 3.11 presents a schematic of the entire DAQ and control system used in the present experiment. Outlined in a blue dashed line is the DAQ system. Signals from the LVDT, optical linear encoder, optical rotary encoder and TTL (transistor-transistor logic) trigger timing controller (if the PIV measurement system was used) are connected to the DAQ connector block. This connector block

centralises and transmits the signals to the custom LabVIEW™ VI digital I/O interface where they are sampled and recorded.

To acquire data simultaneously required a device that centralises all analogue and digital signals (excluding PIV images) before being transmitted to the digital I/O interface hosted by the laboratory computer. Two DAQ connector blocks were used for this purpose. An older 37pin port system was initially used for constant rotation measurements before being replaced by a USB™ port system that was used for rotary oscillation measurements. The old connector block is a National Instruments® BNC-2110 connector block. It was connected to a 37 pin PCI-6221 DAQ board installed in the laboratory computer. This computer runs a digital I/O interface which records all measurement channels and controls the water channel pump and motor controller. The BNC-2110 connector block has eight analogue ± 10 V DC inputs, two analogue ± 10 V DC outputs and a terminal block for digital I/O connections. A new connector block, National Instruments® USB-6218, with a USB™ connection was directly connected to the laboratory PC. It has sixteen analogue ± 10 V DC inputs, two analogue ± 10 V DC outputs and a terminal block for two digital I/O device connections. Both connector blocks are capable of acquiring data at a maximum sampling frequency of 250 kHz.

A custom digital I/O interface was used to sample and record the measurements. This interface utilises a collection of smaller LabVIEW™ VI programs. Each of these VI programs have specific functions. They range from sampling and recording the measurements to those that control the water-channel pump and rotary motion of the cylinder by sending commands to the Parker® 6K motor controller. Recorded data were sorted, processed and analysed using MATLAB® codes and scripts.

3.5.2 Linear displacement measurement

A linear variable differential transformer was used to measure the linear displacement of the cylinder until it was replaced by a linear optical encoder. The LVDT is a non-invasive, non-contact system. As illustrated by fig. 3.12, the principle operations of a LVDT consist of a cylindrical ferromagnetic core and a coil assembly. The core is attached to the body that requires its position to be measured. The coil assembly has three solenoid coils that are positioned end to end within a non-ferrous cylindrical housing. At the centre of the assembly is the primary coil and on either sides are the secondary coils. An alternating current (AC) power supply powers the primary coil that generates magnetic flux and is linked to the secondary coils. This arrangement enables a voltage to be induced in each of the secondary coils. As the ferromagnetic core moves coaxially through the coil assembly, the linkage of magnetic flux changes. Changes in the magnetic flux then changes the induced voltage in the secondary coils. Therefore, the voltage output in each of the secondary coils depends on the position of the core and the body it is attached to. As the two secondary coils are connected, the voltage output is the differential of the two coils. This differential voltage is linearly controlled by the position of the ferromagnetic core and the body it is attached to. The LVDT system has several advantages over other position measurement systems. They are mechanically robust and being a non-contact system given them exceptional service life. Linear variable differential transformers can theoretically detect changes in core position that are infinitesimally small as it principally relies on changes in magnetic flux. This is only limited by the resolution of the DAQ system.

In the present application, the ferromagnetic core was in a long cylindrical tube mechanically attached to one of the oscillating guide shafts in the air bearing. This is illustrated in fig. 3.6. Because the guide shaft was rigidly connected to the rest of the oscillating masses and test cylinder, the displacement of the cylinder can be measured through the displacement of the guide shaft the core is mounted on. The coil assembly containing additional electronics was mounted on to the stationary pillow blocks. The LVDT used was model SE 750-10000 manufactured by Marco Sensors™, USA. A constant 28 V power supply was used to power the LVDT coil. It has an output voltage that ranges from 0 – 10 V and corresponds to a displacement measurement of 0 – 250 mm. The LVDT

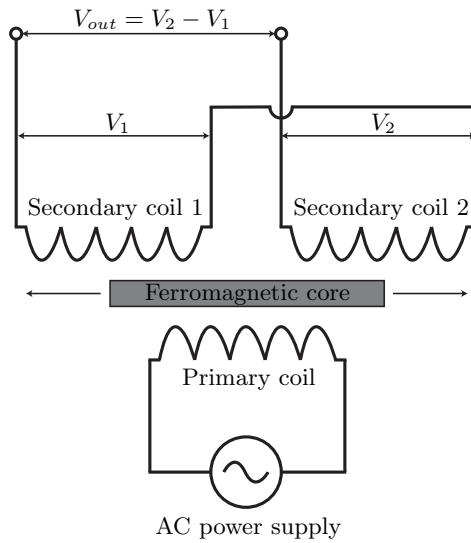


FIGURE 3.12: A wiring schematic of a linear variable differential transformer (LVDT).

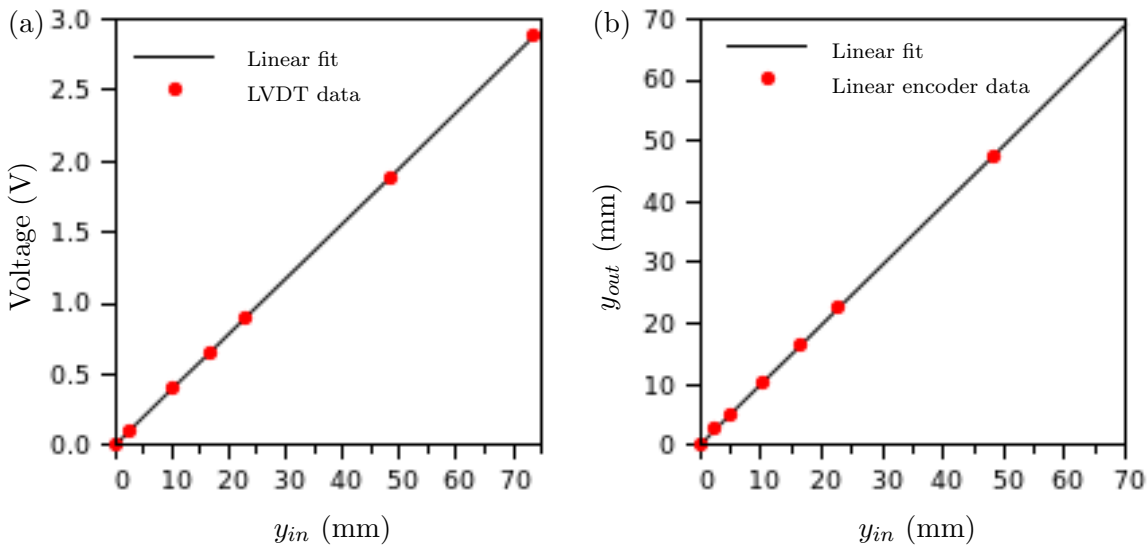


FIGURE 3.13: Examples of linear displacement measurement using (a) LVDT and (b) a linear optical encoder. Controlled displacement input (y_{in}) is achieved through high-precision gauge blocks.

was statically calibrated whilst installed on the air bearing. Figure 3.13(a) presents the differential voltage output from the LVDT as a function of core displacement. It shows the output voltage responded linearly with displacement. Using information obtained from static calibration tests, voltage measurements are converted to displacements that are then used to calculate the cylinder amplitude, frequency responses of the oscillating system.

Zhao (2012) provided a comprehensive report of the LVDT system used at the FLAIR water channel.

Response force and phases are also derived from the displacement measurements as direct force measurements using strain gauges and load cells had been unsuccessful due to the high electrical and mechanical noise of the stepper motor rotating the cylinder. Derived response forces and phases from displacement measurements taken with the LVDT are inaccurate as LVDT is also susceptible to

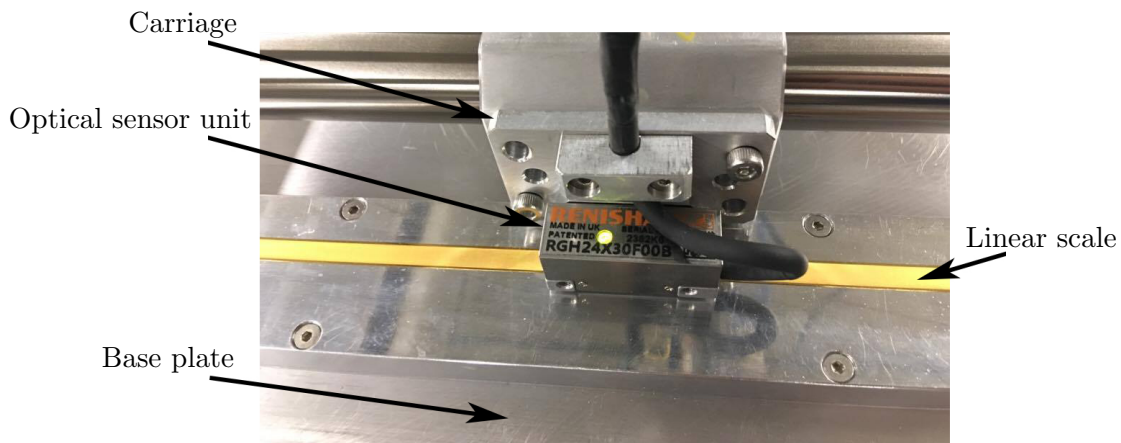


FIGURE 3.14: A photograph of the optical linear encoder used to measure the displacement of the cylinder.

electrical interferences beyond the control of the author. As a result of this, an optical linear encoder is used in place of the LVDT towards the end of the constant rotation study and for the entirety of the rotary oscillation study. The advantage of an optical linear encoder is similar to those of an optical rotary encoder (see §3.5.3). An optical linear encoder is robust; it is unsusceptible to temperature, moderate mechanic vibrations and electrical interferences. However, improper installation of the encoder system and exposure to dirt and dust can compromise the sensor's accuracy. An optical linear encoder comprises of a linear scale and an optical sensor unit. The linear scale is a strip containing alternating reference markers. The linear scale may be transparent depending on the design of the encoder. The optical sensor unit has a light source and a photo sensor. Depending on the design, light shone from the source is either transmitted through or reflected off the linear scale and received by the photo sensor. In application, the linear scale is typically attached to the stationary body while the sensor unit is installed to the moving body. As the sensor unit moves with the body, it shone light on the linear scale's markers and the photo sensor receives pulses of light. When the sensor receives light, it registers a high voltage. A low voltage is registered when the no light is received by the sensor. These high and low voltage registrations are counted and used to compute the physical linear displacement of body. The optical linear encoder's accuracy is limited by the sampling rate of the data acquisition system, and the scale of the reference markers of the linear scale. Due to its accuracy, relative robustness and very low signal noise digital output; displacement measurements taken using the optical linear encoder can produce accurate theoretical VIV force and phase responses.

In the present experiment, the linear scale is attached to the base plate of the air bearing rig and the optical sensor unit is installed onto the side of the moving carriage as shown in fig. 3.14. The optical linear encoder used was model RGH24X30F00B manufactured by Renishaw[®], UK, The linear scale is a gold plated metallic strip that has scale facets with a $20\ \mu\text{m}$ pitch. It was powered by a 5 V external DC power supply. The signal output was processed by a built-in VI program in LabVIEW[™]. Based on encoder specifications, LabVIEW[™] then records the voltage measurements and converts them into displacement in mm. Figure 3.13(b) shows the measured displacement output from the optical linear encoder as a function of input displacement. It shows the optical linear encoder output responded linearly with displacement Post processing analyses the displacement measurements and calculate relevant variables. Variables such as normalised amplitude response, normalised frequency response, theoretical force coefficients and the theoretical phase differences between the force coefficients and the displacement of the cylinder.

3.5.3 Rotary motion measurement

The rotational motion of the cylinder is a key component of the present study. To ensure the cylinder's motion is accurate it was measured by an optical incremental rotary encoder mounted on the rotation rig. An optical rotary encoder comprises of an optical disk and an optical sensor unit. Optical disks are typically constructed from glass or transparent plastic. On the disk are alternating transparent and non-transparent lines. The optical sensor unit has a light source and an optical sensor. Light shone from the source is either transmitted through or reflected off the optical disk and received by the optical sensor. In application, the optical disk is mechanically attached to the rotating component while the sensor unit is fixed. As the disk rotates through transparent and non-transparent lines, the sensor receives pulses of light. When the sensor receives light, it registers a high voltage. A low voltage is registered when the non-transparent line on the disk blocks the light from the sensor.

In the present experiment, the encoder disk was mounted on the shaft of the stepper motor and the sensor unit onto the upper section of the rotation rig. The optical encoder used was model E5-1000-250-IE-S-D manufactured by US Digital[®], USA. It has a 1000 line, 25.4 mm diameter optical disk. It was powered by a 5 V DC power supply from the digital terminal block on the DAQ connector blocks. The typical low and high voltage output of the encoder were 0.2 and 3.4 V, respectively. The signal output was processed by a built-in VI program in LabVIEW[™]. Based on encoder specifications, LabVIEW[™] then records the rotation measurements as revolution per second (rps) for constant rotation and degree angular displacement ($^{\circ}$) for rotary oscillation experiments. Post processing converted the rotary motion measurements into relevant non-dimensionalised variables such as rotation rate (α) for constant rotation studies; frequency ratio (f_{rot}^*) and velocity ratio (A_m) for rotary oscillation studies. Both encoder and motor controller were independently validated by manually measuring the time it took for a very large number of rotations or sinusoidal oscillations.

3.5.4 Flow visualisation: particle image velocimetry (PIV) system

Understanding the fluid structure in the near wake of a body is important because it contains qualitative and quantitative data on the fluid interaction with the body. In the present study, particle image velocimetry (PIV) was used to measure the vortex structure in the near wake of the oscillating cylinder. This technique has been used in many fluid mechanic studies in both wind tunnels and water channels since the early 1990s. It has a number of advantages over traditional flow visualisation methods such as dye, smoke and hydrogen bubble. Particle image velocimetry enables non-invasive, instantaneous, high-spatial resolution velocity field measurements of a region of interest. High-spatial resolution measurements allow the detection and identification of spatial fluid structures in the measurement window. Though post-processing, additional information such as the vorticity field, circulation and pressure distributions can be derived. Particle image velocimetry is extensively documented in Adrian (1991); Raffel *et al.* (2007), this section aims to provide a brief overview on the technique's fundamentals, laboratory equipment set up and post-processing methods.

The FLAIR water channel uses a double-image, single exposure PIV imaging system. Spatial cross-correlation, as documented in Fouras *et al.* (2008), was used to process the captured images.

The present PIV experiment and DAQ configuration is presented in fig. 3.6 and fig. 3.11. The water in the channel was seeded with small micro glass spheres, Vestosint[™] 2158, which were manufactured by Evonik Degussa GmbH. They have a nominal diameter of 21 μm and has a specific weight of 1.016 g/cm^3 . A pair of lasers were used to produce a laser sheet that illuminates the region of interest. The glass spheres traverse this laser sheet and will reflect its light. The pair of miniature pulsed lasers used were Minilite[™] II Q-Switched lasers manufactured by Continuum[®], CA, USA. They have a wavelength of 532 nm and a peak energy output of 25 mJ/pulse .

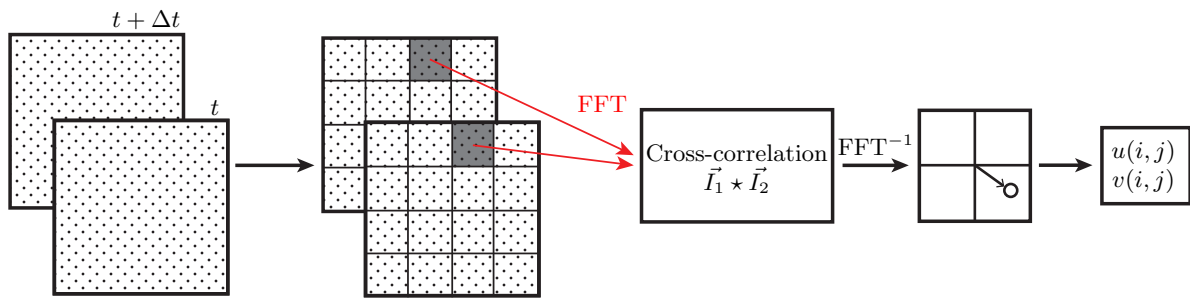


FIGURE 3.15: Analytical procedures to cross-correlate PIV images. Illustration reproduced from Zhao (2012).

A high resolution, high sensitivity camera capable of capturing double images with a single exposure captured the illuminated flow at specific timing and exposure settings. The current study used a pco.dimax S4 high speed CMOS camera manufactured by pco. AG. It has a maximum frame rate of 1279 monochrome frames per second at a maximum resolution of 2016×2016 px. The size of each pixel is $11 \times 11 \mu\text{m}$. Mounted on the camera is a 50 mm F-mount lens manufactured by Nikkor, Nikon Corporation, Japan. The photographic sampling frequency was controlled by a timing signal generator. It sends a trigger signal to the sequencer that then splits the single signal into a sequence of TTL signal outputs with controlled time separations to trigger the camera and lasers. The signal generator's TTL signal pulses were recorded simultaneously with the cylinder displacement signal from the LVDT, such that the position of the cylinder at the instances the image pairs were capture is known. This information enables phase average processing, which will be discussed in further detail later in the section. Both signal generator and sequencer were built in-house by the Department's Electronic Workshop. In a double-image, single exposure PIV system, the first TTL signal triggers the camera to open its shutter and initiate the single exposure. The second and third TTL signal triggers the lasers to illuminate the first and second images of each pair, respectively. The time separation (Δt) between the first and second image of each pair is determined using eq. 3.3. The free-stream velocity was varied to obtain the desired reduced velocity. Optimally, the spatial displacement (d_{opt}) between the sampling of the first and second image is sought to be constant for bluff body studies.

$$\Delta t = \frac{d_{\text{opt}}}{U_{\infty}} \quad (3.3)$$

PIV images were processed then analysed by in-house software by Fouras *et al.* (2008). The process is illustrated by fig. 3.15. Images in pairs were divided into a grid of $16 \times 16 \text{ px}^2$ interrogation windows. Fast Fourier Transform (FFT) was applied to the cross-correlation computation between two interrogation windows from the same image pair with a 50% window overlap. The average displacement ($\Delta x, \Delta y$) of all particles within the interrogation window was computed statistically by using the location of the peak value of the cross-correlation computation. Fouras & Soria (1998) showed, by using the least-square fitting of the Gaussian function, the peak value can be located with very high accuracy. an Inverse Fourier Transfer was then used to compute the displacement vectors in pixels. To convert the vector into physical dimensions, the correlation between the number of pixels in the images and the physical distance it represents within the focal plane of the images has to be determined. An optical calibration procedure, referred to as the 'ruler test', was used to find this relationship. By capturing photographs of an immersed ruler coplanar with the focal plane of the camera and laser sheet, a relationship between the number of pixels and the physical distance

within the images was found. This is the Magnification Factor κ and is given by

$$\kappa = \frac{\text{px}}{d_\kappa} \quad (3.4)$$

where d_κ is the distance measurement from the ruler in mm and px is the number of pixels over the same distance. Knowing both Δt and κ enables the conversion of displacement vectors in pixels to velocity vectors in mm/s as shown by

$$\Delta u = \frac{\Delta x}{\kappa t} \quad (3.5)$$

and

$$\Delta v = \frac{\Delta y}{\kappa t}, \quad (3.6)$$

where Δu and Δv are velocity vectors in the x and y directions, respectively.

Using this computation on all the interrogation windows in an image pair provided a complete velocity field. From a series of such velocity fields the computation of other fluid quantities and a visualisation of how spatial features develop in the wake could be determined.

An important kinematic property is fluid vorticity, which quantifies the rotation of the fluid. Mathematically vorticity is the curl of the flow velocity vector and is given by

$$\vec{\omega} = \nabla \times \vec{\mathbf{u}}, \quad (3.7)$$

where $\vec{\omega}$ is the three-dimensional vorticity vector field ($\vec{\omega}_i, \vec{\omega}_j, \vec{\omega}_k$) and $\vec{\mathbf{u}}$ is the three-dimensional velocity fields in $x - y - z$ Cartesian coordinates, respectively. In Cartesian coordinate, $\vec{\omega}$ in eq.3.7 is expanded into the following form

$$\vec{\omega} = \left(\frac{\partial w}{\partial y} - \frac{\partial v}{\partial z}\right)\vec{i} + \left(\frac{\partial u}{\partial w} - \frac{\partial z}{\partial x}\right)\vec{j} + \left(\frac{\partial v}{\partial x} - \frac{\partial u}{\partial y}\right)\vec{k}. \quad (3.8)$$

The focus of the current study is on the planar vorticity field in the wake of the cylinder that is perpendicular to the $x - y$ plane. The ‘right hand’ rule indicates the planar vorticity field of interest will be based on the z component of vorticity vectors ($\vec{\omega}_k$) and given by

$$\vec{\omega}_k = \frac{\partial v}{\partial x} - \frac{\partial u}{\partial y}. \quad (3.9)$$

The of PIV data can be evaluated statistically. The accuracy of $\vec{\omega}_k$ primarily depends on the spatial displacement (d_{opt}) between velocity points in the interrogation window of the same image pair and the accuracy of $\vec{\mathbf{u}}$ (Fouras & Soria 1998). By applying a second order polynomial fit to local $\vec{\mathbf{u}}$ components with analytic differentiation, Fouras & Soria (1998) showed the accuracy could be improved compared to other methods based on finite difference computation. In the current study, the PIV data processing method utilises a 21 point, second order polynomial fit developed by Fouras & Soria (1998). This method samples 21 neighbouring velocity points to compute the vorticity field.

Instantaneous velocity and vorticity fields contain information of spatial features at the instance the image pairs were captured. They result in smaller, chaotic spatial structures that are the result of smaller perturbations in the free stream flow and not significant vortex structures shed from the body. To better interpret the wake dynamics these small chaotic structures these can be removed by averaging the instantaneous fields. PIV velocity and vorticity fields are phase-averaged with two techniques, phase-locked and phase-band averaging. Phase-lock averaging requires images be captured at specific phases of over the cylinder’s oscillation cycle. This requires the body oscillation to be perfectly sinusoidal for easy implementation and control. The method is more suited for forced sinusoidal oscillation studies such as Carberry *et al.* (2001, 2005); Nazarinia *et al.* (2009).

Free vibration oscillations in VIV studies are never perfectly sinusoidal or periodic, making phase-lock averaging more difficult to implement compare to phase-band averaging. Phase-band averaging is easier to implement as it doesn't depend on capturing images at specific phases of controlled oscillations. The technique requires the recorded TTL triggering pulses and LVDT signal which provides the timing of the captured image pairs and a time history of the cylinder displacement, respectively. These two signals enable the processed contour images (*i.e.* the instantaneous velocity and vorticity fields) to be phase-band averaged based on the position and velocity of the cylinder. Figure 3.16 illustrates the phase-band averaging process. As discussed, the TTL trigger pulses are recorded with the body displacement LVDT signal as presented in fig.3.16(a). Figure 3.16(b) and (c) shows that by using the timing of the TTL trigger pulses, the processed contour images can be sorted into phase bands based on the displacement and velocity of the cylinder. Instantaneous images sorted in each bands were then combined to produce an averaged contour image. The comparison between instantaneous and phase-band averaged image of the same phase is presented in fig. 3.17. The phase-band averaged image shows clear spatial structures in the cylinder's wake.

While the phase-band averaging technique is easier to implement, the image capturing process and post-processing is more time consuming than in phase-lock averaging. Both techniques have some common disadvantages. Both require the cylinder oscillation and vortex shedding to be stable. Neither technique can be used when the cylinder oscillation and wake structures are highly chaotic. Therefore, the present PIV measurements were only taken when the cylinder displacement and frequency is highly periodic.

3.6 Experiment procedures

Damping in any oscillating mechanical system is caused by the dissipation of the excitation energy supplied to the system. Previous work has shown the system damping to have a pronounced effect on reducing the peak amplitude response of elastically-mounted bodies undergoing VIV Feng (1968); Khalak & Williamson (1997a); Govardhan & Williamson (2002). It is essential to quantify and maintain a consistent damping between experiments as it is a key variable in the body's governing equation of motion. The experimental apparatus used in the current study has several sources of damping. Fluid damping is the dissipation of energy due to the hydrodynamic forces by the fluids surrounding the body. Relative motion between mechanical components can cause the dissipation of energy through friction and impacts. These energy losses are caused by structural damping. Energy can be dissipated through material of components, *e.g.* flexing of components. This is the result of internal energy dissipation through material deformation. As the test cylinder and oscillating components are constructed from rigid material, primarily aluminium and steel, material damping is not a significant source of energy dissipation here. Due to this, the present study only considers the structural and fluid damping. To experimentally measure the combined structural damping of the oscillating structure, free decay measurements were taken.

3.6.1 Free decay measurement in air

Free decay measurements were used to determine the combined structural damping and natural frequency of the oscillating structure. This has previously been reported in Khalak & Williamson (1997a) and later by Zhao (2012). The current study is a single-DOF free vibration system with the cylinder motion restricted to the direction transverse to the free-stream flow. When this vibration system is placed in a vacuum with no external forces applied, the governing differential equation of motion can be expressed as

$$m\ddot{y} + c\dot{y} + ky = 0, \quad (3.10)$$

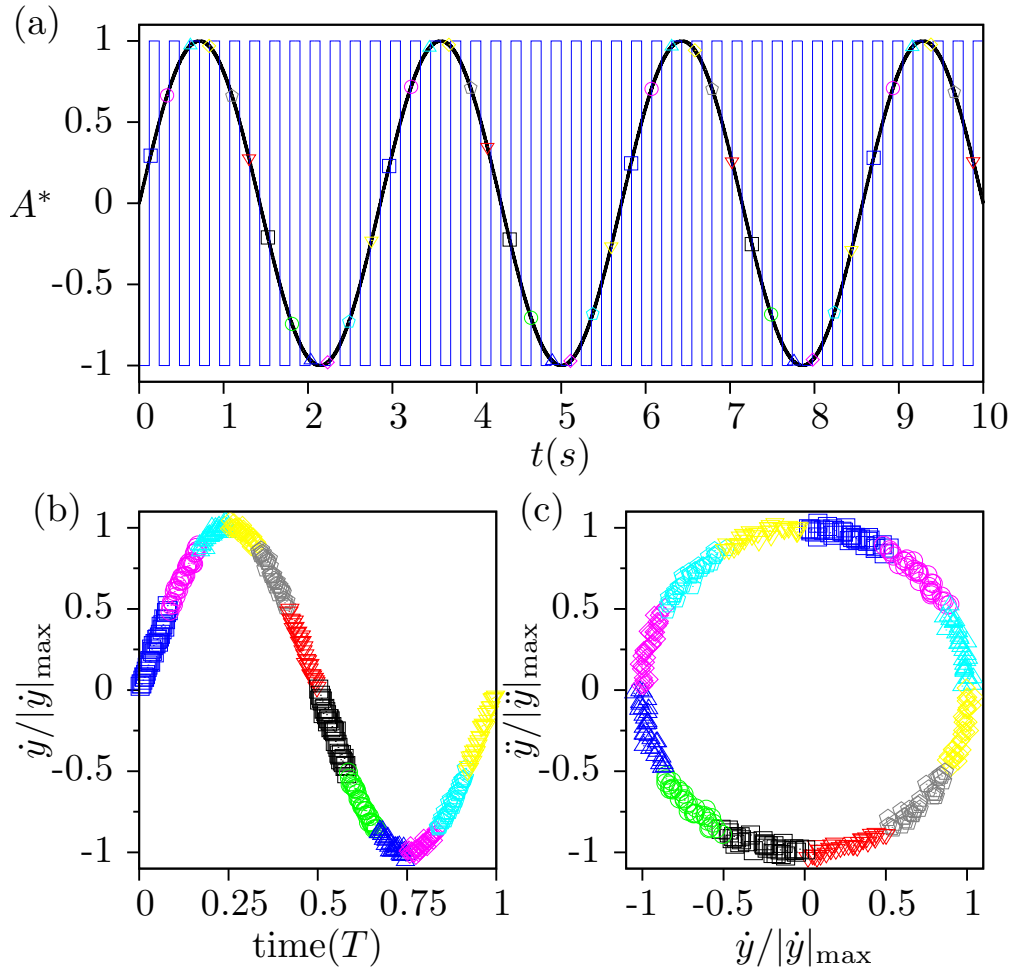


FIGURE 3.16: Phase-band technique used in averaging instantaneous PIV fields.

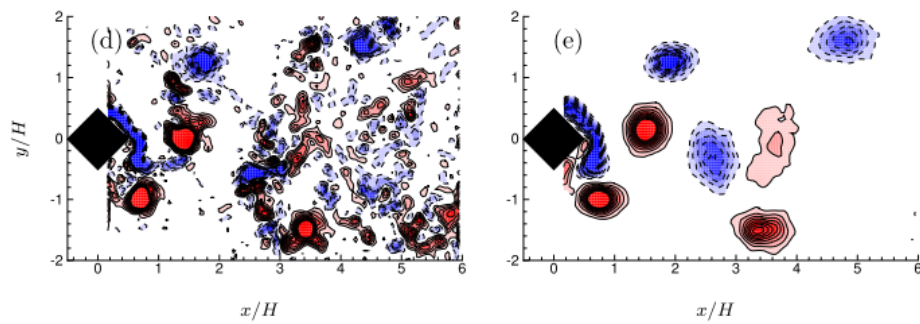


FIGURE 3.17: A comparison of PIV image processing methods. (a) an instantaneous image and (b) a phase-band averaged image produced from over 100 instantaneous images of the same bin. Figure taken from Zhao (2012).

where m is the mass of the oscillating system, c is the combined damping of the structure and k is the spring constant. This equation can be rearranged as

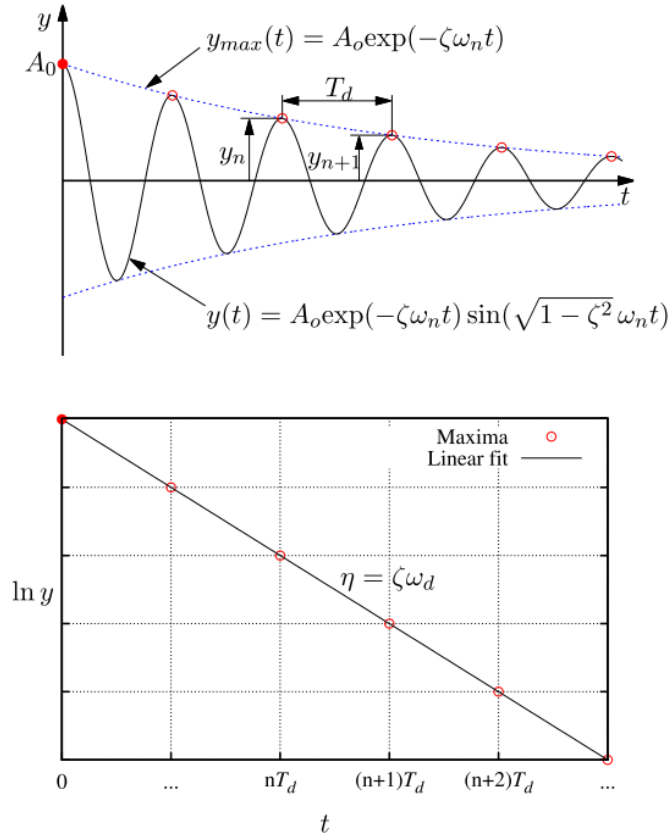


FIGURE 3.18: The response of an underdamped ($0 < \zeta < 1$) one-DOF system. Figure taken from Zhao (2012).

$$\ddot{y} + \zeta\omega_n\dot{y} + \omega_n^2y = 0, \quad (3.11)$$

where the damping ratio is given by $\zeta = c/(2\sqrt{km})$ and defined as the ratio between the combined structural damping and the critical damping; and the natural angular frequency of the system is given by $\omega_n = \sqrt{k/m}$.

Figure 3.18 illustrates an underdamped ($0 \leq \zeta < 1$) free decay system where the oscillating structure was given an initial displacement (A_0), released to freely oscillate and the damped motion of the oscillation recorded. The solution to eq. 3.11 for the underdamped system is given by

$$y(t) = A_0 e^{-\zeta\omega_n t} \sin(\sqrt{1 - \zeta^2}\omega_n t). \quad (3.12)$$

The maximum envelope to eq. 3.12 is given by

$$y_{\max}(t) = A_0 e^{-\zeta\omega_n t}. \quad (3.13)$$

The decay rate, defined as $\lambda = -\zeta\omega_n$, can be computed from the gradient of a plot of $\ln y_{\max}$ and time, t . The damping ratio is then computed from

$$\zeta = \frac{-\lambda}{\omega_n}. \quad (3.14)$$

The damped natural angular frequency (ω_d) can be approximated as the undamped natural angular frequency (ω_n) when the damping ratio is significantly less than unity ($\zeta \ll 1$). This is mathematically presented in eq. 3.15.

$$\zeta_d = \frac{2\pi}{T_d} = \omega_n \sqrt{1 - \zeta^2} \cong \omega_n. \quad (3.15)$$

The logarithmic decrement, which describes the ratio between any two consecutive amplitude peaks, is quantified by

$$\delta \triangleq \ln \frac{y_n}{y_{n+1}} = \zeta \omega_n T_d = \frac{2\pi\zeta}{\sqrt{1 - \zeta^2}} \cong 2\pi\zeta, \quad (3.16)$$

where $T_d = 2\pi/\omega_n$ is the damped oscillation period. The approximation in eq.3.15 enabled the decay rate to be written as

$$\lambda = -\zeta\omega_d = -2\pi\zeta f_d, \quad (3.17)$$

where f_d is the damped natural frequency and it is defined by

$$f_d = \frac{\omega_d}{2\pi} \cong \frac{\omega_n}{2\pi} = \frac{1}{2\pi} \sqrt{\frac{k}{m}}. \quad (3.18)$$

As the free decay measurements were taken in air and not vacuum, the effects of air resistance on the moving structure must be minimised. This was done by removing the test cylinder and replacing its mass for an equal concentrated mass attached to the air bearing rig carriage. As the oscillation system is lightly damped, the natural frequency in air (f_{na}) is assumed to equal to the natural frequency in vacuum (f_d), therefore the natural frequency of the system in air can be expressed as

$$f_{na} \cong \frac{1}{2\pi} \sqrt{\frac{k}{m}} = f_d. \quad (3.19)$$

The structural damping ratio measured in air (ζ_a) is can also be assumed to be equal to the structural damping ratio in vacuum (ζ) and the relationship is expressed as

$$\zeta_a = \frac{c}{2\sqrt{km}} \cong \zeta. \quad (3.20)$$

3.6.2 Free decay measurement in stationary water

To take into consideration the effects of added mass, the natural frequency and structural damping ratio of the oscillating structure was measured in stationary water with a free decay. Blevins (1990); Fredsoe & Sumer (1997) reported the mathematical details of free decay measurements in stationary water. In these free decay measurements, the vibration of the structure is damped by structural damping from mechanical components and also fluid damping from the viscous fluid surrounding the test cylinder. Blevins (1990) described fluid damping as the result of flow separation and viscous shearing of fluid adjacent to the surface of the oscillating structure. Fredsoe & Sumer (1997) further explained that the oscillating structure is subjected to the Morison force, which is a hydrodynamic force (F_y) mathematically described as

$$F_y = -\frac{1}{2}\rho C_D D L |\dot{y}| \dot{y} - m_A \ddot{y}, \quad (3.21)$$

where m_A is the added mass. The added mass is given by

$$m_A = C_A m_{fd}, \quad (3.22)$$

where C_A is the potential added mass coefficient ($C_A = 1$ for circular cylinder) and m_{fd} is the mass of water displaced by the immersed length of the cylinder.

In stationary water, the undamped natural angular frequency (ω_{nw}) is expressed as

$$\omega_{nw} = \sqrt{\frac{k}{m + m_A}} \quad (3.23)$$

where k is the structural stiffness and m is the mass of the oscillating system. Similar to the approximation made to free decay tests in air; the damped natural angular frequency is approximated as the undamped natural angular frequency because the total damping (ζ_d) typically measured in experiments are significantly less than unity ($\zeta_d \ll 1$).

This approximation enabled the computation of the natural frequency in water (f_{nw}) which is given by

$$f_{nw} = \frac{\omega_{nw}}{2\pi} = \frac{1}{2\pi} \sqrt{\frac{k}{m + m_A}}. \quad (3.24)$$

where k is the structural stiffness and m is the mass of the oscillating system.

From this, the structural damping ratio with added mass effect, ζ_{sw} , can be expressed as

$$\zeta_{sw} = \frac{f_{nw}}{f_{na}} \zeta_a. \quad (3.25)$$

The term structural damping ratio, ζ , is commonly used in FIV research. From this section, it is clear that there are a number of damping ratios that ζ may represent and that term lacked specificity. This often confuses readers as they question the true definition behind the term. The research group led by Prof. C.H.K Williamson at Cornell University and the FLAIR group at Monash University have consistently used the term, ‘structural damping ratio ζ ’, to represent the structural damping ratio with added mass effects ζ_{sw} ; *i.e.*

$$\zeta = \zeta_{sw}. \quad (3.26)$$

Therefore, any reports of structural damping ratio ζ in subsequent sections of the thesis refers to ζ_{sw} .

3.7 Chapter summary

This chapter have shown the details of the FLAIR water channel facility used to conduct the proposed experimental studies. An air bearing rig was used to achieve free oscillations in the cross-flow direction. A rotation rig is used to control the rotary motion of the cylinder. The LVDT and optical linear encoder responses linearly with cross-flow displacement. The optical rotary encoder tracks the rotary motion of the cylinder. A PIV system is used to study the flow structure in the near wake of the cylinder. Free decay tests in both air and water were used to quantify the structural properties of the oscillation system. This chapter have shown and validated the experimental apparatus and data acquisition methods used for both the study of an elastically-mounted cylinder undergoing constant rate rotation and sinusoidally-driven rotary oscillations.

Chapter 4

Flow-induced vibration of a rotating cylinder

This chapter presents results for an elastically-mounted cylinder undergoing VIV subject to constant-rate rotation about the cylinder axis. While there have been both experimental and numerical studies of this problem at low Reynolds numbers previously, to the knowledge of the author, this is the first time that the comprehensive VIV response has been recorded at Reynolds numbers sufficiently large where the behaviour is less sensitive to variations in Reynolds number.

To begin, the experimental set up is presented in §4.1.1. Section 4.1.2 presents validation studies to characterise the VIV response of the experimental apparatus used and to validate against relevant previous studies. Validation work on the rotary motion profile is included in Appendix A. The time-averaged displacement of the cylinder is then presented, prior to the observed vibration (amplitude and frequency) response in §4.2. Next, the response is examined at a several selected rotation rates over the reduced-velocity range tested (U^*). Following this, the changes caused by different rotation rates (α) are investigated in detail. The different wake states associated with the changes to the vibration response are presented in §4.3, which leads into an examination of the intermittent wake behaviour observed in the upper response branch in §4.3.1. Finally, section 4.4 presents a comparison in lift force and phases between a non-rotating and rotating cylinder. A summary of the key findings of this chapter is provided to conclude (§4.4.1).

The contents of this chapter have been accepted for publication in the *Journal of Fluid Mechanics*.

4.1 Experiment details and validation

4.1.1 Experimental details

The experiments were conducted in the FLAIR water channel. A specially designed and constructed rotation rig was used to control the rotational motion of the cylinder and an air-bearing system was used to enable low-friction cross-flow oscillations. Details of the experimental apparatus and data acquisition have been discussed in §3.

Critical characteristics of the oscillating system (i.e. the spring constant and damping coefficient) were measured through free-decay tests conducted before and after experiments. For this set of experiments, the cylinder model employed had a diameter of $D = 30$ mm and an immersed length of $l_{ms} = 614$ mm (i.e. approximately $20D$). The total mass of all oscillating components was $m_{osc} = 2.5036$ kg and the mass ratio was $m^* = 5.78$. From free-decay tests, the natural frequency of the oscillating system in water was determined to be $f_{nw} = 0.656$ Hz, and in air as $f_{na} = 0.706$ Hz. Structural stiffness is provided by one pair of springs with an equivalent stiffness of $k = 0.0493$ N/mm. The decay tests allowed the damping ratio to be determined, giving $\zeta = 0.0041$.

This experimental study covers the reduced velocity range $U^* = 2.5 - 14$, equivalent to the Reynolds numbers range of ($1100 \lesssim Re \lesssim 6300$). At each tested U^* , the cylinder was prescribed rotation rates increasing in value and in range of ($0 \lesssim \alpha \lesssim 4$).

4.1.2 Related validation

Before studying the response and wake structure of an elastically-mounted cylinder undergoing constant-rate rotation, it was essential to understand the dynamic response of the air-bearing system with a non-rotating cylinder and to validate the rotary motion of the cylinder. As the air-bearing system was used in previous work (see Zhao *et al.* (2012); Zhao (2012); Nemes *et al.* (2012); Zhao *et al.* (2014a)); the main focus of this section is to present baseline measurements of the dynamic response of a non-rotating cylinder. This provides evidence for the correct operation of the air-bearing system and provides VIV data for a non-rotating cylinder for subsequent comparison with that of a rotating cylinder.

The vibration response of a *non-rotating* circular cylinder undergoing VIV is compared against previous work by Khalak & Williamson (1997a, 1999), and Zhao *et al.* (2014b) in figure 4.1. Figure 4.1(a) presents the amplitude response as a function of reduced velocity, showing that the current experimental configuration produces non-rotating VIV results in good agreement with previous VIV studies. Here, it is important to note the effect of the mass ratio that reduces the peak response, and which is necessarily higher here than for the comparison studies because of the added weight arising from the motor assembly. At the lowest m^* achievable ($m^* = 5.78$), the three VIV amplitude response branches characteristic of a non-rotating cylinder are clearly seen. The *initial branch* exists for $U^* < 4.8$. For $m^* = 5.78$, the *upper branch* covers the range $U^* = 4.8 - 6.4$; the *lower response branch* lies within the range $6.4 \leq U^* \leq 9.5$, and the *desynchronized region* exists for $U^* > 9.5$. Previous studies by Khalak & Williamson (1997a); Zhao *et al.* (2014b) at $m^* = 2.4$ showed a peak amplitude response of $A^* \approx 0.95$. The mean of the highest 10% of amplitude peaks (A_{10}^*) of the current system is $A_{10}^* = 0.82$. This agrees with previous studies on the effects of mass and damping. As the mass and damping ratios are increased, the magnitude of the amplitude response decreases and the range of U^* over which the system self-excites reduces (Feng 1968). A hysteretic transition between the initial and upper branch occurs at $U^* \approx 4.8$ and is accompanied by a jump in A_{10}^* from 0.25 to 0.79. The transition from the upper to the lower branch causes a reduction in A_{10}^* from 0.78 to 0.55, and the desynchronization of the system at $U^* \approx 9.5$ is accompanied by another drop in A_{10}^* from 0.54 to ~ 0.07 . This comparison with results from previous literature shows that the current air-bearing system reproduces an amplitude response variation consistent with previous careful studies.

Figure 4.1(b) presents a power spectra density (PSD) contour plot of the normalised amplitude response (A^*) as a function of f^* and U^* . This consists of individual vertically aligned greyscale-coded power spectra density for each U^* stacked together horizontally to show the frequency response of the system, with darker regions representing frequencies of higher power. The narrowness/broadness of the spectral peaks is also clear from the colour gradation. The variation of the shedding frequency ratio (f_{sh}/f) with U^* is plotted as a dot-dashed line in figure 4.1(b) to highlight U^* regions where $f \approx f_{sh}$. To highlight U^* ranges where f locks to f_{nw} (i.e. $f \approx f_{nw}$), the $f^* = 1$ curve is shown as a dotted line in figure 4.1(b). The body's frequency response (f) follows the shedding frequency ($f \approx f_{sh}$) until the end of the initial amplitude response branch, where it begins to bend towards f_{nw} and subsequently lock-in to it ($f \approx f_{nw}$). The frequency response remains synchronised throughout the upper and lower amplitude response branches until the desynchronized region is reached. At that point, the body frequency response deviates from f_{nw} , returning to follow f_{sh} , although there is still a broad spectral peak close to the natural shedding frequency. For the current experiment, the mean Strouhal number, defined by $St = f_{sh}D/U_\infty$, was measured as $St \approx 0.215$ for the Re range investigated; this agrees with the known St value in the same Re range.

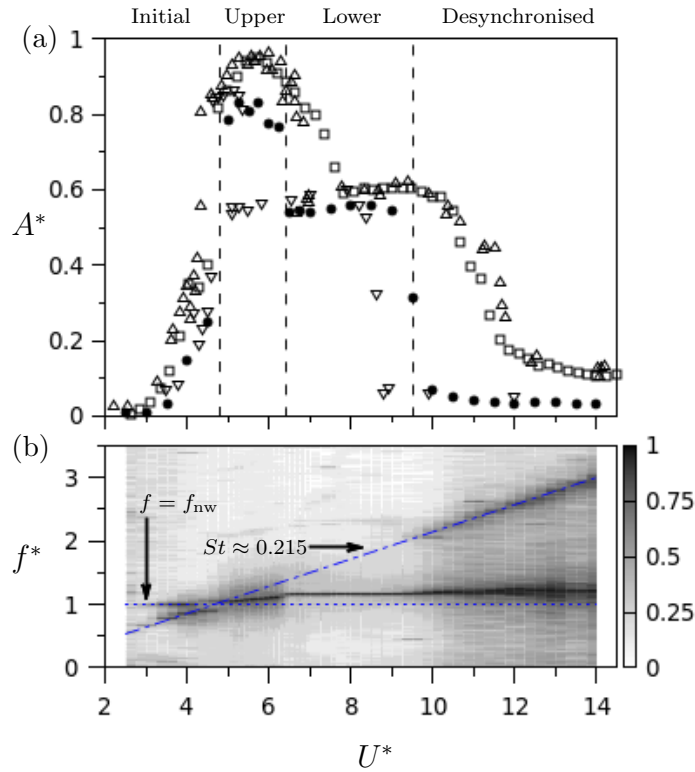


FIGURE 4.1: Vibration response of a non-rotating circular cylinder undergoing VIV. (a) is the normalised amplitude response (A^*) as a function of reduced velocity (U^*). ●, represents the mean of the highest 10% of oscillation amplitude (A_{10}^*) in the present study with $m^* = 5.78$ & $\zeta = 0.0041$; □, represents results from Zhao *et al.* (2014b) with $m^* = 2.4$ & $\zeta = 0.00243$; △, represents results from Khalak & Williamson (1997a) with $m^* = 2.4$ & $\zeta = 0.0045$; ▽, represent results from Khalak & Williamson (1999) with $m^* = 10.3$ and $\zeta = 0.00165$. The vertical dashed lines represent the boundaries of branches for the present study. (b) is a power spectra density (PSD) contour map of A^* as a function of normalised frequency response (f^*) and U^* . Essentially normalised power spectra are assembled together horizontally to construct this map. Note that the PSD is normalised by the peak value at each U^* .

4.2 Vibration response

In this section, the time-averaged displacement, \bar{y} , of the rotating cylinder from its non-rotating neutral position is first discussed. Observations in the cylinder's vibration response (i.e. the oscillation amplitude and frequency response) as reduced velocity (U^*) and rotation rate (α) are varied will follow.

In the present investigation, the observed body oscillations are typically periodic, although there are some variations in the waveform from one cycle to another. An uneven mean pressure distribution about the centreplane is generated when a cylindrical body, such as a circular cylinder, is rotated about its spanwise axis in a viscous fluid. This unsymmetric distribution of the mean pressure is caused by the body rotation, causing fluid to accelerate on the leeward side and decelerate with flow separation on the windward side of the body. As discussed in §2.4, this is generally known as the *Magnus effect*. Over the past century this effect has been extensively studied by a number of researchers (e.g. Prandtl & Tietjens (1934); Coutanceau & Menard (1985); Badr *et al.* (1990); Kang *et al.* (1999); He *et al.* (2000); Stojković *et al.* (2002); Mittal & Kumar (2003); Rao *et al.* (2013)). Due to the unsymmetric mean pressure distribution acting on the cylinder, a net force is generated in the cross-flow direction. The magnitude of this net lift force increases with rotation rate. It is,

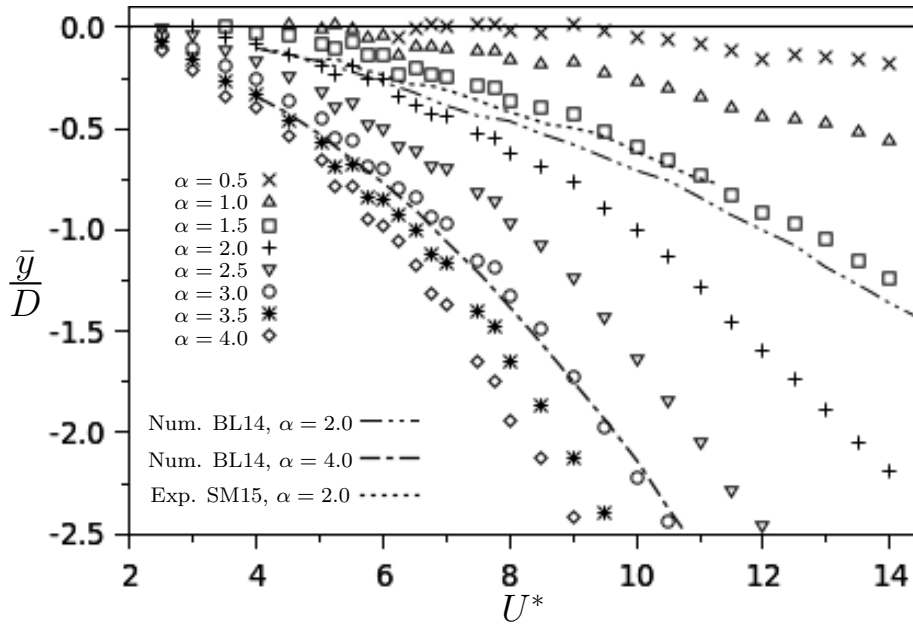


FIGURE 4.2: The time-averaged displacement of the cylinder (\bar{y}) as a function of reduced velocity (U^*) at different rotation rates (α). Numerical prediction results from Bourguet & Lo Jacono (2014) (abbreviated as BL14 in figure) for Reynolds number $Re = 100$ at rotation rates $\alpha = 2.0$ and 4.0 are shown by the dashed and solid lines, respectively. The dot-dashed line shows experimental results of Seyed-Aghazadeh & Modarres-Sadeghi (2015) (abbreviated as SM15 in figure) at $Re = 350 - 1000$ at $\alpha = 2.0$ for comparison.

therefore, expected that at any reduced velocity, an increase in the rate of rotation will cause a corresponding increase in \bar{y} .

Figure 4.2 presents the time-averaged displacement as a function of reduced velocity at several different rotation rates. As expected, the data shows that the time-averaged displacement increases with rotation rate due to an increase in the mean lift. This general observation is in good agreement with the low Reynolds number ($Re = 100$) rotating VIV simulations of Bourguet & Lo Jacono (2014), although the offsets in position in the current experiment are larger than those observed in their numerical work. In fig. 4.2, the numerically predicted displacements for rotation rates $\alpha = 2.0$ (dashed) and $\alpha = 4.0$ (solid) from Bourguet & Lo Jacono (2014) are overlaid for comparison. The experimentally determined \bar{y} at rotation rate $\alpha = 2.0$ from Seyed-Aghazadeh & Modarres-Sadeghi (2015) is also overlaid (dot-dashed line). It is evident that the measurements from Seyed-Aghazadeh & Modarres-Sadeghi (2015) are closer to the numerical results of Bourguet & Lo Jacono (2014) than those from the present study. The general agreement between their results is perhaps attributable to the comparatively low Reynolds numbers of their studies ($Re = 100$ for Bourguet & Lo Jacono (2014) and $Re = 350 - 1000$ for Seyed-Aghazadeh & Modarres-Sadeghi (2015)). In contrast, the Reynolds number of the present study increases from $Re \approx 1000$ at the lowest reduced velocity examined.

To further document the dynamic response of the cylinder, the oscillatory component of its motion is characterised in figures 4.3 and 4.4. The vibration response as a function of reduced velocity is presented in figure 4.3. In figure 4.3(a), the means of the highest 10% of normalised amplitude response peaks (A_{10}^*) about their time-averaged positions are presented as a function of reduced velocity at several rotation rates. To help clarify the overall behaviour of the cylinder response with body rotation, the amplitude response for a number of selected cases ($\alpha = 0, 1.0, 2.0,$ and 3.0) have been highlighted with dashed lines. This figure reveals that large amplitude oscillations exist over

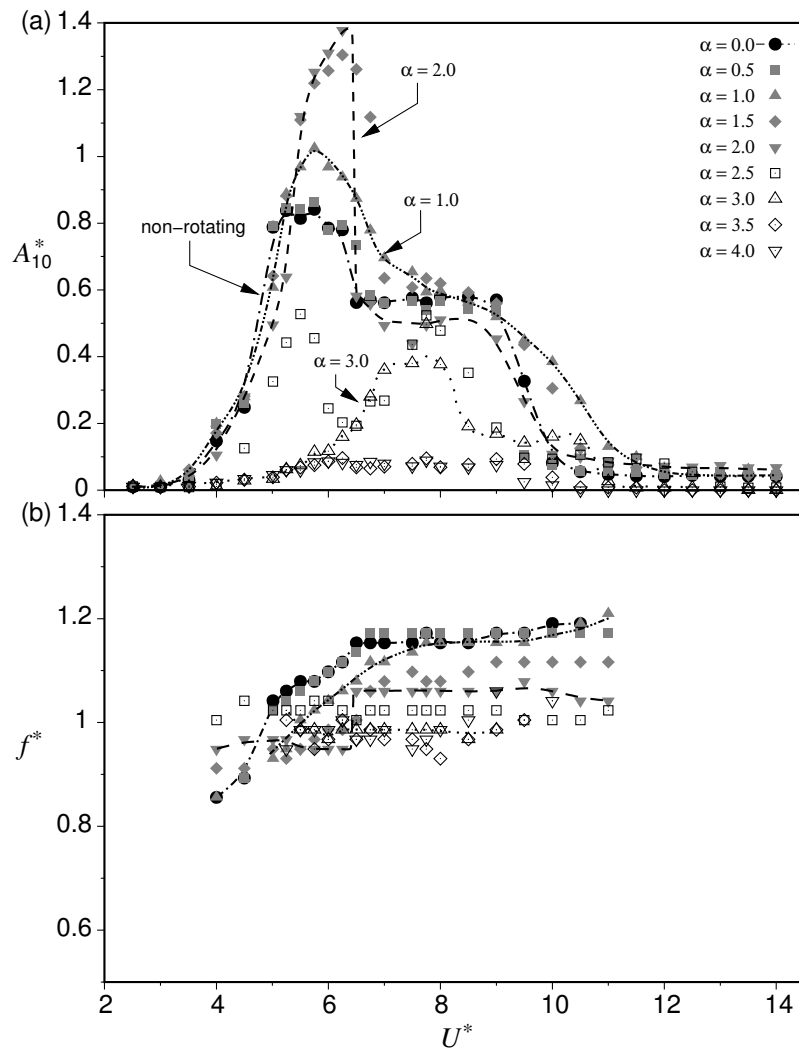


FIGURE 4.3: The vibration response of an elastically-mounted circular cylinder undergoing constant rotation as a function of reduced velocity (U^*) at different rotation rates (α). (a): the means of the highest 10% of normalised amplitude response peaks (A_{10}^*) about their time-averaged positions (\bar{y}), (b): the normalised frequency response (f^*). Approximate fits to rotation cases $\alpha = 0, 1.0, 2.0,$ and 3.0 are shown by the labelled dashed lines.

broad ranges of reduced velocity and rotation rate. The peak amplitude (over U^*) first increases as the rotation rate is increased from $\alpha = 0$. This is evident as the amplitude response increased from $A_{10}^* \approx 0.8$ for the non-rotating cylinder to $A_{10}^* \approx 1.4$ for a cylinder at rotation rate $\alpha = 2.0$. However, increasing the rotation rate beyond $\alpha = 2.0$ results in the peak response decreasing. The peak response decreased to $A_{10}^* \approx 0.1$, for the highest rotation rate investigated of $\alpha = 4.0$.

Despite changes in magnitude, the overall shapes of the amplitude responses for rotation rates $\alpha \leq 2.0$ are comparable to those for the non-rotating cylinder. While there are modifications due to the effects of rotation, the typical three-branch (i.e. the initial, upper and lower branches) amplitude response associated with a low mass-damping system can be clearly identified. At low rotation rates $0 < \alpha \leq 1.5$, an increase in α : increases the peak amplitude response; increases the width of the range of U^* over which body excitation occurs; and makes the transitions between the upper and lower branch and the desynchronization distorted and less distinct. For a cylinder rotating between

$1.5 < \alpha \leq 2.0$, the peak amplitude increases to higher values than those observed at lower rotation rates ($0 < \alpha \leq 1.5$). The range of U^* at which body excitation occurs is comparable to the non-rotation case but the transition between the upper and lower response branches is abrupt. Up to a rotation rate of $\alpha \approx 2.0$, it can be observed that there is an increase in the reduced velocity range corresponding to the increase in the amplitude peak with rotation rate; furthermore, there is a tendency for the amplitude peak to shift to a higher U^* with increased α . In the range of rotation rate $2 < U^* \leq 3$, there are significant reductions in the amplitude response at any U^* , and the shape of the response curve no longer resembles that of a non-rotating cylinder undergoing VIV. Within this range of rotation rate, the typical two- or three-branch response is replaced with a dual-peak response curve at $\alpha = 2.5$, and a smaller, single peak response at $\alpha = 3.0$. In addition to the changes in the shape of the response curve, the range of reduced velocities at which excitation occurs becomes narrower. When the cylinder is rotating at rates $\alpha > 3$, body excitation is minimal.

Figure 4.3(b) presents the normalised frequency response, f^* , about its time-averaged position, \bar{y} , as a function of U^* and α . Similar to the amplitude response curves, the frequency variations are compared for the non-rotating and rotation cases, with the curves for $\alpha = 1.0, 2.0$ and 3.0 again highlighted by dashes lines. The frequency variation for the non-rotating case from the present study is in good agreement with previous non-rotating VIV research. As wake-body synchronisation occurs, the frequency response of the cylinder becomes close to the natural frequency of the oscillating structure in water, f_{nw} , ($f^* = 1$ in figure 4.3(b)); when reduced velocity is increased within the lock-in region, the frequency response departs from f_{nw} . For a rotating cylinder, the frequency response broadly follows the non-rotating VIV case; as α increases the frequency response globally decreases. This finding is in excellent agreement with the simulations of Bourguet & Lo Jacono (2014) and experiments of Seyed-Aghazadeh & Modarres-Sadeghi (2015).

An investigation into the vibration response of the cylinder at fixed rotation rate increments can better show the influence of body rotation on the vibration response, and how each α increment compares to the non-rotating case over the range of tested reduced velocities. The normalised vibration response about its time-averaged position at several reduced velocities of interest were selected and are presented as a function of rotation rate in figure 4.4. These reduced velocity cases were selected based on how each represents the vibration response at comparable U^* , and how well these cases show the progression of the response with increasing rotation rate.

Figure 4.4(a.i) shows the amplitude response (A_{10}^*) response variation about its time-averaged position (\bar{y}) as a function of α at $U^* = 4.00$. At this reduced velocity, the effect of rotation rate on the amplitude response is minimal. The maximum amplitude registered is $A_{10}^* \approx 0.2$ or less over the entire range of rotation rate. Above a rotation rate of $\alpha \approx 2.3$, the cylinder's amplitude response decreases to near zero. Figure 4.4(a.ii) presents the corresponding normalised frequency response as a function of rotation rate at $U^* = 4.00$. As the rotation rate is increased, the frequency of the cylinder converges towards the natural frequency of the oscillating structure in water with an associated decrease in amplitude response. These trends are observed through the initial branch and at the beginning of the upper branch.

As the reduced velocity was increased to the value at which the peak upper branch response occurred for a non-rotating cylinder ($U^* = 6.25$), figure 4.4(b.i) and figure 4.4(b.ii) show that the amplitude response increases significantly up to a rotation rate of $\alpha \approx 2.0$ and A_{10}^* abruptly decreases thereafter. This is highlighted by the vertical dashed line in figure 4.4(b.i). In the current study, the highest A_{10}^* amplitude, globally, was observed at a reduced velocity of $U^* = 6.25$. The amplitude increased from $A_{10}^* = 0.79$ for a non-rotating cylinder to the global peak of $A_{10}^* = 1.39$ at $\alpha = 2.0$. On further increases in rotation rate, the amplitude abruptly drops to $A_{10}^* \approx 0.3$ at $\alpha \approx 2.3$. On increasing rotation rate, the frequency response decreases towards f_{nw} . A small jump in the frequency response is observed. Highlighted by the vertical dashed line in figure 4.4(b.ii), there is small jump in the frequency response which accompanies the abrupt drop in amplitude. As rotation

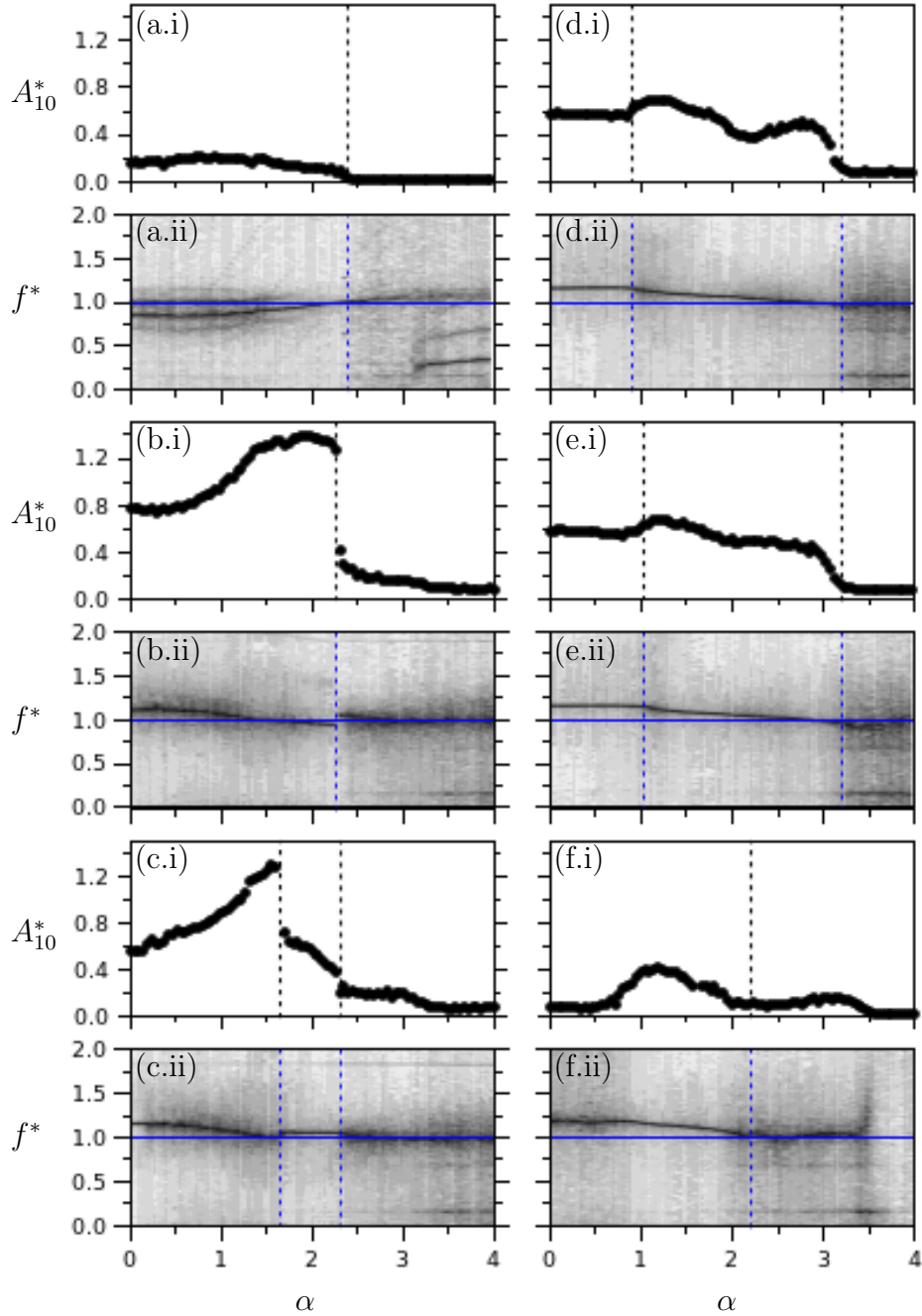


FIGURE 4.4: The vibration response of an elastically-mounted circular cylinder undergoing constant rotation as a function of rotation rate (α) at selected reduced velocities (U^*). (a) at $U^* = 4.00$, (b) at $U^* = 6.25$, (c) at $U^* = 6.50$, (d) at $U^* = 7.50$, (e) at $U^* = 8.00$ and (f) at $U^* = 10.00$. In each reduced velocity case, figure (i) is the means of the highest 10% of normalised amplitude response peaks (A_{10}^*) about their time-averaged positions (\bar{y}); figure (ii) is the power spectra density contour of the normalised frequency response (f^*) normalised by the peak power. The horizontal dashed line in figure (ii) indicates $f^* = 1$ or ($f = f_{nw}$). The vertical dash lines highlight features of interest discussed in the text.

rate is increased from $\alpha = 0$, the oscillation frequency, f , initially converges towards the natural frequency of the oscillating structure in water, f_{nw} ; the body oscillation locks-in to f_{nw} , resulting in

an increase in amplitude response. As the rotation rate is increased above $\alpha \approx 2.25$, the wake mode changes and the body oscillation frequency is no longer locked-in with the natural frequency of the oscillating structure. Details of wake modes and flow structures will be discussed in §4.3.

As the U^* is increased to the onset of the lower amplitude response branch from $U^* = 6.5$, an increase in amplitude response is observed, albeit it is less pronounced than for the $U^* = 6.25$ case. Figure 4.4(c.i) shows that with an increase in rotation rate the amplitude response does drop following the peak. However, in this case the abrupt drop takes place at a lower rotation rate of $\alpha \approx 1.7$ and is followed by a plateau between the peak and the lower amplitude regions at higher α . Within the range of rotation rates where the amplitude plateau exists, the cylinder oscillation frequency locks-in to the natural frequency of the oscillating structure in water, (i.e. $f \approx f_{nw}$). The frequency response of the cylinder becomes similar to that seen in the upper branch case as the rotation rate is increased above a rotation rate of $\alpha \approx 2.25$ (second vertical dotted line in figure 4.4(c.ii)). At rotation rates above $\alpha \approx 2.25$, the frequency response in both the upper ($U^* = 6.25$) and lower ($U^* = 6.50$) amplitude response branch cases begin at values slightly above $f^* = 1$; as α is increased f^* gradually decreases to below $f^* = 1$.

When the reduced velocity is increased to a value at which is approaching the *centre* of the lower amplitude response branch for a non-rotating cylinder ($U^* = 7.50$); the vibration response observed is different to that seen at the beginning of the lower branch at $U^* = 6.5$. Figure 4.4(d.i) shows that the amplitude response is characterised by two peaks, with the second peak appearing at a higher rotation rate than the peaks seen at lower reduced velocities. The cylinder is unresponsive to the effects of rotation as evidenced by the stable amplitude response up to rotation rates of $\alpha \approx 0.8$ (as highlighted by the vertical dashed line in figure 4.4(d.i)). As the rotation rate is increased to within the proximity of $\alpha \approx 2.75$, a second amplitude peak appears. Similar to that of the amplitude response, the frequency exhibits minimal effects of rotation up to $\alpha \approx 0.8$. When the rotation rate is increased above $\alpha \approx 0.8$, there is a corresponding reduction in the frequency response down to and then below $f^* = 1$ ($f = f_{nw}$). The location at which the second amplitude peak occurs and the rotation rate at which f decreases past f_{nw} suggests that the appearance of the second peak is the result of f approaching f_{nw} . There are similar observations at higher reduced velocities, such as $U^* = 8.0$; however, the second amplitude peak becomes less distinct.

In the desynchronized region ($U^* = 10.0$), the vibration response trends are similar to those observed in the lower amplitude response branch, as exhibited in figures 4.4(f.i) and 4.4(f.ii). However, the magnitude of the amplitude response is significantly lower than those seen in the lower branch. Figure 4.4(a.i) shows that body rotation does not appear to have a significant impact on the amplitude response of the body at relatively low reduced velocities, i.e. U^* lies in the initial branch. However, there is an unexpected response in the desynchronized region. As the rotation rate is increased, the amplitude increases from $A_{10}^* \approx 0.1$ to a peak value of $A_{10}^* \approx 0.5$. This frequency response feature is comparable to those seen in the lower branch cases, where the location of the first amplitude peak coincides with the rotation rate value at which f begins to converge towards f_{nw} .

It is of interest to see how do the present results compare to previous numerical and experimental work at different Re , mass and damping ratios. Presented in figure 4.5(a) is a comparison of the normalised amplitude response (A^*) at a rotation rate of $\alpha = 2.0$ with previous studies. Seyed-Aghazadeh & Modarres-Sadeghi (2015) performed their experimental study using a water channel and presented their data on a rotating cylinder undergoing VIV in the form of an amplitude response contour map. The amplitude response curve presented in figure 4.5(a) was extracted from their contour plot. In their experiment, the Reynolds number covered the range $350 \leq Re < 1000$. The maximum amplitude response reported occurred at a reduced velocity of $U^* = 6.5$ corresponding to a Reynolds number of $Re \simeq 600$. The results from the low Reynolds number ($Re = 100$) simulation by Bourguet & Lo Jacono (2014) at the same α is also presented in figure 4.5(a). At a rotation

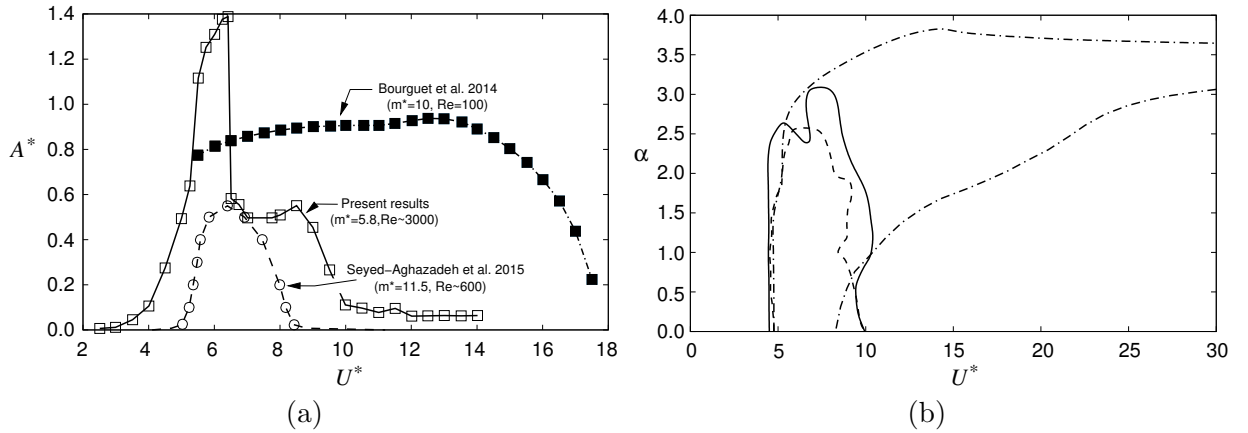


FIGURE 4.5: (a) Comparison of the normalised amplitude response (A^*) of the present study against previous numerical and experimental work at a rotation rate of $\alpha = 2.0$ and as a function of reduced velocity (U^*). Note in particular, the significantly higher amplitude response in the present experiment. (b) presents an approximate boundaries of vibration regions as a function of U^* and α .

rate of $\alpha = 2$, Seyed-Aghazadeh & Modarres-Sadeghi (2015) reported a peak amplitude response of $A^* \simeq 0.6D$. The global peak amplitude in their study occurred at a slightly higher rotation rate of $\alpha \simeq 2.3$; however, their global peak value is only marginally higher than the local peak value reported in the $\alpha = 2$ case shown in fig. 4.5(a). Conversely, Bourguet & Lo Jacono (2014) reported, in their low Re numerical study, that a large amplitude response persists and continues to increase with rotation rate up to $\alpha = 4$, beyond which the amplitude response becomes minimal.

It is also evident that Bourguet & Lo Jacono (2014) observed a significant vibration response over a considerably wider range of reduced velocities than the experimental study of Seyed-Aghazadeh & Modarres-Sadeghi (2015) and also in the present thesis. It seems probable that the observed variations in amplitude response are the result of the significant differences in Reynolds number (the current experiment being at significantly higher Re of $Re \simeq 3000$ at $U^* = 6.5$), rather than the effects of mass and damping. Despite the mass ratio of $m^* = 5.8$ from the current experiment being half the value of the other two studies, it can still be considered comparable ($m^* = 11.5$ for Seyed-Aghazadeh & Modarres-Sadeghi (2015) and $m^* = 10$ for Bourguet & Lo Jacono (2014)) given previous observed variation with mass ratio for non-rotating VIV studies. Moreover, the mass-damping ratios of the three studies are similarly low. Previous work by Feng (1968); Khalak & Williamson (1996, 1997a, 1999) on the effects of mass and damping on a cylinder undergoing VIV have documented that the vibration response of an elastically-mounted cylinder does not show significant changes with reasonable variations in mass and damping ratios.

Figure 4.5(b) delimits regions where the vibration response is non-negligible in the three studies. The boundaries from the two experiments are comparable despite significant differences their Reynolds numbers and amplitude responses. The vibration region from the simulation of Bourguet & Lo Jacono (2014) is comparable at low rotation rates over the initial range of reduced velocities; however, they reported significant amplitude response that, when α is sufficiently high, extends to significantly higher U^* .

Previous VIV studies have shown that changes in the vibration response of the cylinder are often accompanied by a corresponding change in the structure of the wake. To better understand the behaviour of a rotating cylinder undergoing VIV, the wake patterns are examined in the following section.

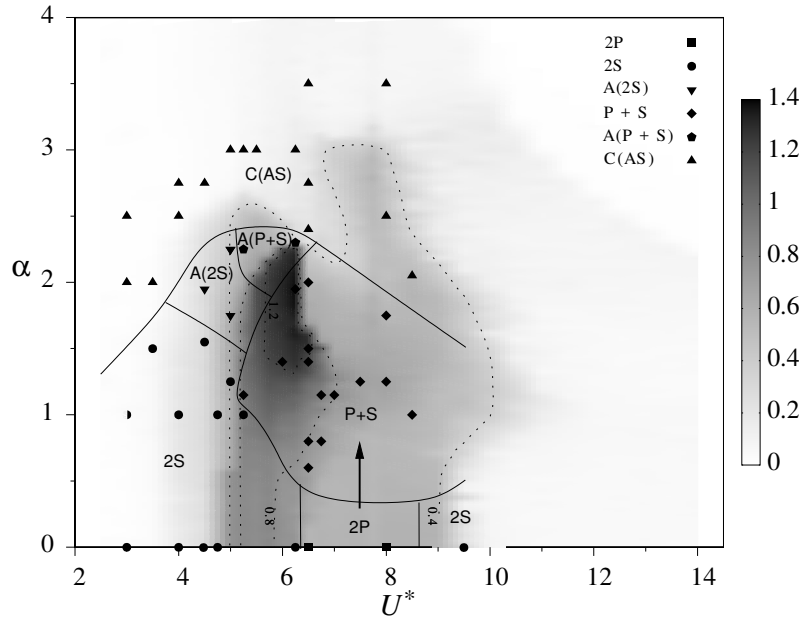


FIGURE 4.6: The wake patterns observed are based on particle image velocimetry data with approximate boundaries shown by the solid lines. This overlays a greyscale contour map of the mean of the highest 10% of amplitude peaks (A_{10}^*) about their time-averaged positions (\bar{y}), in $U^* - \alpha$ parameter space, with amplitude levels indicated by the dashed lines. There appears to be a gradual change from 2P to P+S as the rotation is increased causing a deflection of the wake away from the streamwise centreline.

4.3 Wake structures

The structure of vortices shed into the wake are of great significance as they influence the vibration response of an elastically-mounted structure. A number of studies have discovered and categorised the wake structure of rigidly-mounted cylinders undergoing forced constant rotation and non-rotating cylinders undergoing free and forced vibrations in the cross-flow direction (see Badr *et al.* (1990); Mittal & Kumar (2003); Rao *et al.* (2013); Williamson & Roshko (1988); Khalak & Williamson (1999); Carberry *et al.* (2001); Zhao *et al.* (2014a)). It has been established that the wake structure can vary significantly from the Kármán vortex streets typically observed for a stationary cylinder. The low Re simulations of Bourguet & Lo Jacono (2014) provided evidence that an elastically-mounted cylinder undergoing constant-rate rotation can exhibit wake patterns previously documented in forced-rotation, free-vibration and forced-vibration studies. To better understand the interactions between wake modes and the cylinder's vibration responses, the observed wake modes have been mapped against the primary independent variables, reduced velocity (U^*) and rotation rate (α).

A contour map of the mean of the highest 10% of amplitude peaks in the $U^* - \alpha$ parameter space is presented in fig. 4.6. Iso-amplitude contours are represented by the dashed lines. The wake structures observed for selected PIV data sets (refer to §3.5.4 for processing details) are marked to indicate how the state of the wake affects the cylinder's amplitude response. Approximate boundaries of regions of the same wake state are represented by solid lines. The inclusion of these approximate boundaries is to assist the interpretation of how the wake modes and amplitude responses (measured by A_{10}^*) are related.

Work such as Feng (1968); Khalak & Williamson (1999); Williamson & Govardhan (2004a) have

shown that a non-rotating cylinder undergoing VIV exhibits hysteresis and wake mode switching in transition regions between amplitude response branches. A primary focus of the present study is to characterise the wake modes in U^* - α parameter space. In regions where the amplitude response is low, i.e. at reduced velocities associated with the initial response branch ($U^* < 4.8$) and in the desynchronized region ($U^* \geq 9.5$), the wake mode typically found in non-rotating VIV studies was observed up to a rotation rate of $\alpha \approx 2.0$. This shedding mode, as documented in fig. 4.7, is characterised by the shedding of two single counter-rotating vortices per oscillation cycle and it is commonly referred to as the 2S mode. The 2S mode is the standard wake structure that is commonly found in stationary cylinder and non-rotating VIV studies.

In the same reduced velocity ranges ($U^* < 4.8$, $U^* \geq 9.5$) at rotation rates above $\alpha \approx 2.0$, a new wake structure characterised by the shedding of small, asymmetric vortices was discovered. This mode resembles the shedding structure observed in the second region of wake instability for a rotating cylinder reported by Mittal & Kumar (2003). However, the mode observed by Mittal & Kumar (2003) occurred at significantly higher rotation rates or $\alpha \sim 4.5$. As the flow undergoes the initial transition into this mode, i.e. at its boundary with other wake modes, the vortices shed are larger in size and their shedding is more periodic. On entering this wake mode state, as the rotation rate is further increased, the vortices shed becomes smaller and more chaotic. In addition to the evolution in size and periodicity with rotation rate, it was observed that the wake may switch between a wider and narrower state, with the latter associated with the shedding of larger vortices. Figure 4.8 illustrates the instantaneous spanwise vorticity contours for this mode: the left image illustrates the narrower wake state; and the right image shows the wider state. Further work is needed to characterise the intermittent behaviour of this wake state and details about the switching behaviour. This mode is named C(AS) due to the *Coalescence* of these small *Asymmetric* vortices and its intermittent wake *Switching*.

At moderate reduced velocities associated with the lower amplitude response branch ($6.5 \leq U^* \leq 9.5$) of a non-rotating cylinder, where the amplitude response is $0.4 < A_{10}^* \leq 0.6$ and the rotation rate is below $\alpha \leq 0.5$, two pairs of counter-rotating vortices are shed per oscillation cycle as illustrated in figure 4.7. This resembles the 2P mode previously reported in non-rotating VIV studies such as Williamson & Roshko (1988); Khalak & Williamson (1999).

At moderate rotation rates ($1.25 \leq \alpha < 2.25$), a dominant wake mode is observed that persists across the reduced-velocity vibration region ($5.0 < U^* \leq 9.0$) where wake-body synchronisation occurs. The wake in this region is characterised by the P+S mode, as illustrated in fig. 4.7. The P+S mode is composed of a pair (P) of counter-rotating vortices plus a single (S) vortex shed per oscillation cycle. A number of free and forced vibration studies have reported the observation of this wake mode (e.g. Williamson & Roshko (1988)). The lower Reynolds number simulation by Bourguet & Lo Jacono (2014) and experiments of Seyed-Aghazadeh & Modarres-Sadeghi (2015) of a rotating cylinder undergoing VIV have also reported observing this mode. It should be noted that as the rotation rate is increased, the mean wake becomes more asymmetric about the centreline due to the Magnus effect, and this influences the wake state. This effect is likely to register as a change from 2P shedding at low rotation to P+S at higher rotation. Indeed at intermediate rotation rates, the wake state shows the characteristics of both 2P and P+S modes. Over the same range of reduced velocities in the vibration region ($5.0 < U^* \leq 9.0$), the aforementioned C(AS) wake mode is observed when the rotation rate is increased above $\alpha > 2.25$.

A comparison of figure 4.4 and fig. 4.6 reveals that large changes in the cylinder's oscillation amplitude response correspond with changes to the wake mode. This is most evident in the upper branch ($U^* = 6.25$) case, as shown in figure 4.4(b.i), the abrupt drop in amplitude response and jump in frequency response near a rotation rate of $\alpha = 2.25$ coincides with a change in wake mode from 2S, in the unsteady flow regime, to the C(AS) mode, where the wake flow becomes near steady. Another example is at the onset of the lower branch ($U^* = 6.50$). Figures 4.4(c.i) and 4.4(c.ii)

showed that near a rotation rate of $\alpha = 2.25$, the drop off in the amplitude response from the plateau to a lower amplitude state and the change in frequency response from a single dominant response (associated with the plateau) to a weaker and more scattered response also coincides with a similar wake transition as P+S undergoes transition to C(AS).

To better understand and characterise the influence of increasing α on the wake of the cylinder, the induced changes to the standard 2S mode are examined. The 2S mode was selected as it is the dominant wake mode for a stationary cylinder and for non-rotating free and forced vibration studies. The evolution of the 2S wake mode with increasing rotation rate at a reduced velocity of $U^* = 5.0$ is illustrated in figure 4.3. Figure 4.3 is laid out such that each row shows a different rotation rate case: the top row illustrates the wake of a non-rotating cylinder; the centre row shows the cylinder at $\alpha = 1.0$; and the bottom row shows the $\alpha = 2.25$ case. Visual aids have been added to the figure to help explain the different effects of body rotation on the wake. These visual aids are arranged such that each column within the figure explains a different effect of body rotation on the 2S wake mode.

As the rotation rate is increased (see figure 4.3 left column from top downwards), \bar{y} of the cylinder shifts upwards and the vortices shed deviate further downwards away from the streamwise centreline (marked as a dashed line) as they advect downstream. These observations are expected for the forced body rotation cases wake deflection, as a result of the Magnus effect.

The spacing between clockwise and anti-clockwise vortex cores in the wake is altered by the increased rate of rotation. Positive and negative vortex cores are evenly distributed along the wake for the non-rotating cylinder. However, as the body is forced to rotate, the vortices in the wake exhibit signs of collecting in pairs. This effect is shown in the third column of figure 4.3, and it is enhanced with increases in rotation rate. The vertical dashed lines are visual aids to mark out the boundary of shedding cycles. It is evident that when α is increased, the distance (labelled as ‘a’ in the centre column) between counter-rotating vortex pairs of the same shedding cycle (i.e. the shed anti-clockwise (red) vortex and the subsequently formed clockwise (blue) vortex both on the right side of the vertical dashed line) is less than the distance (labelled as ‘b’ in the right column) between the clockwise vortex (blue, to the right of the dashed line) and the anti-clockwise vortex (red, to the left of the dashed line) of the next shedding cycle.

With increases in rotation rate, the size and strength of the vortices decreases (see figure 4.3 centre column from top downwards). These observations have previously been reported in the wake of a rigidly-mounted cylinder undergoing rotation (see Radi *et al.* (2013), figure 5). This is consistent with body rotation resulting in the two separation points feeding the shed vortices to shift closer together; thereby limiting the vorticity shed into each vortex in the wake and increasing cross-annihilation. Similar observations of the effect of α on the asymmetry of the wake and spacing between vortex cores are seen with the P+S mode.

An inspection of the contours of the P+S mode at different ranges of reduced velocity show an indistinct change in the vortex pattern. Observations of the P+S mode in previous VIV studies showed that the mode consisted of a single vortex on one side of the streamwise centreline with a clockwise and anti-clockwise vortex pair of the other side of the centreline. Because of symmetry, the single and pair of vortices can form interchangeably on both sides of the streamwise centreline in non-rotating VIV wakes. Phase-averaged contours of the P+S mode in the upper amplitude response branch of a non-rotating cylinder at $U^* = 5.50$ (left) and in the lower branch at $U^* = 6.5$ (right) are illustrated in fig. 4.10. The upper branch was observed to have one anti-clockwise vortex on the advancing side of the cylinder and two clockwise vortices on the retreating side of the cylinder. In the lower branch, the anti-clockwise vortex on the advancing side of the cylinder remains; however, on the retreating side there is now a vortex pair consisting of one clockwise and one anti-clockwise vortex. This was an unexpected observation. It had been thought that the asymmetric flow generated by the rotation of the cylinder would promote the vortices to shed in one direction, with a consistent

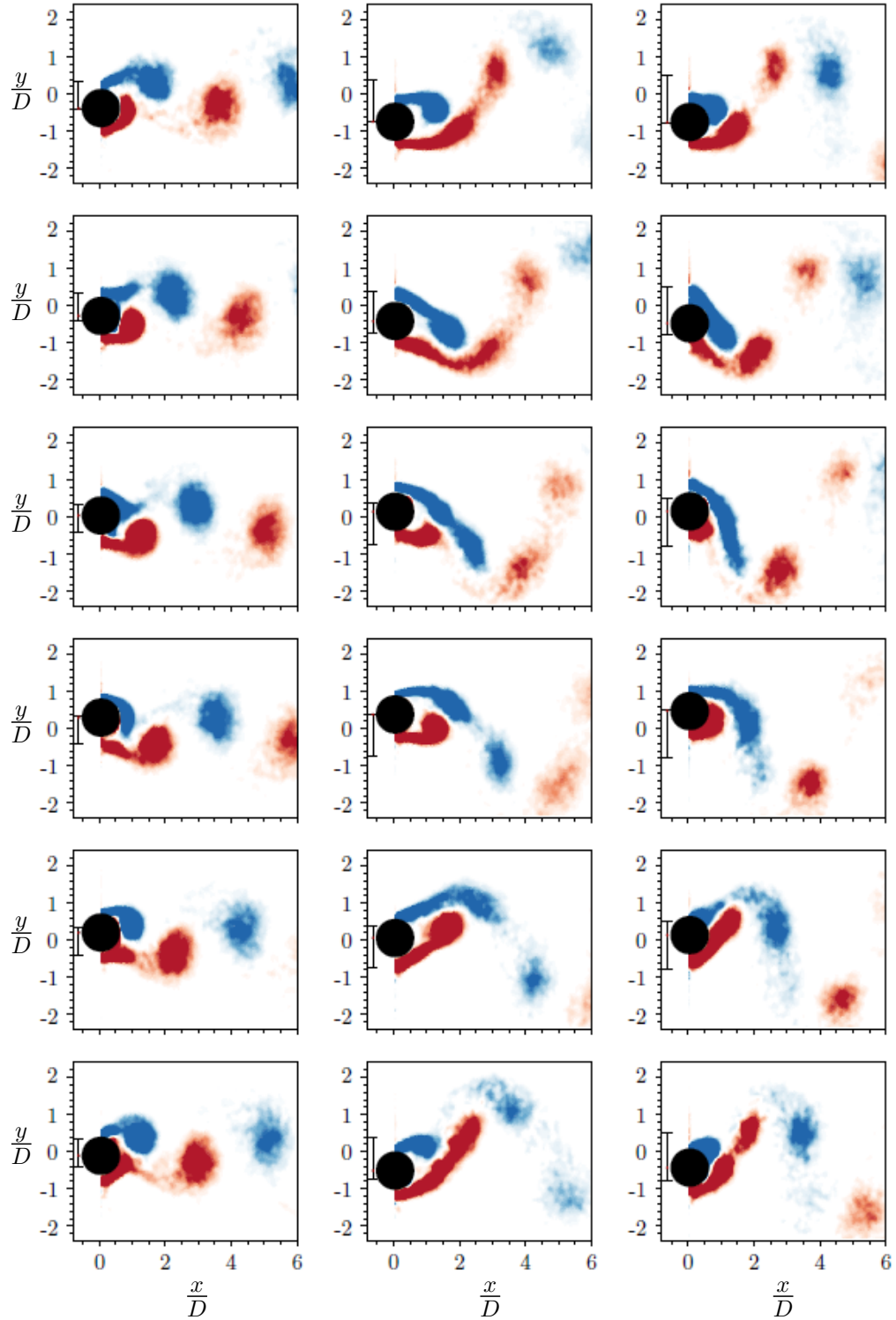


FIGURE 4.7: Phase-averaged spanwise vorticity contours of a 2S mode at reduced velocity $U^* = 5.0$ and rotation rate $\alpha = 1.0$ (left column), 2P mode at $U^* = 8.0, \alpha = 0.0$ (centre column) and P+S mode at $U^* = 6.5, \alpha = 0.6$ (right column) over an oscillation cycle. Cylinder rotation is anticlockwise.

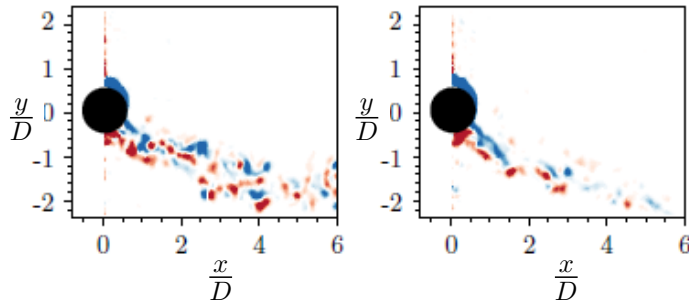


FIGURE 4.8: Instantaneous iso-contours of the C(AS) mode at reduced velocity $U^* = 4.00$ and rotation rate $\alpha = 2.75$. The C(AS) wake pattern is of a chaotic nature and consists of small vortices distributed around a mean trajectory.

vortex pattern seen in previous VIV studies and in figure 4.10 (right). This observation can be seen over a range of α in the upper and lower amplitude response branches. To better understand this behaviour, further work is needed.

4.3.1 Wake intermittency in the upper amplitude branch

Previous work has shown that the wake of a cylinder undergoing VIV in the upper amplitude response branch exhibits intermittent or chaotic behaviour (Zhao *et al.* 2014a; Lucor & Triantafyllou 2008). It is of interest to know whether this mode-switching behaviour observed in the upper branch continues to exist when the cylinder undergoes forced rotation. The forced rotary motion of rigidly-mounted cylinders do indeed modify the wake stability; this is observed in both constant rotation (El Akoury *et al.* 2008; Rao *et al.* 2013, 2015) and rotary oscillation (Lo Jacono *et al.* 2010; D’Adamo *et al.* 2015) studies. In the present study, the cylinder undergoes constant-rate rotation, consequently biasing the produced vorticity towards one side and therefore biasing the topology of the wake; the question of interest is how the dynamics of the wake in the upper-amplitude response branch may be affected?

In order to find out how the wake dynamics in the upper branch is affected, observations on the state of the wake are presented for $U^* = 6.5$ at three rotation rates: $\alpha = 0.0, 0.8$ & 1.5 . The switching of the wake state was identified though examining the ϕ_1 – ϕ_4 POD temporal coefficients. The instantaneous cylinder motion given by the body displacement $y(t)$ was insufficient to unambiguously decipher changes within the wake, as exemplified though figure 4.11 and figure 4.13. However, it is possible to observe many instances of wake mode switching time-resolved PIV images (~ 3100) that covers a large number of shedding cycles (~ 200 -300).

An example of the aforementioned wake-mode switching behaviour of a non-rotating cylinder is presented in fig. 4.11. The transition from the 2P to 2S wake mode is shown in this example. The time history of the cylinder’s normalised position y^* is presented in figure 4.11(a) with the segment in blue showing where wake-mode switching occurred. The cylinder’s normalised position $y^* = y'/D$ is defined as the mean-subtracted displacement $y' = y - \bar{y}$ of the cylinder normalised by the cylinder diameter (D). The temporal evolution of the mode is presented through Lissajous figures of the first and second modes (ϕ_1 & ϕ_2) in figure 4.11(b); and the first and third modes (ϕ_1 & ϕ_3) in figure 4.11(c). The symbols (\bullet) and (\blacktriangle) in figure 4.11(a-c) correspond to the instantaneous vorticity contours illustrating the 2P mode in figure 4.11(d) and 2S mode in figure 4.11(e). The motion time history in figure 4.11(a) exemplified that the information contained in the cylinder displacement $y(t)$ signal is insufficient to reveal switching behaviour within the wake evolution; however, changes in the shape of the Lissajous curves clearly draw a distinction between the two modes. Thus, essential to

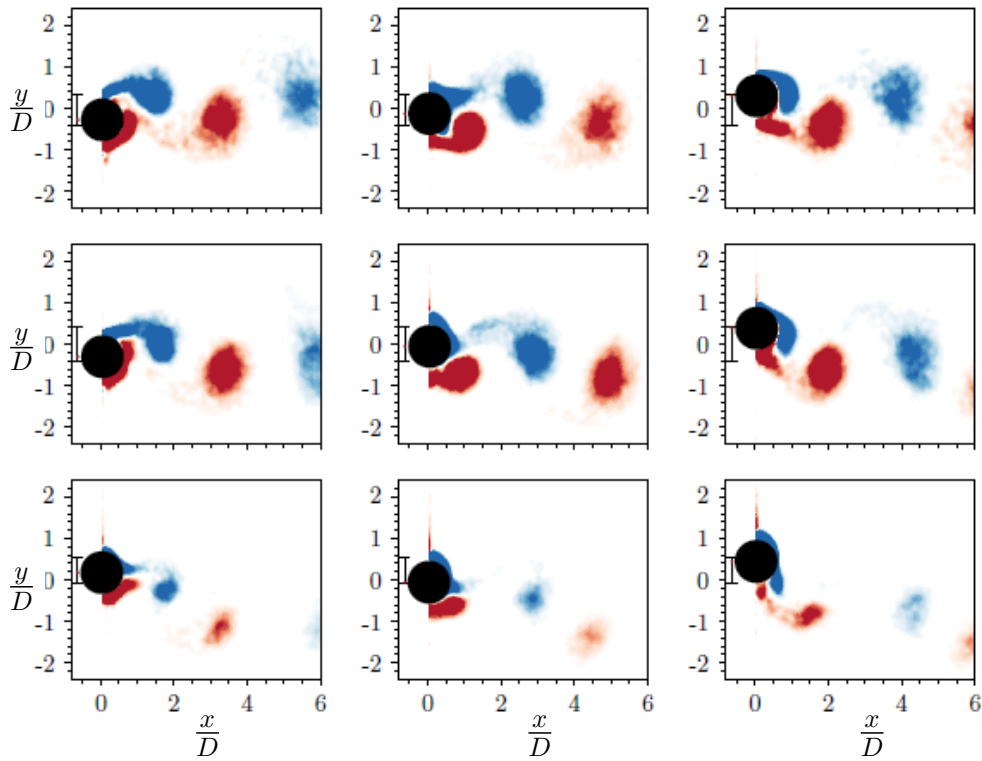


FIGURE 4.9: Phase-averaged spanwise vorticity contours of 2S mode at different rotation rates (α) over an oscillation cycle at reduced velocity $U^* = 5.0$. $\alpha = 0.00$ (top row), $\alpha = 1.00$ (centre row) and $\alpha = 2.25$ (bottom row). Contours were selected to align the leading vortex of each oscillation cycle, *i.e.*, the vortex with positive vorticity, to the trailing vortex of the previous oscillation cycle. This illustrates the effects of α on wake asymmetry and gap between vortices from adjacent oscillation cycles. Therefore, the contours between different α are not necessarily in phase. The horizontal dashed lines in the left column of contours is a visual aids placed to represent the streamwise centre line; dimension ‘a’ qualitatively show the approximate distance between vortex cores belonging to the same shedding cycle; dimension ‘b’ qualitatively show the approximate distance between the trailing clockwise vortex core and the leading anti-clockwise vortex core in the subsequent shedding cycle. The vertical dashed lines in the right column are visual aids placed to represent an imaginary boundary between shedding cycles.

the differentiation of the wake modes and dynamics was the inspection of the POD temporal modes; this was only feasible owing to the large number of shedding cycles recorded.

Another example of wake-mode switching, at a rotation rate of $\alpha = 0.80$, is presented in figure 4.12. In this example, the transition from the P+S⁺ (the S⁺ indicates an anticlockwise single vortex) to a 2S shedding mode is shown. Similar to the previous analysis, the time history of the normalised displacement y^* is presented in figure 4.12(a), with blue sections highlighting the wake-mode switching zone. Again, the temporal evolution is presented through the Lissajous figures, with figure 4.12(b) showing the first and second modes (ϕ_1 & ϕ_2), and figure 4.12(c) showing the first and third modes (ϕ_1 & ϕ_3). The red symbols placed in figure 4.12(a-c) correspond to the instantaneous vorticity contours of a P+S⁺ mode in figure 4.12(d) and a 2S mode in figure 4.12(e). Once again, the changes in the form of the Lissajous curves distinctly differentiates the two wake modes while the time history of the normalised displacement y^* based on the displacement signal $y(t)$ is unable to distinguish the switching of wake modes.

The mode switching behaviour continues as the rotation rate is increased to $\alpha = 1.50$. Figure 4.13

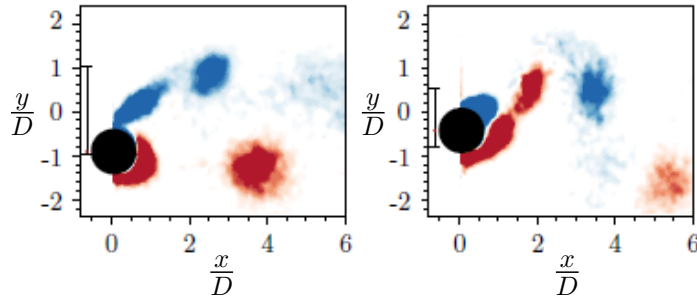


FIGURE 4.10: Phase-averaged iso-contours of the P+S mode at reduced velocity $U^* = 5.50$ and rotation rate $\alpha = 1.15$ in the upper response branch (left) and $U^* = 6.50, \alpha = 0.60$ in the lower response branch (right).

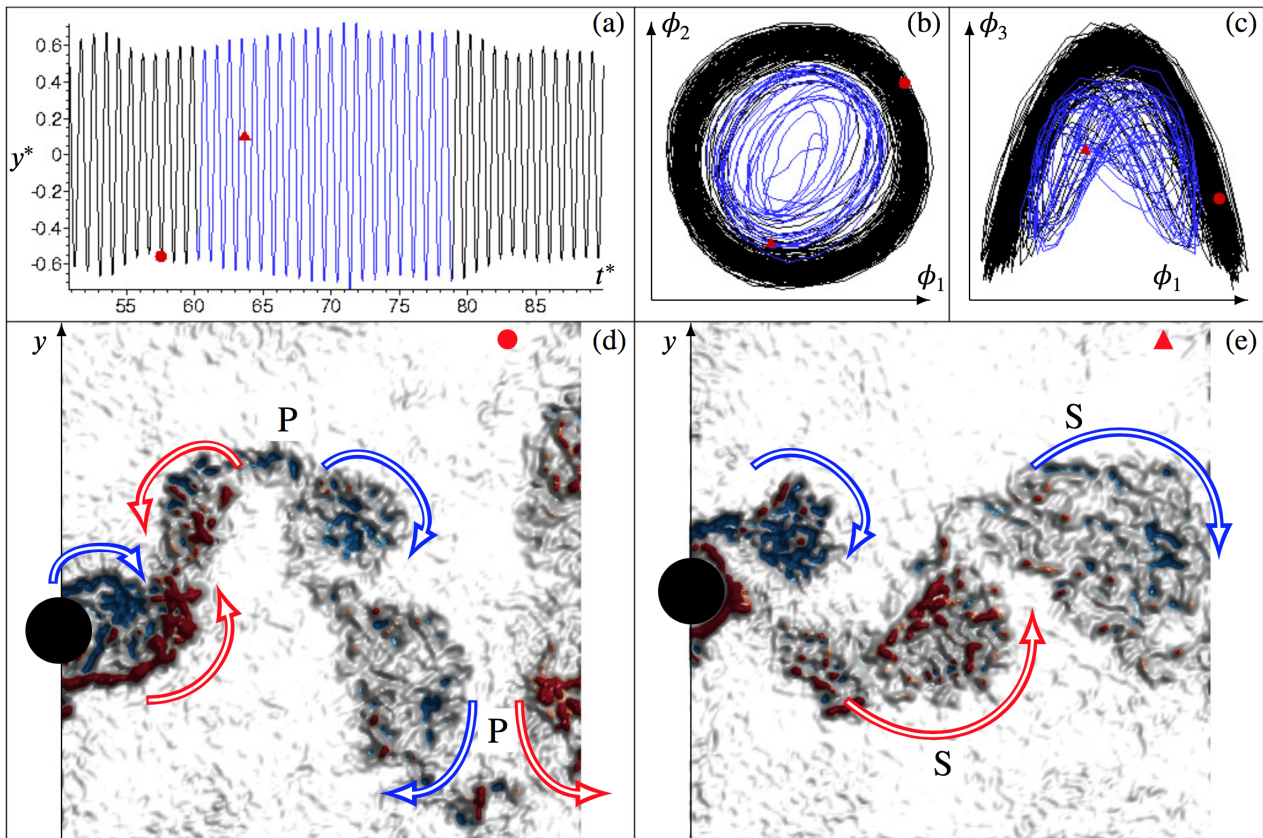


FIGURE 4.11: Instantaneous measurement for reduced velocity $U^* = 6.50$ and rotation rate $\alpha = 0.0$. (a) Time-varying normalised position of the cylinder $y^* = y'/D$, with $y' = y - \bar{y}$, as a function of oscillation cycles, T (*i.e.*, time normalised by the natural period of the oscillating structure $T = t/f_{nw}$). The zone of transition from the 2P to 2S mode is marked in blue. The red filled symbols, circle (\bullet) and triangle (\blacktriangle), match the instantaneous vorticity contours presented in (d) and (e) (showing the 2P and 2S mode, respectively) to the instantaneous positions in the other plots. Plots (b) and (c) are Lissajous figures showing the temporal evolution of the POD modes highlighting the differences over time (*i.e.*, providing different Lissajous shapes).

presents the transition from a P+S⁻ (the S⁻ indicates a clockwise single vortex) to a 2P mode.

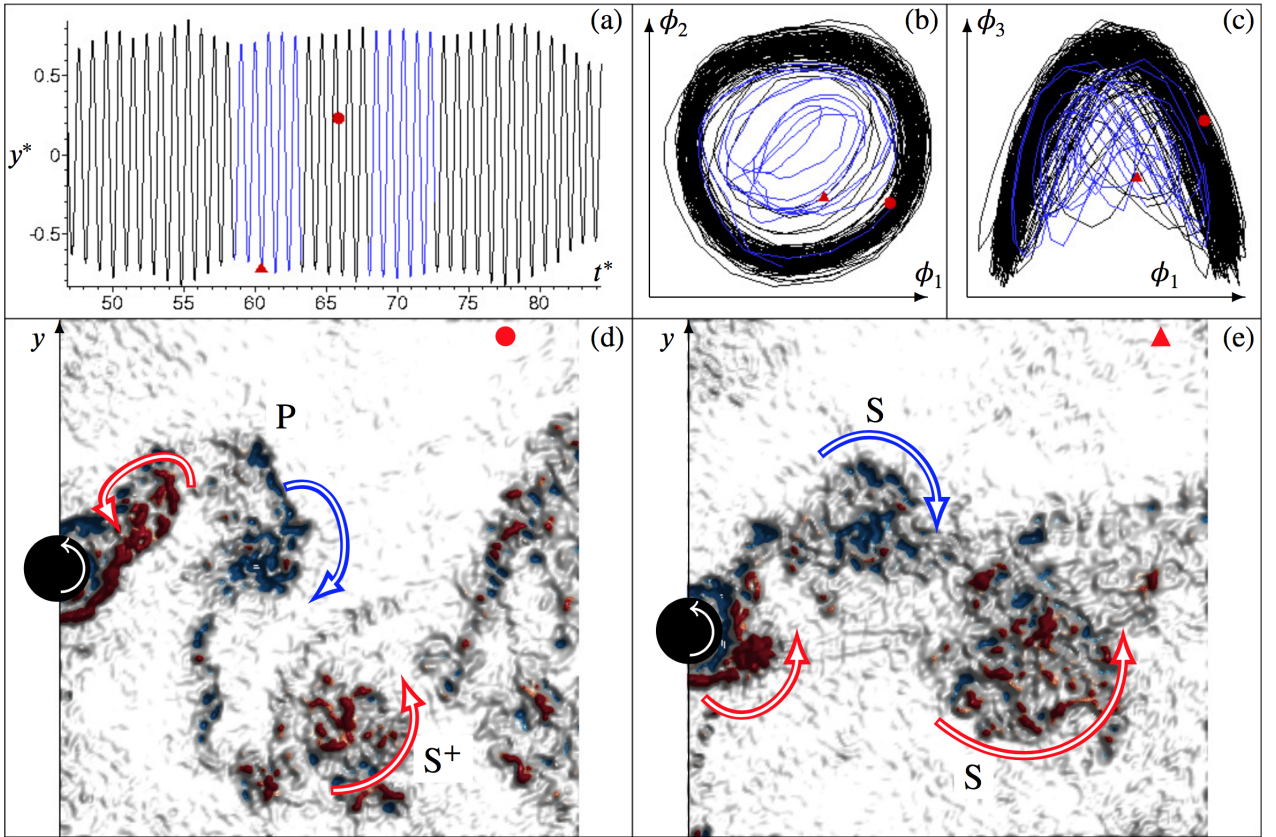


FIGURE 4.12: Instantaneous measurement for reduced velocity $U^* = 6.50$ and rotation rate $\alpha = 0.80$. (a) Time-varying normalised position of the cylinder $y^* = y'/D$, with $y' = y - \bar{y}$, as a function of oscillation cycles T (*i.e.*, time normalised by the natural period of the oscillating structure $T = t/f_{nw}$). Highlighted in blue is the zone of transition from the P+S⁺ to 2S shedding mode. The red filled symbols, circle (●) and triangle (▲), correspond to the instantaneous vorticity contours presented in (d) and (e) showing a P+S⁺ and 2S mode, respectively. Plots (b) and (c) show the Lissajous figures for $(\phi_1 \& \phi_2)$ and $(\phi_1 \& \phi_3)$, respectively. They are representative of the temporal POD mode evolution, highlighting the differences in time (providing different Lissajous shapes).

Similar to the previous two cases, the time history of the normalised displacement y^* is presented in figure 4.13(a), with the blue segment highlighting the switch of wake modes. As before, figures (b) and (c) of fig. 4.13 presents the Lissajous figures of the temporal evolution and they confirm the distinct changes in shape that differentiate the two wake modes.

The present results do not provide a comprehensive collection of all possible wake-mode transition cases; an extensive study is needed to characterise the switching behaviour in the U^* - α parameter space. However, the results reported in this section is sufficient to corroborate that the intermittent wake-mode switching behaviour in the upper amplitude response branch persists even at elevated rates of body rotation rate.

4.4 Force and phases

The fluid forces and their phase angle difference with the body displacement signal is core to understanding the interactions between the fluid and structure. The (force) results presented in this section were obtained using the new air-bearing displacement measurement system. Details of the experiment apparatus and measurement sensors have been provided in §3. The new air-bearing

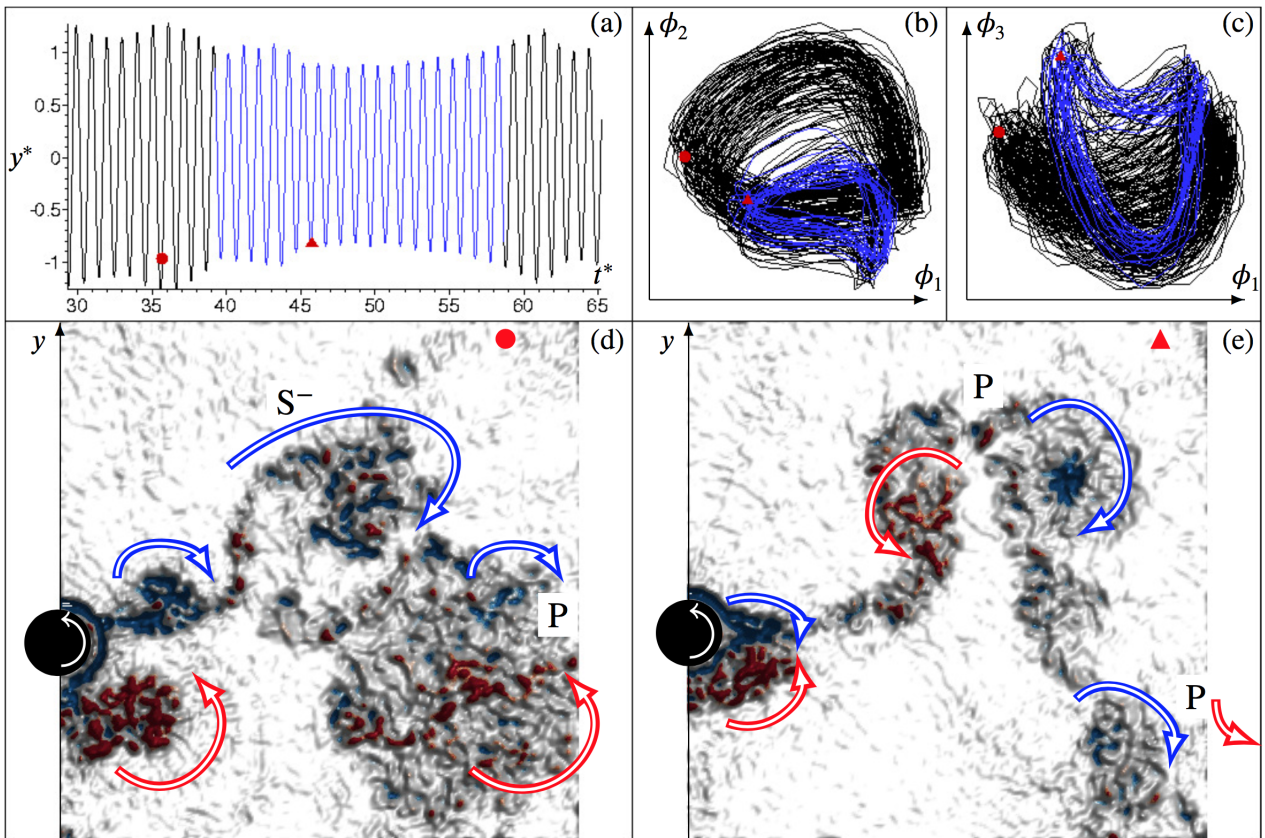


FIGURE 4.13: Instantaneous measurement for reduced velocity $U^* = 6.50$ and rotation rate $\alpha = 1.50$. (a) Time-varying normalised position of the cylinder $y^* = y'/D$, with $y' = y - \bar{y}$, as a function of oscillation cycles, T (*i.e.*, time normalised by the natural period of the oscillating structure $T = t/f_{nw}$). Section in blue highlights the zone of transition from a $P+S^-$ to $2P$ mode. The red filled symbols, circle (\bullet) and triangle (\blacktriangle), correspond to the instantaneous vorticity contours presented in (d) and (e), showing a $P+S^-$ and $2P$ mode, respectively. Plots (b) and (c) show the Lissajous figures for $(\phi_1 \& \phi_2)$ and $(\phi_1 \& \phi_3)$, respectively. They are representative of the temporal POD mode evolution, highlighting the differences in time (providing different Lissajous shapes).

setup has a total mass of $m_{osc} = 2.4481$ kg and the mass ratio is $m^* = 5.641$. From free-decay tests, the natural frequency of the oscillating system in air was $f_{nw} = 0.468$ Hz, and in water was $f_{nw} = 0.429$ Hz. Structural stiffness is provided by one pair of springs and they have an equivalent stiffness of $k = 0.0212$ N/mm; and the oscillating system has a damping ratio of $\zeta = 0.001515$. This new experimental set up was also used for the rotary oscillation study presented in §5.

The incorporation of a precision *digital* optical linear encoder onto the new air-bearing apparatus enabled direct measurement of the body displacement $y(t)$ with minimal electrical interference (that would lead to noisy force transducer signals). The linear encoder allowed the time-varying lift force to be estimated through the cylinder's equation of motion, which was mathematically described in equation 2.5. Hence, the data presented in this section was obtained using only the linear encoder to measure the displacement signal and derive the force signal. (It should be borne in mind that use of a force transducer to extract the lift force still relies on removing the inertial force components, which is estimated from the acceleration derived from the displacement signal.)

The variation in mean of the highest 10% of normalised amplitude peaks (A_{10}^*), RMS lift coefficient ($C_{y,RMS}$), total phase (ϕ_T) and vortex phase (ϕ_V) at two rotation rates ($\alpha = 0.2$) are presented as a function of U^* in figure 4.14. The computation of the RMS lift coefficients was performed after

the mean lift was subtracted from the signal. In figure 4.14, ϕ_T corresponds to the phase-angle difference between the measured lift force, $F_y(t)$, and the body displacement, $y(t)$; and the vortex phase (ϕ_V) represents the phase-angle difference between the lift force excluding the added-mass contribution (*i.e.* $F_{vor}(t) = F_y(t) - F_{pot}(t)$) and $y(t)$. The decomposition of fluid forces was proposed by Lighthill (1986) and was first used in Govardhan & Williamson (2000) in their investigation into VIV of cylinders. It has subsequently been used to characterise the different VIV response branches and the transitions of freely vibrating cylinders. Further details and mathematical relationships between the force components and phases are provided in §2.3.3. For a non-rotating cylinder ($\alpha = 0$) undergoing VIV, the predicted $C_{y,RMS}$, ϕ_T and ϕ_V are in excellent agreement with previous literature on VIV of a cylinder.

Figure 4.14(b) presents a comparison of the total RMS lift coefficient between a non-rotating cylinder and that rotating at a rate of $\alpha = 2.0$. The lift response of both curves exhibits similar trends. The peak force occurs at a reduced velocity value marking the beginning of the upper amplitude response branch.

Khalak & Williamson (1999) and other VIV studies that have followed have documented that for a non-rotating cylinder, a sudden jump in ϕ_T from 0 to 180° can be observed at the transition between the upper and lower response branches. This is also observed in the present experiment. The total phase is sustained at 180° until the onset of wake-body desynchronization. On increasing the reduced velocity beyond the desynchronization transition, the total phase drops to $\phi_T \approx 135^\circ$. When the cylinder undergoes constant rate rotation at $\alpha = 2.0$, ϕ_T changes significantly. It remains at approximately 0° throughout the entire initial, upper and most of lower amplitude response branches. The total phase only begins to increase at the end of the lower branch.

Figure 4.14(d) presents a comparison of the vortex phase and exemplifies the changes in ϕ_V with the addition of body rotation. Previous work by Govardhan & Williamson (2000) on a non-rotating cylinder showed that the vortex phase sharply jumps from 0 to approximately 180° at the transition between the initial and upper amplitude response branches. The present results are in excellent agreement with this. When the cylinder is forced to rotate at $\alpha = 2.0$, the vortex phase did not exhibit a jump in response until the transition between the upper and lower branch, where it abruptly increased to $\phi_V \approx 135^\circ$. This phase is observed over a range of reduced velocity within the first portion of lower branch, before ϕ_V gradually increases to 180° for the second half of that branch.

These differences in phases are significant as previous work has established that phase relationships are closely related to the amplitude response branches and switches in the wake mode. Govardhan & Williamson (2000) showed that for a non-rotating cylinder, the jump in ϕ_V at the transition between the initial and upper branch corresponds to a switch in wake mode from 2S to 2P. Perhaps it is unsurprising that the vortex phase is different to that of a non-rotating cylinder as the 2P mode is not observed in the present study for a cylinder undergoing non-negligible rotation.

4.4.1 Chapter summary

This chapter presented results on the vibration response and wake structure of an elastically-mounted circular cylinder subjected to forced, constant rotation over a range of rotation rates and Reynolds numbers. There are several new findings.

Substantial body vibration was found to occur through wake-body synchronisation over a range of rotation rates, α , and reduced velocities, U^* . Significant cylinder oscillations were observed to occur for rotation rates up to $\alpha \approx 3.5$ over the lock-in range. Interestingly, previous *rigidly-mounted* cylinder studies show that rotation rates beyond $\alpha = 2$ cause suppression of vortex shedding. Overall, the present study shows that forced constant-rate rotation can cause the cylinder to vibrate at up to 1.4 times the cylinder diameter, a 76% increase in A_{10}^* amplitude response over non-rotating VIV. This maximal response was observed when the rotation rate is close to $\alpha = 2.0$, and in the

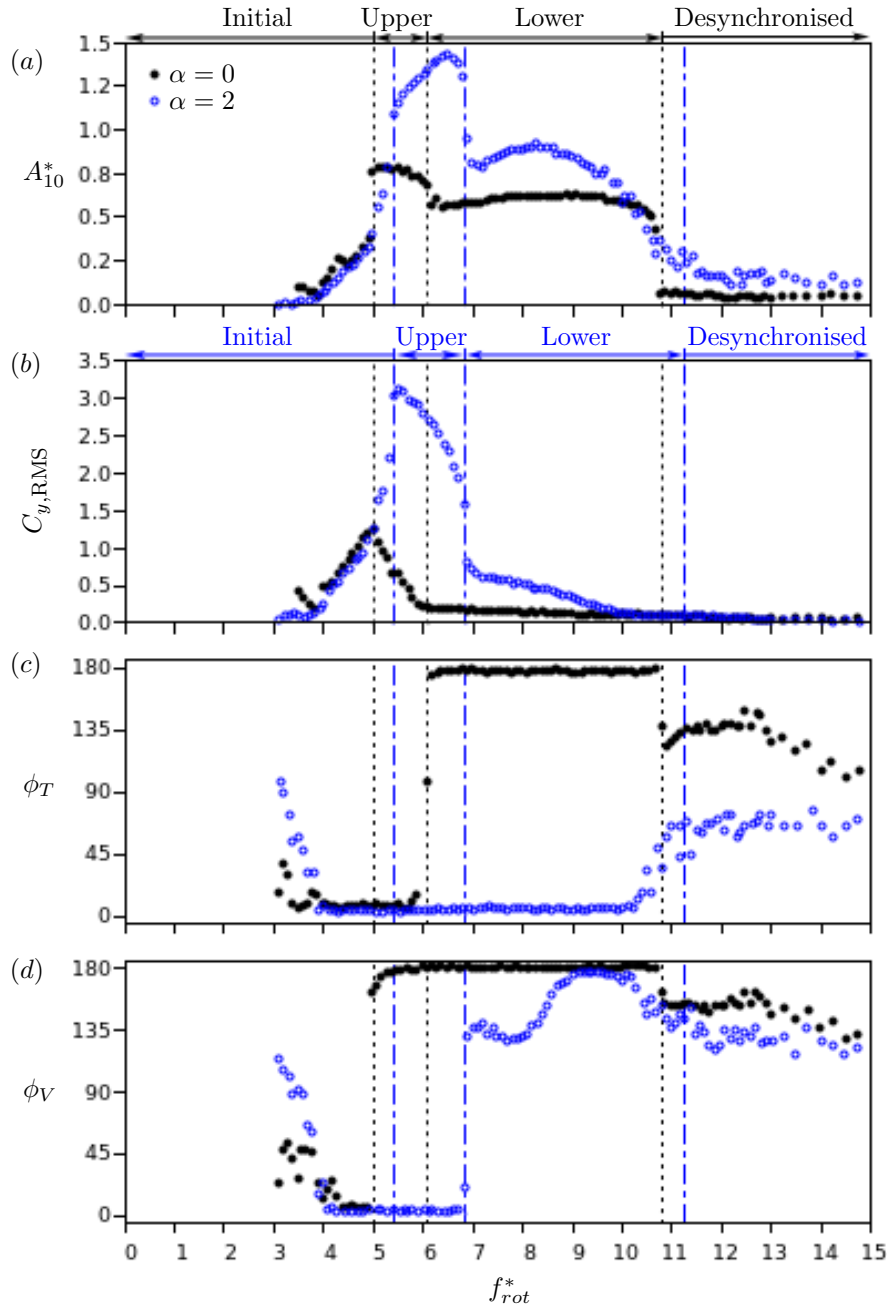


FIGURE 4.14: Comparison of lift force and phase variations with reduced velocity (U^*) for a non-rotating ($\alpha = 0$) and rotating ($\alpha = 2$) cylinder. (a) Mean of the highest 10% of normalised amplitude response peaks (A_{10}^*); (b) the RMS lift coefficient variation after subtracting the mean lift ($C_{y,RMS}$); (c) the total phase (ϕ_T) of the lift signal relative to the displacement signal; and (d) the vortex phase (ϕ_V) relative to the displacement signal are presented as a function of U^* . The vertical lines are visual aids showing the approximate boundaries of the different amplitude response branches for the two cases with the ranges indicated for each α case.

range of reduced velocities associated with the upper amplitude response branch of a non-rotating cylinder. Across the U^* - α parameter space, where a large amplitude response is observed, the cylinder frequency response was observed to be synchronised with the natural frequency of the oscillating system in water. It is the resonance between these two frequencies that enables large vortex-induced oscillations for non-rotating VIV and also enables large oscillations for VIV of a rotating cylinder. Increasing α from 0 to 2 both broadens the range of reduced velocity where large

body oscillations occur and increases the peak amplitude response. As the rotation rate is increased towards $\alpha \approx 2.0$, the normalised frequency response gradually decreases to fall below $f^* = 1$, where the oscillation frequency, f , equals the natural frequency of the structure, f_{nw} . This is correlated with the amplitude response increasing as the rotation rate is increased towards $\alpha \approx 2.0$. An increase in rotation rate beyond $\alpha \approx 2.0$ results a reduced peak amplitude response, noting that the body oscillation becomes desynchronized with the weakened, less coherent vortex shedding.

A number of different wake modes were observed over the parameter space covered by the present study. At low to moderate reduced velocities ($U^* < 6.5$), the 2S mode dominates at all rotation rates studied. At low rotation rates ($\alpha < 1.25$), the 2S and 2P modes characterise the wake at reduced velocities associated with the upper and lower response branches, respectively. In the desynchronized region, the 2S mode appears again. At moderate rotation rates ($1.25 \leq \alpha < 2.25$), the P+S mode, a mode composed of a pair of counter-rotating vortices and a single vortex shed per cycle, was observed for most of the synchronisation region. Chaotic switching of the wake mode was observed in the upper branch. Indeed, it was found that regardless the rotation rate, the upper response branch seemed to maintain a chaotic state. In the desynchronized region, a mode in which small-scale vortices coalesce and shed asymmetrically, C(AS), was observed at rotation rates above $\alpha \approx 1.25$. Beyond rotation rates $\alpha \approx 2.25$, C(AS) dominates in the reduced velocity range associated with the vibration region of a non-rotating cylinder ($U^* \approx 4 - 10$). On further increasing the rotation rate, shed vortices increasingly deviate from the streamwise centreline of the cylinder. This deviation with rotation rate was observed for multiple wake modes, as it is expected from the Magnus effect. In addition, the distance between vortices of adjacent oscillation cycles increases, and the size and peak vorticity of the vortices shed decreases, in line with non-VIV studies.

Of further interest is the significantly lower amplitude response observed experimentally by Seyed-Aghazadeh & Modarres-Sadeghi (2015) relative to that found in this case. Given the substantial Reynolds numbers difference between these studies, this could simply be a low- Re effect but it would be useful to have independent verification of either study. In a sense, it is surprising that rotation significantly enhances vibration amplitudes, given that it tends to make the wake narrower and asymmetric, so a deeper understanding of the near-wake dynamics and the effects on VIV would be useful. Also of interest is the still significant amplitude response observed at $\alpha = 2.5$ and 3, well beyond the rotation rate for suppressing shedding from a fixed rotating cylinder, that warrants further investigation. The present study showed that a number of response trends and wake structures previously observed at very low Reynolds numbers, namely the simulation by Bourguet & Lo Jacono (2014), continue to exist at moderate Reynolds numbers $Re > 1000$, although, of course, there are also notable differences.

Chapter 5

Flow-induced Vibration of a Rotary Oscillating Cylinder

5.1 Introduction

In this chapter, the results of an elastically-mounted cylinder undergoing VIV and sinusoidally-driven rotary oscillations about its spanwise axis are presented and discussed. The experimental details relevant to the chapter's results are reviewed in §5.2. Work done to validate the sinusoidal rotary oscillation motion profile is included in Appendix A. The definition and phenomenon of 'lock-on' is presented and discussed in §5.3 prior to an overview of the cylinder's lock-on regions, vibration amplitude responses, fluid forces and phase responses being presented in §5.4. The impact of varying the forcing f_{rot}^* on the cylinder's response is examined in more depth in §5.5. Results on the effects of varying the forcing velocity ratio, A_m , follow. At selected f_{rot}^* , the evolution of the cylinder's response with varying A_m is examined in §5.6. The wake structure of the cylinder is characterised in §5.7. Section 5.8 discusses the effectiveness of rotary oscillation over a range of reduced velocities, U^* . The key findings are summarised in §5.9.

5.2 Experimental details

The experiment was conducted in the FLAIR water channel. A rotation rig was used to control the rotary motion of the cylinder and an air bearing system was used to provide low friction cross-flow oscillations. Further details on the experimental apparatus were discussed in §3.

Critical characteristics of the oscillating system were measured using free decay tests conducted before and after experiments. For the experiment on an elastically-mounted cylinder undergoing sinusoidally-driven rotary oscillations, the cylinder model used has a diameter of $D = 30$ mm and an immersed length of $l_{ms} = 614$ mm. The total mass of all oscillating components is $m_{osc} = 2.4481$ kg and the mass ratio is $m^* = 5.641$. From free decay tests, the natural frequency of the oscillating system in air is $f_{na} = 0.468$ Hz and in water is $f_{nw} = 0.429$ Hz. Structural stiffness is provided by one pair of springs, these have an equivalent stiffness of $k = 0.0212$ N/mm and the oscillating system has a damping ratio of $\zeta = 0.001515$.

The primary experiment was done at reduced velocities $U^* = 5.5$ and 8.0 ; they belong to the upper and lower amplitude response branches of a cylinder undergoing non-rotating VIV, respectively. The two examined U^* corresponds to Reynolds numbers $Re = 1621$ and 2359 . At each tested U^* , the cylinder was prescribed a forcing velocity ratio in range of ($0 \lesssim A_m \lesssim 2$) and a forcing frequency ratio in range of ($0 \lesssim f_{rot}^* \lesssim 2$). The forcing velocity ratio is held constant as f_{rot}^* is varied in the increasing direction.

Secondary experiments were done with extended parameter ranges in limited cases. To study the presence of the lock-on regions at higher values of forcing velocity ratios ($0 \lesssim A_m \lesssim 3.5$); two tests were conducted at $f_{rot}^* = 1.0$ and 3.0 and at $U^* = 5.5$. The impact of rotary forcing on the cylinder's vibration response over a range of reduced velocities was also examined. In this experiment, the reduced velocity is in range of $U^* = 3 - 20$, equivalent to the Reynolds numbers range of ($885 \lesssim Re \lesssim 5899$).

5.3 The phenomenon of ‘rotary-lock-on’

The phenomenon of lock-on is fundamental to understanding rotary oscillation's ability to suppress vortex shedding. Lock-on, explained in greater detail in §2, occurs when the cylinder's vortex shedding frequency, f_{sh} , follows f_{osc} . Tokumaru & Dimotakis (1991); Cheng *et al.* (2001); Cheng (2001); Choi *et al.* (2002) among others have reported favourable results in drag as lock-on occurs for a rigidly-mounted cylinder. However, VIV researchers studying elastically-mounted bodies are more interested in the cross-flow lift as it affects the oscillation amplitude of the body, which can be more destructive in engineering applications.

Du & Sun (2015) reported observing lock-on in their low Reynolds number ($Re = 350$) simulation of an elastically-mounted cylinder undergoing rotary oscillations. In their spectral analysis of the cylinder displacement and forces they revealed that under the traditional definition of lock-on, the natural frequency of the oscillating system (f_n) may persist. The inability of rotary forcing to suppress oscillation at f_n results in persistent larger amplitude oscillations at some values of f_{rot}^* . While it is not a part of the lock-on definition, Du & Sun (2015) showed that the body oscillation frequency (f) may continue to follow the frequency response of a non-rotating cylinder undergoing VIV, f_{VIV} , and not f_{osc} during lock-on.

A system is considered locked-on given that the dominant lift frequency peak equals the combined $f_{sh} - f_{osc}$ frequency peak. Under this condition, even if the combined $f_{sh} - f_{osc}$ peak is marginally higher in power than the f_n peak, the system is still considered to be under lock-on. While the traditional lock-on definition is unambiguous when identifying the changes to the lift force frequencies, the impact of lock-on of the vibration response is unclear, particularly near the lock-on boundaries where the combined f_{sh} , f_{osc} and f_n peaks are comparable in power. Du & Sun (2015) showed that the body is only locked on to the rotary forcing (*i.e.* $f = f_{osc}$) when the shedding in the wake is synchronised with the rotary forcing motion (*i.e.* $f_{sh} = f_{osc}$).

In light of this the present thesis uses a different lock-on definition. To satisfy the traditional condition of lock-on and to clearly show its influence on the vibration response of the body, the vortex shedding frequency, f_{sh} , is replaced with the oscillation frequency of the body, f . To avoid confusion, this is referred to as ‘rotary-lock-on’ and is defined as

$$f \cong f_{osc}. \quad (5.1)$$

As the locking between f and f_{osc} occurs as a subset of the f_{sh} locking onto f_{osc} , rotary-lock-on can satisfy the lock-on condition while showing clearer links between the rotary forcing and the vibration response of the cylinder. The definition is also suitable for practical applications as it provides engineers a direct relationship between the rotary and translational motions of the cylinder.

Rotary-lock-on is observed throughout all studied A_m values in the present study. The PSD of the displacement signal is presented in fig. 5.1 as a function of normalised frequency response (f^*). From §4, f^* is defined as f normalised by f_{nw} . Four different cases of f_{rot}^* are presented at a fixed reduced velocity of $U^* = 5.5$ and velocity ratio $A_m = 0.9$. In fig. 5.1, the vertical dashed lines represent f_{VIV} and the red dot-dash line represents the forcing f_{rot}^* . It is evident that at a low f_{rot}^* , rotary-lock-on does not occur and the oscillation frequency, f , of the cylinder (labelled in each subplot of fig. 5.1 and fig. 5.2) follows a value close to f_{VIV} and f_{nw} (see fig. 5.1(a)).

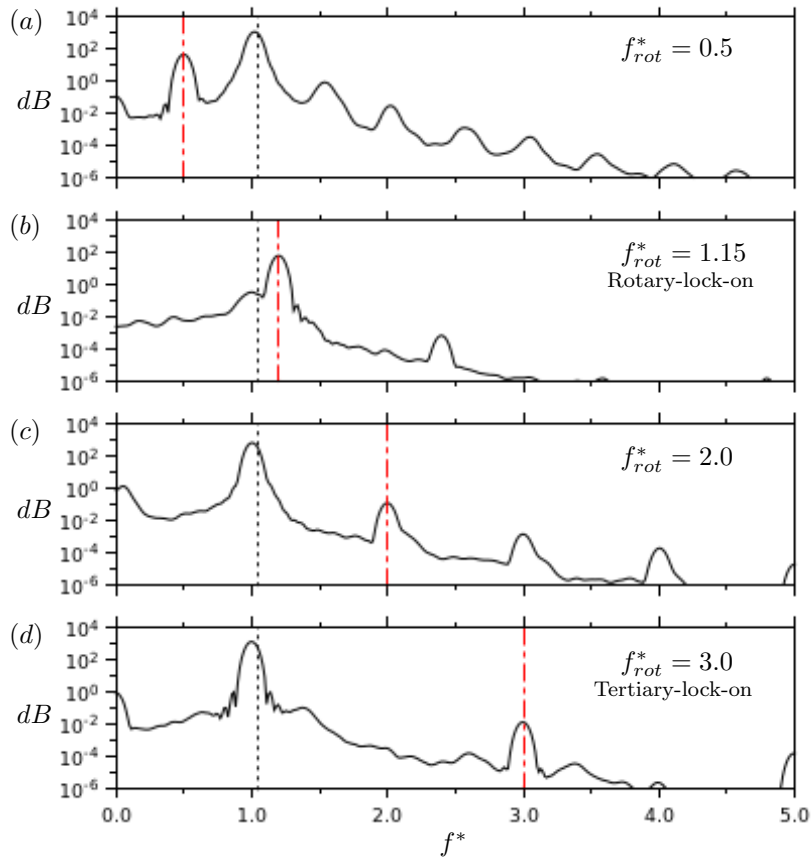


FIGURE 5.1: The power spectral density (PSD) of the displacement signal of four different cases of forcing frequency ratio (f_{rot}^*) are presented at a fixed reduced velocity belonging to the upper amplitude response branch of a non-rotating cylinder undergoing VIV ($U^* = 5.5$) and forcing velocity ratio $A_m = 0.9$. The vertical dashed lines represent the non-rotating VIV oscillation frequency (f_{VIV}) and the red dot-dash line represents f_{rot}^* .

As f_{rot}^* is increased, the body undergoes rotary-lock-on, f follows f_{osc} as the dominant frequency peak overlaps the red dot-dash line in fig. 5.1(b). Further increases in f_{rot}^* result in the body no longer locking on to the forcing and the cylinder’s primary response returns to f_{nw} and is close to the non-rotating cylinder response (as illustrated by the vertical dashed line in fig. 5.1(c)). Increasing f_{rot}^* further results in the cylinder undergoing rotary-lock-on for the second time as shown in fig. 5.1(d). This is known as ‘tertiary-lock-on’ and has been observed in previous rigid cylinder studies (see Choi *et al.* (2002); Thiria *et al.* (2006)) In rigid cylinder studies, tertiary-lock-on occurs when the vortex shedding frequency locks with the sub-harmonic frequency at one-third the forcing frequency (*i.e.* $\frac{1}{3}f_{osc}$). Du & Sun (2015) appear to have not observed tertiary-lock-on. Here the tertiary-lock-on is observed for some ranges of the forcing parameters. The tertiary-lock-on in the present study refers to the body oscillation frequency locking on to one-third of the forcing frequency $\frac{1}{3}f_{osc}$ given the above definition of rotary-lock-on.

From fig. 5.1(a), it is clear that f is synchronised with f_{nw} . However, this is not the case at $U^* = 8.0$, in the upper branch. The PSD of the displacement signals of four f_{rot}^* cases are presented in fig. 5.2 at the same velocity ratio $A_m = 0.9$ as fig. 5.1. As expected with an increase in U^* to the lower branch, fig. 5.2(a) and fig. 5.2(c) clearly show that f_{VIV} increased and shifted further away from f_{nw} . When the cylinder is not under rotary-lock-on, f follows f_{VIV} . The discrepancies between f following f_{nw} in the upper branch and f following f_{VIV} in the lower branch when the cylinder is not

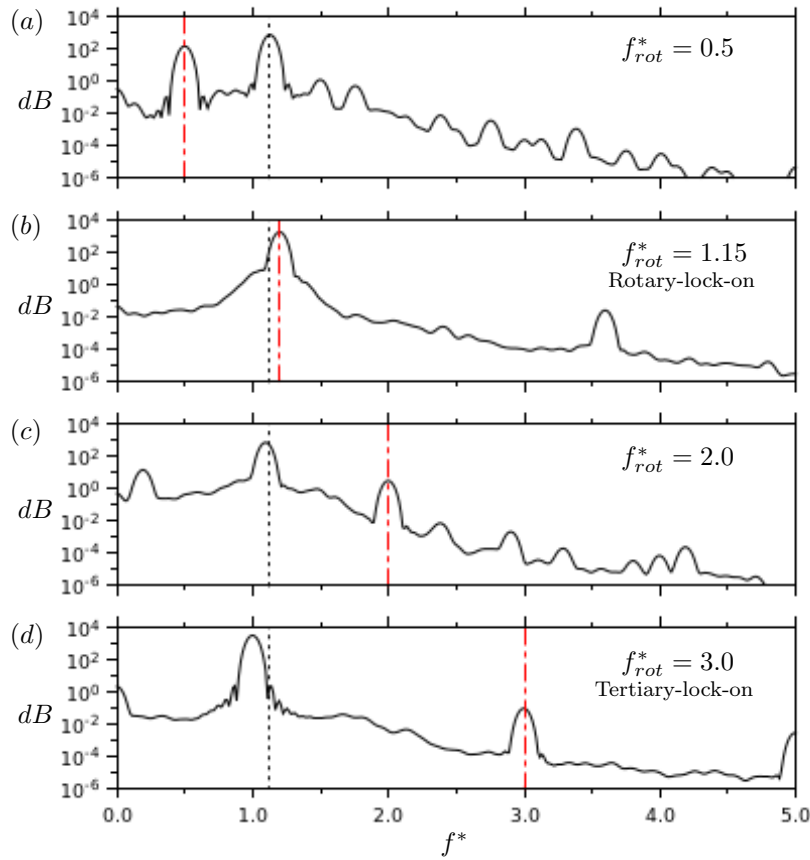


FIGURE 5.2: The power spectral density (PSD) of the displacement signal of four different cases of forcing frequency ratio (f_{rot}^*) are presented at a fixed reduced velocity belonging to the lower amplitude response branch of a non-rotating cylinder undergoing VIV ($U^* = 8.0$) and forcing velocity ratio $A_m = 0.9$. The vertical dashed lines represent the non-rotating VIV oscillation frequency (f_{VIV}) and the red dot-dash line represents f_{rot}^* .

under rotary-lock-on suggests that the oscillation frequency response could switch between following f_{nw} or f_{VIV} . Furthermore, it is probable that this switching behaviour is influenced by the proximity of f_{nw} and f_{VIV} values. Rotary-lock-on persists in the lower branch as f follows f_{rot}^* , as illustrated in fig. 5.2(b). From fig. 5.2(d) it is evident that tertiary-lock-on also exists in the lower branch. Based on these frequency observations, boundaries delimiting rotary-lock-on and tertiary-lock-on zones are defined, and the boundary maps of these regions for the two U^* cases are presented in fig. 5.3(a) and fig. 5.3(b).

Figure 5.3(a) presents the lock-on boundary map in the forcing frequency ratio and velocity ratio domain (f_{rot}^*, A_m) at a $U^* = 5.5$, which is close to the peak of the upper amplitude response branch for a non-rotating cylinder. From a small range of forcing frequency ratios close to $f_{rot}^* \approx 1$ at low A_m , the rotary-lock-on region expands to wider ranges of f_{rot}^* as A_m is increased. The increases in the width of the rotary-lock-on region is skewed towards higher f_{rot}^* and upper- f_{rot}^* boundary rapidly increases to higher f_{rot}^* when the velocity ratio is $A_m \gtrsim 1$.

These trends agree well with observations reported by Choi *et al.* (2002) for a rigid cylinder undergoing rotary oscillations. The tertiary-lock-on region resides near $f_{rot}^* \approx 3$ where the one-third sub-harmonic is $\frac{1}{3}f_{rot}^* \approx f^* \approx 1$. It initially increases in width as the velocity ratio is increased to $A_m \approx 0.5$. Further increases in A_m result in a rapid reduction in the width of the tertiary-lock-on region until it disappears when $A_m > 1.5$. Interestingly, at low velocity ratios ($A_m \lesssim 0.7$), the width

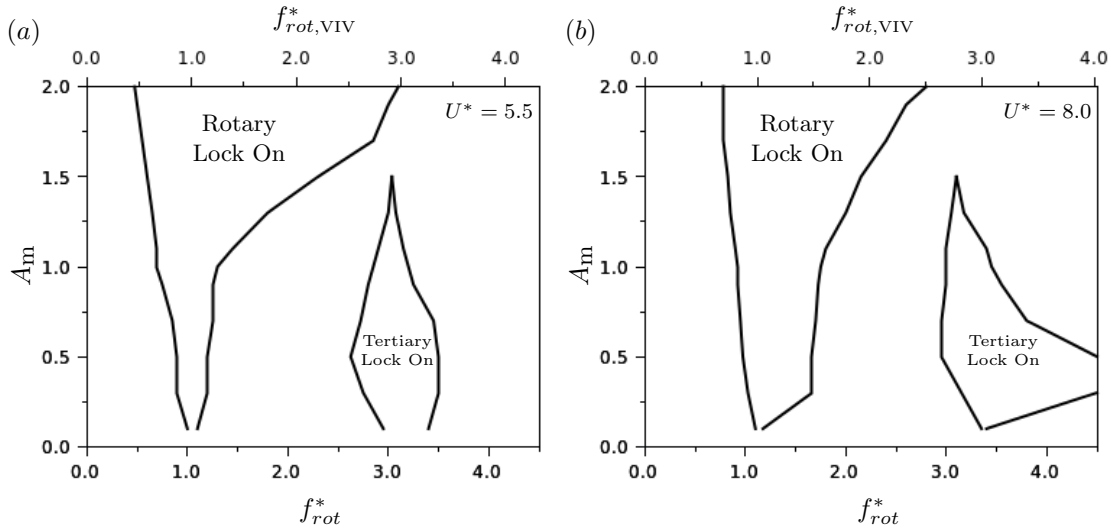


FIGURE 5.3: The approximate boundaries of the rotary-lock-on and tertiary-lock-on regions are presented as a function of the forcing velocity ratio (A_m) and forcing frequency ratio (primary x-axis: $f_{rot}^* = f_{osc}/f_{nw}$, secondary x-axis: $f_{rot,VIV}^* = f_{osc}/f_{VIV}$). (a) presents the reduced velocity case that corresponds to the upper amplitude response branch ($U^* = 5.5$) and (b) presents the reduced velocity case that corresponds to the lower amplitude response branch ($U^* = 8.0$).

of the tertiary-lock-on region is larger than that of the rotary-lock-on.

At $U^* = 8.0$, which is close to the centre of the lower amplitude response branch for a non-rotating cylinder, the boundary map in fig. 5.3(b) exhibits similarities to the upper branch. The rotary-lock-on region starts near $f_{rot}^* \approx 1$ and continues to be fan-shaped but is skewed towards higher f_{rot}^* . However, the evolution of the upper f_{rot}^* boundary is different to the upper branch case. The upper boundary increases to higher frequency ratio values rapidly between $0.1 \leq A_m \leq 0.3$. For $A_m > 0.3$, the widening of the rotary-lock-on region is gradual compared to the upper branch case. The tertiary-lock-on region no longer resembles a teardrop. Between $0.3 \leq A_m \leq 0.5$, the region extends to higher f_{rot}^* beyond the tested range of the present study.

It is plausible that the interpretation of the boundaries could change if, instead of f_{nw} , f_{rot}^* were normalised by f_{VIV} at the same reduced velocity. This new forcing frequency ratio, $f_{rot,VIV}^*$, is defined as

$$f_{rot,VIV}^* = \frac{f_{osc}}{f_{VIV}}, \quad (5.2)$$

where f_{osc} is the forcing frequency and f_{VIV} is the frequency response of a cylinder undergoing non-rotating VIV. This new parameter is used as a secondary x-axis in the top of fig. 5.3. At $U^* = 5.5$, there are no major changes to the rotary-lock-on region when f_{osc} is normalised by f_{VIV} . However, the approximate centre of the tertiary-lock-on region is located closer to $f_{rot,VIV}^* \approx 3$ than $f_{rot}^* \approx 3$. In the upper branch, changes are more obvious (see fig. 5.3(b)). At a low velocity ratio of $A_m = 0.1$, the rotary-lock-on and tertiary-lock-on regions can be observed near frequency ratios $f_{rot}^* \approx 1.1$ and $f_{rot}^* \approx 3.3$, respectively. These correspond to the ratios $f_{rot,VIV}^* \approx 1$ and $f_{rot,VIV}^* \approx 3$.

These observations suggest that using f_{VIV} rather than f_n results in a stronger correlation between lock-on boundaries and the frequency response of a cylinder undergoing non-rotating VIV. The present study was conducted with forcing parameters selected based on the natural frequency of the structure in water, f_{nw} . To avoid confusion, subsequent discussions will be based on the forcing f_{rot}^* normalised by f_{nw} unless specified. For reference, the $f_{rot,VIV}^*$ based on the non-rotating VIV frequency response f_{VIV} will be presented as a secondary axis where it is relevant. It is recommended that the selection forcing parameters in future experiments be based on the non-rotating

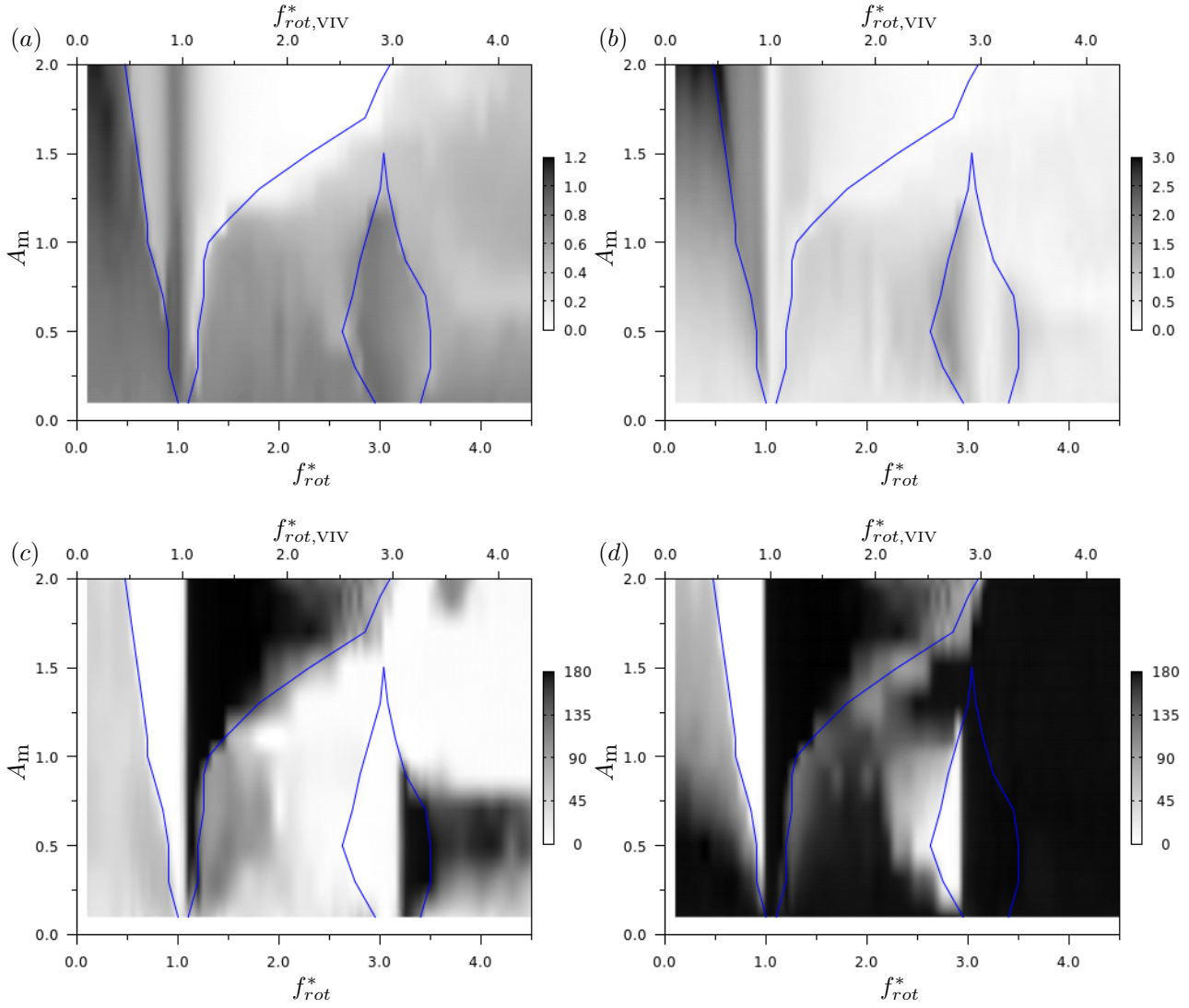


FIGURE 5.4: The contours of four key response quantities presented as a function of the forcing velocity ratio (A_m) and forcing frequency ratio (primary x-axis: $f_{rot}^* = f_{osc}/f_{nw}$, secondary x-axis: $f_{rot,VIV}^* = f_{osc}/f_{VIV}$) at a reduced velocity belonging to the upper amplitude response branch of a non-rotating cylinder undergoing VIV ($U^* = 5.5$). (a) contour of the mean of the highest 10% of normalised amplitude peaks (A_{10}^*), (b) contour of the RMS values of the total lift coefficient ($C_{y,RMS}$), (c) contour of the total phase (ϕ_T) and (d) contour of the vortex phase (ϕ_V). The blue outline in each figure presents the approximate boundaries of the rotary-lock-on and tertiary-lock-on regions.

VIV frequency response f_{VIV} .

5.4 Amplitude responses, fluid forces and phase responses

Due to the extensive data set collected with the independent variables being f_{rot}^* , A_m and U^* this section presents their effect on the cylinder's amplitude response, theoretical forces and phases using contour plots based on the lock-on boundary maps in fig. 5.3(a) and fig. 5.3(b). By overlaying the contours with the approximate boundaries delimiting the rotary-lock-on and tertiary-lock-on regions, it is possible to observe how trends and variations in each response quantity correlate with these regions.

5.4. Amplitude responses, fluid forces and phase responses

Figure 5.4(a) presents a contour of the mean of the highest 10% of normalised amplitude peaks, A_{10}^* , as a function of f_{rot}^* and A_m at $U^* = 5.5$, i.e. the upper amplitude response branch of a non-rotating cylinder. A_{10}^* of the non-rotating VIV case at the U^* is $A_{10}^* \approx 0.8$. It also shows interesting behaviour in how the A_{10}^* varies with changes in forcing parameters. Clearly, a low A_{10}^* region coincides with the rotary-lock-on region, which is expected. However, as rotary-lock-on occurs the system can no longer sustain lock-in, the primary mechanism behind large amplitude oscillations in non-rotating VIV. In the rotary-lock-on region the body oscillation frequency, f , synchronises with f_{osc} and deviates from frequencies at which large body oscillations occur for a non-rotating elastically-mounted body (f_{nw} and f_{VIV}).

Within the rotary-lock-on region there is a small range of forcing frequency ratios ($f_{rot}^* \approx 1$) where large oscillation amplitudes remain. The cylinder's A_{10}^* returns to values close to or above the amplitude response in the non-rotating VIV case as a result of its being forced to oscillate at frequencies close to f_{VIV} and f_{nw} (i.e. $f_{osc} \approx f_{VIV} \approx f_{nw}$).

Within the boundaries of the tertiary-lock-on region, A_{10}^* is higher than in its surrounding regions and is comparable to that of a non-rotating cylinder. This can be explained by the one-third subharmonic of f_{osc} being in close to f_{VIV} and f_{nw} .

Outside the rotary-lock-on and tertiary-lock-on regions, large amplitude responses are observed. At f_{rot}^* below the lower boundary of the rotary-lock-on region A_{10}^* is comparable at low ranges of velocity ratios ($A_m \lesssim 1$), as A_m is increased above $A_m \approx 1$, A_{10}^* increases with A_m . The peak A_{10}^* amplitude response in this U^* case is $A_{10}^* \approx 1.2$. At f_{rot}^* above the upper limits of the rotary-lock-on region and excluding the tertiary-lock-on region, A_{10}^* generally decreases with increasing A_m . In the same region and at low velocity ratios ($A_m \lesssim 0.5$), A_{10}^* is similar to the non-rotating value.

Figure 5.4(b) presents a contour plot of the RMS values of the total lift coefficient, $C_{y,RMS}$, as a function of f_{rot}^* and A_m at $U^* = 5.5$, i.e. in the upper branch of a non-rotating cylinder. Within the rotary-lock-on region, when the frequency ratio is $f_{rot}^* \gtrsim 1$, $C_{y,RMS}$ is comparable to non-rotating cylinder values. However, below a frequency ratio of $f_{rot}^* \approx 1$ $C_{y,RMS}$ is significantly higher than that of a non-rotating cylinder. The global peak $C_{y,RMS}$ occurs near the lower bounds of the rotary-lock-on region at velocity ratios $A_m \gtrsim 1.9$.

Within the rotary-lock-on region, a band of low $C_{y,RMS}$ exist where the forcing frequency is close to the non-rotating VIV frequency response, and the natural frequency (i.e. $f_{osc} \approx f_{VIV} \approx f_{nw}$). At f_{rot}^* immediately below this low-lift band there exists a band of high- $C_{y,RMS}$ that coincides with the location of the high-amplitude (A_{10}^*) band seen in fig. 5.4(a). It is unsurprising to observe this as large total lift forces ($C_{y,RMS}$) naturally results in larger motion responses. However, it is unexpected to observe a global peak value in $C_{y,RMS}$ and large $C_{y,RMS}$ values near the lower boundary of the rotary-lock-on region without a corresponding region of high A_{10}^* . This is explored in more detail in §5.5.

In the tertiary-lock-on region, an area of higher $C_{y,RMS}$ occurs when $f_{rot}^* \lesssim 3$. This high $C_{y,RMS}$ region coincides with a region of higher A_{10}^* . It is also evident that within the rotary-lock-on and tertiary-lock-on regions the cylinder exhibits larger $C_{y,RMS}$ between their lower boundaries and forcing frequencies $f_{rot}^* \approx 1$ (rotary-lock-on) and $f_{rot}^* \approx 3$ (tertiary-lock-on).

Outside the rotary-lock-on and tertiary-lock-on regions, large $C_{y,RMS}$ is observed at f_{rot}^* below the lower boundary of the rotary-lock-on region and their values increase with A_m . At f_{rot}^* above the upper boundary of the rotary-lock-on region and excluding the tertiary-lock-on region, $C_{y,RMS}$ is comparable to, or below, the values for a non-rotating cylinder. As f_{rot}^* and A_m ratios increase, $C_{y,RMS}$ decreases.

Figure 5.4(c) presents a contour of the total phase, ϕ_T , defined as the phase angle difference between the total lift force, C_y , and the cylinder displacement, y , as a function of f_{rot}^* and A_m at $U^* = 5.5$, belonging to the upper amplitude response branch of a non-rotating cylinder. In the same format, fig. 5.4(d) presents vortex phase, ϕ_V , defined as the phase angle difference between the

vortex force, C_v (total lift force, C_y , excluding the effects of added mass) and y . The total phase of the cylinder within the rotary-lock-on region is split into two areas. C_y remains in-phase with the motion as $\phi_T \approx 0^\circ$ up to frequency ratios slightly above $f_{rot}^* = 1$. When the frequency ratio is $f_{rot}^* \gtrsim 1$, C_y and the cylinder's motion move out of phase and the total phase abruptly jumps from $\phi_T \approx 0^\circ$ to $\phi_T \approx 180^\circ$. Similar behaviour is observed in ϕ_V in fig. 5.4(d). However, the jump from in to out-of-phase occurred at a f_{rot}^* slightly below $f_{rot}^* = 1$. As a result of C_y and C_v forces become out of phase with the motion of the cylinder both A_{10}^* and $C_{y,RMS}$ decreases. This behaviour is similar to that observed in non-rotating VIV studies (see Govardhan & Williamson (2000); Zhao (2012)), particularly in the transition between the upper and lower amplitude response branches where the reductions in amplitude response is accompanied by C_y and C_v being out of phase with the motion of the cylinder.

In the rotary-lock-on region, there is a small band of f_{rot}^* values where ϕ_V jumped to $\phi_V \approx 180^\circ$ while the total phase remained at $\phi_T \approx 0^\circ$. In this narrow band of f_{rot}^* there is a large range of total lift values ($C_{y,RMS}$). These vary from high to low values as f_{rot}^* is increased. This occurs while the A_{10}^* remains relatively large. Such behaviour is similar to what is seen in the upper amplitude response branch from non-rotating VIV cases. The present results suggest similar phase behaviour exist in the tertiary-lock-on region. However, the band of frequency ratios where ϕ_V jumped to $\phi_V \approx 180^\circ$ and the total phase remained at $\phi_T \approx 0^\circ$ has broadened. In this range of f_{rot}^* the transition from a higher to lower total lift and reduced amplitude response is more subtle. At f_{rot}^* below the lower boundaries of the rotary-lock-on region, ϕ_T is slightly higher in value ($\phi_T \approx 45^\circ$) than that of a non-rotating cylinder ($\phi_T \approx 0^\circ$). In the same region, at low velocity ratios ($A_m \lesssim 0.5$) ϕ_V , similar to a non-rotating cylinder, remained at $\phi_V \approx 180^\circ$. As velocity ratio is increased ($A_m \gtrsim 0.5$), the vortex phase decreases to $\phi_V \approx 90^\circ$. At f_{rot}^* above the upper boundary of the rotary-lock-on region and excluding the tertiary-lock-on region, C_y remains mostly in phase with motion while C_v remains mostly out of phase.

Figure 5.5(a) presents a contour of the mean of the highest 10% of normalised amplitude peaks, A_{10}^* , as a function of f_{rot}^* and A_m at $U^* = 8.0$ belonging to the lower amplitude response branch of a non-rotating cylinder. In addition to the changes in the boundaries of the rotary-lock-on and tertiary-lock-on regions discussed in §5.3, there are changes to the cylinder's amplitude response when the reduced velocity is increased.

In the rotary-lock-on region, large amplitude reductions continue to exist where the frequency ratio is $f_{rot,VIV}^* \gtrsim 1$ (or $f_{rot}^* \gtrsim 1.1$). The high-amplitude band previously observed in the upper branch ($U^* = 5.5$) widens to lower frequency ratio values ($f_{rot,VIV}^* \lesssim 1$) that are close to the lower boundary of the rotary-lock-on region in the lower branch. The global peak for $U^* = 8.0$ occurs in this high-amplitude band at $f_{rot}^* \approx 1$ and $A_m = 2$. From the two U^* cases, it is observed that within this high-amplitude band, the A_{10}^* amplitude response increases with A_m . (It is possible A_{10}^* will increase to higher values with further increases in A_m .) Near the lower boundary a narrow zone of low A_{10}^* amplitude response is observed. Similar behaviour is observed in the upper branch where A_{10}^* decreases abruptly as the cylinder becomes rotary-locked-on. As the forcing frequency is increased A_{10}^* also increases up to $f_{rot,VIV}^* \approx 1$. Comparison of the two U^* cases shows that the lower boundary of the rotary-lock-on region shifts to higher f_{rot}^* and that the low-amplitude zone below the high-amplitude band widens as U^* is decreased. An immediate increase in A_{10}^* above that of a non-rotating cylinder is observed at the lower f_{rot}^* boundary of the tertiary-lock-on region.

As f_{rot}^* is increased within the tertiary-lock-on region the A_{10}^* amplitude response decreased. At frequency ratios below the lower rotary-lock-on region boundary A_{10}^* is close to the non-rotating value at low A_m . As A_m is increased above $A_m \approx 1.3$, there is a gradual increase in A_{10}^* . Between the upper f_{rot}^* boundary of the rotary-lock-on region and the lower boundary of the tertiary-lock-on region there exists an area where A_{10}^* is comparable to that of a non-rotating cylinder at $A_m \lesssim 1.3$. However, when $A_m \gtrsim 1.3$ there is a decrease in A_{10}^* that is more abrupt than those observed in the

5.4. Amplitude responses, fluid forces and phase responses

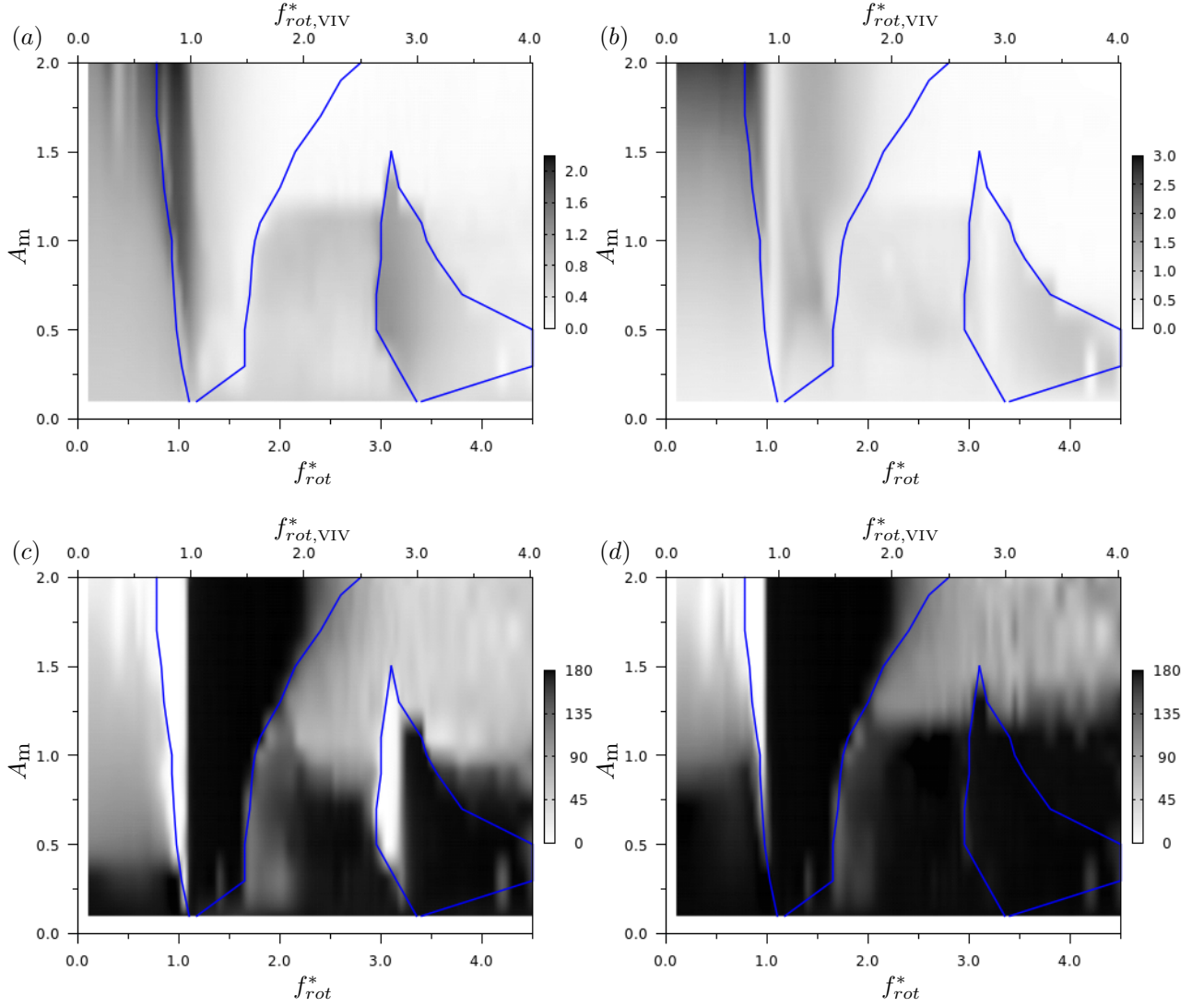


FIGURE 5.5: The contours of four key response quantities presented as a function of the forcing velocity ratio (A_m) and forcing frequency ratio (primary x-axis: $f_{rot}^* = f_{osc}/f_{nw}$, secondary x-axis: $f_{rot,VIV}^* = f_{osc}/f_{VIV}$) at a reduced velocity belonging to the lower amplitude response branch of a non-rotating cylinder undergoing VIV ($U^* = 8.0$). Refer to fig. 5.4 caption for detailed description of the figure.

upper branch case.

The total lift ($C_{y,RMS}$) of the cylinder in the lower branch ($U^* = 8.0$) exhibits similar trends to what was seen in the upper branch ($U^* = 5.5$). Figure 5.5(b) shows $C_{y,RMS}$ as a function of f_{rot}^* and A_m at $U^* = 8.0$. In the rotary-lock-on region $C_{y,RMS}$ is higher near the lower f_{rot}^* boundary. As f_{rot}^* increases past $f_{rot}^* \approx 1.1$, there exist a band of low $C_{y,RMS}$, not unlike that observed in the upper branch $U^* = 5.5$. At frequency ratios above $f_{rot}^* \approx 1.1$, $C_{y,RMS}$ is lower than what is observed near the lower f_{rot}^* boundary of the rotary-lock-on region but remains at values above the non-rotating case. Trends in the tertiary-lock-on region and outside the rotary-lock-on region are similar to those previously described for the upper branch ($U^* = 5.5$).

Figure 5.5(c) presents a contour of ϕ_T as a function of forcing frequency ratios and velocity ratios at $U^* = 8.0$. Fig. 5.5(d) presents ϕ_V of the cylinder. From these figures, it is clear that the trends in ϕ_T and ϕ_V phases within the rotary-lock-on and tertiary-lock-on regions are the same as those in the upper amplitude response branch ($U^* = 5.5$).

In the rotary-lock-on region ϕ_T jumped from $\phi_T \approx 0^\circ$ to $\phi_T \approx 180^\circ$ at a frequency ratio of $f_{rot}^* \approx 1.1$. The same jump in phase angle occurred at a slightly lower frequency ratio of $f_{rot}^* \approx 1$ for ϕ_V . The tendency for ϕ_T and ϕ_V to jump within the rotary-lock-on region are similar to that seen in the upper branch ($U^* = 5.5$). This suggests that the mean ϕ_T magnitude and its transitions within the rotary-lock-on region are largely independent of the U^* of the cylinder, though further work is needed to make this suggestion definitive.

In the tertiary-lock-on region ϕ_T retains similar trends to that seen in the upper branch. The mean vortex phase, however, remains out of phase and do not jump from $\phi_V \approx 0^\circ$ to $\phi_V \approx 180^\circ$.

Outside the rotary-lock-on and tertiary-lock-on regions, the phases also exhibit differences to the upper branch case. Below the lower f_{rot}^* boundary of the rotary-lock-on region and at velocity ratios $A_m \lesssim 0.3$ C_y remains out of phase with the motion ($\phi_T \gtrsim 160^\circ$). As C_y of a non-rotating cylinder undergoing VIV is also out of phase with the motion of the cylinder, it is unsurprising that C_y remains out of phase with the motion. As the velocity ratio and its influence on the cylinder's response both increased, C_y becomes more in phase with the motion and the mean total phase decreases to $\phi_T \approx 90^\circ$. In the same region, ϕ_V remained at $\phi_V \approx 180^\circ$ up to a velocity ratio of $A_m \approx 0.7$, the ϕ_V decreases shortly thereafter.

Above the upper f_{rot}^* boundary of the rotary-lock-on region and outside the tertiary-lock-on region, the total force, C_y , remains out of phase up to a velocity ratio of $A_m \approx 0.8$. With further increases in velocity ratio above $A_m \approx 0.8$ the mean total phase decreases from $\phi_T \approx 180^\circ$ to $\phi_T \approx 45^\circ$. In the same parameter space region, ϕ_V of the cylinder remained close to $\phi_V \approx 180^\circ$ and only decreased to $\phi_V \approx 90^\circ$ after the velocity ratio is increased pass $A_m \approx 1.3$.

The results presented these contours plots provides an overview of the changes in the response variables with reference to the rotary-lock-on and tertiary-lock-on regions. To better understand the changes in each response quantity with the forcing parameters an in-depth investigation into the relationships between different responses is needed, this is presented in the following sections. In §5.5, the response of the cylinder with the cylinder over a range of f_{rot}^* at selected fixed A_m cases will be presented in detail. Section 5.6 will present the response of the cylinder with the cylinder over a large range of A_m at selected fixed f_{rot}^* cases.

5.5 Response at fixed forcing velocity ratios

Here, the responses of an elastically-mounted cylinder undergoing sinusoidally-driven rotary oscillations is examined in greater detail at selected velocity ratio, A_m , cases. These cases are located in the A_m - f_{rot}^* domain, they are illustrated in fig. 5.6(a) for the upper branch ($U^* = 5.5$) and in fig. 5.6(b) for the lower branch ($U^* = 8.0$) cases. In fig. 5.6(a) and (b), the red lines represent fixed A_m cases, the arrow head indicates the direction in which f_{rot}^* were varied. Red circles in fig. 5.6(a) and (b) represent points in the A_m - f_{rot}^* domain where the time history, PSD and of the cylinder's response characteristics were examined.

The response of the cylinder over the range of forcing frequency ratios tested ($f_{rot}^* = 0 - 4.5$) at $A_m = 0.5$ and $U^* = 5.5$ is presented in fig. 5.7. Figure 5.7(a) presents the mean of the highest 10% of normalised amplitude peaks (A_{10}^*) as a function of f_{rot}^* . The black dashed line shows the response of the non-rotating case. Figure 5.7(b) presents a PSD contour of the cylinder's displacement (y) as a function of normalised frequency response (f^*) and f_{rot}^* . The power density is normalised by the peak power at each f_{rot}^* value. The blue dotted line shows f^* is equal to f_{rot}^* . The blue dot-dashed lined illustrates the one-third subharmonic of the forcing frequency ratio $f^* = f_{rot}^*/3$. Figure 5.7(c) and fig. 5.7(d) presents the force coefficients and phases as a function of f_{rot}^* .

In both Figure 5.7(c) and fig. 5.7(d), the black markers represent the RMS total force coefficient, $C_{y,RMS}$, and mean total phase, ϕ_T . Similarly, in in both figures, the blue markers represent $C_{v,RMS}$ and ϕ_V . The black dotted line and blue dot-dashed line represent the total and vortex component

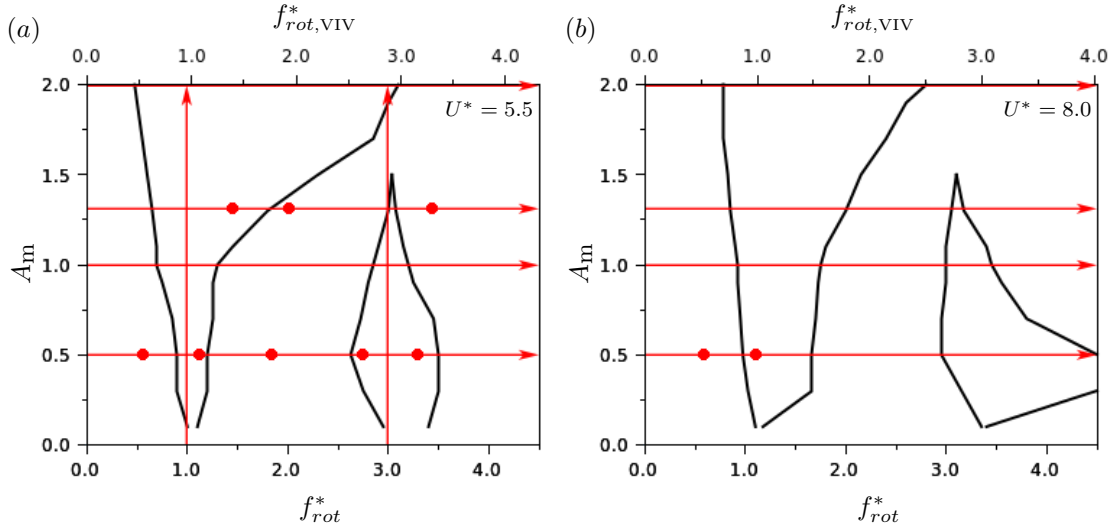


FIGURE 5.6: Cases of the fixed forcing velocity ratio (A_m) and fixed forcing frequency ratio (f_{rot}^*) where the response of the cylinder is examined in more detail is presented in form of a visual map in the $A_m - f_{rot}^*$ parameter space. (a) presents the cases in the upper branch at reduced velocity of $U^* = 5.5$ and (b) presents the cases in the lower branch at a reduced velocity of $U^* = 8.0$. Red lines represent the locations of the fixed parameter cases and the arrow head indicates the direction in which the forcing parameter was increased. Red circle markers indicate points in the $A_m - f_{rot}^*$ domain where the time history, power spectra density (PSD) and distribution of the cylinder's response quantities will be examined

values of a non-rotating cylinder, respectively. In fig. 5.7, the rotary-lock-on and tertiary-lock-on regions are highlighted by vertical red lines. Figures presenting subsequent fixed A_m cases follow the same format.

Figure 5.7(a) shows that as f_{rot}^* is increased towards the lower f_{rot}^* boundary of the rotary-lock-on region the amplitude response increases from $A_{10}^* \approx 0.8$ for the non-rotating cylinder to a local peak of $A_{10}^* \approx 0.95$. The local peak A_{10}^* occurs as the cylinder's oscillation frequency, f , passes f_{nw} . There is a corresponding peak in RMS total force coefficient, $C_{y,RMS}$, and an abrupt drop in RMS vortex force coefficient, $C_{v,RMS}$. As the A_{10}^* amplitude response approaches the local peak, ϕ_T increased marginally to $\phi_T \approx 60^\circ$ while ϕ_V decreased from $\phi_V \approx 180^\circ$ to 0° . Fig. 5.7, shows that the increase in A_{10}^* in this range of f_{rot}^* is the result of both the total (ϕ_T) and vortex (ϕ_V) phases being in phase with the motion of the cylinder, resulting in large total lift forces, C_y .

As the cylinder enters the rotary-lock-on region, A_{10}^* and $C_{y,RMS}$ decrease sharply and the total ϕ_T and vortex ϕ_V phases increased to approximately 180° , indicating that the fluid forces are out of phase with the motion of the cylinder. Increasing f_{rot}^* results in the cylinder leaving the rotary-lock-on region and A_{10}^* and $C_{y,RMS}$ increase to values similar to those before the cylinder underwent rotary-lock-on.

The vortex force component, C_v , becomes out of phase as vortex phase returned to $\phi_V \approx 180^\circ$ and the total phase increased to $\phi_T \approx 120^\circ$. At most of the f_{rot}^* between the upper boundary of the rotary-lock-on region and the lower boundary of the tertiary-lock-on region A_{10}^* remains close to the non-rotating value and ϕ_T gradually decreases towards $\phi_T \approx 0^\circ$ with f_{rot}^* . At the onset of the tertiary-lock-on region A_{10}^* decreased, the normalised frequency response, f^* , gradually decreased pass f_{VIV} , and ϕ_V decreased from $\phi_V \approx 180^\circ$ to 0° .

As the cylinder initially undergoes tertiary-lock-on, there is a sharp increase in A_{10}^* and $C_{y,RMS}$. Both these quantities reach a secondary peak as the f^* of the cylinder approaches f_{VIV} , A_{10}^* and $C_{y,RMS}$ decreased thereafter. The total ϕ_T and vortex ϕ_V phases remain close to 0° during the initial increase in amplitude response in the tertiary-lock-on region. ϕ_V jumps to 180° as f^* passes f_{VIV}

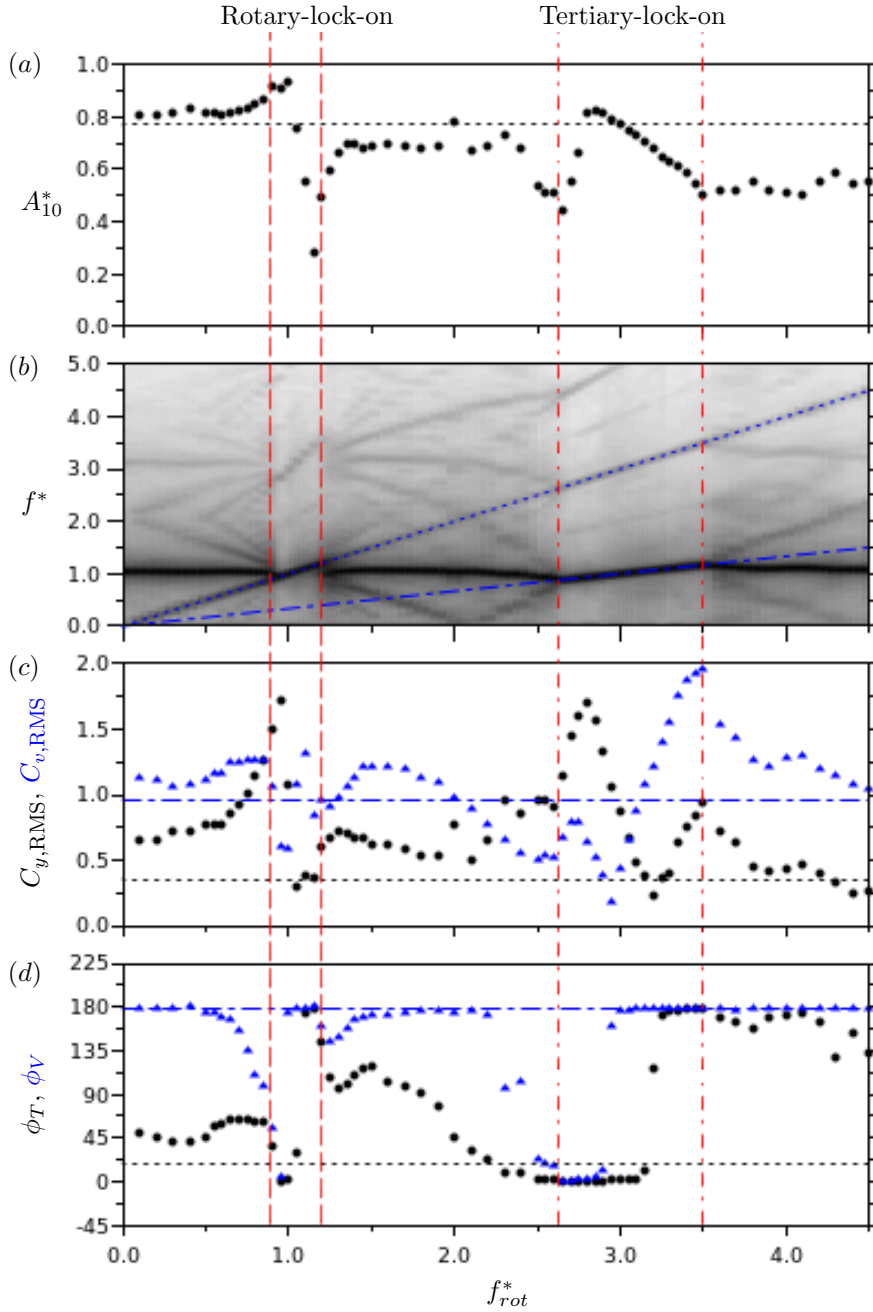


FIGURE 5.7: The response quantities of an elastically-mounted cylinder undergoing rotary oscillations is presented as a function of forcing frequency ratio (f_{rot}^*) at a fixed forcing velocity ratio of $A_m = 0.5$ and at a reduced velocity of $U^* = 5.5$. The rotary-lock-on and tertiary-lock-on regions are highlighted by vertical red lines. (a) presents the mean of the highest 10% of normalised amplitude peaks (A_{10}^*). The black dashed line represents the non-rotating VIV value. (b) presents a power spectra density (PSD) contour of the cylinder's displacement (y). The PSD is normalised by the peak power at each f_{rot}^* value. The blue dotted line illustrates the normalised frequency response, f^* , being equal to f_{rot}^* ($f^* = f_{rot}^*$). The blue dot-dashed lined illustrates the one-third subharmonic of f_{rot}^* ($f^* = f_{rot}^*/3$). (c) and (d) presents the RMS force coefficients ($C_{y,RMS}$, $C_{v,RMS}$) and mean phases (ϕ_T , ϕ_V), respectively. In both (c) and (d), the black markers represent the total component and the blue markers represent the vortex component. The black dotted line and blue dot-dashed line represent the total and vortex component values of a non-rotating cylinder, respectively.

($f \approx f_{VIV}$) while ϕ_T remains near 0° . These response trends associated with the rotary-lock-on and tertiary-lock-on regions were also observed in other fixed A_m cases.

From fig. 5.7, there are a number of interesting features. Principally, the rotary-lock-on and tertiary-lock-on is based on changes in the shedding frequency (f_{sh}), followed by the oscillating frequency (f) following the forcing frequency (f_{osc}) (or its sub-harmonic in the case of tertiary-lock-on). From the amplitude and frequency response plots in fig. 5.7(a) and (b), it is evident that these changes occur but the behavioural trends there are noticeable differences in the forces and phases between rotary-lock-on and tertiary-lock-on regions. A possible explanation for these differences could lie in the wake structure, this will be examined in §5.7.

To gain a clearer understanding on the cylinder's behaviour, the time history and distribution of its response quantities at several points of interest will be presented. Figure 5.8(a), (b) and (c) presents a sample of the time history of the cylinder's normalised displacement $y/D(t)$, forces ($C_y(t)$, $C_v(t)$) and phases ($\phi_T(t)$, $\phi_V(t)$). Figure 5.8(d) presents a distribution of all the amplitude peak values (A^*) of the entire recorded data sample. The count of each amplitude peak value is normalised by the highest count value. Figure 5.8(e) presents a PSD of the cylinder's displacement as a function of the normalised frequency response. The power density is normalised by the peak power and the vertical dashed line represents the f_{osc} . Figure 5.8(f) presents a distribution of all the total force, C_y (black), and vortex force, C_v (blue), coefficient values of the entire recorded data sample. Similar to fig. 5.8(d), the count of each coefficient value is normalised by the highest respective count value. Figure 5.8(g) presents a distribution of all the total phase, ϕ_T (black), and vortex phase, ϕ_V (blue), angle values of the entire recorded data sample. The count of each phase angle value is normalised by the highest respective count value. Later figures presenting the time history and the distribution of response quantities will follow this format.

Fig. 5.8(a) exhibits frequency modulation similar to those previously documented in Cheng *et al.* (2001); Choi *et al.* (2002) on the rotary oscillation of rigidly-mounted cylinders. Here, the amplitude of the cylinder switches between a higher state, where the normalised amplitude response (A^*) of the cylinder is close to $0.8D$, and a lower state, where the A^* is approximately $0.65D$ and a transition region where the value of A^* is between the higher and lower state.

The distribution of the amplitude peaks is shown in fig. 5.8(d) and shows clearly the three distinct amplitude states. Examining the displacement time history, it can be seen that the switching between these amplitude states occurs at a lower frequency than the oscillation frequency of the cylinder, with the switching occurring every one or two oscillation periods.

The PSD of the cylinder's displacement presented in fig. 5.8(e) shows two distinct peaks at frequency responses below $f^* < 1.5$. The frequency with the highest power (the frequency response of a non-rotating cylinder) is at $f^* \approx 1.05$, and the frequency with the second highest power is close to the forcing frequency ratio at $f^* \equiv f_{rot}^* \approx 0.65$. The rotary motion's influence persists even for an elastically-mounted cylinder, as evident in how it alters the cylinders cross-flow amplitude and frequency responses. The inconsistent switching behaviour is attributed by the frequency $f^* \approx f_{rot}^* \approx 0.65$ not being a subharmonic of the frequency response of a non-rotating cylinder ($f^* \approx 1.05$). At a forcing frequency ratio of $f_{rot}^* = 0.5$ the frequency modulation and amplitude switched consistently at twice the period of the oscillation frequency of the cylinder. As a result of the frequency modulation phenomenon, the time history of the fluid forces presented in fig. 5.8(b) exhibit switching and were not strongly sinusoidal. The distribution of the fluid forces presented in fig. 5.8(f) also showed evidence of scattering. The total ϕ_T and vortex ϕ_V phase time histories in fig. 5.8(c) show periodic jumps in value. The phase distribution in fig. 5.8(g) shows a split in the total phase between being out of phase at $\phi_T \approx 170^\circ$ to being in phase at $\phi_T \approx 0^\circ$. The vortex phase, however, remained at over $\phi_V \approx 100^\circ$.

Figure 5.9 presents the response of the cylinder while it undergoes rotary-lock-on at $f_{rot}^* \approx 1.15$ a velocity ratio of $A_m = 0.5$. The displacement time history in fig. 5.9(a) shows a periodic

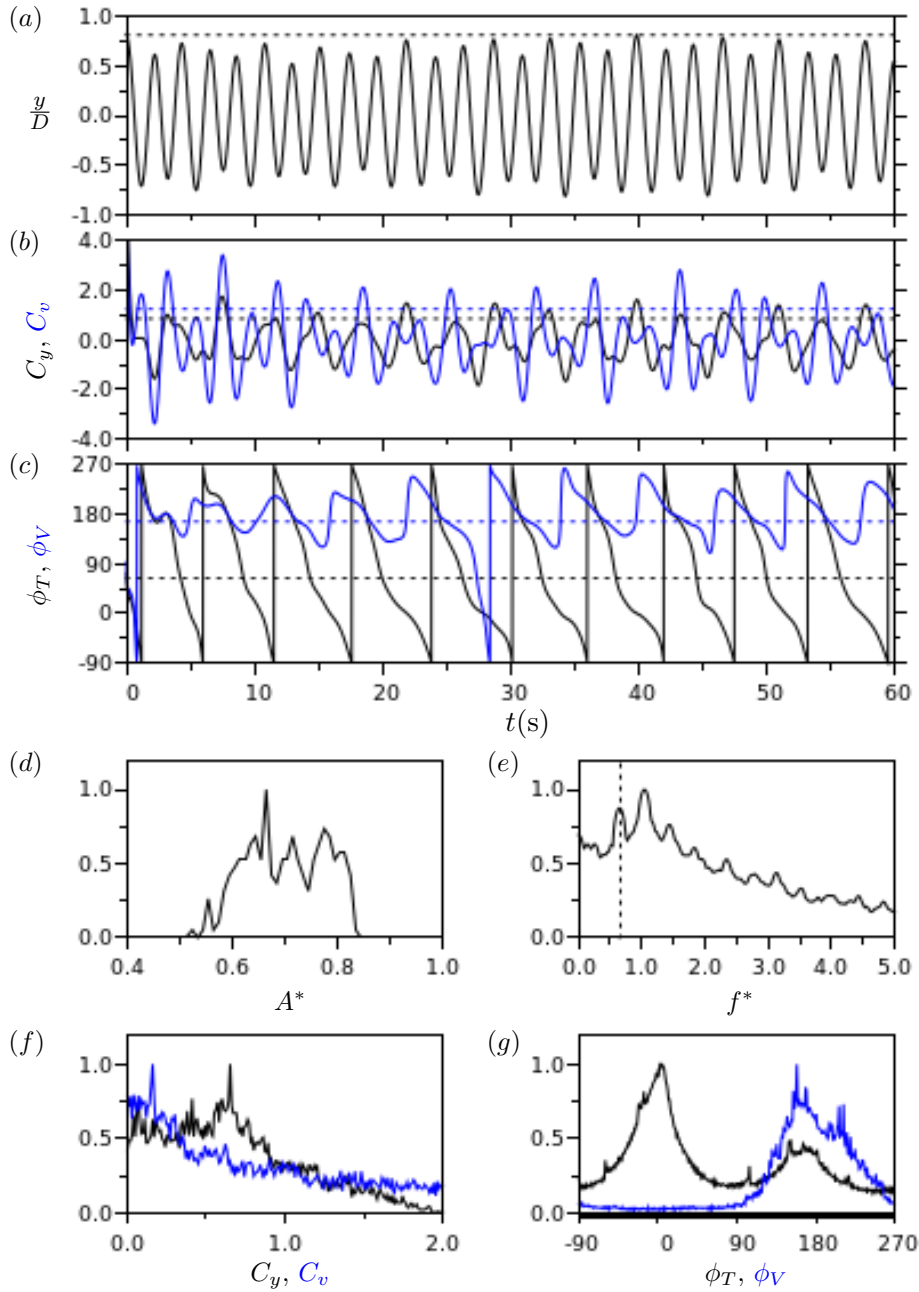


FIGURE 5.8: The response time histories and distribution of quantities of an elastically-mounted cylinder undergoing rotary oscillations at forcing frequency ratio $f_{rot}^* = 0.65$, forcing velocity ratio $A_m = 0.5$ and reduced velocity $U^* = 5.5$. (a), (b) and (c) presents a 60s sample of the normalised displacement (y/D), force coefficients (C_y, C_v) and phases (ϕ_T, ϕ_V) time histories, respectively. The distribution of amplitude peaks (A^*), force coefficients (C_y, C_v) and phases (ϕ_T, ϕ_V) are presented in (d), (f) and (g), respectively. The power of each quantity in (d), (f) and (g) is normalised by their respective peak power. (f) presents a power spectra density (PSD) of y/D , its power density is normalised by the peak power. In (b), (c), (f) and (g), the total and vortex components are represented by the black and blue data series, respectively. The black dashed line in (a) represents the mean of the highest 10% of the normalised amplitude peaks (A_{10}^*). The dashed lines in (b) represents the RMS values of the force coefficients ($C_{y,RMS}, C_{v,RMS}$), and the dashed lines in (c) represents the mean values of the phases. The vertical dashed line in (f) represents the forcing frequency (f_{osc}).

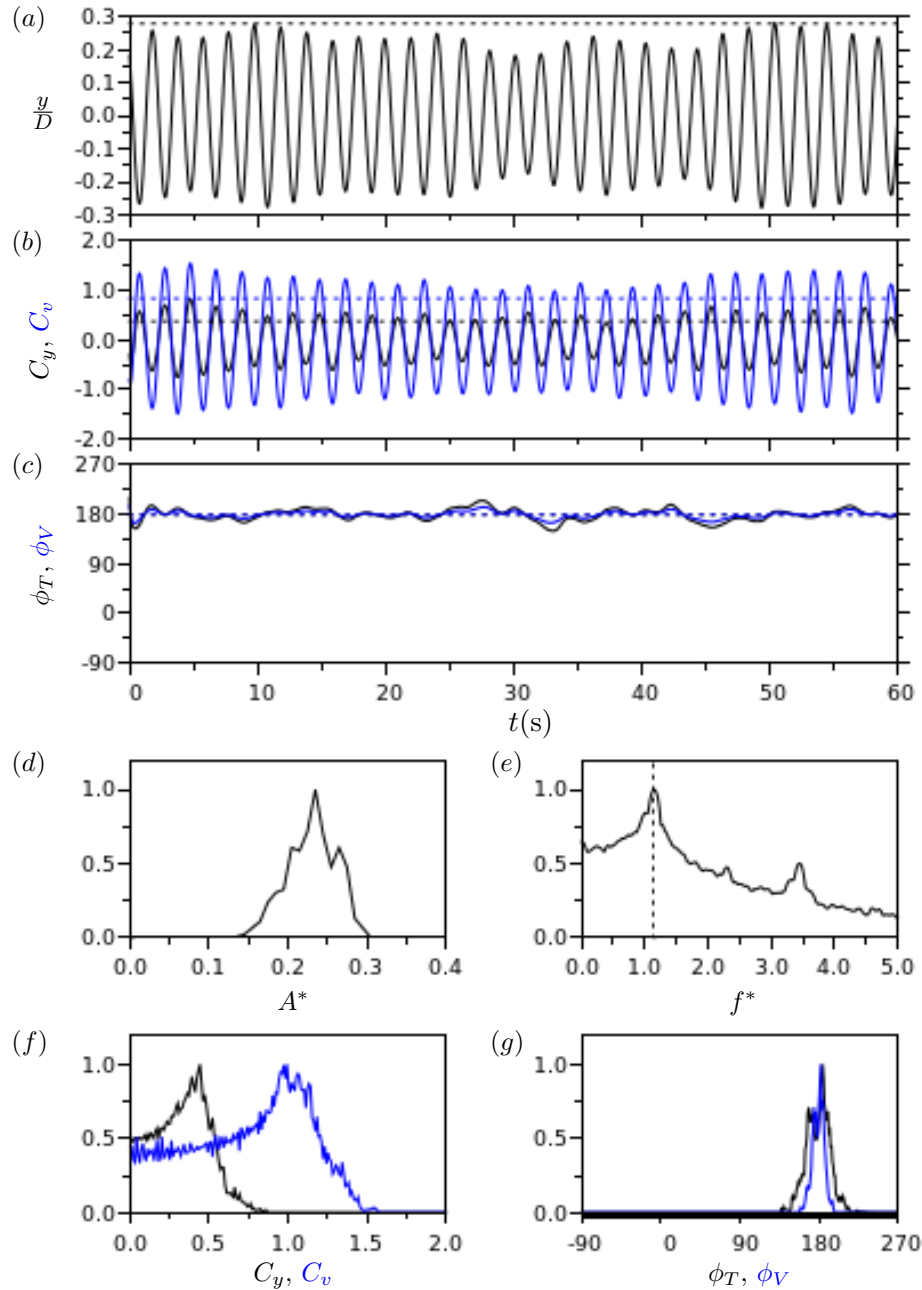


FIGURE 5.9: The response time histories and distribution of quantities of an elastically-mounted cylinder undergoing rotary oscillations at forcing frequency ratio $f_{rot}^* = 1.15$, forcing velocity ratio $A_m = 0.5$ and reduced velocity $U^* = 5.5$. Refer to fig. 5.8 caption for detailed description of the figures.

and sinusoidal signal with signs of beating. This is not unusual as the displacement of a cylinder undergoing non-rotating VIV can exhibit similar beating behaviour. As shown in fig. 5.9(d), there is a standard bell-shape distribution of amplitude peaks. While there is a single-peak instability the distribution the shape of the peak is quite broad compared to other f_{rot}^* cases. This may be caused by the slight difference between the frequency response of a non-rotating cylinder at $f^* \approx 1.05$ and the combined cylinder oscillation and rotary forcing frequency response at $f^* \equiv f_{rot}^* = 1.15$. The fluid forces are periodic and sinusoidal (see fig. 5.9(b)) and they exhibit single-peak distributions (see fig. 5.9(f)). Figure 5.9(c) and (g) show that both ϕ_T and ϕ_V phases are narrowly distributed around 180°. As f follows f_{osc} under rotary-lock-on, it is expected that the cylinder's response

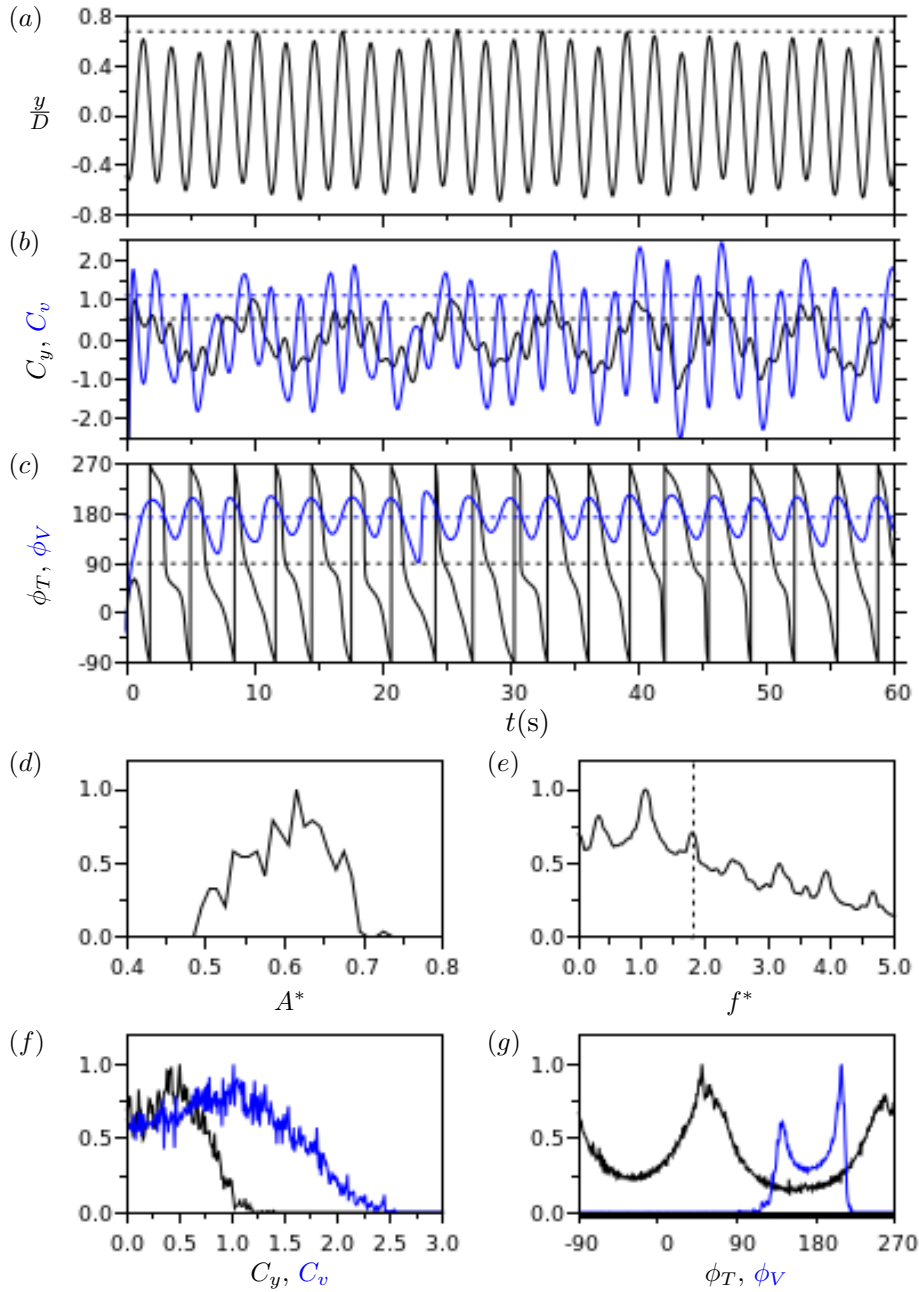


FIGURE 5.10: The response time histories and distribution of quantities of an elastically-mounted cylinder undergoing rotary oscillations at forcing frequency ratio $f_{rot}^* = 1.80$, forcing velocity ratio $A_m = 0.5$ and reduced velocity $U^* = 5.5$. Refer to fig. 5.8 caption for detailed description of the figures.

remains strong and sinusoidal despite large reductions in A_{10}^* amplitude response compared with the non-rotating case.

When $f_{rot}^* = 1.80$, between the rotary-lock-on and tertiary-lock-on region, there are changes to the cylinder's response from the rotary-lock-on case. Fig. 5.10 time histories show that the cylinder exhibits frequency modulation and response trends similar to those previously seen when f_{rot}^* is below the rotary-lock-on region (see fig. 5.8). The PSD of the cylinder's motion in fig. 5.10(e) shows the cylinder is oscillating at a frequency close to the frequency response of a non-rotating cylinder, $f^* \approx 1.05$, while the forcing frequency ratio is at $f^* \equiv f_{rot}^* \approx 1.80$. A_{10}^* and force coefficients are distributed over a larger range of values as a result of the frequency modulation (see fig. 5.10(d) and

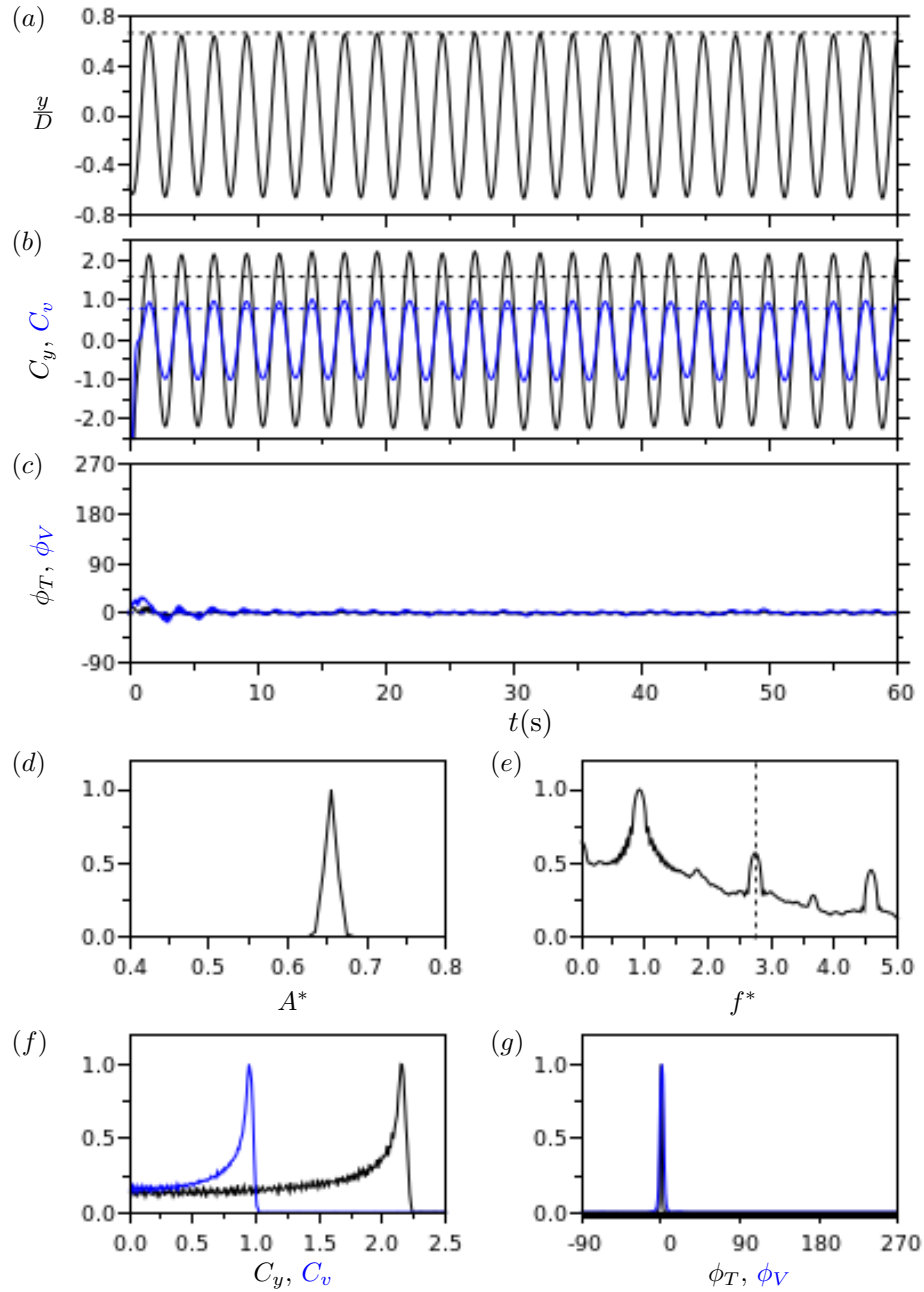


FIGURE 5.11: The response time histories and distribution of quantities of an elastically-mounted cylinder undergoing rotary oscillations at forcing frequency ratio $f_{rot}^* = 2.75$, forcing velocity ratio $A_m = 0.5$ and reduced velocity $U^* = 5.5$. Refer to fig. 5.8 caption for detailed description of the figures.

(f)). The distribution of phases, as shown in fig. 5.10(g), is comparable to those seen at f_{rot}^* below the rotary-lock-on region (see fig. 5.8). Since the response of the cylinder below the rotary-lock-on region and between the rotary-lock-on and tertiary-lock-on regions are so similar it is unsurprising for the cylinder in these regions of the forcing parameter space to have the similar wake structures.

It was previously mentioned that as f_{rot}^* is increased there is a jump in ϕ_T and ϕ_V as the frequency response of the cylinder increased past the frequency response of a non-rotating cylinder (f_{VIV}) at $f^* \approx 1.05$. Figure 5.11 and fig. 5.12 present the response time history of the cylinder at two points within the tertiary-lock-on region. Figure 5.11 presents the response where the ϕ_T and ϕ_V are both at 0° , i.e. when the fluid forces are in phase with the cylinder's motion at a frequency ratio, of

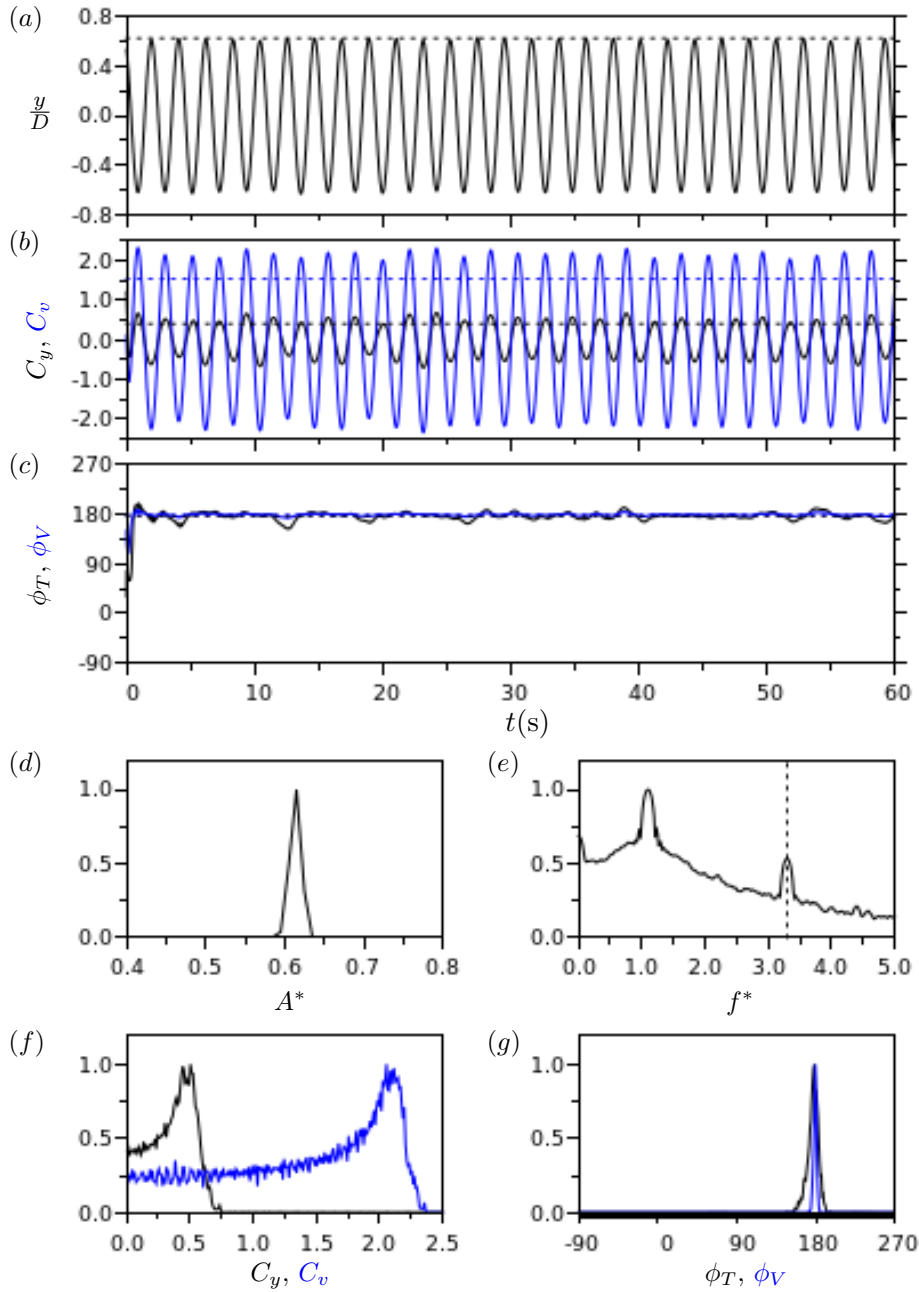


FIGURE 5.12: The response time histories and distribution of quantities of an elastically-mounted cylinder undergoing rotary oscillations at forcing frequency ratio $f_{rot}^* = 3.30$, forcing velocity ratio $A_m = 0.5$ and reduced velocity $U^* = 5.5$. Refer to fig. 5.8 caption for detailed description of the figures.

$f_{rot}^* = 2.75$. Fig. 5.12 presents the response when ϕ_T and ϕ_V are at approximately 180° , when the forces are out of phase with the motion, at $f_{rot}^* = 3.30$.

The time histories of the amplitude response and both fluid forces are highly periodic and sinusoidal. The single dominant frequency response peak is near $f^* \approx 1$ and the large separation between the oscillation and forcing frequency peaks is attributed to the strong and consistent motion of the cylinder. As a result of the consistent oscillation of the cylinder, the amplitude response and fluid force peaks are narrowly distributed above a single value and do not show any signs of signal switching or beating. ϕ_T and ϕ_V are very stable and both phases remained at 0° at frequency ratio $f_{rot}^* = 2.75$ and 180° at $f_{rot}^* = 3.30$. Similarly, the A_{10}^* amplitude response and forces, the

5.5. Response at fixed forcing velocity ratios

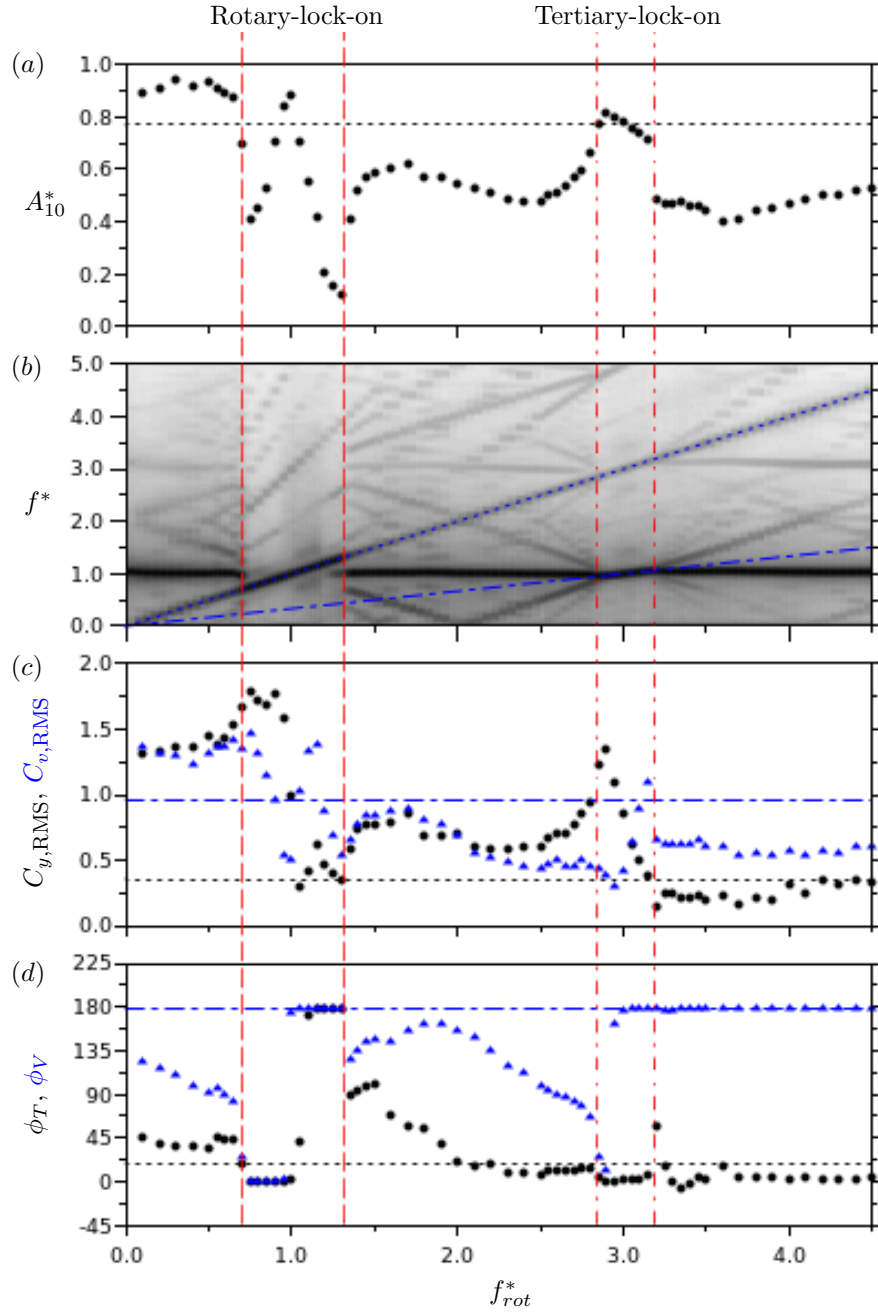


FIGURE 5.13: The response quantities of an elastically-mounted cylinder undergoing rotary oscillations is presented as a function of forcing frequency ratio (f_{rot}^*) at a fixed forcing velocity ratio of $A_m = 1.0$ and at a reduced velocity of $U^* = 5.5$. Refer to fig. 5.7 caption for detailed description of the figures.

phases are narrowly distributed in both cases. The ϕ_T and ϕ_V are the only response quantities that changed significantly, while the A_{10}^* amplitude and the forces are very similar between the two f_{rot}^* cases. The data collected in the present study will not be sufficient to explain this jump in phases in the tertiary-lock-on region, a detailed study of the cylinder wake and direct force measurement could provide more insight into the cylinder response in this f_{rot}^* range.

As the velocity ratio is increased to $A_m = 1.0$, *i.e.* where the peak velocity of the cylinder surface equals the free-stream velocity, U_∞ , the cylinder exhibits some minor changes to its responses, however, most of the trends previously described for the $A_m = 0.5$ persist. Figure 5.13 presents the response of the cylinder over the tested range of forcing frequency ratios ($f_{rot}^* = 0 - 4.5$) at a fixed

forcing velocity ratio of $A_m = 1.0$ and a reduced velocity of $U^* = 5.5$. Figure 5.13(a) shows that the amplitude response at frequency ratios below the lower boundary of the rotary-lock-on region continue to remain above the non-rotating value. Amplitude response in fact jumped from $A_{10}^* \approx 0.78$ in the non-rotating case to $A_{10}^* \approx 0.9$ when the cylinder undergoes even the lowest frequency rotary oscillation. The magnitude of this initial jump in A_{10}^* was found to increase with A_m . The RMS total force coefficient, $C_{y,RMS}$, in the same f_{rot}^* range is significantly higher than the non-rotating case and the lower velocity ratio case of $A_m = 0.5$. As the f_{rot}^* is increased and approaches the lower rotary-lock-on boundary at $f_{rot}^* \approx 0.75$, there is an abrupt drop in A_{10}^* that coincides with decreases in the total ϕ_T and vortex ϕ_V phases. Interestingly, the RMS total ($C_{y,RMS}$) and RMS vortex ($C_{v,RMS}$) force coefficients reached a local peak after A_{10}^* began to decrease. Further increases in f_{rot}^* and the cylinder undergoes rotary-lock-on.

As f_{rot}^* approaches the lower rotary-lock-on boundary A_{10}^* drops to $A_{10}^* \approx 0.4$ while both fluid forces remain large and in phase with the motion of the cylinder (see fig. 5.13(c) and (d)). This is different to the observations at $A_m = 0.5$ where fig. 5.7 showed that the drop in A_{10}^* within the rotary-lock-on region is accompanied by having both ϕ_T and ϕ_V at approximately 180° . In the present case, both phases remain close to 0° from the boundary of rotary-lock-on where the amplitude response is decreasing to a peak in amplitude within the rotary-lock-on region.

Increasing f_{rot}^* further causes A_{10}^* to decrease to a local minima, during this reduction ϕ_T and ϕ_V remain at 180° . Within the rotary-lock-on region, given the fluid forces are in phase with displacement of the cylinder, it is unsurprising that there is an increase in amplitude response. Similarly, when the fluid forces act in the opposite direction to the motion of the cylinder it is expected that A_{10}^* will decrease. The interesting finding is that the location of the amplitude peak within the rotary-lock-on region it is located at a frequency ratio of $f_{rot}^* = 1$, the same as the local maximum of A_{10}^* in the lower velocity ratio case ($A_m = 0.5$). Also, in both A_m cases the phases jumped from 0° to 180° in close proximity to the amplitude peak within the rotary-lock-on region. The ϕ_T jumped at frequency ratios between $f_{rot}^* = 1 - 1.1$, and ϕ_V jumped at $f_{rot}^* = 0.95 - 1.0$. This shows the amplitude peak and phase jump within the rotary-lock-on region are related to f_{osc} equalling f_{nw} and in close proximity to the frequency response of a non-rotating cylinder ($f_{osc} \approx f_{nw} \approx f_{VIV}$). The widening of the rotary-lock-on region to lower f_{rot}^* occurs as A_m is increased.

When f_{rot}^* increases to values between the rotary-lock-on and tertiary-lock-on regions, the trends of the cylinder's responses are similar to those observed at lower velocity ratios. Increasing f_{rot}^* to the onset of tertiary-lock-on causes the A_{10}^* to return to values similar to that of a non-rotating cylinder and C_y and C_v become in phase with the cylinder's motion. Within the tertiary-lock-on region, the cylinder reaches a local amplitude peak as ϕ_V jumps from 0° to 180° at $f_{rot}^* = 2.90$. The ϕ_T remained close to 0° and only jumped to 180° at $f_{rot}^* = 3.15$. This is consistent with the other lower velocity ratio (*e.g.* $A_m = 0.5$ presented in fig. 5.7). Moreover, the f_{rot}^* at which the phases jumped within the tertiary-lock-on region are approximately three times that of the f_{rot}^* values at which phase jumps occurred within the rotary-lock-on region. The jump in mean vortex phase coincides with the natural frequency of the oscillating structure in water (presented as $f_{rot}^* \approx 1$ in fig. 5.13(b)) in the rotary-lock-on region and three times f_{nw} (presented as $f_{rot}^* \approx 3$ in fig. 5.13(b)) in the tertiary-lock-on region. ϕ_T seem to respond to f_{VIV} as, in the rotary-lock-on region, ϕ_T jumped to 180° at a frequency ratio of $f_{rot}^* \approx 1.05$, which is the equivalent of $f_{rot,VIV}^* \approx 1$. Similarly, in the tertiary-lock-on region ϕ_T jumped to 180° at a frequency ratio of $f_{rot}^* \approx 3.15$, which is the equivalent of three times f_{VIV} ($f_{rot,VIV}^* \approx 3$). This further implies there is a correlation between the natural response of the oscillating system and changes in the phase responses of a rotary oscillating cylinder. However, given the close proximity of f_{nw} ($f_{rot}^* = 1$) and f_{VIV} ($f_{rot}^* \approx 1.05$) it is difficult to conclusively determine if the jump in ϕ_T at f_{VIV} (or $f_{rot}^* \approx 1.05$) is related to: (1) f_{VIV} , or (2) f_{nw} with ϕ_T responding more slowly when compared to the jump in ϕ_V .

Examination of the lower branch responses provides a clearer understanding between the jump

in phases and the forcing frequencies. In the lower amplitude response branch f_{VIV} moves further away from f_{nw} , if there is a relationship between ϕ_T and f_{VIV} , the jump in ϕ_T in the rotary-lock-on and tertiary-lock-on regions should occur at a higher value of f_{rot}^* (discussed later in this section).

When the f_{rot}^* is increased above the tertiary-lock-on region the cylinder exhibits reductions in A_{10}^* and force responses are similar to those observed at a lower velocity ratio (*e.g.* $A_m = 0.5$ case). There are, however, striking differences in ϕ_T compared to lower A_m cases. In this region, the C_y remained in phase with the motion of the cylinder ($\phi_T \approx 0^\circ$), in the lower velocity ratio case of $A_m = 0.5$, ϕ_T remain close to 180° . As other response trends persist at a higher velocity ratio of $A_m = 1.0$, this change in ϕ_T may be an indicator of changes in the structure of the wake, this will be explored in §5.7.

Further increases in $A_m = 1.3$ results in the rotary-lock-on region widening and extending to higher frequency ratios. Figure 5.14 presents the response of the cylinder over the tested range of forcing frequency ratios ($f_{\text{rot}}^* = 0 - 4.5$) at a fixed $A_m = 1.3$ and $U^* = 5.5$. Below a frequency ratio of $f_{\text{rot}}^* \approx 1.3$, the cylinder's response trends are similar to those in the velocity ratio case of $A_m = 1.0$. Above the frequency ratio $f_{\text{rot}}^* \approx 1.3$ and within the wider rotary-lock-on region, VIV is effectively suppressed by the sinusoidal rotary forcing as the amplitude response decreased to values less than $0.1D$. This reduction in amplitude response, A_{10}^* , is accompanied by significant reductions in the fluid forces as shown in fig. 5.14(c). Both C_y and C_v remain out of phase with the motion of the cylinder as ϕ_T and ϕ_V phases remain between $90^\circ - 180^\circ$ throughout the range of frequency ratios for which the cylinder's amplitude response is effectively suppressed ($< 0.1D$). Increases in f_{rot}^* to values outside the rotary-lock-on region results in the rotary oscillation no longer being able to effectively suppress VIV. Hence, as f_{rot}^* increases there is a steady increase in A_{10}^* . As this occurs, the total force, C_y , becomes in phase with the cylinder motion ($\phi_T \approx 0^\circ$) and the vortex force becomes out of phase ($\phi_V \approx 180^\circ$). The tertiary-lock-on region is no longer observed at this A_m . To better understand the response of the cylinder as VIV is suppressed the time history and distribution of the cylinder's responses were examined at several points of interest, as highlighted by the red circle markers.

Figure 5.15 presents the response of the cylinder while it undergoes rotary-lock-on at a forcing frequency ratio of $f_{\text{rot}}^* \approx 1.40$. VIV is again effectively suppressed and the A_{10}^* response drops below $0.1D$ within the rotary-lock-on. The displacement time history in fig. 5.15(a) shows that the cylinder continues to exhibit periodic and sinusoidal oscillations despite the small amplitude response. The response of A_{10}^* and fluid forces (C_y , C_v) reflects the regular cylinder vibrations as both response quantities exhibit a single, narrow peak distribution of values. The oscillating frequency follows the forcing frequency within the rotary-lock-on region, as the peak with the highest power in fig. 5.15(e) is located at the same response value as the forcing value represented by the vertical dashed line. Both C_y and C_v remain consistently out of phase (see fig. 5.15(c)) and the two phases are narrowly distributed around 180° (see fig. 5.15(g)). From this, it is clear that the responses of the cylinder, while it undergoes rotary-lock-on, remains consistent even when the cylinder barely vibrates.

As the frequency ratio is increased above the upper boundary of rotary-lock-on region ($f_{\text{rot}}^* = 2.00$), the influence of f_{osc} and f_{VIV} on the cylinder's response increases. The PSD of the cylinder's displacement in fig. 5.16(e) showed that the frequency response of the cylinder follows that of a non-rotating cylinder, f_{VIV} , as the frequency response with the highest power is located at $f_{\text{rot}}^* \approx 1.05$. There is a secondary frequency peak at slightly lower power, which occurs at the rotary forcing value of $f_{\text{rot}}^* = 2$. Because of the similar power of these frequency peaks, frequency modulation is observed in the displacement and force time histories (see fig. 5.16(a) and (b)) and there is switching in the phase time history (see fig. 5.16(c)). The forces in fig. 5.16(f) and phases in fig. 5.16(g) exhibit a wider distribution because of the frequency modulation.

At high frequency ratios, above the upper boundary of the tertiary-lock-on region, there exist a difference in the cylinder's phases between higher velocity ratio cases such as $A_m = 1.0$ 1.3 and

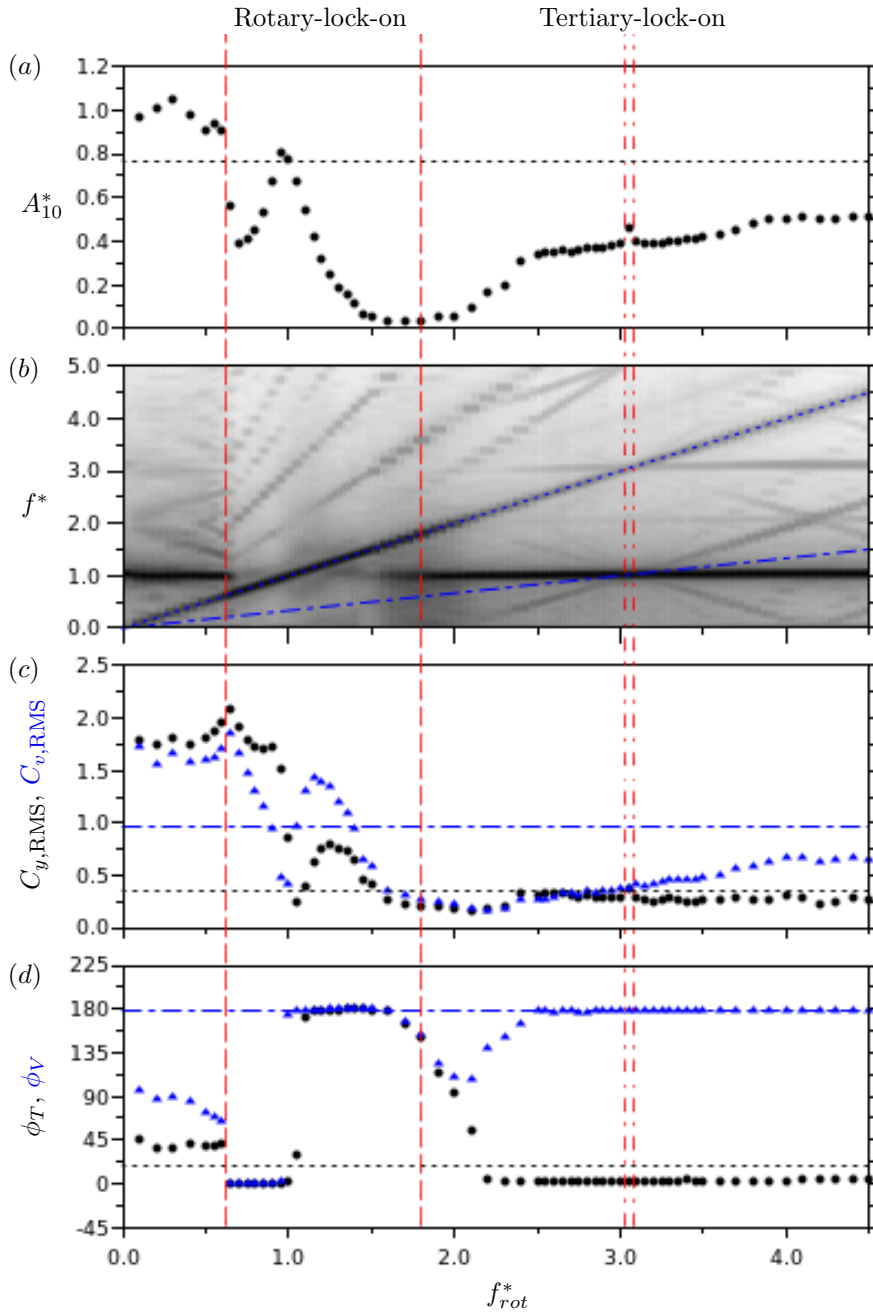


FIGURE 5.14: The response quantities of an elastically-mounted cylinder undergoing rotary oscillations is presented as a function of forcing frequency ratio (f_{rot}^*) at a fixed forcing velocity ratio of $A_m = 1.3$ and at a reduced velocity of $U^* = 5.5$. Refer to fig. 5.7 caption for detailed description of the figures.

that of lower values such as the $A_m = 0.5$ case. At $A_m = 0.5$, C_y remain out of phase as ϕ_T stayed above 120° . However, at elevated A_m and at similar f_{rot}^* , C_y is consistently in phase, with ϕ_T close to 0° . Figure 5.17 presents the response of the cylinder at a higher forcing frequency ratio of $f_{rot}^* = 3.40$. The cylinder displacement and forces are highly sinusoidal and periodic as shown by their time histories in fig. 5.17(a) and (b). Their distributions are, as a consequence, clustered closely around a single peak. The time history and distribution of the phases in fig. 5.17(c) and (g) also exhibits a strong, consistent signal. As the ϕ_T and the magnitudes of the forces are the only differences between the cylinder response at low and that at moderate velocity ratios, further studies into the wake structure and direct force measurements is needed at these forcing parameter points

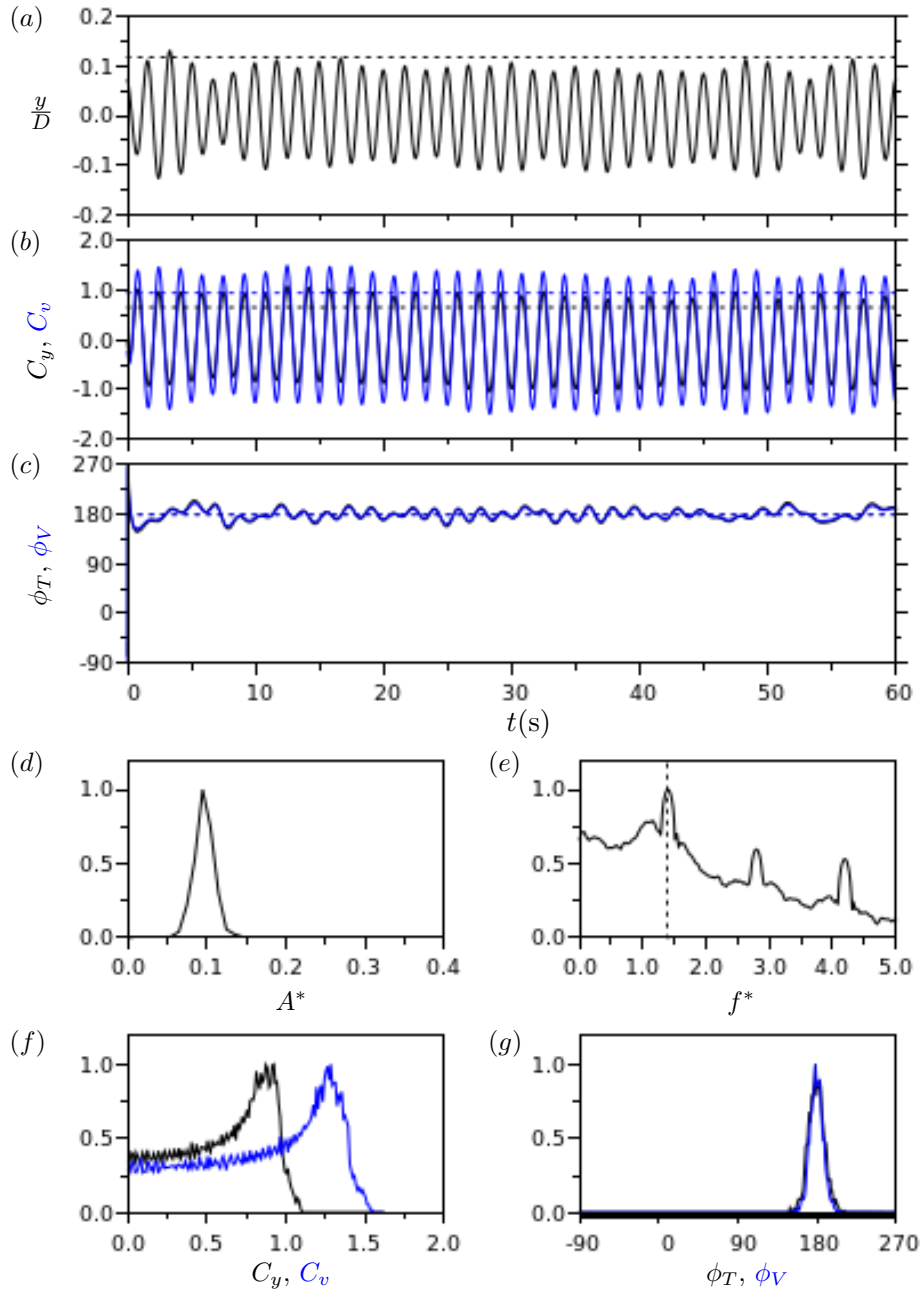


FIGURE 5.15: The response time histories and distribution of quantities of an elastically-mounted cylinder undergoing rotary oscillations at forcing frequency ratio $f_{rot}^* = 1.40$, forcing velocity ratio $A_m = 1.3$ and reduced velocity $U^* = 5.5$. Refer to fig. 5.8 caption for detailed description of the figures.

to understand their differences.

When the velocity ratio is increased to the highest tested value of $A_m = 2.0$, it is evident that the rotary-lock-on region spans across a significant range of the tested f_{rot}^* (see fig. 5.18). Figure 5.18(a) shows that the increase in A_{10}^* as the cylinder initially undergo rotary oscillation is significantly larger than those observed at lower velocity ratios. With increases in A_m and the widening of the rotary-lock-on region, large VIV amplitude response remains suppressed over a larger range of f_{rot}^* and the transition for C_y changes from being out of phase to being in phase occur more gradually. The response trends in and above the rotary-lock-on region are the same as those reported for the velocity ratio $A_m = 1.3$ case and were also observed at $A_m = 1.5 - 1.9$.

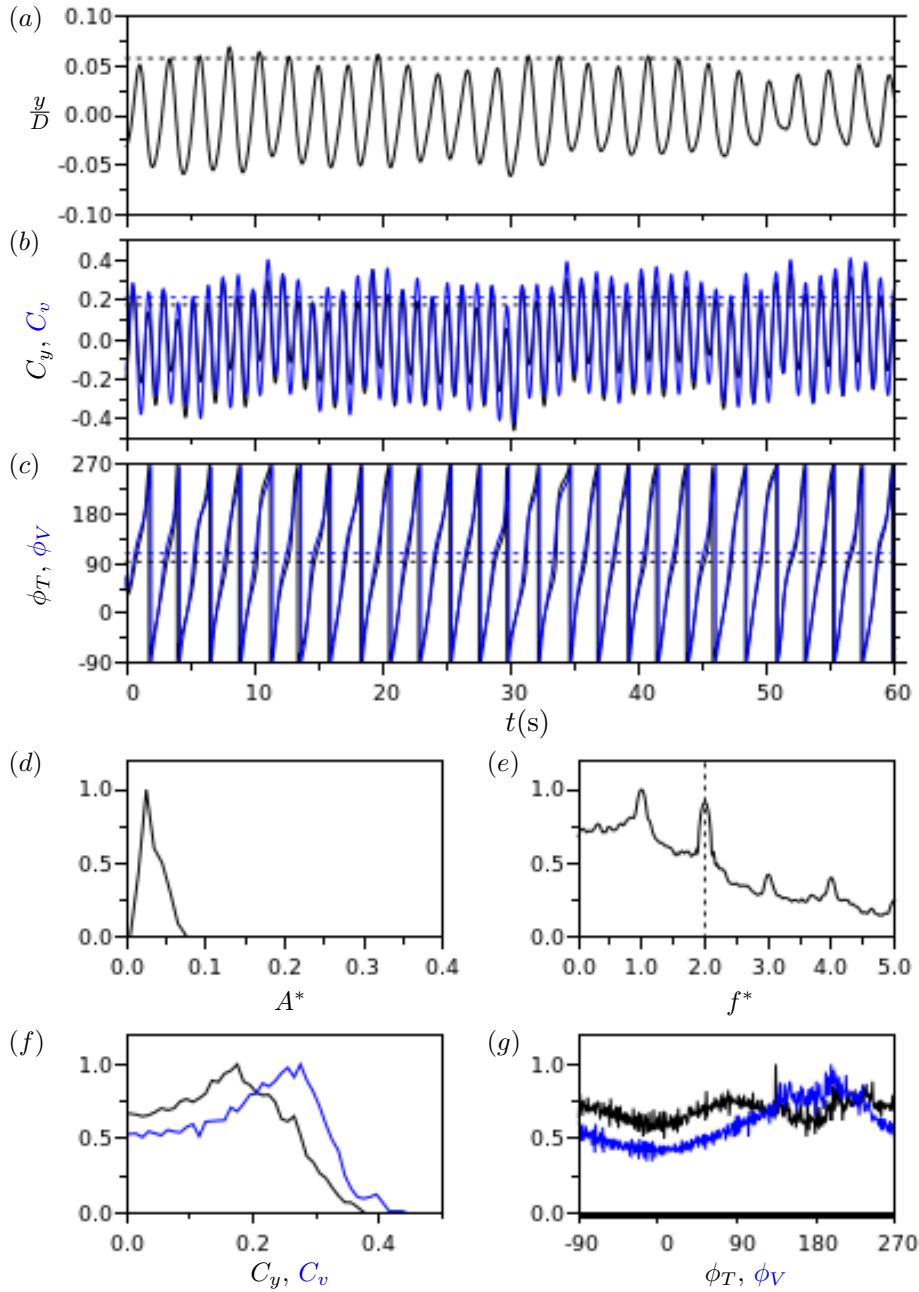


FIGURE 5.16: The response time histories and distribution of quantities of an elastically-mounted cylinder undergoing rotary oscillations at forcing frequency ratio $f_{rot}^* = 2.00$, forcing velocity ratio $A_m = 1.3$ and reduced velocity $U^* = 5.5$. Refer to fig. 5.8 caption for detailed description of the figures.

This shows that in the upper amplitude response branch of a non-rotating cylinder ($U^* = 5.5$), the response trends of the cylinder remain largely the same from $A_m \approx 1.3 - 2.0$. Furthermore, sinusoidal-driven rotary oscillations have been shown to be effective in causing the cylinder to undergo rotary-lock-on, which then suppresses large VIV responses. As reported in rigidly-mounted rotary oscillating cylinder studies by Cheng *et al.* (2001); Cheng (2001); Choi *et al.* (2002), the range of frequency ratios at which rotary-lock-on occur increases with A_m . Du & Sun (2015) showed that rotary oscillations are effective at suppressing VIV at very low Reynolds numbers and at specific values of the forcing parameters. The present results proved that rotary oscillation remains effective at moderate Re and that its effectiveness increases with velocity ratio when $A_m \gtrsim 1.1$. A number

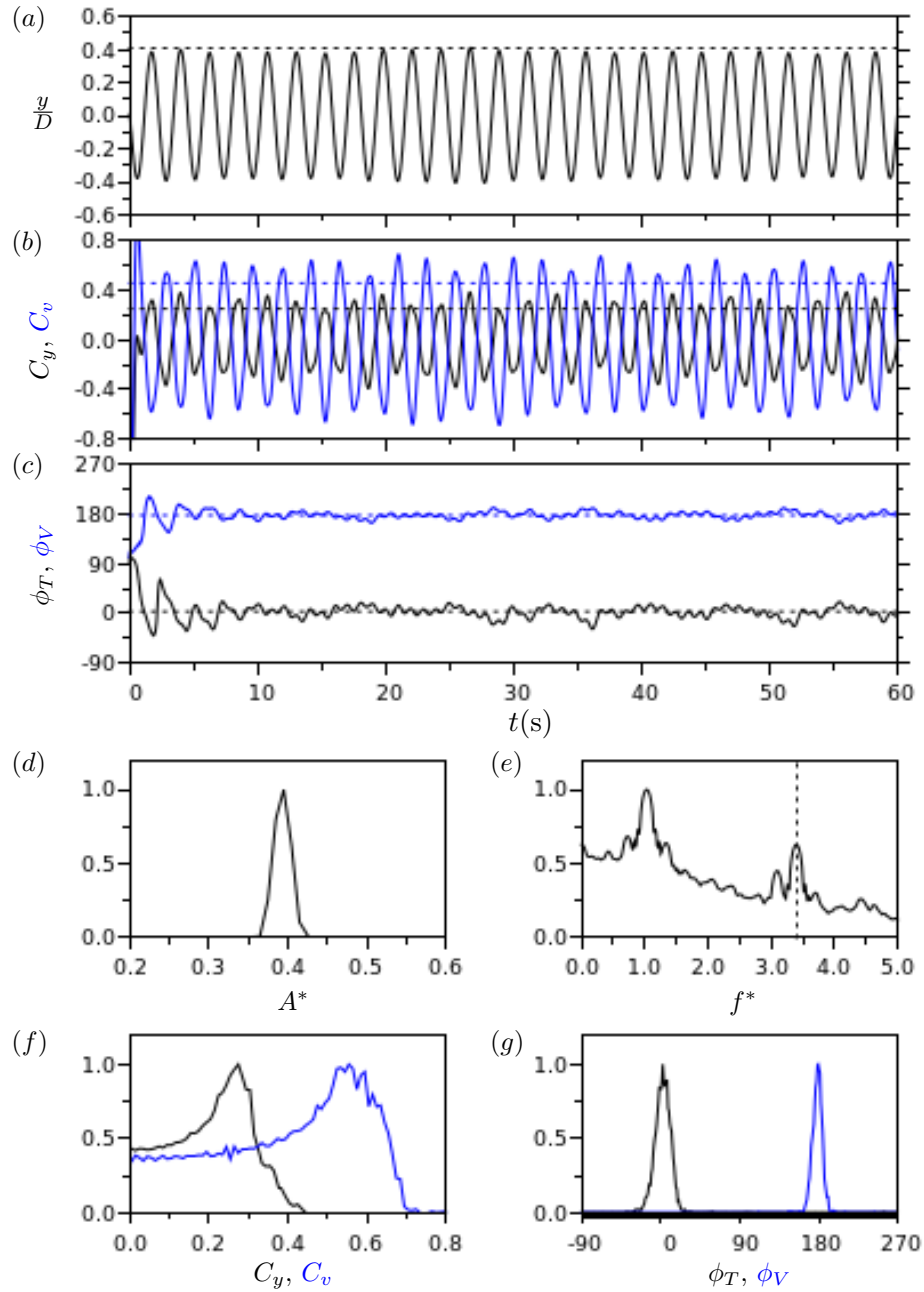


FIGURE 5.17: The response time histories and distribution of quantities of an elastically-mounted cylinder undergoing rotary oscillations at forcing frequency ratio $f_{rot}^* = 3.40$, forcing velocity ratio $A_m = 1.3$ and reduced velocity $U^* = 5.5$. Refer to fig. 5.8 caption for detailed description of the figures.

of studies involving elastically-mounted cylinders, including Du & Sun (2015), focused on the upper amplitude response branch, as it is where the large amplitude response is observed, less attention has focussed on the lower branch where the cylinder's amplitude response is still significant.

The response of the cylinder undergoing sinusoidally-driven rotary oscillations for $f_{rot}^* = 0 - 4.5$ and $A_m = 0.5$ at a reduced velocity of $U^* = 8.0$ is presented in fig. 5.19. Compared to the cylinder's response in the upper branch with the same forcing parameters, there are several similarities. There exists rotary-lock-on and tertiary-lock-on regions. However, in the lower branch these two regions span over a larger range of f_{rot}^* than is seen the upper branch (see fig. 5.19(a)). The A_{10}^* peaks associated with the rotary-lock-on and tertiary-lock-on regions are also present in the lower branch.

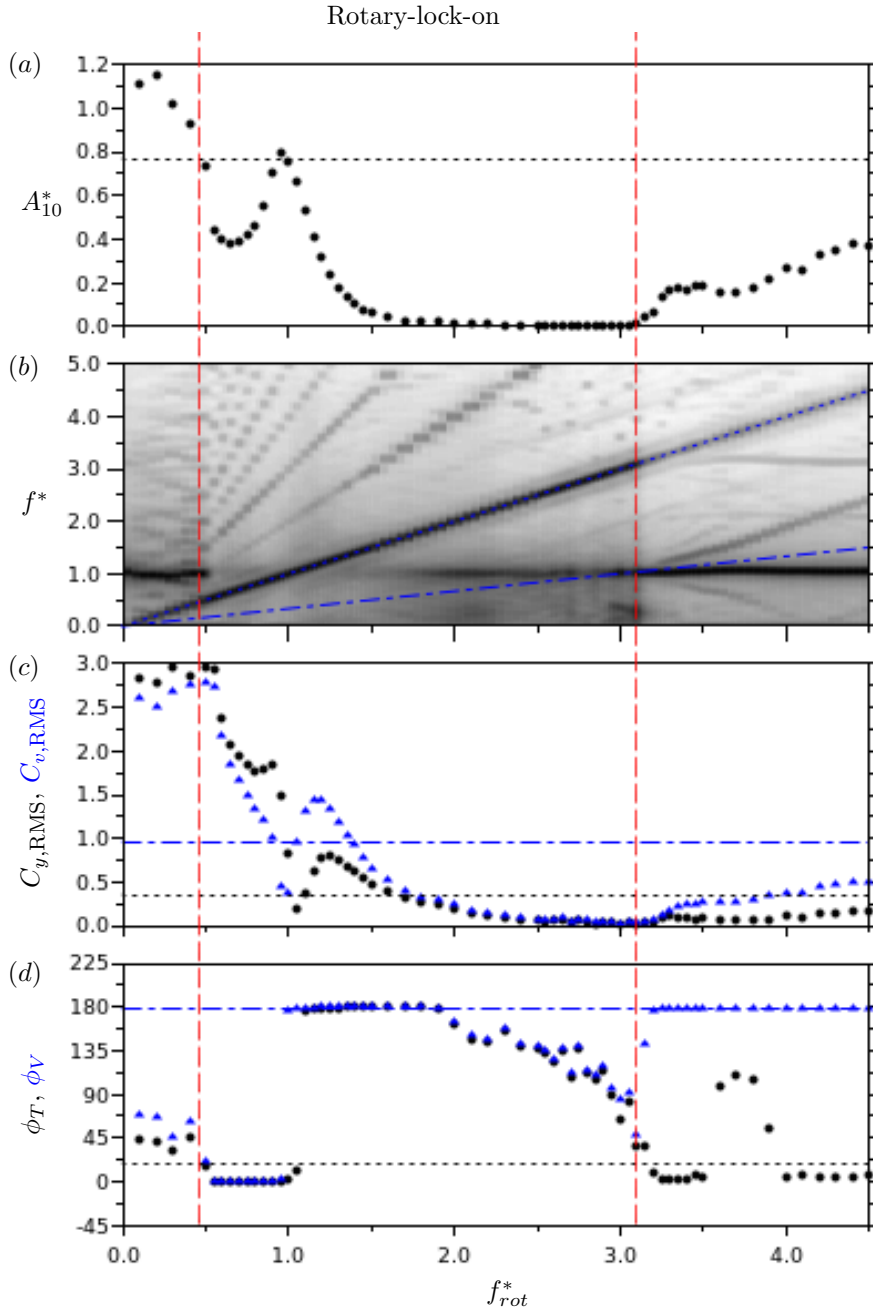


FIGURE 5.18: The response quantities of an elastically-mounted cylinder undergoing rotary oscillations is presented as a function of forcing frequency ratio (f_{rot}^*) at a fixed forcing velocity ratio of $A_m = 2.0$ and at a reduced velocity of $U^* = 5.5$. Refer to fig. 5.7 caption for detailed description of the figures.

Compared to their upper branch counterparts, the A_{10}^* peaks in the lower branch have larger increases over the non-rotating case and reached higher peak magnitudes. Between the rotary-lock-on and tertiary-lock-on regions, A_{10}^* decreased to values below the non-rotating case. The trends in $C_{y,RMS}$ and $C_{v,RMS}$ are different to those seen in the upper branch. In the lower branch, $C_{v,RMS}$ is consistently larger than $C_{y,RMS}$ over the range of f_{rot}^* . The mean total ϕ_T and mean vortex ϕ_V phases also exhibit some differences. The fluid forces are 180° out of phase with the motion for a non-rotating cylinder oscillating in the lower branch. As the cylinder began to undergo low-frequency ($f_{rot}^* \lesssim 0.9$) rotary oscillations, the total phase decreased to $\phi_T \approx 120^\circ$ until the onset of rotary-lock-on and the vortex phase remained at $\phi_V \approx 180^\circ$. As f_{osc} approached f_{nw} (i.e. $f_{rot}^* = 1$), ϕ_T abruptly decreased to

5.5. Response at fixed forcing velocity ratios

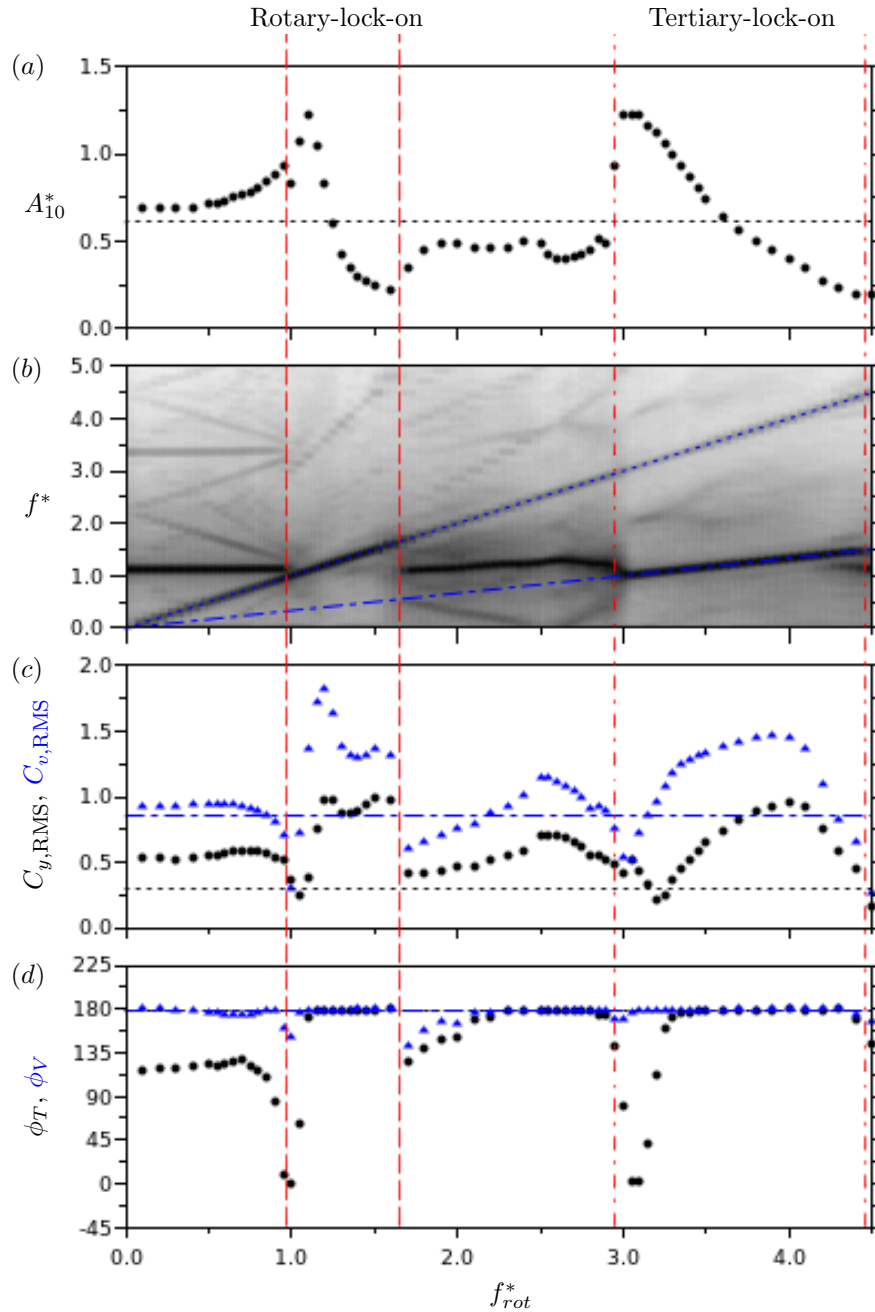


FIGURE 5.19: The response quantities of an elastically-mounted cylinder undergoing rotary oscillations is presented as a function of forcing frequency ratio (f_{rot}^*) at a fixed forcing velocity ratio of $A_m = 0.5$ and at a reduced velocity of $U^* = 8.0$. Refer to fig. 5.7 caption for detailed description of the figures.

approximately 0° and there was a small dip in ϕ_V over the same frequency ratios. Shortly thereafter, both phases sharply increased back to 180° .

It was previously mentioned that f_{nw} and f_{VIV} are likely to have an impact on the f_{rot}^* at which ϕ_T transitions from 0° (in phase) to 180° (out of phase) within the rotary-lock-on and tertiary-lock-on region. As shown in fig. 5.19(d), ϕ_T jumped from 0° to 180° between frequency ratios $f_{rot}^* = 1 - 1.1$, as was seen in the upper branch case. As f_{nw} and f_{VIV} in both the upper ($f_{rot}^* = 1.04$) and lower ($f_{rot}^* = 1.12$) branch lie between $f_{rot}^* \approx 1 - 1.1$, it is still unclear if f_{osc} equalling f_{nw} or f_{VIV} triggered the jump in ϕ_T . In the upper branch (refer to fig. 5.7(d)) in the tertiary-lock-on region, ϕ_T began to jump to 180° at $f_{rot}^* \approx 3.15$ (three times $f_{rot}^* \approx 1.05$ observed at the ϕ_T jump in the rotary-lock-on

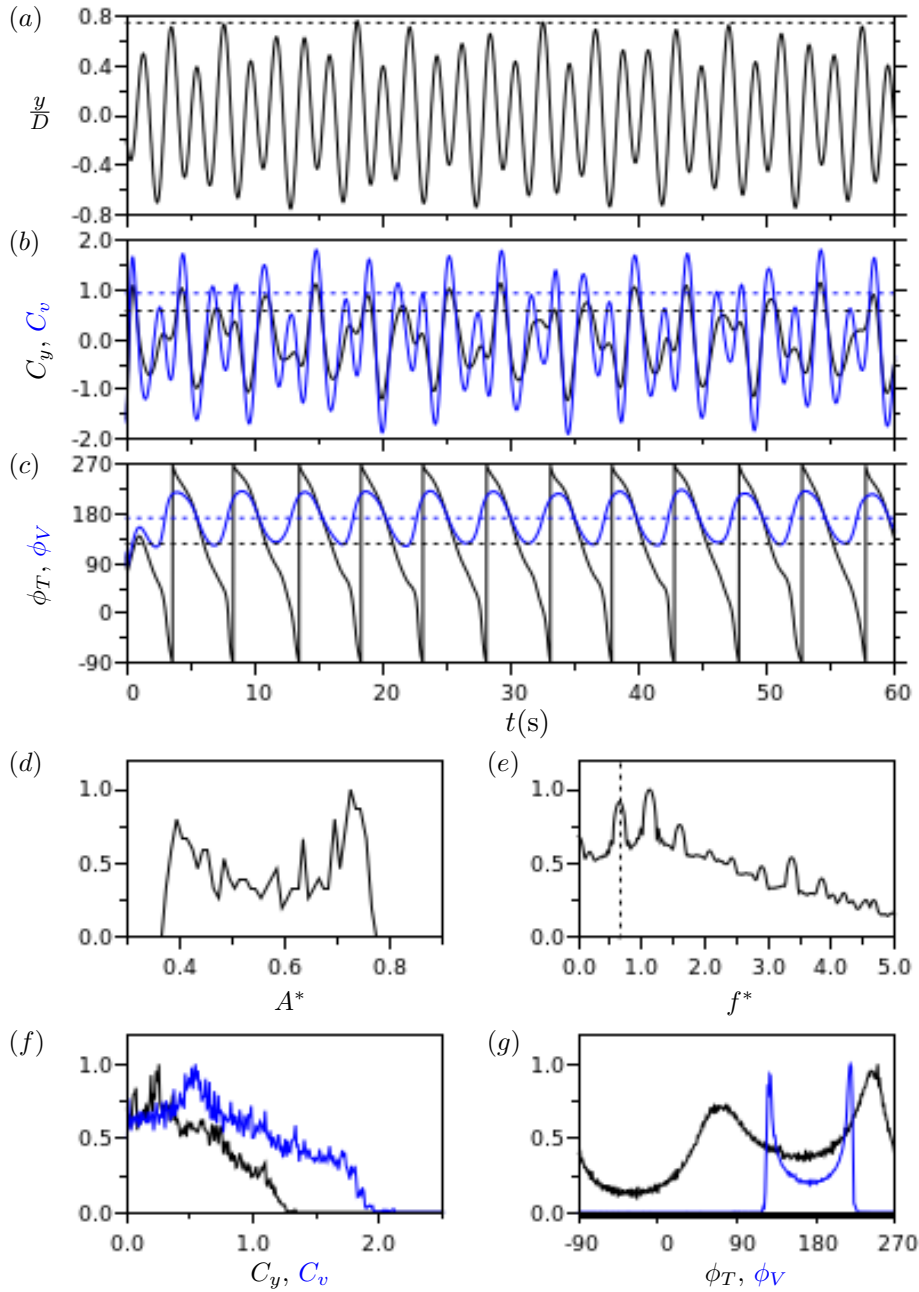


FIGURE 5.20: The response time histories and distribution of quantities of an elastically-mounted cylinder undergoing rotary oscillations at forcing frequency ratio $f_{rot}^* = 0.65$, forcing velocity ratio $A_m = 0.5$ and reduced velocity $U^* = 8.0$. Refer to fig. 5.8 caption for detailed description of the figures.

region). If ϕ_T jump was triggered by f_{osc} passing f_{VIV} , ϕ_T should jump to 180° at $f_{rot}^* \approx 3.36$ (three times $f_{rot}^* \approx 1.12$). However, this is not observed in the lower branch in fig. 5.19(d). Instead, the total phase began jumping to $\phi_T \approx 180^\circ$ at the same frequency ratios ($f_{rot}^* \approx 3.1$) that were observed in the upper branch. This suggests that f_{osc} passing f_{nw} ($f_{rot}^* = 1$) is the mechanism that triggered the jump in ϕ_T . The time history and distribution of response quantities at several points of interest in the forcing parametric domain will be presented and discussed. This is done to assist in understanding the response of the cylinder and help highlight the similarities and differences between the cylinder's response in the upper and lower branches under the same rotary forcing parameters.

Figure 5.20 presents the response of the cylinder below the rotary-lock-on region at $f_{rot}^* = 0.65$

and $U^* = 8.0$. The cylinder exhibits frequency modulation as seen in fig. 5.20(a) and the time history of the forces in fig. 5.20(b). Typical of cases that exhibit frequency modulation of A_{10}^* the results are distributed across a range of values with two dominant peaks, one at higher and one at lower A_{10}^* values. The frequency response in fig. 5.20(e) has two peaks, one is f_{osc} and the other is f . With the exception of the magnitude of the phases, the cylinder's responses in the lower amplitude response branch are similar to those seen the upper branch. At identical forcing parameters, the responses of the cylinder at both amplitude branches exhibit similar trends: frequency modulation and a broad distribution of amplitude peaks over two or more A_{10}^* values. It is evident from this that sinusoidal rotary oscillations continue to have the same impact on the response of an elastically-mounted cylinder below the rotary-lock-on region at higher reduced velocities and Reynolds numbers.

At a frequency ratio within the rotary-lock-on region ($f_{rot}^* = 1.15$) and in the lower branch, the response trends of the cylinder are nearly identical to the upper branch counterpart. From fig. 5.21(e) it can be seen that as rotary-lock-on occurs f follows the forcing frequency f_{osc} and results in a single high-power frequency peak. Consequently, the cylinder's motion is sinusoidal and highly periodic (see fig. 5.21(a)), and its amplitude response, A_{10}^* , is consistent and narrowly distributed over a small range of values (see fig. 5.21(d)). At f_{rot}^* between the rotary-lock-on and tertiary-lock-on regions, the trends in the time history and distribution of the cylinder's responses is similar for the upper and lower amplitude response branches.

In the lower amplitude response branch ($U^* = 8.0$), as the forcing velocity ratio is increased to $A_m = 1.0$, there exist some small changes to the response of the cylinder, however, their trends remain very similar to that observed at $A_m = 0.5$. The response of the cylinder while $f_{rot}^* = 0-4.5$ at $A_m = 1.0$ and $U^* = 8.0$ is presented in fig. 5.22. At the elevated A_m the rotary-lock-on region widens while the tertiary-lock-on region shrinks. The evolution of A_{10}^* with f_{rot}^* shows two local peaks within the rotary-lock-on and tertiary-lock-on regions. The peak A_{10}^* amplitude value is located within the rotary-lock-on region and it is almost three times that of the non-rotating case. The magnitude of the phases of the cylinder at low frequency ratios ($f_{rot}^* \lesssim 0.6$) as it initially undergoes rotary forcing (*i.e.* from non-rotating to rotating) decreased with increases in A_m . This trend continues with further increases in A_m until both the ϕ_T and ϕ_V are below 25° in the $A_m = 2.0$ case (see fig. 5.24(d)).

At a velocity ratio of $A_m = 1.3$, the amplitude peak within the rotary-lock-on region increased to $A_{10}^* = 1.8$ with corresponding increases in C_y and C_v (see fig. 5.23(a) and (c)). The rotary-lock-on region widens further and it is evident that rotary oscillation effectively suppresses VIV (amplitude response is below $A_{10}^* = 0.1$) over most of the frequency ratios above $f_{rot}^* \approx 1.6$ but excluding the tertiary-lock-on region. The tertiary-lock-on region shrunk to a narrow range of f_{rot}^* , within the small tertiary-lock-on region, large amplitude oscillations were observed, C_y became in phase while C_v became out of phase with the motion of the cylinder. with further increase in velocity ratio to $A_m = 2.0$ the tertiary-lock-on region disappears and large amplitude oscillations remain suppressed at frequency ratios $f_{rot}^* \gtrsim 1.5$ (see fig. 5.24).

From this, it becomes obvious that there exist trends in the cylinder's response that are common to the two investigated reduced velocity cases. The amplitude response, A_{10}^* , comes to some local peak value in the rotary-lock-on region and tertiary-lock-on region, if it exists at that particular A_m . In the upper branch, the amplitude response of the cylinder A_{10}^* at frequency ratios below the rotary-lock-on region increases with A_m , and in the lower branch the magnitude of the amplitude peak within the rotary-lock-on region increases. For both amplitude branches, magnitude of the amplitude peak observed in the tertiary-lock-on region decreases with A_m . The phase response of the cylinder in the proximity of and within the rotary-lock-on and tertiary-lock-on seems to be independent of U^* and the effects of Reynolds number. The fluid forces become aligned to specific values in the rotary-lock-on and tertiary-lock-on regions. At the onset of rotary-lock-on (and tertiary-lock-on), the total force becomes in phase (total phase at $\phi_T \approx 0^\circ$). Shortly thereafter, the

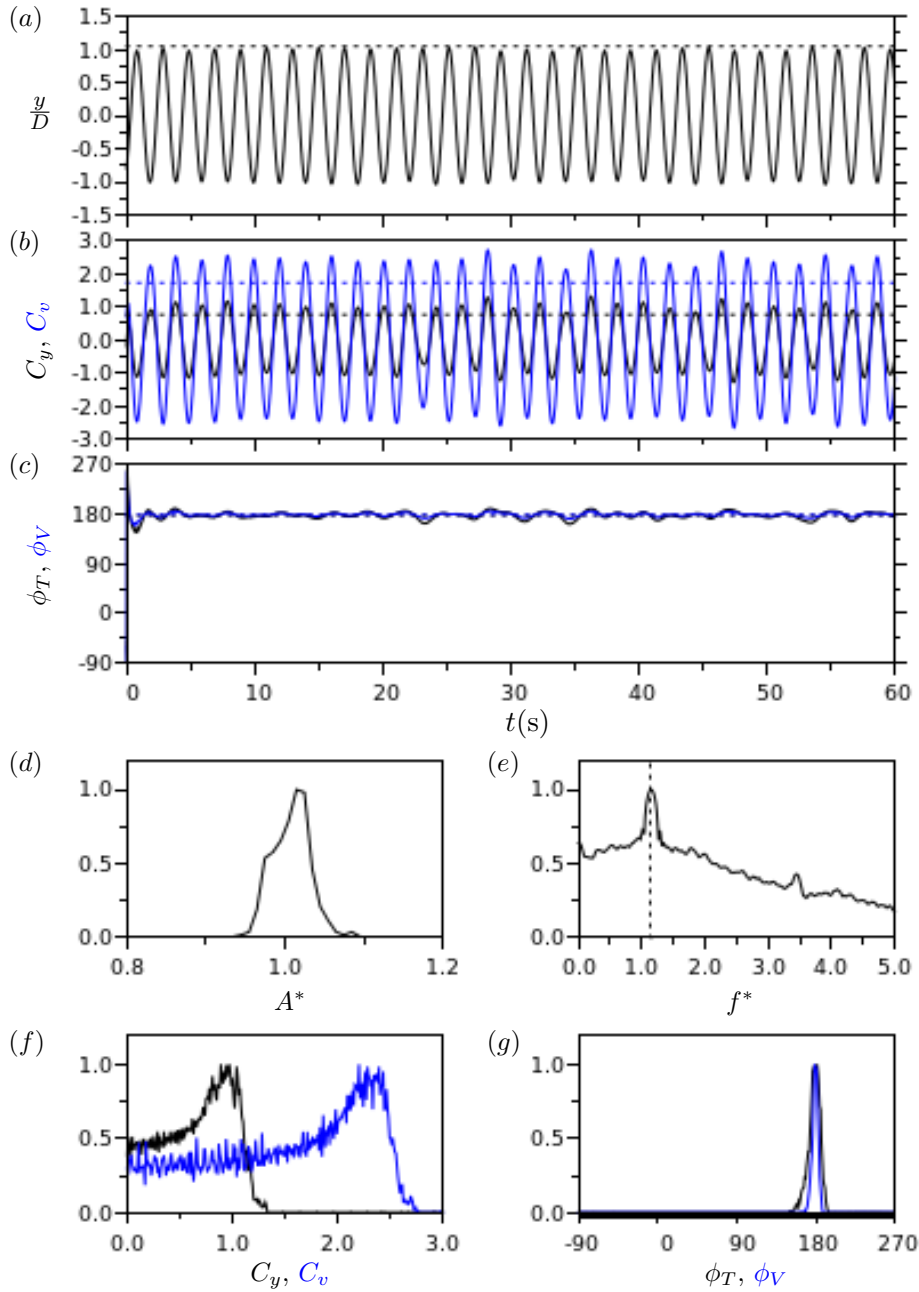


FIGURE 5.21: The response time histories and distribution of quantities of an elastically-mounted cylinder undergoing rotary oscillations at forcing frequency ratio $f_{rot}^* = 1.15$, forcing velocity ratio $A_m = 0.5$ and reduced velocity $U^* = 8.0$. Refer to fig. 5.8 caption for detailed description of the figures.

vortex force becomes out of phase (vortex phase jumps to $\phi_V \approx 180^\circ$) and this is soon followed by the total force (total phase jumps to $\phi_T \approx 180^\circ$). For the remainder of the rotary-lock-on and tertiary-lock-on region, the forces remained out of phase (phases at 180°) and large reductions in the cylinder’s vibration amplitude is observed. Furthermore, the suppression of VIV and large amplitude oscillations persist even outside rotary-lock-on and tertiary-lock-on regions. However, this generally occurs after A_m is increased to values where rotary oscillation becomes effective (*i.e.* at values where the amplitude is suppressed below $A_{10}^* \lesssim 0.1$ over a range f_{rot}^*).

Examination of the time history and distribution of the cylinder’s responses showed that within the central regions of the rotary-lock-on and tertiary-lock-on regions the cylinder response is highly

5.5. Response at fixed forcing velocity ratios

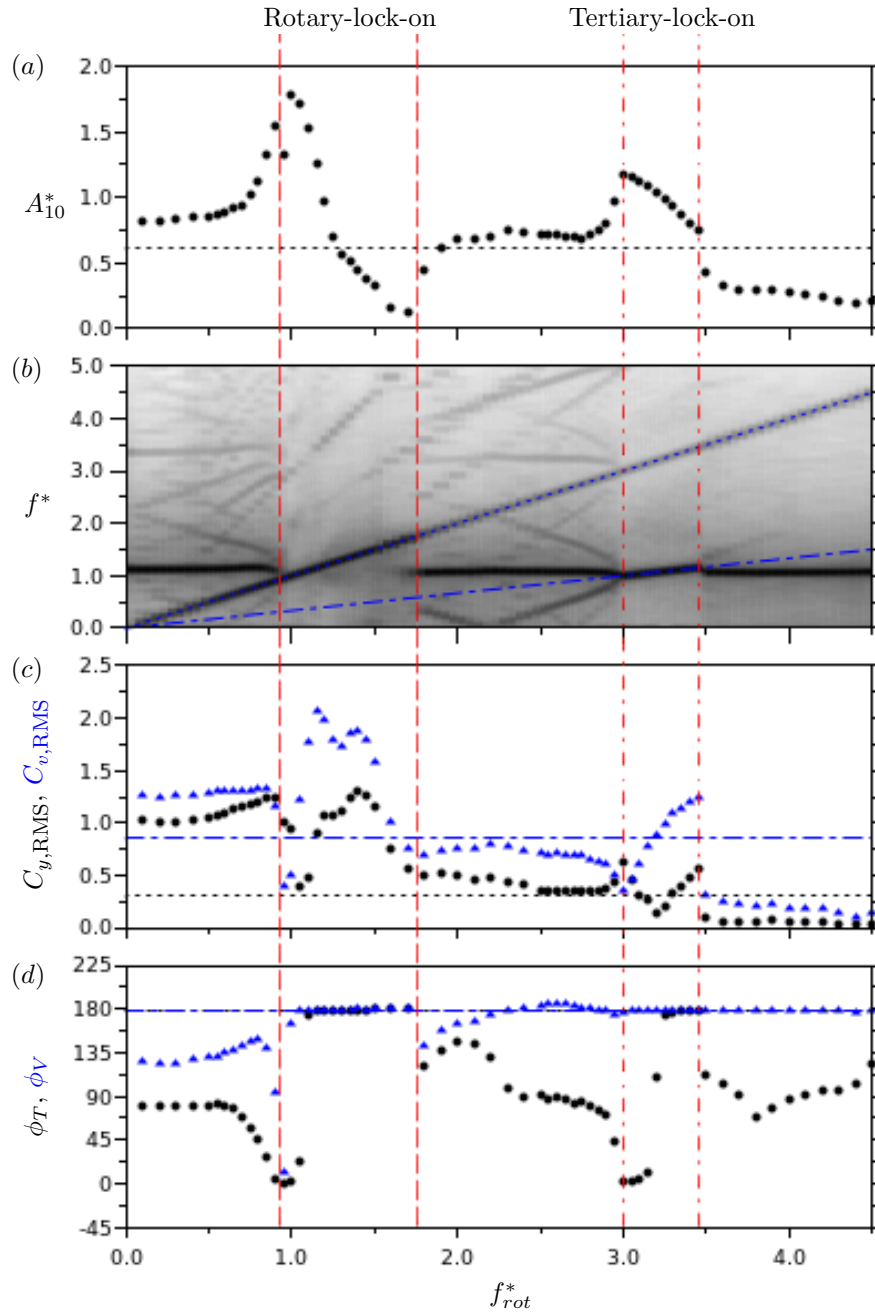


FIGURE 5.22: The response quantities of an elastically-mounted cylinder undergoing rotary oscillations is presented as a function of forcing frequency ratio (f_{rot}^*) at a fixed forcing velocity ratio of $A_m = 1.0$ and at a reduced velocity of $U^* = 8.0$. Refer to fig. 5.7 caption for detailed description of the figures.

periodic and sinusoidal. The cylinder exhibits one dominant frequency response as the oscillation frequency, f , follows the forcing frequency, f_{osc} . As the cylinder undergoes rotary forcing at values close to the rotary-lock-on and tertiary-lock-on boundaries and outside the two regions, the cylinder exhibits frequency modulation. Frequency modulation results in a broad distribution of amplitude response peaks and fluid forces, and periodic switching in phases is also observed. The severity of frequency modulation largely depends on how close in power the cylinder's frequency response peak and the forcing frequency peak are. Larger differences in the power of the two frequency peaks leads to weaker effects on frequency modulation. Closeness of the values of the cylinder's frequency response and the forcing frequency also have an influence.

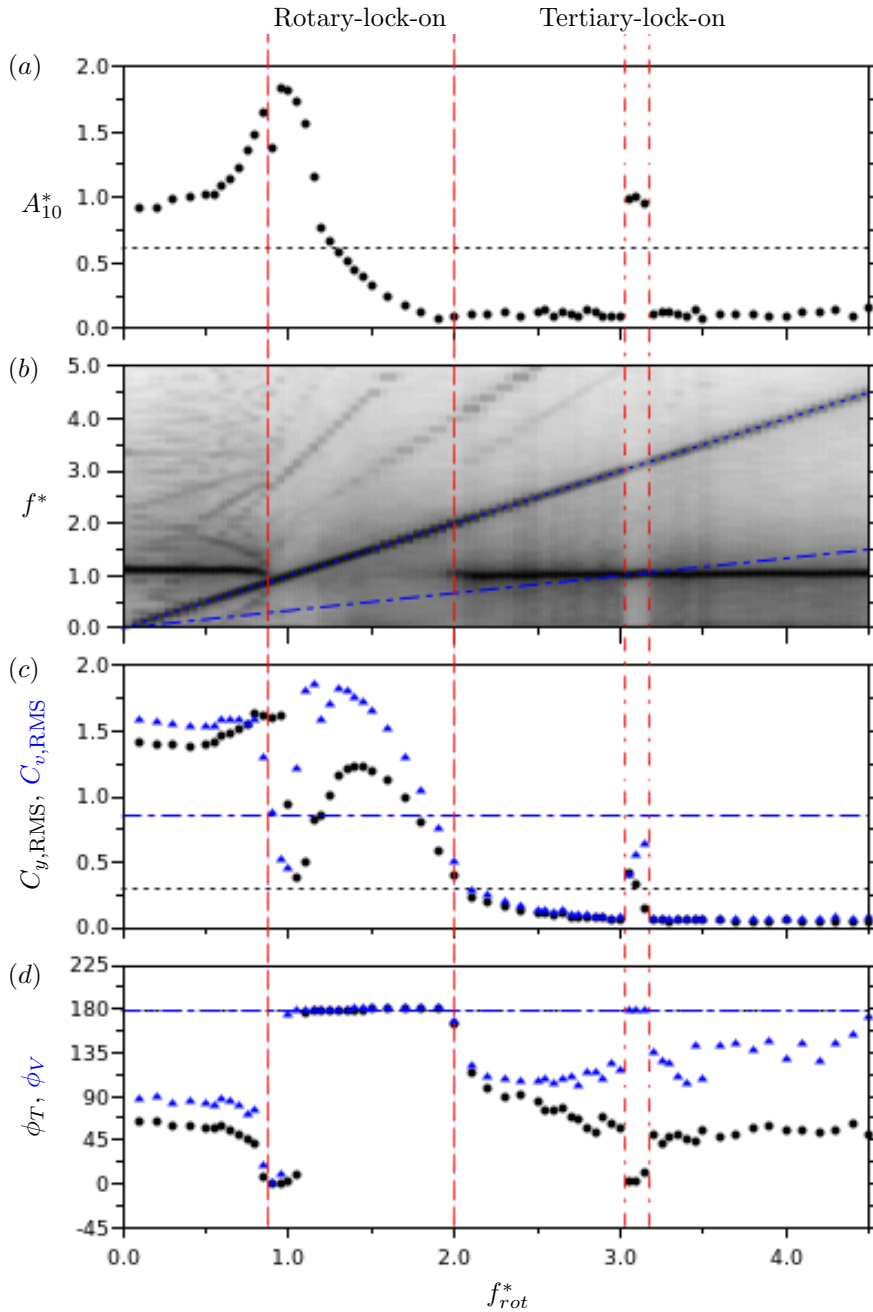


FIGURE 5.23: The response quantities of an elastically-mounted cylinder undergoing rotary oscillations is presented as a function of forcing frequency ratio (f_{rot}^*) at a fixed forcing velocity ratio of $A_m = 1.3$ and at a reduced velocity of $U^* = 8.0$. Refer to fig. 5.7 caption for detailed description of the figures.

From the above it is clear that the vibration response an elastically-mounted cylinder undergoing sinusoidally-driven rotary oscillations at different forcing parameters and U^* show some trends that are independent to U^* (and Reynolds number, Re), These trends are consistent and depend on the rotary-lock-on and tertiary-lock-on phenomenon. Understanding the consistency of the cylinder’s response in different regions of the forcing A_m and f_{rot}^* domain will have implications from the view point of fundamental and applied studies flow-induced vibration. From the fundamental point of view, the consistent vibrational response suggests the possibility of consistent wake mode within the same region. The wake of the cylinder is discussed in §5.7. From a practical point of view, a consistent response makes the vibration system predictable and safer for engineering applications.

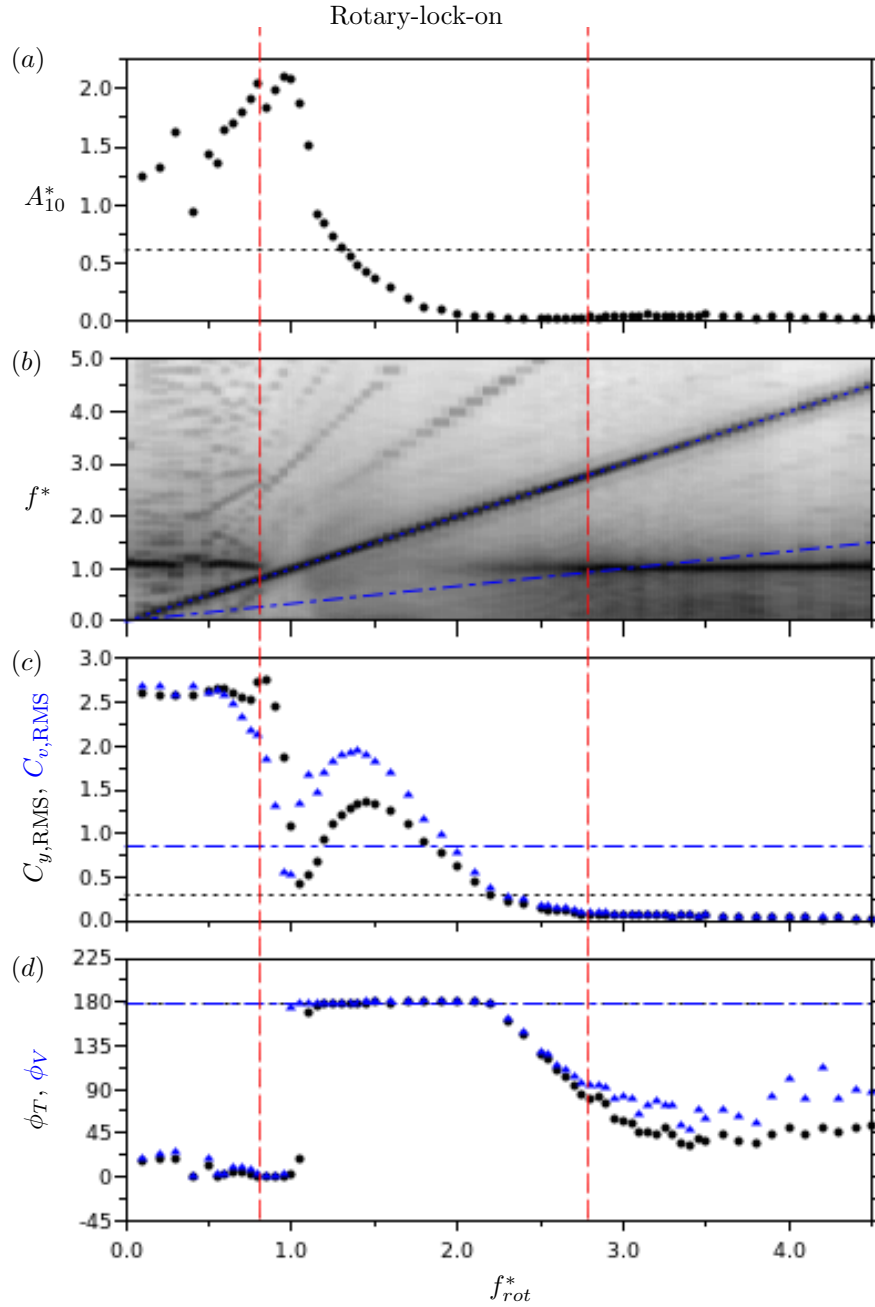


FIGURE 5.24: The response quantities of an elastically-mounted cylinder undergoing rotary oscillations is presented as a function of forcing frequency ratio (f_{rot}^*) at a fixed forcing velocity ratio of $A_m = 2.0$ and at a reduced velocity of $U^* = 8.0$. Refer to fig. 5.7 caption for detailed description of the figures.

From the present study, it is abundantly clear that, at specific values of A_m and f_{rot}^* , sinusoidal rotary oscillation is very effective at suppressing VIV and large amplitude body oscillations associated with it.

The evolution of the cylinder's response presented in this section focused on increasing the f_{rot}^* at a fixed value of A_m . Limited cases of the vibration response results will be presented and discussed where the A_m , at finer increments, is increased at two fixed values of f_{rot}^* . These results are discussed in the following section.

5.6 Response at fixed forcing frequency ratios

As the primary experimental study was conducted at relatively large increments of A_m , a secondary, targeted study was conducted over a larger range of A_m at finer increments. This was motivated by a desire to better understand if the rotary-lock-on region persists and to see if the tertiary-lock-on region reappears at higher A_m . Figure 5.25 presents the response of the cylinder over a range of A_m at a reduced velocity belonging to the upper branch ($U^* = 5.5$) and a fixed frequency ratio that lies within the rotary-lock-on region ($f_{rot}^* = 1.0$). Figure 5.26 presents the response at a fixed frequency ratio that lies within the tertiary-lock-on region ($f_{rot}^* = 3.0$).

Figure 5.25(a) presents the mean of the highest 10% of normalised amplitude peaks, A_{10}^* , as a function of A_m . The black dashed line represents the response value of the non-rotating case. Figure 5.25(b) presents a PSD contour of the cylinder's displacement, y , as a function of the normalised frequency response, f^* , and the A_m . The power density is normalised by the peak power at each A_m value. The blue dotted line illustrates f^* being equal to the forcing f_{rot}^* ($f^* = f_{rot}^*$). Figure 5.25(c) and fig. 5.25(d) presents the force coefficients and phases as a function of the A_m , respectively. In both fig. 5.25(c) and fig. 5.25(d), the black markers represent the RMS total force coefficient, $C_{y,RMS}$, and mean total phase, ϕ_T . Similarly, in the same figures, the blue markers represent the RMS vortex force coefficient, $C_{v,RMS}$, and mean vortex phase, ϕ_V . The black dotted line and blue dot-dashed line represent the total and vortex component values of a non-rotating cylinder, respectively. Figure 5.26 follows the same format.

Figure 5.25(b) shows that the cylinder continues to undergo rotary-lock-on at velocity ratios $A_m > 2$. At velocity ratios $A_m \gtrsim 1.8$, the amplitude of the cylinder monotonically decreases with increasing A_m (see fig. 5.25(a)). However, large amplitude vibrations persist. Between velocity ratios $A_m = 0 - 0.3$, the amplitude sharply increased from the non-rotating value and remained above $A_{10}^* \approx 0.9$ up to an $A_m \approx 1$. The amplitude response, A_{10}^* , decreased to values comparable to that of a non-rotating cylinder. As shown in fig. 5.25(d), the phases of the cylinder do not show much significant changes with increases in A_m . From this, it is evident that the rotary-lock-on region exist even at velocity ratios up to $A_m = 3.5$. However, with the monotonic decrease in A_{10}^* , it is possible for that large amplitude oscillations will become suppressed with sufficiently large A_m . Due to the physical limitations of the apparatus, it was not possible to sustain prolonged operation at velocity ratios $A_m \gtrsim 2$.

The frequency response, f^* , when rotary oscillations at a frequency ratio of $f_{rot}^* = 3.0$ are applied is presented in fig. 5.26(b). The cylinder undergoes tertiary-lock-on between velocity ratios $A_m = 0.1 - 1.6$ as the primary frequency peak remains close to $f^* \approx 1$, the cylinder no longer undergoes tertiary-lock-on beyond this. This is evident as the primary frequency peak jumped from $f^* \approx 1$ to $f^* \approx 3$ to follow the forcing frequency and not its one-third harmonic. Furthermore, this change is accompanied by the suppression of large VIV amplitude response (see fig. 5.26(a)), which continues up to a velocity ratio of $A_m \approx 2.6$. Surprisingly, with further increases in velocity ratio $A_m \gtrsim 2.6$, the cylinder undergoes tertiary-lock-on once again as the primary frequency peak returned to $f^* \approx 1$. The cylinder's phases also show the return of tertiary-lock-on at high A_m . ϕ_T and ϕ_V ranges are consistent with previously seen velocity ratios where the cylinder undergoes tertiary-lock-on ($A_m = 0.1 - 1.6$ $A_m \gtrsim 2.6$), and ϕ_T remains close to 0° while ϕ_V remains near 180° . As the cylinder undergoes tertiary-lock-on for the second time, there is a small bump in A_{10}^* near a velocity ratio $A_m \approx 3$. However, this decreased shortly after as the A_m is increased near the upper limit of the present study. From these results, it seems probable that the cylinder will no longer undergo tertiary-lock-on at velocity ratios $A_m > 3$.

This study shows that the rotary-lock-on region persists to much higher A_m than the tertiary-lock-on region.

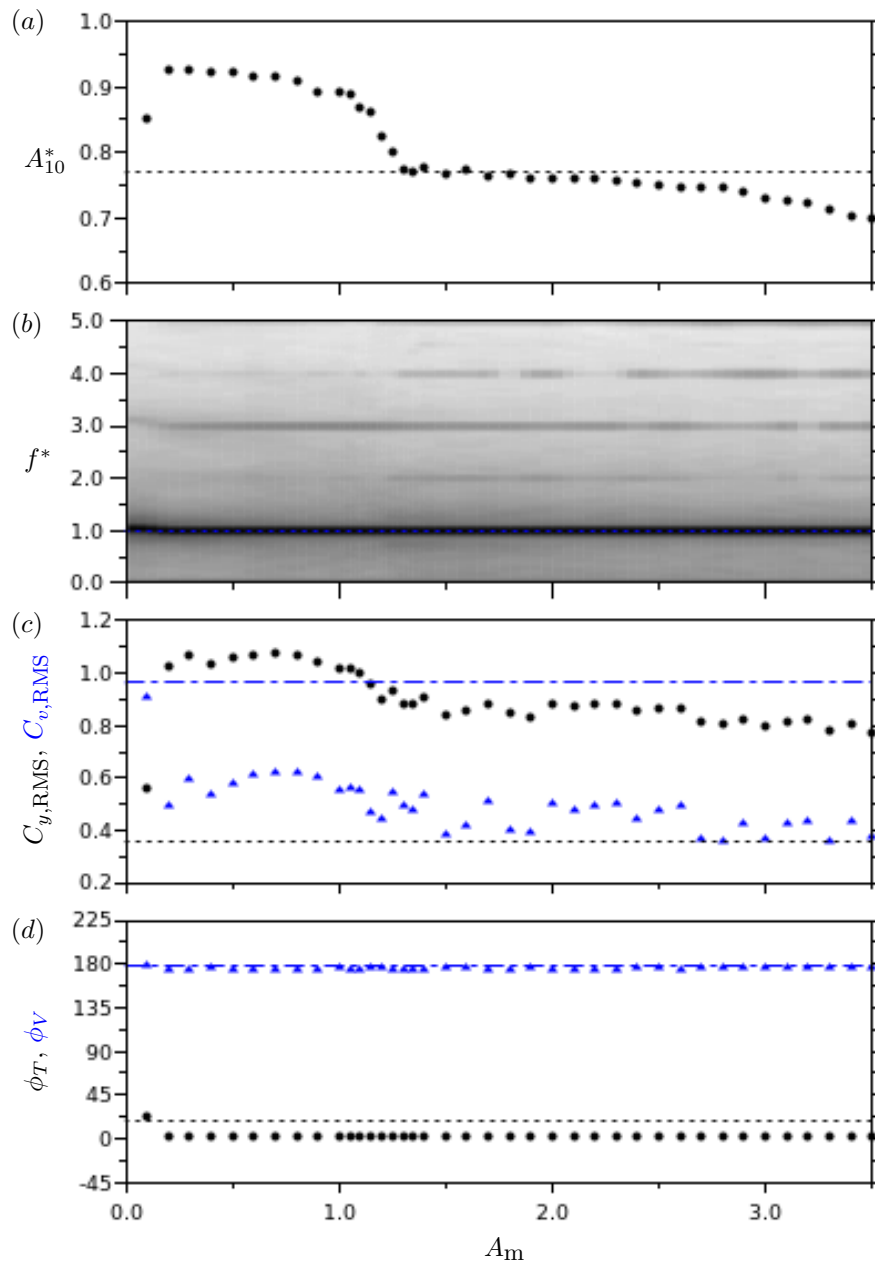


FIGURE 5.25: The response quantities of an elastically-mounted cylinder undergoing rotary oscillations is presented as a function of forcing velocity ratio (A_m) at a fixed forcing frequency ratio of $f_{rot}^* = 1.0$ and at a reduced velocity of $U^* = 5.5$. (a) presents the mean of the highest 10% of normalised amplitude peaks (A_{10}^*). The black dashed line represents the non-rotating VIV value. (b) presents a power spectra density (PSD) contour of the cylinder's displacement, y . The power density is normalised by the peak power at each A_m value. The blue dotted line illustrates the normalised frequency response, f^* , being equal to f_{rot}^* ($f^* = f_{rot}^*$). (c) and (d) presents the RMS force coefficients ($C_{y,RMS}$, $C_{v,RMS}$) and mean phases (ϕ_T , ϕ_V), respectively. In both (c) and (d), the black markers represent the total component and the blue markers represent the vortex component. The black dotted line and blue dot-dashed line represent the total and vortex component values of a non-rotating cylinder, respectively.

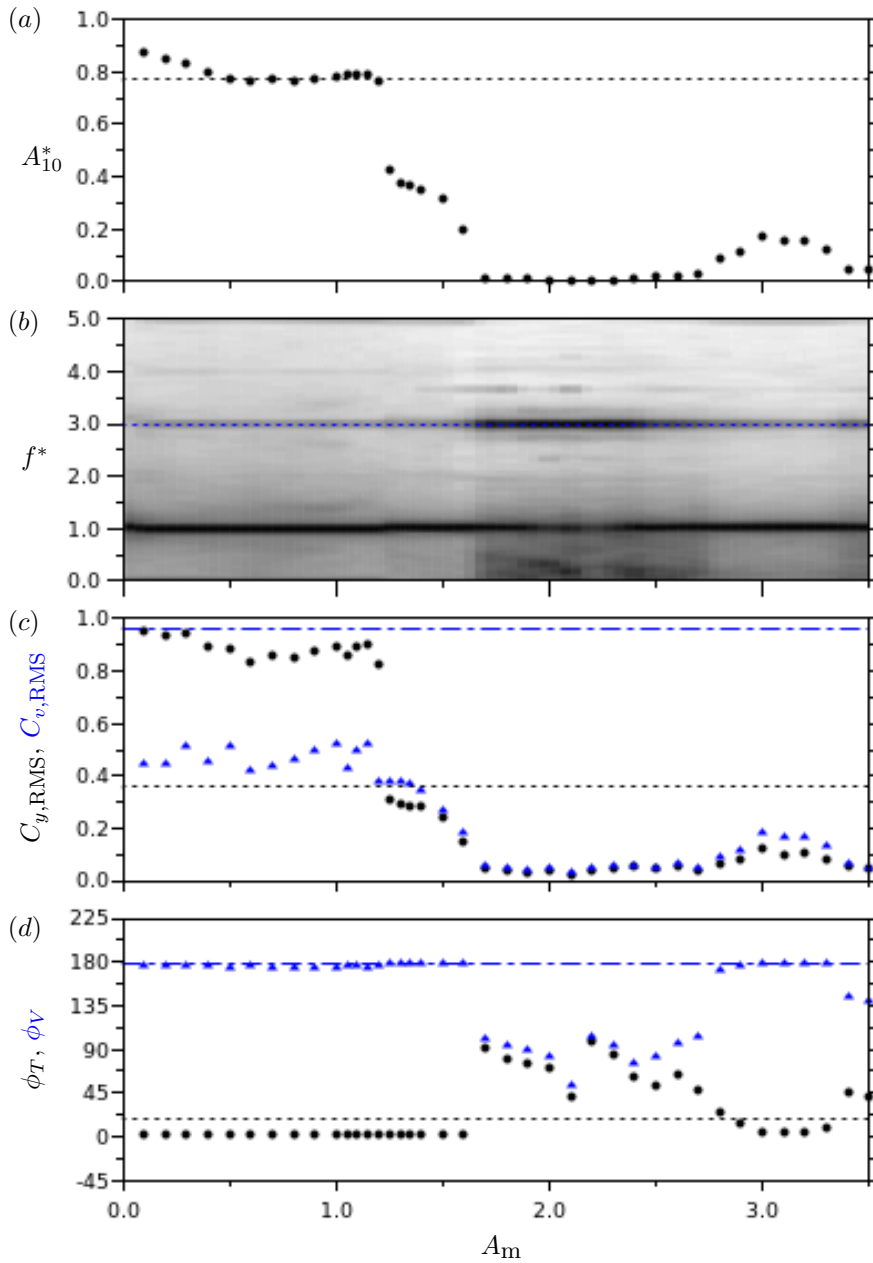


FIGURE 5.26: The response quantities of an elastically-mounted cylinder undergoing rotary oscillations is presented as a function of forcing velocity ratio (A_m) at a fixed forcing frequency ratio of $f_{rot}^* = 3.0$ and at a reduced velocity of $U^* = 5.5$. Refer to fig. 5.26 caption for detailed description of the figures.

5.7 Wake modes

The structure of vortices shed into the wake are interesting to researchers because they can influence the vibration response of an elastically-mounted structure. Here, the elastically-mounted cylinder is subjected to sinusoidally-driven rotary oscillations about its spanwise axis. Previous work on rotary oscillation of rigidly-mounted cylinders have shown the wake of the cylinder can change significantly from the Kármán vortex street observed in stationary cylinder studies. Depending on the forcing velocity and frequency ratios, the rotary oscillating cylinder can exhibit different wake modes (*e.g.* Tokumaru & Dimotakis (1991); Cheng *et al.* (2001); Cheng (2001); Choi *et al.* (2002)).

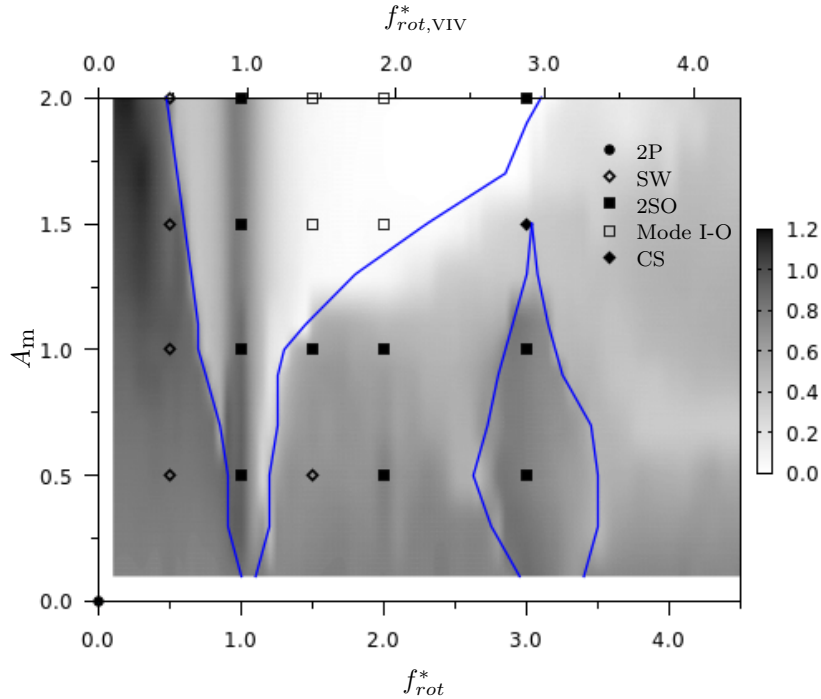


FIGURE 5.27: The wake patterns observed are based on particle image velocimetry data taken at a reduced velocity ($U^* = 5.5$) that belongs to the upper amplitude response branch of a non-rotating cylinder. The rotary-lock-on and tertiary-lock-on boundaries are shown by the solid lines. This overlays a greyscale contour map of the mean of the highest 10% of amplitude peaks (A_{10}^*) in the $A_m - f_{rot}^*$ forcing parameter space.

This section presents and discusses PIV results to help understand the wake modes of the elastically-mounted cylinder and how these vary from the structures observed in rotary oscillation of rigid cylinders and non-rotating VIV studies.

To better understand the interactions between wake modes and the cylinder's vibration, the observed wake modes have been mapped against the primary independent variables, A_m and f_{rot}^* at the two reduced velocities previously investigated. Figure 5.27 presents the wake map while the cylinder is undergoing VIV at $U^* = 5.5$ (upper response branch of a non-rotating cylinder). Figure 5.28 presents a similar map at $U^* = 8.0$ (lower branch).

At $U^* = 5.5$ and f_{rot}^* below the lower boundary of the rotary-lock-on region, the wake of the cylinder exhibits switching behaviour and in some cases chaotic vortex shedding. This is expected because outside the rotary-lock-on region the response of the cylinder mainly depends on the f and f_{osc} frequencies, which can cause the cylinder to exhibit strong frequency modulation. Studies involving rotary oscillating rigid cylinders showed that while the forcing motion determines the structure of the wake and the wake are generally variations of the 2S and 2P mode (see Tokumaru & Dimotakis (1991); Cheng *et al.* (2001); Cheng (2001); Choi *et al.* (2002)). Non-rotating VIV studies such as Khalak & Williamson (1999); Govardhan & Williamson (2000, 2002) have shown that the natural wake mode of an elastically-mounted cylinder in the upper amplitude response branch is 2P.

In this region (below the lower f_{rot}^* boundary of the rotary-lock-on region), the cylinder often switches between 2S (two single, counter rotating vortices shed per cycle), 2SO (two single, counter rotating vortices shed per cycle offset from the streamwise centreline) and 2P (two counter-rotating vortex pairs shed per cycle) mode. This is the result of frequency modulation as the oscillating body switches between the forcing frequency (f_{osc}) and the frequency response of a cylinder undergoing non-rotating VIV (f_{VIV}). As the cylinder switches between the 2S, 2SO and 2P; it intermittently exhibits the P+S structure during transition between the three aforementioned modes. The P+S

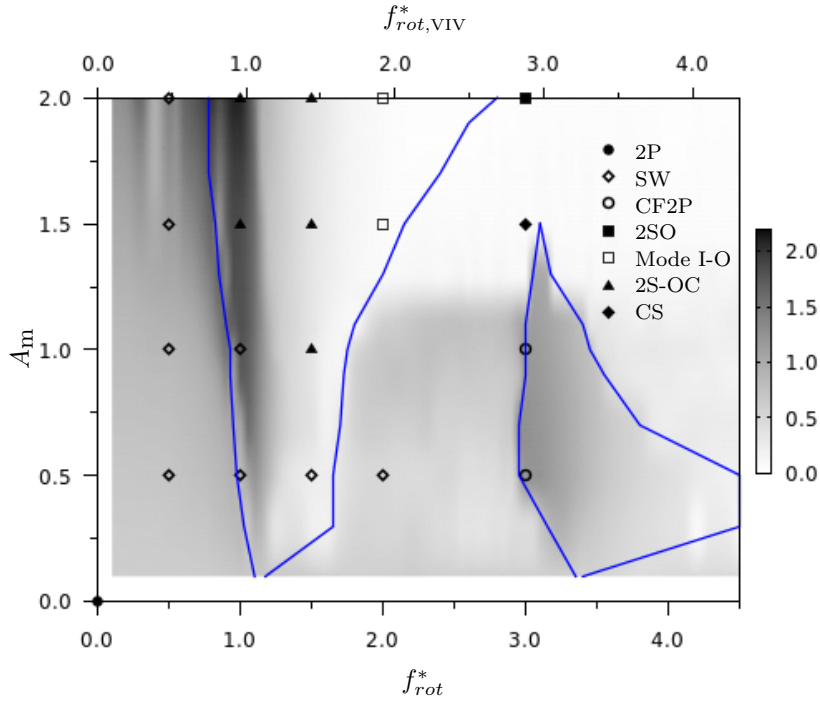


FIGURE 5.28: The wake patterns observed are based on particle image velocimetry data taken at a reduced velocity ($U^* = 8.0$) that belongs to the low amplitude response branch of a non-rotating cylinder. The rotary-lock-on and tertiary-lock-on boundaries are shown by the solid lines. This overlays a greyscale contour map of the mean of the highest 10% of amplitude peaks (A_{10}^*) in the $A_m - f_{rot}^*$ forcing parameter space.

mode is a transitional structure between 2S, 2SO and 2P, it is not observed for more than several instantaneous frames when it occurs. 2SO mode will be discussed later and the P+S mode is characterised by a pair of counter-rotating and a single vortex shed per cycle. As a result of the switching between the three wake modes, this mode is simply labelled as SW for *switching*. To better show the switching behaviour of the SW mode, the instantaneous iso-contours of the cylinder's wake at different points in its displacement time history is presented in fig. 5.29. The switching behaviour of the SW mode can be seen from fig. 5.29 where the red sections of the time history in fig. 5.29(a) exhibits the 2SO mode while the blue sections exhibits the 2S mode typically seen in stationary cylinder and VIV studies. Instantaneous vorticity iso-contours of the 2SO, 2S and P+S modes are shown in fig. 5.29(b.i - b.vi), fig. 5.29(c.i - c.iii) and fig. 5.29(d.i - d.iii), respectively. The wake switched from 2SO mode to 2S mode and back to 2SO mode in less than five oscillation periods. This shows how frequent the wake structure can switch. The wake briefly switched from 2SO to P+S mode for approximately one oscillation period before switching back to 2SO. This mode is observed at low frequency ratios ($f_{rot}^* \lesssim 0.5$) where the cylinder's amplitude response, A_{10}^* , remains comparable or larger in value when compared to the non-rotating case.

As the cylinder undergoes rotary oscillations at $f_{rot}^* = 1$ (within the rotary-lock-on region), the structure of the wake is characterised by the shedding of two counter rotating vortices away from the streamwise centreline per shedding cycle. This is similar to Mode I reported in rotary oscillation studies of rigidly-mounted cylinders. However, the difference between the wake structure observed in the present study and Mode I is that only two single counter-rotating vortices. The observed wake pattern is inherently different to 2S and Mode I. Mode I sheds two pairs of vortices of the same sign (see Tokumaru & Dimotakis (1991); Choi *et al.* (2002)), the present structure sheds two single counter-rotating vortices. Because the *two single* counter-rotating vortices are shed *offset* from the streamwise centreline, this wake mode observed in the present study is referred as 2SO.

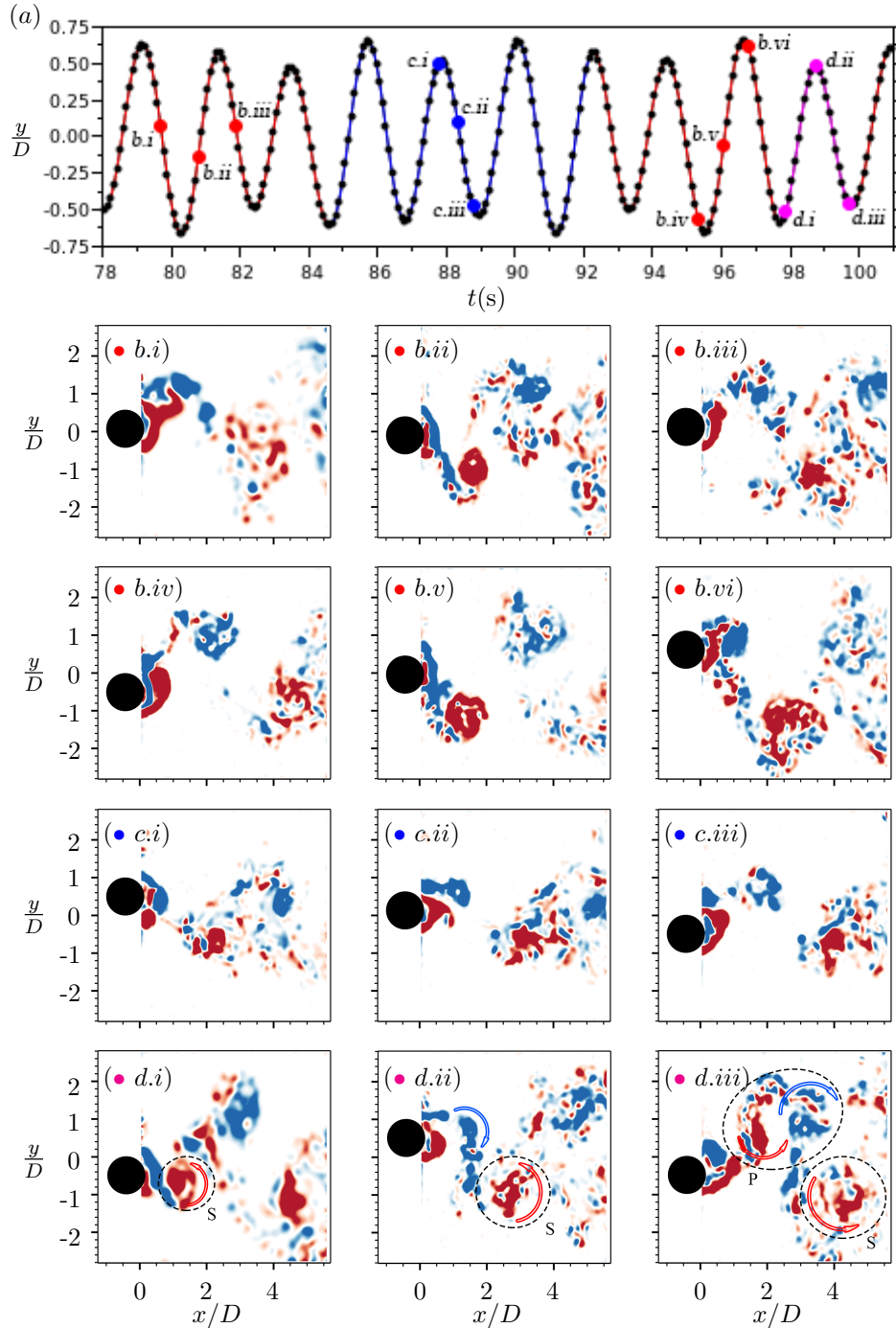


FIGURE 5.29: The intermittency and switching behaviour of the SW wake mode is presented. PIV data presented were taken at reduced velocity $U^* = 5.5$, forcing velocity ratio $A_m = 0.5$ and forcing frequency ratio $f_{rot}^* = 1.5$. (a) presents a short time history sample of the normalised displacement (y/D). Circle markers are locations where images were taken. The red data series represent the presence of a wake pattern similar to Mode I. The labelled red circle markers are locations of the instantaneous vorticity iso-contours presented sequentially in $b(i - vi)$. The blue data series represent a wake pattern similar to the 2S mode. The labelled blue circle markers are locations of the instantaneous vorticity iso-contours presented sequentially in $c(i - iii)$. The magenta data series represent a wake pattern similar to the P+S mode. The labelled magenta circle markers are locations of the instantaneous vorticity iso-contours presented sequentially in $d(i - iii)$.

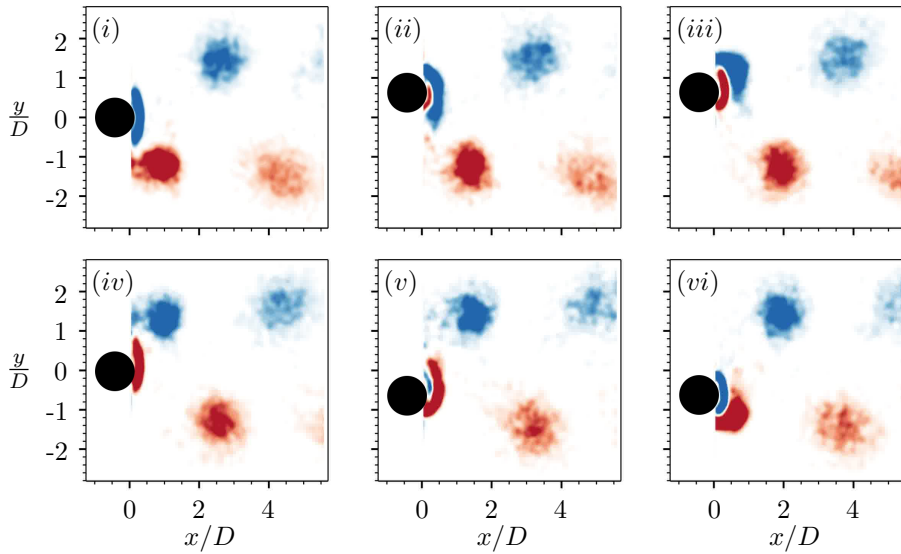


FIGURE 5.30: 2SO wake pattern observed at reduced velocity $U^* = 5.5$, forcing velocity ratio $A_m = 1.5$ and forcing frequency ratio $f_{rot}^* = 1.0$. $i - vi$ sequentially presents the phase-averaged iso-contours of the vorticity over one shedding cycle.

The phase-averaged iso-contours of the 2SO pattern are presented in fig. 5.30($i - vi$). In the area between the rotary-lock-on and tertiary-lock-on regions, 2SO is also observed. Data from the present study suggests that 2SO is observed at sufficiently large values of forcing frequency ratio ($f_{rot}^* \gtrsim 0.5$) and it is associated with relatively large values of A_m^* . The vorticity of the vortices shed in this wake mode increases with A_m . This phenomenon is not unexpected. Since A_m is the ratio between the peak surface tangential velocity, $r\dot{\theta}$, and the free-stream velocity, U_∞ ; an increase in A_m is the result of an increase in the peak surface tangential velocity when U_∞ is fixed. Increase in the peak surface tangential velocity, $r\dot{\theta}$, is caused by the controlled increase in the cylinder's angular velocity, θ . Therefore, an increase in the peak angular velocity, θ , will increase the circulation being fed into the vortices shed.

A variation of the 2SO wake pattern is observed within the rotary-lock-on region. From the phase-averaged vorticity iso-contours presented in fig. 5.31(a.i - a.vi), it can be seen that this variation of 2SO exhibits a tongue-shaped structure as a vortex is being shed. From fig. 5.31(a.i - a.iii), as the counter-clockwise (red) vortex is being shed, it draws a tongue-shaped region of clockwise (blue) vorticity from the other side of the cylinder (across the streamwise centreline) towards itself. This occurs within $2.5D$ downstream of the cylinder. This was observed at forcing velocity ratios $A_m \gtrsim 1.5$ and frequency ratios $f_{rot}^* \gtrsim 1.5$. An examination of the instantaneous vorticity iso-contours presented in fig. 5.31(c.i - c.iv) at positions highlighted in fig. 5.31(b) revealed an interesting phenomenon. The contours show a smaller vortex opposite in sign (labelled as A2 and B2) is shed with the primary vortex (labelled as A1 and B1) on each side of the streamwise centreline per half shedding cycle. What was seen as a tongue-shaped structure in fig. 5.31(a.i - a.vi) is in fact a smaller vortex of opposite vorticity. In terms of vortex count per shedding cycle, this mode is more similar to 2P than Mode I, as two pairs of counter rotating vortices are shed per cycle. However, in terms of the overall wake structure, it strongly resembles Mode I. Similar wake structures were reported in Du & Sun (2015) and Chou (1997). However, in the present study, the smaller vortex is found to orbit around the larger vortex in the near wake as they move downstream. As a result of their counter-rotating vorticity, the two vortices self-annihilate. At a sufficient distance downstream of the cylinder, the smaller vortex will be annihilated by the primary vortex. The primary vortex will be weakened

by the smaller vortex and drawn towards the streamwise centreline by the opposite vorticity of the smaller vortex. These are new observations for an elastically-mounted cylinder, as the behaviour of the smaller vortex and the overall structure of the wake was not reported or discussed in the simulation by Du & Sun (2015), and the observations by Chou (1997) on their simulation was for a rigidly-mounted cylinder. Due to its similarity to Mode I and the *orbiting* behaviour of the smaller vortex, this mode is referred as Mode I-O. This mode is observed in an area within the rotary-lock-on region where the cylinder exhibits amplitude responses significantly smaller in A_{10}^* value than the non-rotating case.

In general, the wake of the cylinder undergoing rotary oscillations is well defined. However, this is not always the case, imaging results taken at the tertiary-lock-on boundary at velocity ratio $A_m = 1.5$ and frequency ratio $f_{rot}^* = 3.0$ showed the wake of the cylinder lacked distinctive shedding structures. Figure 5.32(a.i - a.vi) presents the phase-averaged vorticity iso-contours of the cylinder's wake. These contours show that the wake exhibit some shedding structure. The instantaneous vorticity iso-contours in fig. 5.32(c.i - c.iv) showed that the cylinder sheds small counter-rotating vortices into the wake at irregular rates. These small vortex structures quickly decay as they flow downstream. While this mode is not completely without any form or structure, especially in the near wake, due to the *chaotic* shedding and decay of *small* vortex structures, this mode is referred as CS. This mode is also observed at other forcing parameters near the boundaries of the rotary-lock-on region. However, it is generally observed as a secondary wake mode where its occurrence is less than the primary wake mode.

At U^* associated with the lower amplitude response branch ($U^* = 8.0$) some of wake modes observed in the upper branch continue to exist. As shown by the wake mode map presented in fig. 5.28, at f_{rot}^* below the lower f_{rot}^* boundary of the rotary-lock-on region, the wake of the cylinder continues to be characterised by the SW mode. In low A_{10}^* areas of the rotary-lock-on region, Mode I-O was observed. A number of new wake modes were observed in the lower branch.

At the lower f_{rot}^* boundary of the tertiary-lock-on region, a new variant of the 2P mode was observed. The instantaneous vorticity iso-contours of this 2P variant are presented in fig. 5.33(b.i - b.vi). The typical 2P wake mode consist of a pair of counter-rotating vortices shed per half shedding cycle. The closewise and counter-clockwise vortices in each vortex pair are aligned in the streamwise direction. The new variant of the 2P mode also sheds two pairs of counter rotating vortices over a complete shedding cycle, however, each vortex pair is aligned in the *cross-flow* direction. As a result of the number of vortex pairs and their orientation, this mode is referred as CF2P.

In parts of the rotary-lock-on region where body vibrations persist (at frequency ratios $f_{rot}^* \lesssim 1.5$), a variant of the 2S mode was observed. It is characterised by the shedding of two counter rotating vortices per shedding cycle. Figure 5.34(i - vi) presents the phase-averaged vorticity iso-contours of this wake mode. The vortices are shed to either side of the streamwise centreline. As the shed vortices flow downstream they have a tendency to coalesce in the streamwise direction and break down within several cylinder diameters, D . This type of behaviour was previously reported in free and forced oscillation studies by Williamson (1988); Govardhan & Williamson (2002) and in the low Re simulation of an elastically-mounted cylinder undergoing constant rate rotation by Bourguet & Lo Jacono (2014). They refer to this type of wake structure as C(2S). Similar wake pattern have also been reported in studies of rigidly-mounted cylinders undergoing rotary oscillations. Studies by Tokumaru & Dimotakis (1991); Cheng *et al.* (2001); Cheng (2001); Choi *et al.* (2002) observed a similar wake structure and Tokumaru & Dimotakis (1991); Choi *et al.* (2002) refer this pattern as Mode II. As this wake mode sheds *two single* counter-rotating vortices per cycle, *offset* from the streamwise centreline and *coalesces* as the vortices flow downstream, this mode is referred as 2S-OC. This help differentiates this wake mode to the 2SO pattern where larger offsets from the streamwise centreline are observed with no signs of coalescing.

From the study of the fluid structure downstream to the cylinder, it is evident that there exist

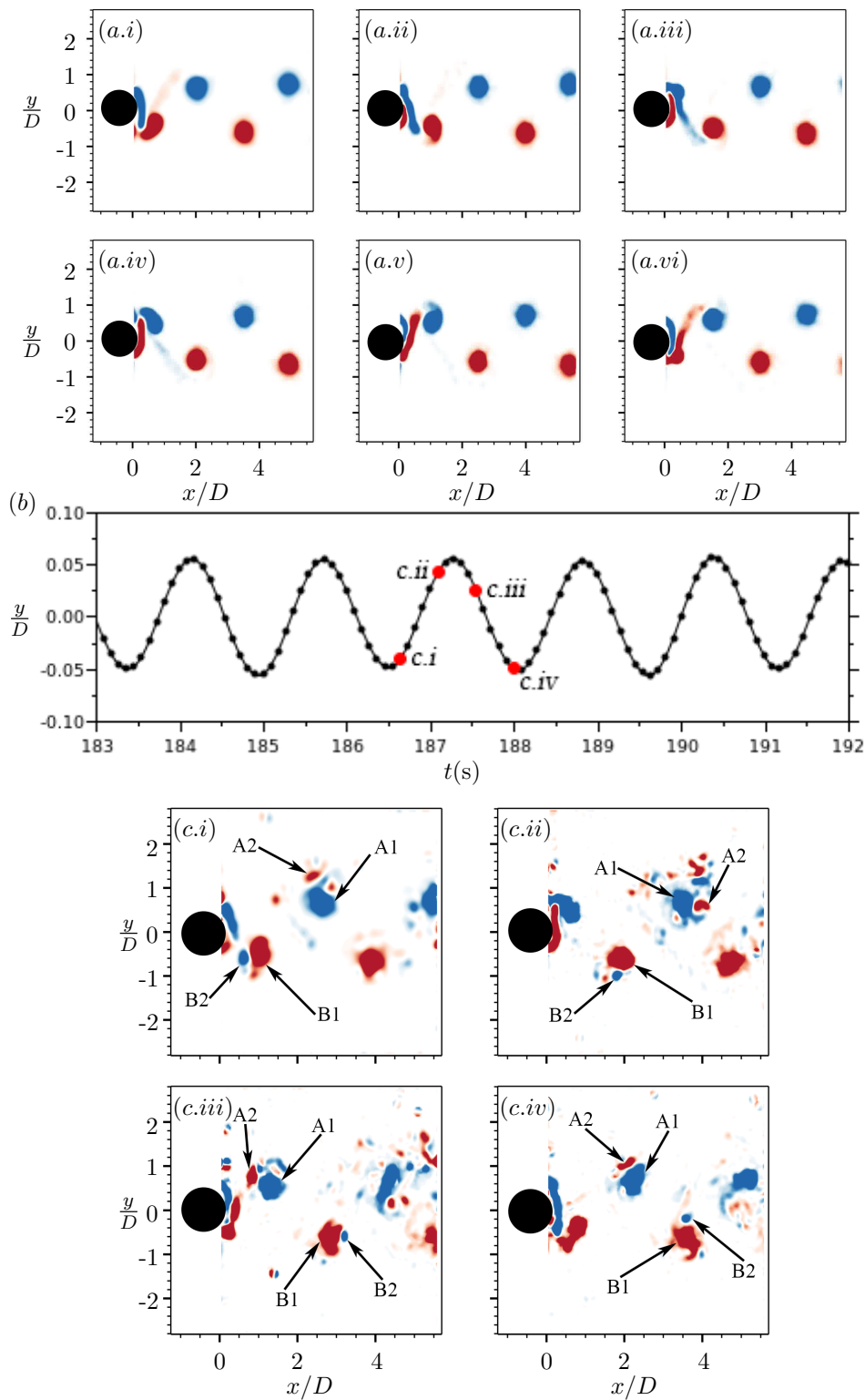


FIGURE 5.31: Mode I-O observed at reduced velocity $U^* = 5.5$, forcing velocity ratio $A_m = 1.5$ and forcing frequency ratio $f_{rot}^* = 1.5$. a(i - vi) sequentially presents phase-averaged iso-contours of the vorticity of the Mode I-O wake pattern over one shedding cycle. (b) presents a short time history sample of the normalised displacement (y/D). Black circle markers are locations where images were taken and red circle markers represent the instantaneous cases presented in c(i - iv).

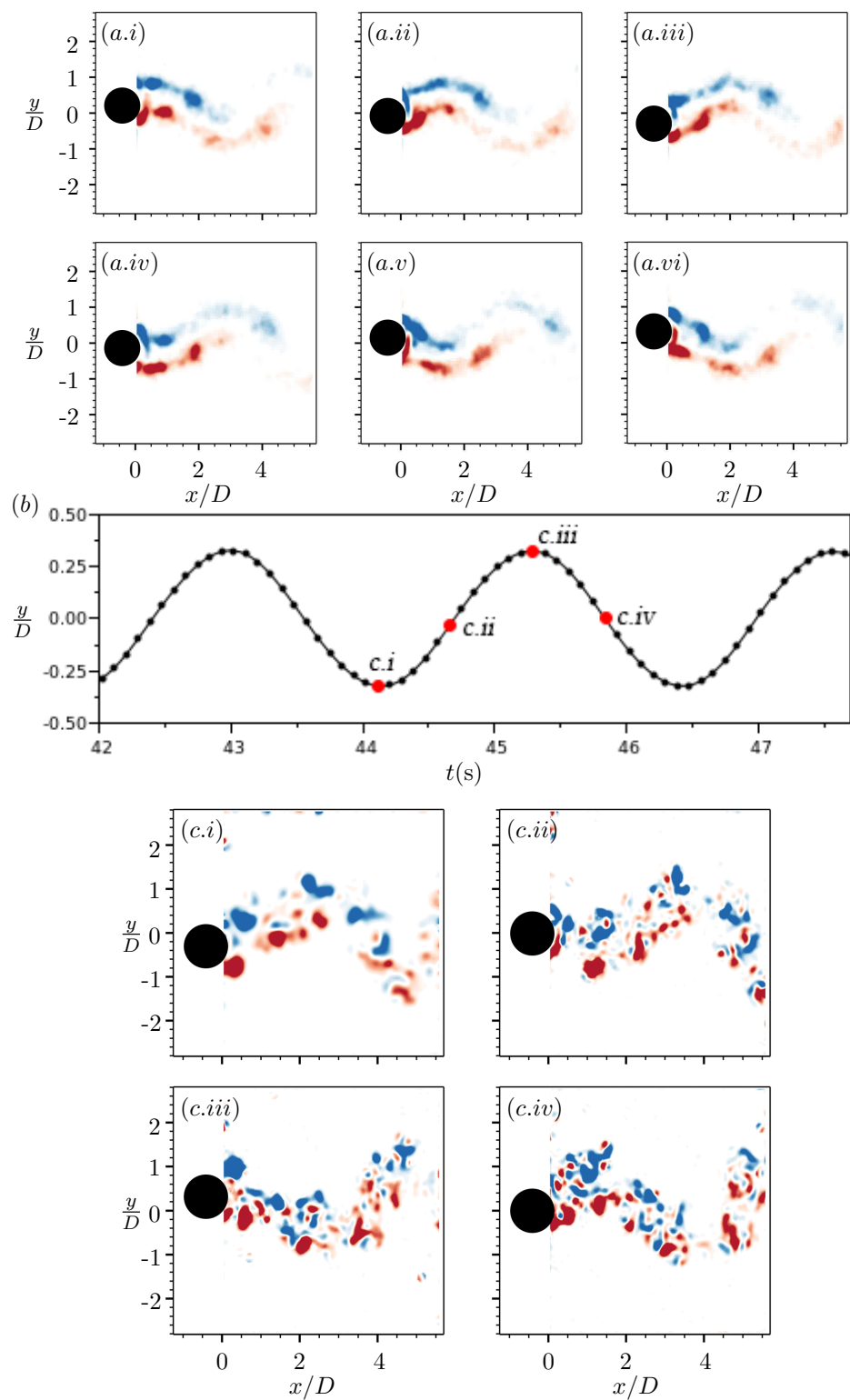


FIGURE 5.32: CS wake pattern observed at reduced velocity $U^* = 5.5$, forcing velocity ratio $A_m = 1.5$ and forcing frequency ratio $f_{rot}^* = 3.0$. a(i - vi) sequentially presents phase-averaged iso-contours of the vorticity of the CS wake pattern over one shedding cycle. (b) presents a short time history sample of the normalised displacement (y/D). Black circle markers are locations where images were taken and red circle markers represent the instantaneous cases presented in c(i - iv).

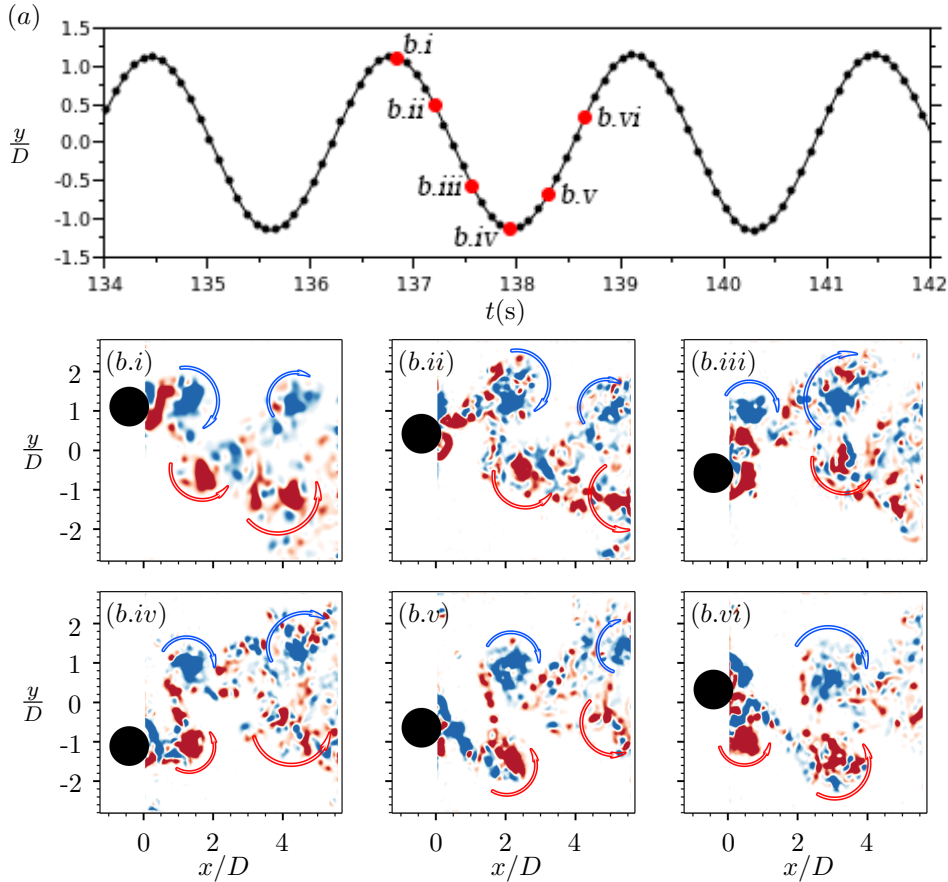


FIGURE 5.33: CF2P observed at reduced velocity $U^* = 8.0$, forcing velocity ratio $A_m = 1.0$ and forcing frequency ratio $f_{rot}^* = 3$. (a) presents a short time history sample of the normalised displacement (y/D). Black circle markers are locations where images were taken and red circle markers represent the instantaneous vorticity iso-contours presented sequentially in b(i - iv). Blue and red coloured arrows highlight the clockwise and counter-clockwise vortex structures, respectively.

a number of different wake modes. Based on the collected imaging data, it is clear that some wake patterns are observed in specific regions of the forcing parameter space. In particular, Mode I-O is observed exclusively in very low amplitude response, A_{10}^* , areas within the rotary-lock-on region. While a number of new wake modes are observed in the present study, they are variants of the 2S and 2P mode. As discussed, the wake of a rigid cylinder undergoing rotary oscillations largely exhibit variants of the 2S mode while an elastically-mounted cylinder oscillating in the upper and lower amplitude response branches exhibit variants of the 2P mode. Therefore, it is expected that these new wake modes are based on some elements of the 2S and 2P mode, particularly, the number of single or vortex pairs shed per cycle.

As the PIV images from the present study were taken concurrently with the response data at chosen locations of interest, the wake maps are somewhat coarse in resolution and specific questions concerning transitions in the cylinders response and how they correlate to the wake structure cannot be answered. While better resolution of the map would be desirable, to achieve that, given the large parameter set and space, would have required more resources than were available. To better characterise each wake mode and how they correlate with some of the response changes, as reported in §5.5, could be the basis for future studies on this subject.

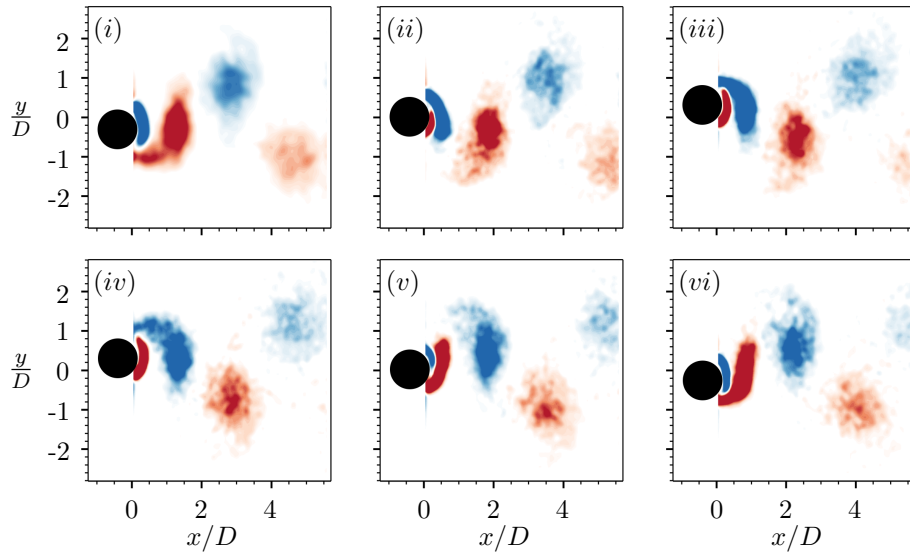


FIGURE 5.34: The 2S-OC observed at reduced velocity $U^* = 8.0$, forcing velocity ratio $A_m = 2.0$ and forcing frequency ratio $f_{rot}^* = 1.5$. *i-vi* sequentially presents phase-averaged iso-contours of the vorticity of the Mode II wake pattern over one shedding cycle.

5.8 Response over a range of reduced velocities

It has been shown in the present study that sinusoidally-driven rotary oscillations of an elastically-mounted cylinder can effectively suppress VIV and large amplitude oscillations at specific forcing velocity ratios and frequency ratios in both upper and lower amplitude response branches. From the results presented in §5.5, it is clear that at certain forcing parameters the elastically-mounted cylinder can reach A_{10}^* amplitude values more than three times that of a non-rotating cylinder. Of interest to researchers and engineers is how an elastic system will behave when subjected to the less favourable forcing parameters, *i.e.* where large increases in A_{10}^* over the non-rotating case were observed. In the present study, the large amplitude response increases were generally observed at forcing frequency ratio of $f_{rot}^* \approx 1.0$ and at velocity ratios $A_m \gtrsim 1$. In order to examine how the response of an elastically-mounted cylinder changes with non-ideal forcing parameters, the cylinder is subjected to rotary-lock-on at velocity ratio $A_m = 1.0$ and frequency ratio $f_{rot}^* = 1.0$ over a large range of reduced velocities, $U^* = 3 - 20$.

The cylinder's response at $A_m = 1.0$ and $f_{rot}^* = 1.0$ is presented as a function of U^* in fig. 5.35. Figure 5.35(a) presents the mean of the highest 10% of normalised amplitude peaks, A_{10}^* . The open circle markers represent the A_{10}^* amplitude response of a non-rotating, elastically-mounted cylinder, and the red square markers represents the A_{10}^* of a cylinder rotary oscillating with favourable forcing parameters ($A_m = 1.3$ and $f_{rot}^* = 2.0$). Figure 5.35(b) presents a PSD contour of the cylinder's displacement, y , as a function of the normalised frequency response, f^* , and U^* . The power density is normalised by the peak power at each A_m value. A comparison of A_{10}^* shows that the amplitude of the cylinder oscillating at non-ideal rotary forcing parameters is significantly higher than that of a non-rotating cylinder across most of the tested range of U^* . At reduced velocities ($U^* \approx 5 - 5.5$) associated with the beginning of the upper amplitude response branch of a non-rotating cylinder, the A_{10}^* of the cylinder rotary oscillating at non-ideal parameters is similar to the non-rotating case. While undergoing rotary oscillation at a velocity ratio $A_m = 1.0$ and a $f_{rot}^* = 1.0$, the A_{10}^* of the cylinder increases monotonically with reduced velocity when $U^* \gtrsim 12$. This monotonic increase in A_{10}^* amplitude is similar to the response observed in galloping studies Zhao *et al.* (2014b). However,

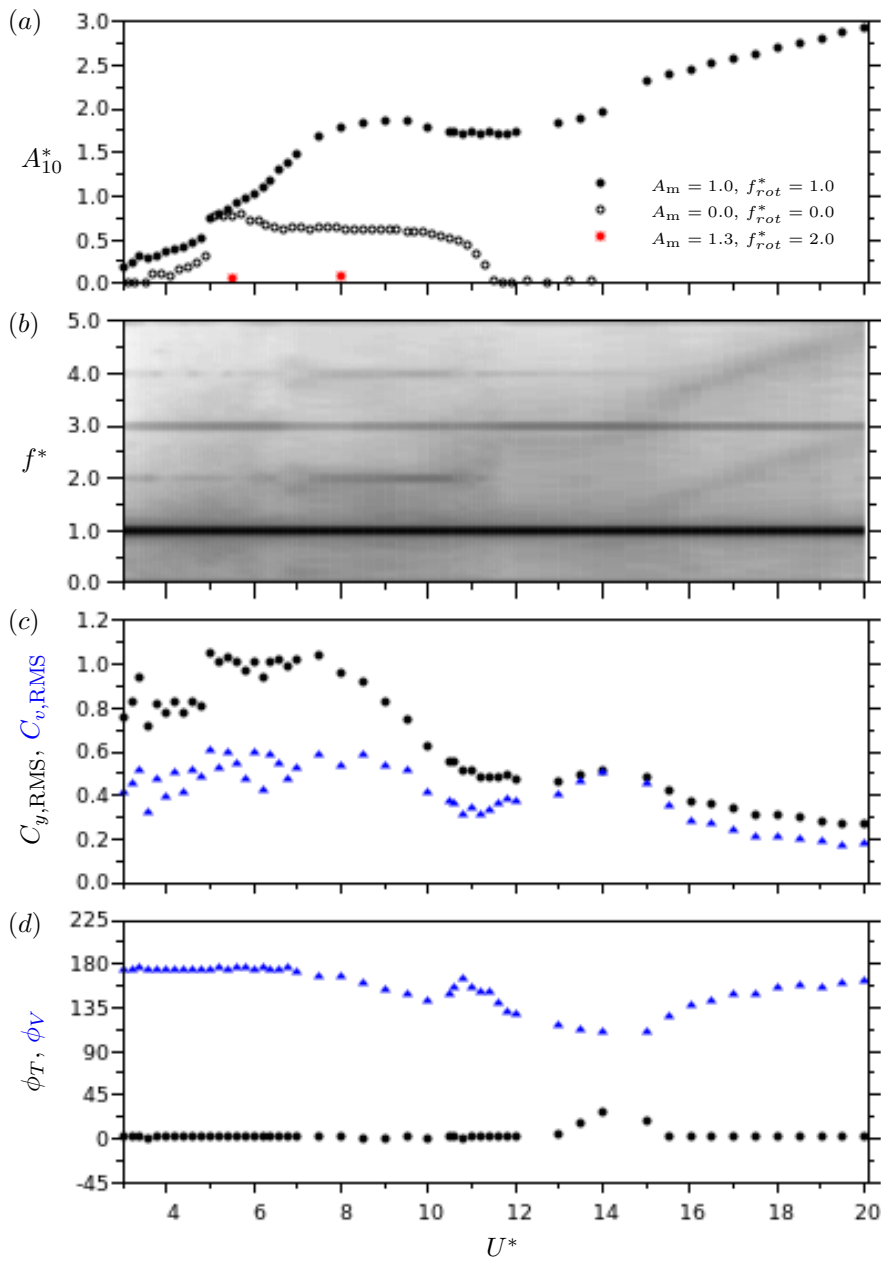


FIGURE 5.35: The response quantities of an elastically-mounted cylinder undergoing rotary oscillations is presented as a function of reduced velocity (U^*) at a fixed forcing velocity ratio of $A_m = 1.0$ and at fixed forcing frequency ratio of $f_{rot}^* = 1.0$. (a) presents the mean of the highest 10% of normalised amplitude peaks (A_{10}^*). The open circle markers represent the A_{10}^* of a non-rotating cylinder undergoing VIV. The red squares represents the A_{10}^* at $A_m = 1.3$ and $f_{rot}^* = 2.0$. (b) presents a power spectra density (PSD) contour of the cylinder's displacement, y . The power density is normalised by the peak power at each U^* value. (c) and (d) presents the RMS force coefficients ($C_{y,RMS}, C_{v,RMS}$) and mean phases (ϕ_T, ϕ_V), respectively. In both (c) and (d), the black markers represent the total component and the blue markers represent the vortex component.

unlike galloping, the frequency response of the cylinder shown in fig. 5.35(b) remains rotary-locked-on to the natural frequency of the oscillating system, *i.e.* $f_{rot}^* = f^* = 1$, while galloping typically occurs at lower frequencies.

Figure 5.35(c) and fig. 5.35(d) presents the force coefficients and phases, respectively. In both

fig. 5.35(c) and (d), the black markers represent the RMS total force coefficient, $C_{y,\text{RMS}}$, and mean total phase, ϕ_T . Similarly, in the same figures, the blue markers represent the RMS vortex force coefficient, $C_{v,\text{RMS}}$, and mean vortex phase, ϕ_V . For a non-rotating cylinder undergoing VIV, ϕ_T remains close to 0° and jumps to 180° at the upper to lower branch transition. With the addition of rotary oscillation, ϕ_T remained close to 0° across the entire vibration region of a non-rotating cylinder.

5.9 Chapter summary

This chapter has presented results of an elastically-mounted cylinder free to oscillate in the cross-flow direction and undergoes sinusoidally-driven rotary oscillations at moderate Reynolds numbers ($Re > 1000$). The sinusoidal rotary oscillation motion profile is validated at a range of A_m and f_{rot}^* .

The results from the present study show that the ‘lock-on’ phenomenon previously reported in rotary oscillation of rigid cylinders (see Cheng *et al.* (2001); Choi *et al.* (2002)); and the low Re simulation of an elastically-mounted cylinder undergoing rotary oscillations by Du & Sun (2015) persist at $Re > 1000$. At the two tested reduced velocities ($U^* = 5.5, 8.0$), two regions exist where the cylinder’s oscillation frequency, f , synchronises with the rotary forcing frequency, f_{osc} , or its subharmonic. At forcing parameters where f follows f_{osc} , *i.e.* $f = f_{osc}$, it is referred as the rotary-lock-on region. The rotary-lock-on region is found near frequency ratio $f_{rot}^* \approx 1$. This region increases in width covering a larger range of f_{rot}^* as A_m is increased. Cheng *et al.* (2001); Cheng (2001); Choi *et al.* (2002) also reported similar widening of their lock-on regions as A_m is increased. At forcing parameters where f follows the one-third subharmonic of the f_{osc} , *i.e.* $f = 1/3f_{osc}$, this is referred as the tertiary-lock-on region. The tertiary-lock-on region is found near frequency ratio $f_{rot}^* \approx 3$. It is in the shape of a spinning top. With increasing A_m , the range of f_{rot}^* at which the cylinder undergoes tertiary-lock-on first increases from a single point to a maximum, then it decreases to a single point again before disappearing.

The dynamic response of a rotary-oscillating cylinder showed that the rotary oscillation’s effectiveness at reducing large amplitude VIV is dependent on the forcing parameters. In the upper amplitude response branch at reduced velocity $U^* = 5.5$, large amplitude VIV is observed in most of the areas outside the rotary-lock-on and tertiary-lock-on regions in the A_m - f_{rot}^* domain. At f_{rot}^* below the lower f_{rot}^* boundary of the rotary-lock-on region and at velocity ratios $A_m \gtrsim 1.0$, amplitudes (A_{10}^*) larger than the non-rotating VIV case is observed. Large amplitude oscillations were observed at two other areas; the first is a narrow range of frequency ratios ($0.8 \lesssim f_{rot}^* \lesssim 1.1$) within the rotary-lock-on region and second within the tertiary-lock-on region. The remainder of the rotary-lock-on region achieved significant reductions in A_{10}^* ; especially at forcing frequency ratios $f_{rot}^* \gtrsim 1.3$. In the lower amplitude response branch ($U^* = 8.0$), the response of the cylinder is generally similar to that of the upper branch case ($U^* = 5.5$). Large amplitude VIV was observed at low frequency ratios $f_{rot}^* \lesssim 1.1$ and high velocity ratios $A_m \gtrsim 0.5$. The largest amplitude response measured was more than three times that of the non-rotating response and it is within the rotary-lock-on region. At forcing velocity ratios $A_m \gtrsim 1.3$ and frequency ratios $f_{rot}^* \gtrsim 1.3$, large amplitude responses (A_{10}^*) cease to exist. When comparing the range of A_m and f_{rot}^* at which large amplitude oscillations were suppressed in previous work, they are in good agreement. In the low Re simulation by Du & Sun (2015), they reported large decreases in amplitude response, A^* , at frequency ratios $f_{rot}^* \gtrsim 1$ and at velocity ratios $A_m \gtrsim 1.3$. This demonstrates the efficacy of rotary oscillation to suppress VIV even at moderate Reynolds numbers $Re > 1000$.

An experiment was done to study whether the rotary-lock-on region will disappear at sufficiently high A_m and if the tertiary-lock-on region will reappear. This study was done over a large range of forcing velocity ratios ($A_m = 0 - 3.5$) at fixed frequency ratios $f_{rot}^* = 1.0$ and 3.0 in the upper amplitude response branch ($U^* = 5.5$). Response results showed that large amplitude oscillations

persist and f continues to follow f_{osc} at all tested range of A_m at $f_{rot}^* = 1.0$. This demonstrates that rotary-lock-on continue to occur at very high A_m . At a fixed frequency ratio of $f_{rot}^* = 3.0$, the tertiary-lock-on region disappears between velocity ratio $1.6 \lesssim A_m \lesssim 2.4$ and reappears at $A_m \gtrsim 2.4$.

Following the cylinder's dynamic responses, the wake structure was studied using PIV. A number of new and existing wake modes were observed. The SW mode is characterised by the switching of wake patterns. These wake patterns resemble the 2S and 2P modes observed in previous studies of forced and freely oscillating cylinders. This mode is typically observed at low f_{rot}^* regions where the effect of frequency modulation is strong. 2SO and 2S-OC are two wake modes that consist of two single counter-rotating vortices shed per cycle. The vortices in both modes are shed away from the streamwise centreline. The difference between these two modes are largely the shed vortices' closeness to the streamwise centreline and the decay of the vortical structures that. While these two wake patterns share some likeness to the 2S mode observed in VIV studies, their separation from the streamwise centreline is a feature that resembles Mode I and Mode II from rigid rotary oscillating cylinder studies. These modes were observed over a large range of A_m and f_{rot}^* . Mode I-O was observed within the rotary-lock-on region where large amplitude vibration response is minimal. This mode consists of two pairs of counter-rotating vortices shed per cycle. Each pair has a larger primary vortex and a smaller secondary vortex of opposite vorticity that orbits around the primary vortex. A similar wake structure was shown in Du & Sun (2015) but little about its behaviour was discussed. A similar wake structure was observed in a simulation of a rigid cylinder at a Reynolds number of $Re = 1000$ by Chou (1997). The CS wake pattern was observed close to the boundary of the tertiary-lock-on region. This new wake mode consists of chaotic shedding of small vortex structures. The CF2P mode is another new wake pattern observed at high f_{rot}^* in the lower amplitude response branch ($U^* = 8.0$). It sheds the same number of counter-rotating vortex pairs as regular 2P mode seen in VIV studies; however, the vortex pairs in the CF2P mode is aligned in the cross-flow direction whereas the vortex pairs in a 2P mode are aligned streamwise. From the study of the cylinder's wake structure, it is evident that some features of the wake patterns observed in rotary oscillation of rigid cylinder studies continue to exist even when the body becomes elastically-mounted.

Furthermore, the dynamic response of a rotary oscillating cylinder is compared with a non-rotating cylinder over a large range of reduced velocities. It was observed that at a forcing velocity ratio of $A_m = 1.0$ and a forcing frequency ratio of $f_{rot}^* = 1.0$, the addition of rotary forcing increases the amplitude response (A_{10}^*) of the cylinder, significantly. At all tested reduced velocities, U^* , the amplitude response of the cylinder remained higher than the non-rotating case. This clearly demonstrates the limitations of using sinusoidal rotary oscillations as a mean of suppressing VIV. The present work also showed the need for specific combinations of A_m and f_{rot}^* for rotary oscillation to be beneficial to engineering applications.

Chapter 6

Conclusions and Recommendations for Future Investigations

6.1 Conclusions

In this thesis, two of the most researched active control methods to suppress vortex-induced vibration (VIV) were experimentally investigated on an elastically-mounted cylinder that is free to oscillate in the cross-flow direction. The experiments were conducted at low mass and damping ratios over a range of moderate Reynolds numbers ($Re \gtrsim 1000$). The first investigation involves rotating the elastically-mounted cylinder at a constant rate, the parametric studies were based on the independent variables: reduced velocity, U^* , and rotation rate, α . The second investigation involves forcing the elastically-mounted cylinder to undergo sinusoidally-driven rotary oscillations at specific forcing values in the forcing velocity ratio and forcing frequency ratio domain. In both investigations, the dynamic response of the cylinder is studied and compared to the non-rotating cases and similar studies previously done at lower Reynolds numbers. The wake of the cylinder was also studied using particle image velocimetry (PIV) in both investigations. A summary of the main findings from this thesis is presented in the following sections.

6.1.1 Flow-induced vibration of a cylinder undergoing constant rate rotation

The results of an elastically-mounted cylinder undergoing constant rate rotation at moderate Reynolds numbers ($Re \gtrsim 1000$) have exhibited response features that agree with previous low- Re studies and have also shown new wake structures. The mean displacement of the cylinder increases with rotation rate at any fixed reduced velocity and also increases with at any fixed α . This is in excellent agreement with previous trends observed at lower Reynolds numbers in Bourguet & Lo Jacono (2014); Zhao *et al.* (2014c); Seyed-Aghazadeh & Modarres-Sadeghi (2015). It is expected that the cylinder's time-averaged displacement increases with rotation rate as the net lift, the Magnus force, is proportional to the cylinder's rate of rotation.

The amplitude response of the cylinder undergoing constant rate rotation exhibits significant differences to the non-rotating response. Up to a rotation rate of $\alpha \approx 1.5$, the peak amplitude response increases and the range of reduced velocities over which large amplitude oscillations ($A_{10}^* > 0.1D$) were observed also increased. The global peak amplitude response was observed at a reduced velocity associated with the upper amplitude response branch of a non-rotating cylinder and at a rotation rate of $\alpha \approx 2.0$. The global peak amplitude response was approximately 80% higher than the non-rotating case at $1.4D$. The largest increases in amplitude response, A_{10}^* , over the non-rotating case were observed in the upper branch and beginning of the lower branch. The amplitude response of the cylinder decreases abruptly as the rotation rate is increased pass $\alpha \approx 2.25$. With increasing

rotation rate, there is a global decrease in the normalised frequency response of the cylinder. These findings are in good agreement with the trends observed in the low Reynolds number ($Re = 100$) simulation by Bourguet & Lo Jacono (2014). They reported significant increases in amplitude response, A^* , over the non-rotating case with a global peak of $A^* \approx 1.9D$ and global decreases in frequency response with increasing rotation rate. A comparison of the size of the vibration region (where the amplitude response is $A_{10}^* \gtrsim 0.1D$) in the reduced velocity and rotation rate domain revealed some differences between the present study and previous work. The low Reynolds number ($Re = 350 - 1000$) experiments by Seyed-Aghazadeh & Modarres-Sadeghi (2015) did not exhibit the same increases in amplitude response, however, their observations on the time-averaged displacement and frequency response trends are in agreement with those seen in Bourguet & Lo Jacono (2014) and the present study. While the response trends from Bourguet & Lo Jacono (2014) are in good with the present work, their vibration region are distinctively different to the present study's. Their vibration region persists up to a rotation rate of $\alpha \approx 3.75$ and extends across to the upper reduced velocity limit of their study, whereas the vibration regions of the present study disappears when $\alpha \gtrsim 3.2$ and are limited to reduced velocities between the beginning of the initial branch and the end of the lower branch ($4.8 \lesssim U^* \lesssim 10.5$). Despite some differences in other response trends, the vibration region in Seyed-Aghazadeh & Modarres-Sadeghi (2015) is very similar to the present study. It is evident that experimental parameters such as the oscillating systems' structural properties and the effect of Reynolds number will have an impact on the cylinder's response and may explain variations in the response trends.

Imaging of the rotating cylinders wake showed that wake modes typically seen in forced and freely vibrating cylinders such as 2S, 2P and P+S continue to exist over a range of reduced velocities and rotation rates. With increasing rotation rate, modes such as 2S and P+S becomes asymmetric and deviates from the streamwise centreline. Furthermore, vortex and vortex pairs in each shedding cycle have an increased tendency to collect in groups with increasing rotation rate. The close proximity of these vortices in collected groups caused increased cross-annihilation resulting in smaller and weaker vortices as they flow downstream. A new C(AS) mode was found and it is characterised by the coalescence of small asymmetric vortices and its intermittent switching between a wider and narrower state. This mode is found at $\alpha \gtrsim 2$. Compared to Bourguet & Lo Jacono (2014), the present study did not observe wake patterns such as the T+S and U modes. This is expected after a comparison of the cylinder's response as the two studies have distinctively different vibration regions.

From the study of an elastically-mounted cylinder undergoing constant rate rotation, it is concluded that constant rate rotation continues to have a significant impact on the dynamic response and wake structure of the cylinder at a range of moderate Reynolds numbers ($1000 \lesssim Re \lesssim 6300$). Compared with previous low Reynolds number studies these results show that some response trends and wake structures observed at $Re \leq 1000$ continue above $Re = 1000$.

6.1.2 Flow-induced vibration of a cylinder undergoing sinusoidally-driven rotary oscillations

The flow-induced vibration of a cylinder undergoing sinusoidally-driven rotary oscillations was investigated at Reynolds numbers $Re > 1000$. The dynamic response and wake structure of an elastically-mounted cylinder undergoing rotary forcing showed similarities to previous work involving rotary oscillating cylinder. Analysis of the cylinder's frequency response have shown that the lock-on phenomenon reported in previous low Re studies (see Cheng *et al.* (2001); Cheng (2001); Choi *et al.* (2002); Du & Sun (2015)) continues to exist at moderate Re . The present thesis defined the phenomenon where the oscillation frequency of the cylinder following the rotary forcing frequency, f_{osc} , as 'rotary-lock-on'. Furthermore, when the oscillation frequency of the cylinder follows the one-third subharmonic of the rotary forcing frequency $1/3f_{osc}$, this is referred as 'tertiary-lock-on'. In the present forcing parameter space ($A_m - f_{rot}^*$), a rotary-lock-on region is observed near $f_{rot}^* \approx 1$,

and a tertiary-lock-on region is observed near $f_{rot}^* \approx 3$. These two regions exist in both reduced velocity cases examined ($U^* = 5.5$ and 8.0). The observation of a rotary-lock-on region was previously reported in a number of works. The presence of the rotary-lock-on region is expected since the forcing frequency approaches the non-rotating VIV frequency response, the oscillation frequency will follow the higher power f_{osc} to some value above the frequency response in non-rotating VIV (f_{VIV}) before the oscillation frequency (f) returns to f_{VIV} . The range of forcing frequency ratios over which rotary-lock-on occurs increases with forcing velocity ratio, A_m . This observation is in excellent agreement with previous rigid cylinder studies. Tertiary-lock-on was previously discussed in rigid cylinder studies by Choi *et al.* (2002); Thiria *et al.* (2006), however, the low Reynolds number $Re = 350$ simulation of an elastically-mounted cylinder by Du & Sun (2015) did not report on tertiary-lock-on. In the present study, tertiary-lock-on was observed over a substantial range of forcing velocity and frequency ratios.

The amplitude response of the cylinder outside the rotary-lock-on and tertiary-lock-on regions are at similar or are lower than non-rotating VIV values. However, at forcing frequency ratios below the lower boundary of the rotary-lock-on region and at velocity ratios $A_m \gtrsim 1$, the amplitude response increases significantly with A_m . Large amplitude oscillations were also observed within the rotary-lock-on region at forcing frequency ratios close to $f_{rot}^* = 1$. Within the tertiary-lock-on region, large amplitude vibrations were observed near the lower boundary and the amplitude response decreases with increasing frequency ratio. These trends exist in both the upper branch ($U^* = 5.5$) and lower branch ($U^* = 8.0$) cases. In the upper branch, within the rotary-lock-on region at velocity ratios $A_m \gtrsim 1.0$ and frequency ratio $f_{rot}^* \gtrsim 1.3$, the amplitude response decreases below $A_m \approx 0.1$. The range of rotary forcing parameters over which large reductions in amplitude response over the non-rotating value were observed is similar to those reported by Du & Sun (2015), despite the significantly lower Reynolds number. This shows that the rotary oscillation mechanism remains effective at suppressing VIV up to moderate Reynolds numbers ($Re > 1000$).

Two experiments were conducted in the upper branch ($U^* = 5.5$) to examine the presence of, or lack of, the rotary-lock-on and tertiary-lock-on regions. The response data of the cylinder also showed that the rotary-lock-on region extends to velocity ratios up to the limit of the present study at $A_m = 3.5$. Tertiary-lock-on initially disappears when the velocity ratio is increased pass $A_m \approx 1.6$, however, with further increases in A_m , tertiary-lock-on reappears at $A_m > 2.4$.

Using PIV, the wake of an elastically-mounted cylinder undergoing sinusoidal rotary oscillations was studied. A number of existing and new wake modes were observed. The 2SO and 2S-OC are wake patterns that resembles those previously reported in rotary oscillation of rigid cylinders (*e.g.* Tokumaru & Dimotakis (1991); Choi *et al.* (2002)). Both the 2SO and 2S-OC mode consist of the shedding of two single counter-rotating vortices offset from the streamwise centreline per cycle. Their differences are that the 2S-OC shed vortices comparatively closer to the streamwise centreline and that the vortices coalesce as they flow downstream. These two wake patterns were seen in and outside the rotary-lock-on region where the amplitude response is not minimal ($A_{10}^* \gtrsim 0.2$). Another wake mode that is foreign to previous VIV studies is the Mode I-O pattern. It involves the shedding of a pair of counter-rotating vortices per half shedding cycle, in each vortex pair, the smaller secondary vortex orbits around the larger primary vortex. It is observed in low amplitude response areas ($A_{10}^* \lesssim 0.2$) within the rotary-lock-on region. A similar wake structure was observed in a simulation of a rigid cylinder at a Reynolds number of $Re = 1000$ by Chou (1997). Du & Sun (2015) presented results showing the shedding of two pairs of tandem, counter-rotating vortices but they did not discuss other aspects of their behaviour. The CS mode, short for the chaotic shedding and decay of small vortex structures, was observed close to the boundary of the tertiary-lock-on region. Another new wake mode characterised by the shedding of two counter-rotating vortex pairs aligned in the cross-flow direction was observed in the tertiary-lock-on region in the lower amplitude response branch ($U^* = 8.0$). This mode is referred as CF2P.

From the study of an elastically-mounted cylinder undergoing sinusoidally-driven rotary oscillations, it is evident that rotary forcing and the phenomenon of ‘lock-on’ continue to have a significant impact on the dynamic response and wake structure of the cylinder at a range of moderate Reynolds numbers ($Re \gtrsim 1000$). Comparisons with previous low Re studies showed that trends such as the rotary-lock-on and tertiary-lock-on regions continue to exist at higher Reynolds numbers. In fact, the range of forcing velocity ratio and frequency ratio over which the largest reduction in the cylinder’s amplitude response was achieved is very similar between the present experimental study at $Re \gtrsim 1000$ and the low Reynolds number ($Re = 350$) simulation by Du & Sun (2015). It is concluded that rotary-oscillation remains effective at suppressing VIV at moderate Reynolds numbers.

6.2 Recommendations for future investigations

It is hoped that this thesis contributes to expanding the knowledge on the dynamic response and wake structure of an elastically-mounted cylinder undergoing constant rate rotation and sinusoidally-driven rotary oscillations. However, it is inevitable that a number of new fundamental questions have arisen from the results presented in this thesis. Some of these questions are listed in the final sections of the thesis.

6.2.1 Flow-induced vibration of a cylinder undergoing constant rate rotation

- It is known that an elastically-mounted cylinder undergoing VIV will exhibit hysteresis when it switches between the initial and upper amplitude response branches, *i.e.* when U^* is increased or decreased. Due to the expansive parameter space to survey, α was varied only in the increasing direction in the present study. It is possible for the cylinder to exhibit hysteresis as α is increased then decreased. In particular, at α values where there are abrupt jumps or drops in A_{10}^* amplitude and/or frequency responses
- Due to finite resources, it was impossible to capture PIV images at every data point. There are areas in the wake map where the wake structure of the cylinder is not quantified or understood. It has been shown that the C(AS) mode was observed across the entire vibration region at sufficiently high α . However, there is a discrepancy in the values of α at which the wake transitions from a 2S or P+S based mode to the C(AS) mode. More work should be done to study this boundary between the unsteady, 2S and 2P, and the steady, C(AS), wake modes. The vorticity sign switching phenomenon associated with the P+S mode at certain values of α and U^* is another interesting discovery that should be investigated. Furthermore, no PIV imaging was performed in the desynchronised region where the cylinder showed some variations in amplitude response (see $U^* = 10$, $\alpha = 0.5 - 2.5$). It is unknown if the variation in amplitude response is associated with any changes to the wake structure of the cylinder. These are some of the questions that have arisen from the present study.

6.2.2 Flow-induced vibration of a cylinder undergoing sinusoidally-driven rotary oscillations

- From the present study, it is evident that the response of the cylinder with rotary forcing showed some differences between the two U^* cases. Limited work has been done to examine the evolution of the cylinder’s response over a large range of U^* when the cylinder is undergoing rotary forcing at fixed values of velocity ratio (A_m) and frequency ratio (f_{rot}^*). At a fixed velocity ratio of $A_m = 1$ and frequency ratio of $f_{rot}^* = 1$, the cylinder showed amplitude responses that are significantly higher than the non-rotating equivalent. Additional combinations of A_m and f_{rot}^* should be investigated. A case that is of particular interest is at velocity

ratio $A_m = 1.5$, and frequency ratio $f_{rot}^* = 2$. This is a point in the A_m - f_{rot}^* domain where vibration is effectively suppressed by rotary forcing.

- As PIV imaging was employed to survey the $A_m - f_{rot}^*$ parameter space in a grid-like matter, some points of interest such as the boundaries of the rotary-lock-on and tertiary-lock-on regions were not thoroughly investigated. Further investigation in selective areas can better show how the wake evolves and behaves as the cylinder becomes rotary-lock-on.
- The two reduced velocity cases examined in the present thesis belong to the peak of the upper branch ($U^* = 5.5$) and centre of the lower branch ($U^* = 8.0$). A parametric study at reduced velocities associated with the highest point of the initial branch, the beginning of the upper branch, the end of the upper branch and the beginning of the lower branch will provide a better understanding of the response of an elastically-mounted cylinder undergoing rotary forcing at U^* associated with amplitude branch transitions. This will be a highly complicated study as the switching behaviour associated with frequency modulation in rotary oscillation will be combined with switching and hysteresis behaviour of VIV.
- Hysteresis is a known phenomenon in VIV studies. Due to the expansive parameter space, A_m remained constant while f_{rot}^* is increased in the present study. A study on the hysteresis of varying A_m and f_{rot}^* can provide a better understanding of the dynamic response of the cylinder near the rotary-lock-on and tertiary-lock-on boundaries.

Appendix A

Rotary Motion Validation

A.1 Constant rate rotation motion profile validation

A rotation device was used to attach the test cylinder and control its rotational motion. Motor control systems are susceptible to errors and require fine tuning and testing. It was therefore imperative to validate that the prescribed motion was achieved over a range of rotation rates investigated. Figure A.1 presents validation data of the cylinder's constant rotation motion. Figure A.1(a) shows that the measured output (ω_{out}) from the rotary encoder overlaps the ideal input value (ω_{in}) and varied linearly. Figure A.1(b) presents the relative error (δ_{ω}) of ω_{out} over the tested range of ω_{in} . The mean value of δ_{ω} over the tested range of rotation rates is 0.222%. This shows that the motion of the cylinder as it undergoes constant rate rotation is accurate.

A.2 Sinusoidal rotary oscillation motion profile validation

The sinusoidal rotary oscillation motion profile of the cylinder was measured as the rotation rig and test cylinder were subjected to tests on a rigid test jig. The motion profile was measured through the optical rotary encoder built into the rotation rig. The measured profiles were analysed and compared against an ideal signal of the same forcing parameters. A number of forcing parameters were tested, here two cases are presented to cover the extremities of the independent parameters: (1) reduced velocity (U^*), (2) forcing velocity ratio (A_m), and (3) forcing frequency ratio (f_{rot}^*).

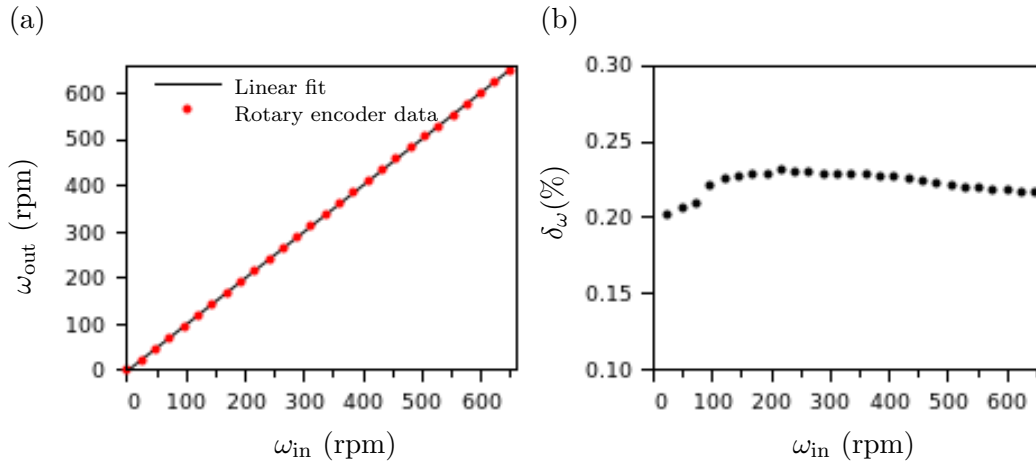


FIGURE A.1: Validation of the constant rotation motion of the cylinder. (a) presents a comparison of the input (ω_{in}) and measured output (ω_{out}) rotation rate of the cylinder in rpm. (b) presents the relative error (δ) between ω_{in} and ω_{out} .

Appendix A. Rotary Motion Validation

Fig. 5.1(a) presents the low U^* case, which is associated with the initial amplitude response branch of a non-rotating cylinder ($U^* = 3.0$) and at a low forcing velocity ratio of $A_m = 0.1$ and a low frequency ratio of $f_{rot}^* = 0.25$. Fig. 5.1(b) presents the high U^* case that is associated with the lower amplitude response branch of a non-rotating cylinder ($U^* = 8.0$) and at a high forcing velocity ratio of $A_m = 2.0$ and a high frequency ratio of $f_{rot}^* = 4.50$.

Fig. A.2(a) presents a small sample of the time history of the cylinder's rotary motion and fig. A.2(c) presents a larger sample of the rotary displacement time history. The rotary displacement, in terms of velocity ratio (A_m), is presented as a function of oscillation periods (T). The reader should be mindful that the A_m of the cylinder varies with time depending on the phase of the rotary oscillation cycle. Based on the definition described in eq. 2.27, the forcing parameter commonly referred as 'velocity ratio' (A_m) is the peak value. The measured and ideal motion profiles are represented by the black and red data series, respectively. From the figure (a) it is evident that the measured rotary motion profile follows the ideal input very closely. At higher forcing values, the measured rotary motion continues to follow the ideal input (see fig. A.3(a) and (c)).

Fig. A.2(b) presents a power spectra density (PSD) of the cylinder's rotary displacement as a function of normalised frequency response, f^* . The power density is normalised by the peak power and the vertical dashed line represents the input rotary forcing frequency, f_{osc} . Fig. A.2(b) shows that the measured $f_{rot}^* = 0.2422$, is within 3% of the input value. This value is typical at low values of U^* , A_m and f_{rot}^* . As the values of the three independent variables were increased, f_{rot}^* typically falls within 0.5% of the input value. This is shown in fig. A.3(b) where the measured $f_{rot}^* = 4.4922$ is within 0.2% of the input value of 4.5.

Physical limitations of the motor and motor controller meant the motion the cylinder was not perfectly sinusoidal. Small mechanical slippages can cause the sinusoidal motion profile to deviate from its zero position. When small this deviation, or drift, from the rotational zero position is unlikely to affect the overall response of the cylinder, large values, however, could be detrimental to the quality of the study.

Fig. A.2(d) presents the rotational deviation (θ_{dev}), in radians, of the cylinder from its zero position as a function of T . It can be seen that the measured rotary motion is not perfectly sinusoidal about its zero position as the motor slips in one direction as it oscillates. This results in monotonic increases in θ_{dev} with T . However, θ_{dev} is small as the total deviation over 10 oscillation periods are less than $\theta_{dev} \lesssim 0.035$ rad. As the values of the three independent variables were increased (see Fig. A.3(d)), θ_{dev} decreases as its value fall to within $\theta_{dev} \pm 0.002$ rad over T .

Fig. A.2(e) presents the mean relative error (δ_{A_m}) in A_m between the measured and ideal motion profiles over a complete oscillation cycle, as a function of T . This error analysis shows that over each oscillation cycle, the δ_{A_m} is less than 0.4%. As the values of the three independent variables were increased (see fig. A.3(e)), δ_{A_m} decreased to values less than 0.1%.

The analysis of the rotary motion profile shows that the apparatus and control software used in the present experiment can accurately simulate and control the cylinder model to undergo sinusoidal motions at a range of forcing velocity and frequency ratios.

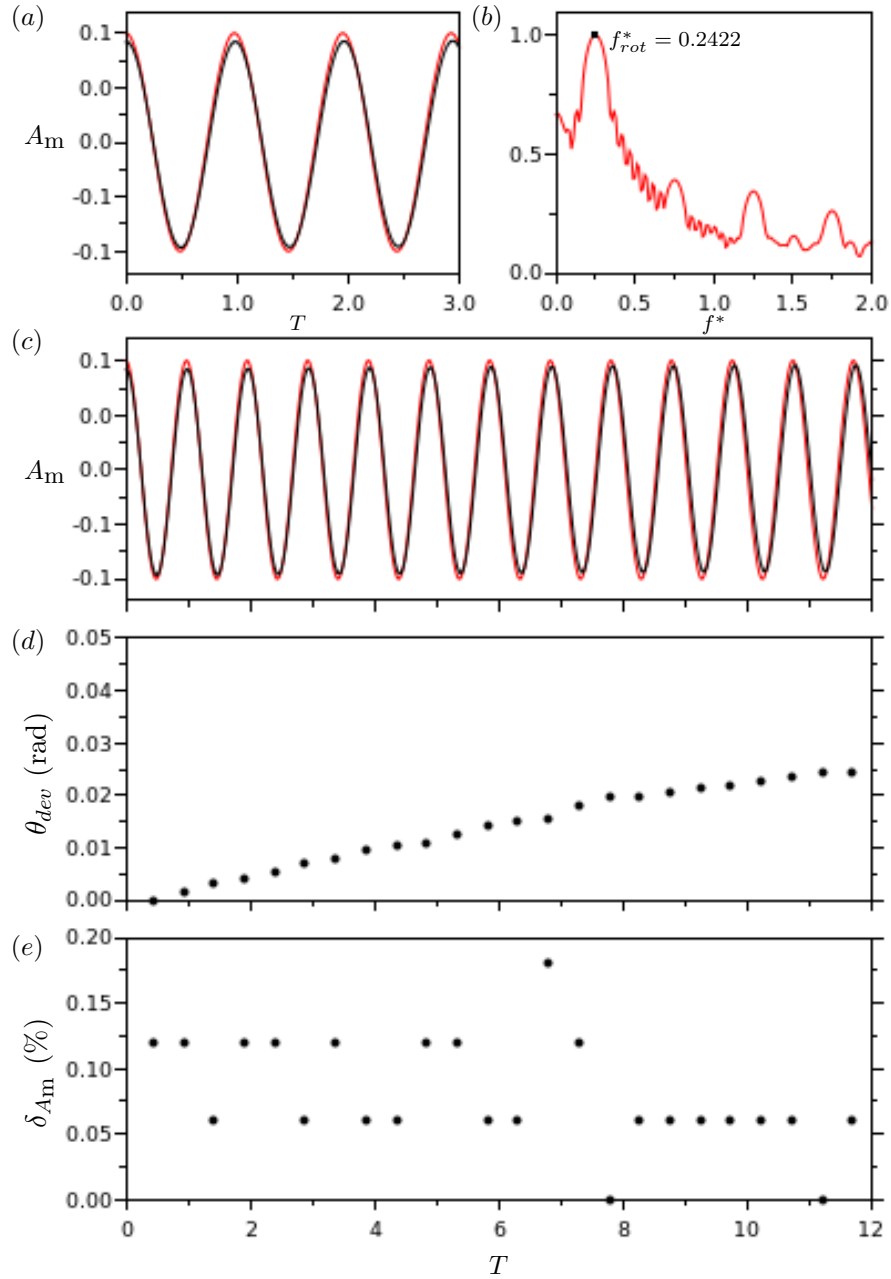


FIGURE A.2: The motion profile of a cylinder undergoing sinusoidal rotary oscillations at a reduced velocity that is associated with the upper amplitude response branch of a non-rotating cylinder ($U^* = 5.0$) and at low forcing velocity ratio of $A_m = 0.1$ and a low frequency ratio of $f_{rot}^* = 0.25$. (a) presents a close-up view of the sinusoidal rotary displacement time history as a function of A_m and oscillation period (T). (c) presents a larger sample of the rotary displacement time history. In (a) and (c), the red data series is the ideal input and the black data series is the measured rotary displacement. (b) presents the power spectra density of the cylinder's rotary displacement as a function of f_{rot}^* . The f_{rot}^* that corresponds to the peak power is labelled. (d) presents the rotational deviation (θ_{dev}), in radians, of the cylinder from its zero position as a function of T . (e) presents the mean relative error (δ_{A_m}), in percent, of A_m between the measured and ideal motion profiles over a complete oscillation cycle as a function of T .

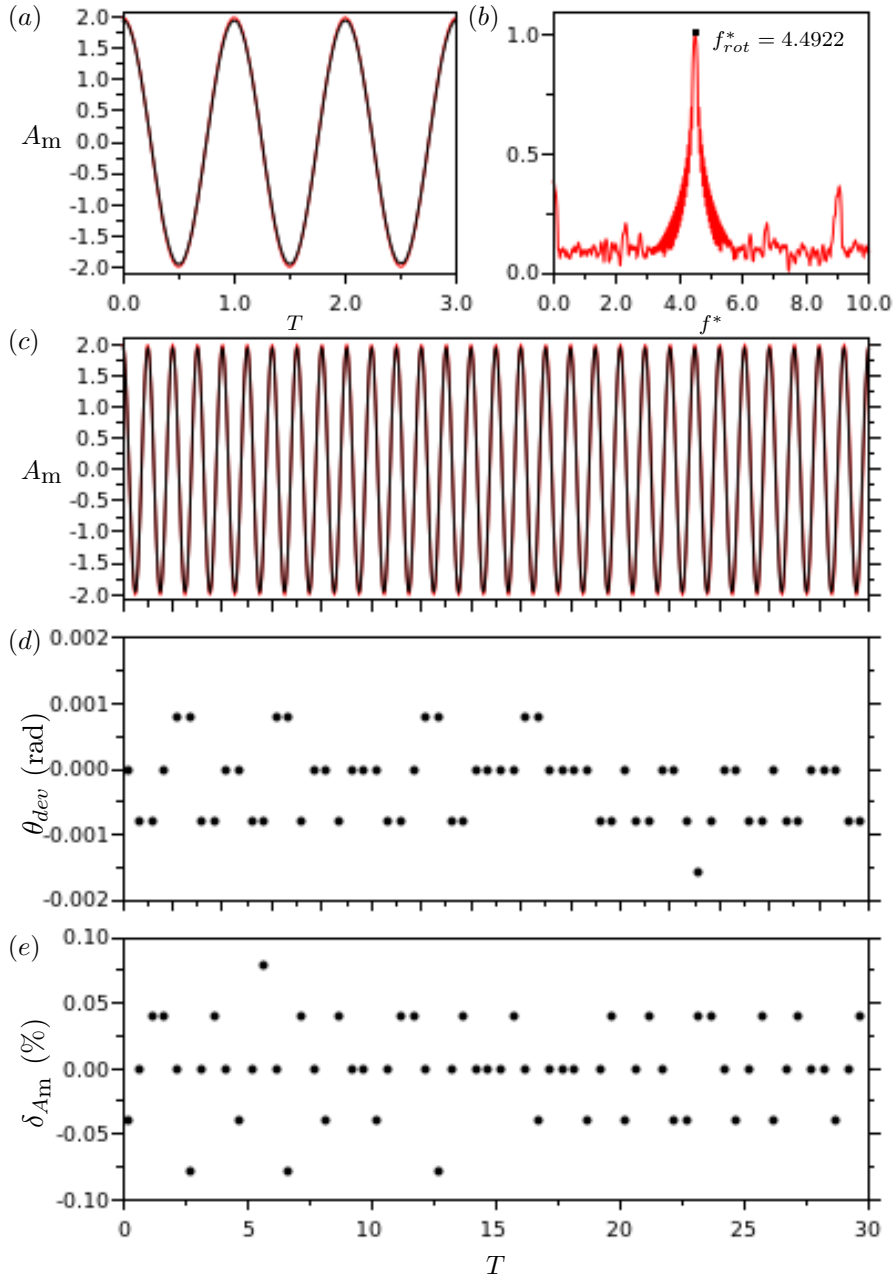


FIGURE A.3: The motion profile of a cylinder undergoing sinusoidal rotary oscillations at a reduced velocity that is associated with the lower amplitude response branch of a non-rotating cylinder ($U^* = 8.0$) and at low forcing velocity ratio of $A_m = 2.0$ and a low frequency ratio of $f_{rot}^* = 4.5$. (a) presents a close-up view of the sinusoidal rotary displacement time history as a function of A_m and oscillation period (T). (c) presents a larger sample of the rotary displacement time history. In (a) and (c), the red data series is the ideal input and the black data series is the measured rotary displacement. (b) presents the power spectra density (PSD) of the cylinder's rotary displacement as a function of f_{rot}^* . The f_{rot}^* that corresponds to the peak power is labelled. (d) presents the rotational deviation (θ_{dev}), in radians, of the cylinder from its zero position as a function of T . (e) presents the mean relative error (δ_{A_m}), in percent, of A_m between the measured and ideal motion profiles over a complete oscillation cycle as a function of T .

References

- ADRIAN, R. 1991 Particle-Imaging Techniques For Experimental Fluid-Mechanics. *Annual Review of Fluid Mechanics* **23**, 261–304.
- ASSI, G., BEARMAN, P. & KITNEY, N. 2009 Low drag solutions for suppressing vortex-induced vibration of circular cylinders. *Journal of Fluids and Structures* **25** (4), 666–675.
- BADR, H., COUTANCEAU, M., DENNIS, S. & MENARD, C. 1990 Unsteady flow past a rotating circular cylinder at reynolds numbers 10³ and 10⁴. *Journal of Fluid Mechanics* **220**, 459–484.
- BAEK, S. & SUNG, H. 2000 Quasi-periodicity in the wake of a rotationally oscillating cylinder. *Journal of fluid mechanics*. *Journal of Fluid Mechanics* **408**, 275–300.
- BAEK, S.-J. & SUNG, H. J. 1998 Numerical simulation of the flow behind a rotary oscillating circular cylinder. *Physics of Fluids* **10** (4), 869–876.
- BEARMAN, P. 1984 Vortex shedding from oscillating bluff bodies. *Annual Review of Fluid Mechanics* **16** (1), 195–222.
- BEARMAN, P. & BRANKOVIĆ, M. 2004 Experimental studies of passive control of vortex-induced vibration. *European Journal of Mechanics - B/Fluids* **23** (1), 9–15.
- BILLAH, K. & SHINOZUKA, M. 1991 Fluctuations of dynamic pressure and white noise assumption in flow-induced vibration problems. *Journal of Sound and Vibration* **147** (1), 179–183.
- BISHOP, R. & HASSAN, A. 1964 The lift and drag forces on a circular cylinder oscillating in a flowing fluid. In *Proceedings of the Royal Society of London A: Mathematical, Physical and Engineering Sciences*, , vol. 277, pp. 51–75. The Royal Society.
- BLACKBURN, H. & HENDERSON, R. 1999 A study of two-dimensional flow past an oscillating cylinder. *Journal of Fluid Mechanics* **385**, 255–286.
- BLEVINS, R. 1977 *Flow-induced vibration*, 1st edn. Van Nostrand Reinhold, Co., New York, NY.
- BLEVINS, R. 1990 *Flow-induced vibration*, 2nd edn. Malabar: Krieger Publishing Company.
- BOURGUET, R. & LO JACONO, D. 2014 Flow-induced vibrations of a rotating cylinder. *Journal of Fluid Mechanics* **740**, 342–380.
- BRANKOVIC, M. 2004 Vortex induced-vibration attenuation of circular cylinders with low mass and damping. Phd, Imperial College London.
- BRIKA, D. & LANEVILLE, A. 1993 Vortex-induced vibrations of a long flexible circular cylinder. *Journal of Fluid Mechanics* **250**, 481–508.
- CARBERRY, J., SHERIDAN, J. & ROCKWELL, D. 2001 Forces and wake modes of an oscillating cylinder. *Journal of Fluids and Structures* **15** (1), 523–532.

References

- CARBERRY, J., SHERIDAN, J. & ROCKWELL, D. 2005 Controlled oscillations of a cylinder: forces and wake modes. *Journal of Fluid Mechanics* **538**, 31–69.
- CHEN, M.-H. 2000 Numerical study of vortex shedding from a rotating cylinder immersed in a uniform flow field. *International Journal for Numerical Methods in Fluids* **32**, 545–567.
- CHEN, Y.-M., OU, Y.-R. & PEARLSTEIN, A. 1993 Development of the wake behind a circular cylinder impulsively started into rotary and rectilinear motion. *Journal of Fluid Mechanics* **253**, 449–484.
- CHENG, M. 2001 Numerical investigation of a rotationally oscillating cylinder in mean flow. *Journal of Fluid Mechanics* **15**, 981–1007.
- CHENG, M., LIU, G. & LAM, K. 2001 Numerical simulation of flow past a rotationally oscillating cylinder. *Computers & Fluids* **30** (3), 365–392.
- CHEW, Y., CHENG, M. & LUO, S. 1995 A numerical study of flow past a rotating circular cylinder using a hybrid vortex scheme. *Journal of Fluid Mechanics* **299**, 35–71.
- CHOI, S., CHOI, H. & KANG, S. 2002 Characteristics of flow over a rotationally oscillating cylinder at low Reynolds number. *Physics of Fluids* **14** (8), 2767–2777.
- CHOU, M.-H. 1997 Synchronization of vortex shedding from a cylinder under rotary oscillation. *Computer & Fluids* **26** (8), 755–774.
- COUTANCEAU, M. & MENARD, C. 1985 Influence of rotation on the near-wake development behind an impulsively started circular cylinder. *Journal of Fluid Mechanics* **158**, 399–446.
- D'ADAMO, J., GODOY-DIANA, R. & WESFREID, J. E. 2015 Centrifugal instability of stokes layers in crossflow: the case of a forced cylinder wake. In *Proc. R. Soc. A*, , vol. 471, p. 20150011. The Royal Society.
- DÍAZ, F., GAVALDÀ, J., KAWALL, J., KEFFER, J. & GIRALT, F. 1983 Vortex shedding from a spinning cylinder. *Physics of Fluids* **26** (12), 3454–3460.
- DONG, S., TRIANTAFYLLOU, G. & KARNIADAKIS, G. 2008 Elimination of vortex streets in bluff-body flows. *Physical Review Letters* **100** (20), 204501.
- DU, L. & SUN, X. 2015 Suppression of vortex-induced vibration using the rotary oscillation of a cylinder. *Physics of Fluids* **27** (2), 023603.
- EL AKOURY, R., BRAZA, M., PERRIN, R., HARRAN, G. & HOARAU, Y. 2008 The three-dimensional transition in the flow around a rotating cylinder. *Journal of Fluid Mechanics* **607**, 1–11.
- FENG, C. 1968 The measurement of vortex induced effects in flow past stationary and oscillating circular and d-section cylinders. Masters, National Taiwan University.
- FOURAS, A., LO JACONO, D. & HOURIGAN, K. 2008 Target-free stereo piv: A novel technique with inherent error estimation and improved accuracy. *Experiments in Fluids* **44** (2), 317–329.
- FOURAS, A. & SORIA, J. 1998 Accuracy of out-of-plane corticity measurements derived from in-plane velocity field data. *Experiments in Fluids* **25** (5), 409–430.
- FREDSOE, J. & SUMER, M. 1997 *Hydrodynamics around cylindrical structures*. World Scientific.

-
- FUJISAWA, N., IKEMOTO, K. & NAGAYA, K. 1998 Vortex shedding resonance from a rotationally oscillating cylinder. *Journal of Fluids and Structures* **12**, 1041–1053.
- GABBAI, R. & BENAROYA, H. 2005 An overview of modeling and experiments of vortex-induced vibration of circular cylinders. *Journal of Sound and Vibration* **282**, 575–616.
- GERRARD, J. 1966 The mechanics of the formation region of vortices behind bluff bodies. *Journal of fluid mechanics* **25**, 401–413.
- GOVARDHAN, R. & WILLIAMSON, C. 2000 Modes of vortex formation and frequency response of a freely vibrating cylinder. *Journal of Fluid Mechanics* **420**, 85–130.
- GOVARDHAN, R. & WILLIAMSON, C. 2002 Resonance forever: existence of a critical mass and an infinite regime of resonance in vortex-induced vibration. *Journal of Fluid Mechanics* **473**, 147–166.
- GOVARDHAN, R. & WILLIAMSON, C. 2006 Defining the modified griffin plotin vortex-induced vibration: revealing the effect of reynolds number using controlled damping. *Journal of Fluid Mechanics* **561**, 147–180.
- GRIFFIN, O., SKOP, R. & KOOPMANN, G. 1973 The vortex-excited resonant vibrations of circular cylinders. *Journal of Sound and Vibration* **31** (2), 235–249.
- HE, J.-W., GLOWINSKI, R., METCALFE, R., NORDLANDER, A. & PERIAUX, J. 2000 Active Control and Drag Optimization for Flow Past a Circular Cylinder. *Journal of Computational Physics* **163**, 83–117.
- HOVER, F. S., TVEDT, H. & TRIANTAFYLLOU, M. S. 2001 Vortex-induced vibrations of a cylinder with tripping wires. *Journal of Fluid Mechanics* **448**, 175–195.
- HUERRE, P. & MONKEWITZ, P. A. 1990 Local and global instabilities in spatially developing flows. *Annual Review of Fluid Mechanics* **22** (1), 473–537.
- KANG, S., CHOI, H. & LEE, S. 1999 Laminar flow past a rotating circular cylinder. *Physics of Fluids* **11** (11), 3312–3321.
- KARABELAS, S., KOUMROGLOU, B., ARGYROPOULOS, C. & MARKATOS, N. 2012 High reynolds number turbulent flow past a rotating cylinder. *Applied Mathematical Modelling* **36** (1), 379–398.
- KHALAK, A. & WILLIAMSON, C. 1996 Dynamics of a hydroelastic cylinder with very low mass and damping. *Journal of Fluids and Structures* **10** (5), 455–472.
- KHALAK, A. & WILLIAMSON, C. 1997a Fluid forces and dynamics of a hydroelastic structure with very low mass and damping. *Journal of Fluids and Structures* **11**, 973–982.
- KHALAK, A. & WILLIAMSON, C. 1997b Fluid forces and dynamics of a hydroelastic structure with very low mass and damping. *Journal of Fluids and Structures* **11** (8), 973–982.
- KHALAK, A. & WILLIAMSON, C. 1999 Motions, forces and mode transitions in vortex-induced vibrations at low mass-damping. *Journal of fluids and Structures* **13** (7-8), 813–851.
- KLAMO, J. 2007 Effects of damping and Reynolds number on vortex-induced vibrations. Phd, California Institute of Technology.
- KUMAR, R., SOHN, C.-H. & GOWDA, B. 2008 Passive Control of Vortex-Induced Vibrations: An Overview. *Recent Patents on Mechanical Engineering* **1** (1), 1–11.
-

References

- LEONTINI, J., STEWART, B., THOMPSON, M. & HOURIGAN, K. 2006 Wake state and energy transitions of an oscillating cylinder at low reynolds number. *Physics of Fluids* **18** (6), 067101.
- LEONTINI, J., THOMPSON, M. & HOURIGAN, K. 2007 Three-dimensional transition in the wake of a transversely oscillating cylinder. *Journal of Fluid Mechanics* **577**, 79.
- LIGHTHILL, J. 1986 Fundamentals concerning wave loading on offshore structures. *Journal of Fluid Mechanics* **173**, 667–681.
- LO JACONO, D., LEONTINI, J., THOMPSON, M. & SHERIDAN, J. 2010 Modification of three-dimensional transition in the wake of a rotationally oscillating cylinder. *Journal of Fluid Mechanics* **643**, 349–362.
- LU, X.-Y. & SATO, J. 1996 A numerical study of flow past a rotationally oscillating circular cylinder. *Journal of Fluids and Structures* **10** (8), 829–849.
- LUCOR, D. & TRIANTAFYLLOU, M. 2008 Parametric study of a two degree-of-freedom cylinder subject to vortex-induced vibrations. *Journal of Fluids and Structures* **24** (8), 1284–1293.
- MAGNUS, G. 1993 On the deviation of projectiles; and on a remarkable phenomenon of rotating bodies. *Memoirs of the Royal Academy, Berlin* p. 210.
- MITTAL, S. 2001 Control of flow past bluff bodies using rotating control cylinders. *Journal of fluids and structures* **15** (2), 291–326.
- MITTAL, S. & KUMAR, B. 2003 Flow past a rotating cylinder. *Journal of Fluid Mechanics* **476**, 303–334.
- MORSE, T., GOVARDHAN, R. & WILLIAMSON, C. 2008 The effect of end conditions on the vortex-induced vibration of cylinders. *Journal of Fluids and Structures* **24** (8), 1227–1239.
- NAUDASCHER, E. & ROCKWELL, D. 2005 *Flow-induced vibration*, 1st edn. Dover Publications, Inc., New York, NY.
- NAZARINIA, M., LO JACONO, D., THOMPSON, M. & SHERIDAN, J. 2009 Flow behind a cylinder forced by a combination of oscillatory translational and rotational motions. *Physics of Fluids* **21** (5), 051701.
- NEMES, A., ZHAO, J., LO JACONO, D. & SHERIDAN, J. 2012 The interaction between flow-induced vibration mechanisms of a square cylinder with varying angles of attack. *Journal of Fluid Mechanics* **710**, 102–130.
- NORBERG, C. 1994 An experimental investigation of the flow around a circular cylinder: influence of aspect ratio. *Journal of Fluid Mechanics* **258**, 287–316.
- NORBERG, C. 2001 Flow around a circular cylinder: aspects of fluctuating lift. *Journal of Fluids and Structures* **15** (3-4), 459–469.
- OKAJIMA, A., TAKATA, H. & ASANUMA, T. 1975 Viscous flow around a rotationally oscillating circular cylinder. *ISAS report* **12**, 311–338.
- OWEN, J. C., BEARMAN, P. W. & SZEWCZYK, A. A. 2001 Passive control of viv with drag reduction. *Journal of Fluids and Structures* **15** (3-4), 597–605.
- PAIDOUSSIS, M., PRICE, S. & DE LANGRE, E. 2007 *Fluid-structure interactions: cross-flow-induced instabilities*, 1st edn. Cambridge University Press.

-
- PARKINSON, G. & WAWZONEK, M. 1981 Some considerations of combined effects of galloping and vortex resonance. *Journal of Wind Engineering and Industrial Aerodynamics* **8** (1-2), 135–143.
- PRALITS, J., BRANDT, L. & GIANNETTI, F. 2010 Instability and sensitivity of the flow around a rotating circular cylinder. *Journal of Fluid Mechanics* **650**, 513.
- PRALITS, J., GIANNETTI, F. & BRANDT, L. 2013 Three-dimensional instability of the flow around a rotating circular cylinder. *Journal of Fluid Mechanics* **730**, 5–18.
- PRANDTL, L. 1925 The magnus effect and windpowered ships. *Naturwissenschaften* **13**, 93–108.
- PRANDTL, L. & TIETJENS, O. 1934 *Applied hydro-and aerodynamics*.
- RADI, A., THOMPSON, M., RAO, A., HOURIGAN, K. & SHERIDAN, J. 2013 Experimental evidence of new three-dimensional modes in the wake of a rotating cylinder. *Journal of Fluid Mechanics* **734**, 567–594.
- RAFFEL, M., WILLERT, C., WERELEY, S. & KOMPENHANS, J. 2007 *Particle Image Velocimetry: A practical guide*, 2nd edn. Springer.
- RAO, A., LEONTINI, J., THOMPSON, M. & HOURIGAN, K. 2013 Three-dimensionality in the wake of a rotating cylinder in a uniform flow. *Journal of Fluid Mechanics* **717**, 1–29.
- RAO, A., RADI, A., LEONTINI, J., THOMPSON, M., SHERIDAN, J. & HOURIGAN, K. 2015 A review of rotating cylinder wake transitions. *Journal of Fluids and Structures* **53**, 2–14.
- ROSHKO, A. 1993 Perspectives on bluff body aerodynamics. *Journal of Wind Engineering and Industrial Aerodynamics* **49**, 79–100.
- RYAN, K., THOMPSON, M. & HOURIGAN, K. 2005 Variation in the critical mass ratio of a freely oscillating cylinder as a function of reynolds number. *Physics of Fluids* **17** (3), 038106.
- SARPKAYA, T. 1995 Hydrodynamic damping, flow-induced oscillations, and biharmonic response. *Journal of Offshore Mechanics and Arctic Engineering* **117**, 232–238.
- SARPKAYA, T. 2004 A critical review of the intrinsic nature of vortex-induced vibrations. *Journal of Fluids and Structures* **19** (4), 389–447.
- SEYED-AGHAZADEH, B. & MODARRES-SADEGHI, Y. 2015 An experimental investigation of vortex-induced vibration of a rotating circular cylinder in the crossflow direction. *Physics of Fluids* **27** (6), 067101.
- SHIELS, D. & LEONARD, A. 2001 Investigation of a drag reduction on a circular cylinder in rotary oscillation. *Journal of Fluid Mechanics* **431**, 297–322.
- SINGH, S. & MITTAL, S. 2005 Vortex-induced oscillations at low reynolds numbers: hysteresis and vortex-shedding modes. *Journal of Fluids and Structures* **20** (8), 1085–1104.
- STANSBY, P. & RAINEY, R. 2001 On the orbital response of a rotating cylinder in a current. *Journal of Fluid Mechanics* **439**, 87–108.
- STAUBLI, T. 1983 Calculation of the vibration of an elastically mounted cylinder using experimental data from forced oscillation. *ASME J. Fluids Eng* **105** (2), 225–229.
- STOJKOVIĆ, D., BREUER, M. & DURST, F. 2002 Effect of high rotation rates on the laminar flow around a circular cylinder. *Physics of Fluids* **14** (9), 3160–3178.
-

References

- STOJKOVIĆ, D., SCHÖN, P., BREUER, M. & DURST, F. 2003 On the new vortex shedding mode past a rotating circular cylinder. *Physics of Fluids* **15** (5), 1257–1260.
- STROUHAL, V. 1878 Über eine besondere art der tonerregung. *Annalen der Physik und Chemie* **5**, 216–251.
- SWANSON, W. 1961 The Magnus effect: A summary of investigations to date. *Journal of Basic Engineering* .
- SZEPESSY, S. & BEARMAN, P. 1992 Aspect ratio and end plate effects on vortex shedding from a circular cylinder. *Journal of Fluid Mechanics* **234**, 191–217.
- TANEDA, S. 1956 Experimental investigation of the wakes behind cylinders and plates at low reynolds numbers. *Journal of the Physical Society of Japan* **11** (3), 302–307.
- TANEDA, S. 1978 Visual observations of the flow past a circular cylinder performing a rotatory oscillation. *Journal of the Physical Society of Japan* **45** (3), 1038–1043.
- THIRIA, B., GOUJON-DURAND, S. & WESFREID, J. 2006 The wake of a cylinder performing rotary oscillations. *Journal of Fluid Mechanics* **560**, 123–147.
- THOM, A. 1935 *On the effect of discs on the air forces on a rotating cylinder*. HM Stationery Office.
- TOKUMARU, P. & DIMOTAKIS, P. 1991 Rotary oscillation control of a cylinder wake. *Journal of Fluid Mechanics* **224**, 77–90.
- TOKUMARU, P. & DIMOTAKIS, P. 1993 The lift of a cylinder executing rotary motions in a uniform flow. *Journal of Fluid Mechanics* **255**, 1–10.
- WILLIAMSON, C. 1988 The existence of two stages in the transition to three-dimensionality of a cylinder wake. *Physics of Fluids* **31** (11), 3165–3168.
- WILLIAMSON, C. 1989 Oblique and parallel modes of vortex shedding in the wake of a circular cylinder at low Reynolds numbers. *Journal of Fluid Mechanics* **206**.
- WILLIAMSON, C. 1992 The natural and forced formation of spot-like vortex dislocations in the transition of a wake. *Journal of Fluid Mechanics* **243**, 393–441.
- WILLIAMSON, C. 1996 Vortex dynamics in the cylinder wake. *Annual Review of Fluid Mechanics* .
- WILLIAMSON, C. & BROWN, G. 1998 A series in $1/Re$ to represent the strouhal–reynolds number relationship of the cylinder wake. *Journal of Fluids and Structures* **12** (8), 1073–1085.
- WILLIAMSON, C. & GOVARDHAN, R. 2004a Vortex-Induced Vibrations. *Annual Review of Fluid Mechanics* **36** (1), 413–455.
- WILLIAMSON, C. & GOVARDHAN, R. 2004b Vortex-induced vibrations. *Annual Review of Fluid Mechanics* **36**, 413–455.
- WILLIAMSON, C. & GOVARDHAN, R. 2008 A brief review of recent results in vortex-induced vibrations. *Journal of Wind Engineering and Industrial Aerodynamics* **96**, 713–735.
- WILLIAMSON, C. & ROSHKO, A. 1988 Vortex formation in the wake of an oscillating cylinder. *Journal of fluids and structures* **2** (4), 355–381.

- WONG, H. & KOKKALIS, A. 1982 A comparative study of three aerodynamic devices for suppressing vortex-induced oscillation. *Journal of Wind Engineering and Industrial Aerodynamics* **10** (1), 21–29.
- ZHAO, J. 2012 Flow-Induced Vibration of Circular and Square Cylinders with Low Mass and Damping. Phd, Monash University.
- ZHAO, J., LEONTINI, J., LO JACONO, D. & SHERIDAN, J. 2014a Chaotic vortex induced vibrations. *Physics of Fluids* **26** (12), 121702.
- ZHAO, J., LEONTINI, J., LO JACONO, D. & SHERIDAN, J. 2014b Fluid–structure interaction of a square cylinder at different angles of attack. *Journal of Fluid Mechanics* **747**, 688–721.
- ZHAO, J., NEMES, A., JACONO, D. L. & SHERIDAN, J. 2012 Comparison of fluid forces and wake modes between free vibration and tracking motion of a circular cylinder. In *18th Australian Fluid Mechanics Conference. Launceton, Australia*.
- ZHAO, M., CHENG, L. & LU, L. 2014c Vortex induced vibrations of a rotating circular cylinder at low Reynolds number. *Physics of Fluids* **26** (7), 073602.